CO₂ Capture by Aqueous Absorption

Summary of Fourth Quarterly Progress Reports 2012

by Gary T. Rochelle

Supported by the Luminant Carbon Management Program

and the

Industrial Associates Program for CO₂ Capture by Aqueous Absorption

Department of Chemical Engineering

The University of Texas at Austin

January 31, 2013

Introduction

This research program is focused on the technical obstacles to the deployment of CO_2 capture and sequestration from flue gas by alkanolamine absorption/stripping and on integrating the design of the capture process with the aquifer storage/enhanced oil recovery process. The objective is to develop and demonstrate evolutionary improvements to monoethanolamine (MEA) absorption/stripping for CO_2 capture from gas-fired and coal-fired flue gas. The Luminant Carbon Management Program and the Industrial Associates Program for CO_2 Capture by Aqueous Absorption support 16 graduate students. Most of these students have prepared detailed quarterly progress reports for the period October 1, 2012 to December 31, 2012.

Conclusions

Thermodynamics and Rates

The high temperature P_{CO2}^* result for 8 m MAPA matches low temperature data at low loading. The heat of CO_2 absorption in 8 m MAPA is 81 kJ/mol at lean loading.

6 m PZ/2 m EDA has a capacity of 0.63 mol CO_2/kg solv, which is about 25% lower than that of 8 m PZ but 25% higher than 7 m MEA. The heat of absorption is 75 kJ/mol at lean loading, which is competitive with 7 m MEA. This blend has a high absorption rate across the operating range, with a $k_g'_{avg}$ of 8.6 $X10^7$ mol/Pa·s·m², which is competitive with 8 m PZ, and approximately twice that of 7 m MEA.

A rigorous thermodynamic model has been developed for PZ-AEP-H₂O-CO₂ in Aspen Plus® using the Electrolyte Nonrandom Two-Liquid (e-NRTL) activity coefficient model.

Modeling

Increasing the solvent flow rate from 1.1 times the minimum L/G to 1.2 times the minimum L/G decreases absorber height by 25 to 30% and decreases capacity by 8 to 11%.

The interheated stripper reduces W_{EQ} by reducing steam losses in the stripper.

Increasing the regeneration temperature from 120 °C to 150 °C for 8 m PZ improves W_{EQ} for all configurations, but the improvement is on the order of 0.1–0.3 kJ/mol CO_2.

1

Adding a low temperature adiabatic flash to the two-stage flash with cold rich bypass has a negligible effect on process performance.

Comparison of 3 intercooling configurations for NGCC applications (4.1% CO_2) resulted in the following:

- When compared at an operating point of $1.2*L_{minimum}$, the simple recycle intercooling design provides benefits (reduced packing requirement, increased rich loading) over in and out intercooling at recycle rates above ~ 1 $L_{Recycle}/G$.
- When compared at constant rich loading (0.365 mols CO_2/mols alkalinity), recycle with bypass resulted in the lowest packing requirements at low recycle rates (0.5 to 2 $L_{Recycle}/G$). The bypass intercooling reduced packing requirements by 47% over simple recycle and by 8% over in and out intercooling when operated at 0.5 $L_{Recycle}/G$.
- At higher recycle rates (>2 $L_{Recycle}/G$), the bypass and simple recycle design are indistinguishable. At a recycle rate of 8 $L_{Recycle}/G$, a packing reduction of 46% compared to in and out intercooling is achieved with either recycle design.
- The bypass configuration should be used at low recycle rates (0.5 to 2 $L_{Recycle}/G$) while the simple recycle design should be used for high recycle rates (>2 $L_{Recycle}/G$). Economic analysis is needed to determine the operating point which maximizes benefits over standard in and out intercooling design.

In the simple stripper with cold rich bypass, rich packing height affects energy equivalent work more significantly than lean packing.

By varying rich packing from no packing to 1.0 meter, 12.7% energy savings can be achieved, however, the effect of increasing lean packing height is less than 1% improvement.

In a simple stripper with rich exchanger bypass configuration, optimum bypass is 6.5% giving 29.6 (kJ/mol CO_2) equivalent work.

For structured packing, mixing point density can be calculated by the equation:

$$M = \frac{6}{B * h * B \tan \theta}$$

Random packing with a smaller nominal size has larger $k_{L/G}$ because it has more mixing points.

For random packing, mixing points density can be calculated by the equation:

$$M = \rho_0 * M_0 = \frac{a_P * M_0}{a_0}$$

k_L and k_G models considering mixing points density (M), liquid/gas superficial velocity ($u_{L/G}$), and packing size (a_P) were developed giving:

For structured packing: $k_L = 0.024 * u_L^{0.71} M^{0.38} a_P^{-1.46}$

$k_G = 13.2 * u_G^{0.53} M^{0.44} a_P^{-2.19}$

For random packing: $k_L = C_1 * u_L^{0.71} M^{0.25}$, $C_1 = 4.5E-5$

$k_G = C_2 * u_G^{0.88} M^{0.81}$, $C_2 = 2.95E-7$

The Advanced Flash Stripper with cold, warm, and hot bypass and excess packing provides an equivalent work value of 29.7 kJ/mol (7.5% improvement) with 8 m PZ.

A pilot plant configuration with rich exchange bypass and warm rich bypass should provide an equivalent work of 29.0 kJ/mol.

Solvent Management

PZ has a higher thermal degradation rate (50–150%) than the tertiary amines in PZ-activated solutions containing DEA, DMAE, MDEA, EDEA, and DEAE, suggesting that reactive intermediate degradation products are responsible for the loss of PZ.

In thermal degradation, PZ loss is nearly identical in magnitude to the tertiary amine loss in PZ-activated DMAP and DMAEE, suggesting that the intermediate breakdown product is relatively stable.

HMDA and BAE have thermal degradation rates of about a quarter and about a half, respectively, of PZ when used to activate MDEA. HMDA and BAE also have higher rates of thermal degradation than MDEA, suggesting that the reactive intermediates of thermal degradation degrade the activator.

PZ-activated DMAB has a thermal loss rate about an order of magnitude greater than other tertiary amines, suggesting that another reaction mechanism is responsible for degradation in addition to S_N2 substitution.

The structure of the tertiary amine appears to have a strong effect on thermal degradation. S_N2 attack of hydroxyethyl groups is the slowest, followed by ethyl groups and then by methyl groups in PZ-activated tertiary amine solvents.

All amines found to be stable to oxidation at low temperature oxidized at high temperatures. Amine stability was in the order of AMP > PZ = PZ+2MPZ > MDEA = MDEA+PZ >= MEA.

Dissolved oxygen uptake can be used as an indicator of oxidative stability at high temperature. Oxidation continued after all dissolved oxygen was consumed; no plateau was observed for high-temperature oxidation up to 160 °C.

AMP was the most resistant to oxidation at 120 °C but increased most rapidly at higher temperatures

Ammonia production can be used as an absolute indicator of oxidation for MEA, PZ, and 2MPZ, and as a relative indicator for AMP oxidation.

Oxidized MDEA did not produce any gas phase ammonia; acetaldehyde and formaldehyde were produced.

Oxidation of MDEA with high-temperature cycling was first-order in oxygen concentration in the oxidative reactor

Oxidation of 4 m PZ + 4 m 2MPZ increased with higher oxidative reactor temperatures

Formaldehyde was not a significant degradation product for any of the pilot plant campaigns studied.

Significant degradation has occurred in the pilot plant samples in the form of currently unquantified aldehydes or ketones, as measured by the reaction of DNPH with the degraded PZ pilot plant samples.

Hydrogen peroxide can be used to rapidly oxidize PZ. The degradation products observed from peroxide oxidation are similar to those observed in other experiments, including 10% of degradation in the form of total formate.

2.7 mmol/kg of MNPZ accumulated during OE25 at 70 °C, showing that MNPZ can form from the oxidation of PZ to nitrite even without the addition of nitrite or cycling to higher temperatures. This represents 0.1% of total PZ oxidation.

Laboratory Safety

All experimental work is performed under the Laboratory Safety Guidelines (http://www.utexas.edu/safety/ehs/lab/manual/) of the University of Texas. The laboratory personnel have all completed four safety training courses certified by the University: general lab safety, hazardous materials, fire extinguisher, and site specific safety. Routine personal safety protection includes safety glasses, lab coats, gloves, long pants, and closed toe shoes. Goggles are used for specific hazardous operations. Food and drink are prohibited in the laboratories. Safety inspections of all labs are conducted by a different student every month. The University Safety Office conducts random safety evaluations of each lab, usually about twice a year.

Most of the experimental work with amines is conducted in exhaust hoods. We have recently added ventilated gas cabinets for cylinders of nitrogen mixed with ammonia, NO, NO_2, and SO_2. All work on undiluted nitrosamine samples is contained in one laboratory that has no desks assigned to students for continuous occupancy. We have developed a standard operating procedure to be used in an experiment with closed cylinders of amine solution heated to 175 °C in convection ovens. These experiments are also contained in the nitrosamines lab.

Dr. Rochelle is the Chairman of the Safety Committee of the Department of Chemical Engineering. The committee meets once a month to review safety issues and safety experiences, and to address initiatives for improving safety.

1. CO_2 Solubility and Absorption Rate in Aqueous Amines   p. 12
by Le Li

High temperature CO_2 solubility in 8 m MAPA was measured using the total pressure apparatus during this quarter to confirm the temperature dependence observed in the low temperature results. The high temperature results match low temperature data at low loading, but show inconsistency around 0.5 loading. A consistent semi-empirical model using all experimental data cannot be generated with physical significance. This is likely the result of both slight inaccuracies in the experimental data, and also the simplicity in the mathematical form of the empirical model, which cannot describe complex change in the VLE of 8 m MAPA. Thus, two models were each regressed using part of the experimental data to best predict solvent performance. The new heat of absorption for the solvent is calculated to be 81 kJ/mol at lean loading and 77 kJ/mol at mid-loading, which is higher than 7 m MEA and only slightly lower than the previously calculated values.

A new PZ blend using ethylenediamine (EDA) was screened as a potential solvent for CO_2 absorption at 6 m PZ/2 m EDA. The new solvent was tested in the WWC for $P_{CO2}{}^*$ and liquid

film mass transfer coefficient (k_g'), and in the total pressure apparatus for high temperature VLE. The VLE results from the WWC and the total pressure apparatus agree well with each other. A semi-empirical model was regressed and used to calculate solvent capacity and heat of absorption. The new blend has a capacity of 0.63 mol/kg solv, which is lower than 8 m PZ and similar to other PZ blends using primary diamines. 6 m PZ/2 m EDA has a competitive heat of absorption at lean loading, 75 kJ/mol, and 68 kJ/mol at mid-loading, which is similar to 8 m PZ. The absorption rate of the new blend is high, at 8.6×10^7 mol/Pa·s·m^2, which is competitive with 8 m PZ and similar to other PZ blends.

2. Aqueous Piperazine/aminoethylpiperazine for CO$_2$ Capture   p. 24

by Yang Du

A model accurately predicting thermodynamic and kinetic properties for CO$_2$ absorption in aqueous amine solutions is essential for simulation and design of such CO$_2$ capture process. In this quarter, a rigorous thermodynamic model has been developed for the PZ-AEP-H$_2$O-CO$_2$ system in Aspen Plus® using the Electrolyte Nonrandom Two-Liquid (e-NRTL) activity coefficient model. Unavailable thermodynamic parameters of AEP related species, including AEP, AEPH$^+$, AEP(H$^+$)$_2$, AEPCOO$^-$, AEP(COO$^-$)$_2$, H$^+$AEPCOO$^-$ and H$^+$AEP(COO$^-$)$_2$, were estimated by built-in models in Aspen Plus®, or by referring to corresponding PZ-related species as the starting point, and then sequential regressions were applied using related experimental data. The vapor-liquid equilibrium (VLE) data for AEP-H$_2$O-CO$_2$ were used to determine the standard-state properties (free energy of formation and heat of formation) of the AEP-related species. After that, the VLE data for PZ-AEP-H$_2$O-CO$_2$ were used to identify the e-NRTL interaction parameters for the molecule-electrolyte binaries. The heat capacity and the species concentrations for PZ-AEP-H$_2$O-CO$_2$ were predicted using this model as validation

3. Rate-Based Absorber and Stripper Model   p. 36

by Peter Frailie

The goal of this study is to evaluate the performance of an absorber/stripper operation that utilizes MDEA/PZ. Before analyzing unit operations and process configurations, thermodynamic, hydraulic, and kinetic properties for the blended amine must be satisfactorily regressed in Aspen Plus®. The approach used in this study is first to construct separate MDEA and PZ models that can later be reconciled via cross parameters to model accurately the MDEA/PZ blended amine. During the past quarter a rate-based absorber model was constructed for both intercooled and non-intercooled cases. Using the rich solutions generated by the absorber models, four stripper configurations were evaluated: (1) simple stripper, (2) interheated stripper, (3) two-stage flash with cold rich bypass, and (4) two-stage flash with cold rich bypass and a low temperature adiabatic flash. All results were generated using the Independence model. The goal for the next quarter is to finish testing process configurations and conditions so that Q2 2013 can be spent writing the dissertation.

Increasing the solvent flow rate from 1.1 times the minimum L/G to 1.2 times the minimum L/G decreases absorber height by 25 to 30% and decreases capacity by 8 to 11%. The interheated stripper reduces W_{EQ} by reducing steam losses in the stripper. Increasing the regeneration temperature from 120 ^{o}C to 150 ^{o}C for 8 m PZ improves W_{EQ} for all configurations, but the improvement is on the order of 0.1–0.3 kJ/mol CO$_2$. Adding a low temperature adiabatic flash to the two-stage flash with cold rich bypass has a negligible effect on process performance.

4. Pilot Plant Testing of Advanced Process Concepts using Concentrated Piperazine

by Dr. Eric Chen

In this reporting period, the proposal to DOE for aerosol work in the 2013 SRP pilot plant campaign was approved. New considerations regarding the aerosol analyzer have resulted in the decision to pursue the purchase of an in-situ Phase Doppler Interferometry analyzer (PDI) by Artium Technologies Inc. for $120,000 instead of the TSI Laser Aerosol Spectrometer, which uses extractive sampling.

New developments of advanced absorber and stripper configurations have resulted in plans for modifications to the two-stage flash and SRP pilot plant. The new advanced stripper configuration uses rich bypass exchange and warm rich bypass to improve energy performance. The new absorber configuration utilizes double intercooling spray configuration to enhance mass transfer performance in the SRP absorber column. Another possibility under consideration is to use the existing SRP stripper column as an extension of the absorber column and use the top stripper section as a water wash.

Finally, parametric runs at the CSIRO Tarong pilot plant in Australia using concentrated piperazine (PZ) and stripping temperatures of 120 and 150 °C have been completed. The Tarong pilot plant will be operated for another 3 months through March 2013 to complete two long duration runs, each at one specific operating condition.

5. Novel Absorber Intercooling Configurations   p. 44

by Darshan Sachde

A modeling study was initiated to evaluate three intercooling design configurations ("in-and-out" intercooling, recycle intercooling, recycle intercooling with bypass) for 3 CO_2 flue gas concentrations corresponding to potential capture applications (natural gas combined cycle (4% CO_2), coal-fired power plant (12–14% CO_2), and cement/steel/industrial (>20% CO_2). During the past quarter, preliminary analysis of the natural gas combined cycle application was completed. Results for a constant rich loading analysis at low recycle rates (0.5 to 2 $L_{Recycle}$/G) indicate that the recycle with bypass is significantly better than the simple recycle design (up to 47% packing reduction) and provides benefits over in-and-out intercooling (up to 13% packing reduction). At higher recycle rates (> 2 $L_{Recycle}$/G), the simple recycle and bypass become indistinguishable, and no longer justify the use of a bypass. At the maximum recycle rate considered in this work (8 $L_{Recycle}$/G), and at a constant rich loading, the simple recycle design results in a 46% packing reduction compared to the intercooling design. The simple recycle design shows improvements in both rich loading and packing requirements when compared to in-and-out intercooling as the recycle rate is increased, though diminishing returns occur with the incremental recycle rate increases. Therefore, recycle intercooling designs show improvement over in-and-out intercooling over the full range of recycle rates (bypass design at low rates, simple design at high rates). Economic analysis is required to determine plausible operating points and potential optimum operating conditions for the recycle intercooling configurations.

The natural gas application design cases for TOTAL have been completed, including equipment and stream tables. All results and data will be included in a report to be completed in early 2013.

6. Stripper Modeling and Optimization   p. 57

by Yu-Jeng Lin

In this work, alternative stripper configurations have been modeled and optimized using Aspen Plus[®]. Equivalent work is used as an indicator of energy performance instead of only heat duty. Two configurations are investigated, a simple stripper with cold rich bypass and a simple stripper with rich bypass.

In the simple stripper with cold rich bypass configuration, stripping steam heat is recovered using cold rich bypass. Optimization of packing height has been done using 0.30 lean loading with 7.5% bypass. Rich packing height affects energy equivalent work more significantly than lean packing. By varying the rich packing from no packing to 1.0 meter, 12.7% energy savings can be realized. However, the energy improvement of increased packing height is less than 1%.

In the simple stripper with rich exchanger bypass, a cross exchanger is applied to recover heat from hot stripped vapor using cold rich solvent. Optimum bypass is obtained at 6.5% with 29.6 (kJ/mol CO_2) equivalent work.

7. *Measurement of Packing Effective Area and Mass Transfer Coefficients* *p. 65*

by Chao Wang

In this quarter, liquid film and gas film mass transfer coefficients models including the influence of corrugation angle and packing nominal size were developed. A new concept, mixing points density (M), was introduced to represent the impact of corrugation angle and nominal size on mass transfer.

Mixing points are the turning points where liquid and gas flows change directions, mix with each other, and create turbulence. Intensive mass transfer between liquid and gas phase happens at the mixing points. Structured packing with a lower corrugation angle has larger $k_{L/G}$ because it has more mixing points than packing with a higher corrugation angle at the same packed height.

To quantify the mixing points density in packing, packing geometric structures were studied. Structured packings are composed of corrugated metal sheets crossing with each other. The crossing points are the mixing points, which divide structured packings into hundreds of small square pyramids. The number of mixing points per m^3 equals to the number of square pyramids per m^3 multiplied by the number of mixing points per pyramid. Thus, mixing points density (M) for structured packing can be calculated by the equation: $M = \dfrac{6}{B * h * B \tan \theta}$

Random packings are composed of hundreds of small packing pieces. The mixing points are the turning points at each piece. The number of mixing points per m^3 equals the number of packing pieces per m^3 (ρ_0) multiplied by the number of mixing points per piece (M_0). Thus, mixing points density (M) for random packing can be calculated by the equation: $M = \rho_0 * M_0 = \dfrac{a_P * M_0}{a_0}$.

Preliminary mass transfer models are developed based on three factors influencing mass transfer: the liquid/gas superficial velocity ($u_{L/G}$), the packing size (a_P), and the mixing points density (M). Through data regression, the experimental constant and the exponents for each factor can be calculated. The mass transfer models are:

For structured packing:
$$k_L = 0.024 * u_L^{0.71} M^{0.38} a_P^{-1.46}$$

$$k_G = 13.2 * u_G^{0.53} M^{0.44} a_P^{-2.19}$$

For random packing:
$$k_L = C_1 * u_L^{0.71} M^{0.25}, \ C_1 = 4.5E - 5$$

$$k_G = C_2 * u_G^{0.88} M^{0.81}, \ C_2 = 2.95E - 7$$

8. Stripper Modeling and Pilot Plant Configurations   p. 77

by Tarun Madan

Stripper complexity is an important tool in minimizing the energy penalty of amine scrubbing. Different stripper and flash configurations can be optimized for energy consumption by identifying and changing the various degrees of freedom. A new configuration of 'Advanced Flash Stripper' was studied in this quarter. This configuration recovers the waste heat of stripping steam more reversibly by using a combination of cold, warm, and rich bypass. Complex advanced flash configurations, corresponding to warm bypass, cold and hot bypass, and cold, warm, and rich bypass had equivalent work values of 31.4, 30.3, and 29.7 kJ/mol CO_2 using the Independence solvent model for 8 m PZ in Aspen Plus[®].

Alternate pilot plant configurations based on the advanced flash stripper were also modeled. Best performance of 29.0 kJ/mol CO_2 was achieved using heat recovery by warm rich bypass and heat exchange between cold rich and hot CO_2 streams.

9. Non-rigorous 4 m 2MPZ/4 m PZ and Rigorous 8 m 2MPZ Thermodynamic Models   p. 86

by Brent Sherman

A non-rigorous 4 m 2MPZ/4 m PZ model was made by modifying $\Delta_f H_{PZCOO^-}^{\infty, aq}$ in the rigorous 8 m PZ model. This model does not include 2MPZ or its derivative species, and so PZ and its derivatives serve as pseudocomponents. Still, this non-rigorous thermodynamic model gives acceptable performance. A kinetic model was attempted, but not completed owing to a shift in focus to the rigorous 8 m 2MPZ model. The current version (V0.0) improves on the prior version by stripping the model down to just a 2MPZ in addition to changing the chemistry set and viscosity subroutine to conform to current standards, specifically the elimination of proton and hydroxide ions and use of the modified Weiland equation. In examining this rigorous model for weaknesses, a ~5 kJ/mol discrepancy at high loadings between calculating the heat of absorption via calorimetry and via Lewis-and-Randall (formerly Gibbs-Helmholtz) was uncovered. All recent and under development models have been centralized, assigned a version number, and a metadata file to ensure consistency among modelers present and future.

10. Equation-Based Representations of Mass Transfer, Heat Transfer, and Reaction Kinetics in Gas/Liquid Contactors   p. 98

by Matt Walters
Co-supervised by Thomas EdgarDifferences exist in previously developed models of gas/liquid contactors used in amine scrubbing. It is recommended that the continuity equation approach be used to represent mass and heat transfer in a continuous packed bed, but discontinuous sections of the bed, including liquid feed points, intercooling sections, and interheating sections, be

treated as a well-mixed segment. Two-film theory assuming binary diffusion should be used to avoid the estimation of multiple binary diffusion coefficients needed in the Maxwell-Stefan formulation. In the liquid phase, it is valid to assume that the internal energy hold-up of a segment is equal to enthalpy hold-up, but this is not valid for the compressible vapor phase. It is most advantageous to represent reaction kinetics in the absorber using a liquid film mass transfer coefficient since this can be experimentally determined and enhancement factors have additional parameter uncertainty. These recommendations will be used when implementing a gas/liquid contactor model in gPROMS® for an amine scrubbing system.

11. Thermal Degradation of Activated Tertiary Amine Blends for Carbon Capture from Coal Combustion and Gas Treating   p. 107

by Omkar Namjoshi

The thermal degradation of activated tertiary amine solvents has been studied this quarter. The thermal degradation of triethanolamine (TEA), dimethylaminoethanol (DMAE), methyldiethanolamine (MDEA), diethylaminoethanol (DEAE), dimethylaminopropanol (DMAP), dimethylaminobutanol (DMAB), ethyldiethanolamine (EDEA), and 2-[2-(Dimethylamino)ethoxy]ethanol (DMAEE) activated by piperazine (PZ) was studied. The thermal degradation of MDEA activated by hexamethylenediamine (HMDA) and 2-(2-aminoethoxy)ethylamine (BAE) was also studied. The solvent composition was as follows for each amine system: 5 m tertiary amine/5 m activator with an initial loading of 0.225 mol CO_2/mol alkalinity. Degradation was studied at 135–175 °C. A first-order rate model with respect to parent amine concentration was used to estimate thermal degradation rates.

Tertiary amine pKa does not appear to influence thermal degradation rates of the tertiary amine; however, the structure of the tertiary amine does appear to have a strong effect on thermal degradation. S_N2 attack of hydroxyethyl groups is the slowest, followed by ethyl groups and then by methyl groups in PZ-activated tertiary amine solvents. Intermediate secondary amine breakdown products of the tertiary amine can rapidly react with the amine activator and accelerate the loss of the activator if the breakdown product contains a hydroxyethyl functional group.

At 150 °C and with an initial concentration of 5 m tertiary amine/5 m PZ, thermal degradation was quantified for the following amines: TEA (5.81E-4 1/h), MDEA (1.17E-3 1/h), EDEA (7.15E-4 1/h), DMAE (1.50E-3 1/h), DMAP (8.63E-4 1/h), DMAB (8.08E-3 1/h), DMAEE (1.22E-3 1/h). PZ has a higher thermal degradation rate (50–150%) than the tertiary amines in PZ-activated solutions containing DEA, DMAE, MDEA, EDEA, and DEAE, suggesting that reactive intermediate degradation products are responsible for the loss of PZ. However, PZ loss is nearly identical in magnitude to the tertiary amine loss in PZ-activated DMAP and DMAEE, suggesting that the intermediate breakdown product is relatively stable.

HMDA and BAE have thermal degradation rates of about a quarter and a half, respectively, of PZ when used to activate MDEA. HMDA and BAE also have higher rates of thermal degradation than MDEA, suggesting that the reactive intermediates of thermal degradation degrade the activator. PZ-activated DMAB has a loss rate about an order of magnitude greater than other tertiary amines, suggesting that another reaction mechanism is responsible for degradation in addition to S_N2 substitution.

12. Oxidation of Amines with High Temperature Cycling   p. 120

by Alex Voice

Screening of CO_2 capture amine solvents for oxidative stability was carried out by cycling the amine to stripper temperatures in the presence of dissolved oxygen (DO). Performance of each amine solvent was assessed using four metrics: amine loss, DO uptake, ammonia production, and total formate production. To cycling systems, the integrated solvent degradation apparatus (ISDA) and high temperature cycling system (HTCS) were used in this evaluation.

Oxidative stability was found to be in the order: 2-amino-2-methyl-1-propanol (AMP) > (PZ) and PZ+2-methyl-piperazine (2MPZ) > methyl-diethanolamine (MDEA) and MDEA+PZ > monoethanolamine (MEA). MEA is the only amine susceptible to oxidation at low temperature; these results provide differentiation among the other oxidatively stable amines.

These four indicators of amine oxidation showed good agreement, with the exception of MDEA. MDEA, MDEA+PZ, and MEA showed similar levels of total formate production and amine loss in the ISDA, however DO uptake in the ISDA and amine loss in the HTCS were both higher for MEA. No ammonia production was observed from MDEA, however formaldehyde and acetaldehyde were observed in the gas phase

13. Aerosol and Volatile Emission Control in CO$_2$ Capture   p. 129

by Steven Fulk

In this quarter, a concentric-tube particle growth column was designed in more detail. Droplet growth will be measured under varying operating conditions representative of CO_2 capture in an amine scrubbing system. The miniature absorber column will have an inner diameter of 1.5 inches with a packed height of up to 6 feet. The gas rate will vary from 25–125 LPM. The solvent rate will vary from 0.05–1.00 GPM corresponding to an L/G range of 6–30 mol/mol under all gas flow rates. A heating jacket along the length of the packed section using externally-circulated oil will maintain isothermal conditions (40 °C) during absorption and provide heat (80 °C) for stripping.

Seed particles will be generated by either salt nuclei from a Brechtel Manufacturing Inc. model 9200 Aerosol Generation System or by injecting vaporized H_2SO_4 using a syringe pump connected to a heated injection port. Particle count and size will be measured in-situ using a Phase Doppler Particle Analyzer (PDPA). Droplet content will also be measured using in-situ swirl-tubes and inertial impactors connected to an FTIR analyzer. The FTIR will quantify the content and composition of droplets not collected on the upstream gas-particle separators.

Goals for next quarter include continued design and construction of the aerosol growth chamber.

14. Amine Degradation in Pilot Plants   p. 134

by Paul Nielsen

In this quarter, a method for detecting formaldehyde and other aldehydes and ketones in degraded solvent was developed. The method consists of reacting 2,4-dinitrophenylhydrazine (DNPH) with degraded solvent to produce an aldehyde-DNPH derivative that can be separated and detected by HPLC with UV. DNPH reacts selectively with aldehydes and ketones, and does not react with alcohols, carboxylic acids, amino acids, amides, or carbamates. Testing previously-collected pilot plant samples, insubstantial amounts of formaldehyde were detected. However, a significant amount of DNPH reacted with the degraded samples, equivalent to 75 mmol/kg of aldehyde in the degraded SRP PZ sample and 130 mmol/kg in the degraded PP2

MEA sample. This indicates the presence of an unidentified significant degradation product that is likely an aldehyde or ketone.

PZ was shown to react with hydrogen peroxide. Total formate accounted for 10% of the total degradation observed. This is an identical ratio to that observed in previous oxidation experiments, indicating that oxidation almost certainly occurs along a radical peroxide pathway. Adding hydrogen peroxide may be an easy way to rapidly simulate oxidation in future experiments.

2.7 mmol/kg of MNPZ was measured at the end of the OE25 batch PZ oxidation experiment. This accounts for 0.1% of the oxidation observed in the experiment.

15. Quantification of Nitrosamines in Amine Scrubbing   p. 144

by Nathan Fine

This quarter, a group analysis method was developed for the quantification of nitrosamines in amine scrubbing conditions. The total nitrosamine (TONO) method uses hydrobromic acid to selectively produce nitric oxide (NO) gas from a nitrosamine. The NO is purged from the reactor and enters a chemiluminescent NO_x analyzer, which produces a voltage proportional to the NO concentration. The area under the voltage-time curve is integrated and then calibrated with the total nitrosamine concentration. The calibration is linear across three orders of magnitude with a limit of quantification (LOQ) of 0.1 ppm nitrosamine in the amine sample. The LOQ can be easily decreased to 1 ppb by using a more sensitive NO_x analyzer.

Appendix

CO$_2$ solubility and absorption rate measurements

Abstract

High temperature CO$_2$ solubility in 8 m MAPA was measured using the total pressure apparatus during this quarter to confirm the temperature dependence observed in the low temperature results. The high temperature results match low temperature data at low loading, but show inconsistency around 0.5 loading. A consistent semi-empirical model using all experimental data cannot be generated with physical significance. This is likely the result of both slight inaccuracies in the experimental data, and also the simplicity in the mathematical form of the empirical model, which cannot describe complex change in the VLE of 8 m MAPA. Thus, two models were each regressed using part of the experimental data to best predict solvent performance. The new heat of absorption for the solvent is calculated to be 81 kJ/mol at lean loading and 77 kJ/mol at mid-loading, which are higher than 7 m MEA and only slightly lower than the previously calculated values.

A new PZ blend using ethylenediamine (EDA) was screened as a potential solvent for CO$_2$ absorption at 6 m PZ/2 m EDA. The new solvent was tested in the WWC for P$_{CO2}$* and liquid film mass transfer coefficient (k$_g$'), and in the total pressure apparatus for high temperature VLE. The VLE results from the WWC and the total pressure apparatus agree well with each other. A semi-empirical model was regressed and used to calculate solvent capacity and heat of absorption. The new blend has a capacity of 0.63 mol/kg solv, which is lower than 8 m PZ and similar to other PZ blends using primary diamines. 6 m PZ/2 m EDA has a competitive heat of absorption at lean loading, 75 kJ/mol; and 68 kJ/mol at mid-loading, which is similar to 8 m PZ. The absorption rate of the new blend is high, at 8.6 X10^7 mol/Pa·s·m^2, which is competitive with 8 m PZ and similar to other PZ blends.
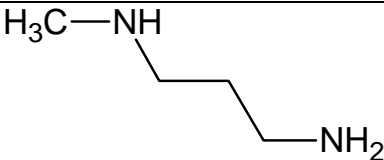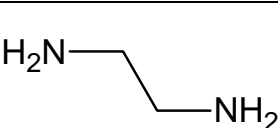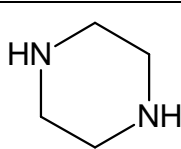
Introduction

The solvent 8 m (methylamino)propylamine (MAPA) was tested previously in the wetted wall column. VLE and absorption rate were measured at 40–100 ˚C (Chen, 2011). The WWC result shows 8 m MAPA to have a high heat of absorption, which is competitive with 7 m MEA. However, it has lower absorption rate and cyclic capacity than 8 m PZ. During this quarter, the total pressure apparatus was used to measure CO$_2$ VLE in 8 m MAPA at variable rich loading at 100–160 ˚C. High temperature VLE measurements would improve the accuracy in the

estimation of heat of absorption for 8 m MAPA by expanding the temperature range of the available data.

Amine blends using piperazine (PZ) and a small amount of a primary diamine were screened previously as potentially good solvents. Among the primary diamines tested are hexamethylenediamine (HMDA) and diaminobutane (DAB). Both molecules have a straight carbon chain with the amino groups on its ends, and DAB has two fewer carbons than HMDA. Structurally similar to these two amines is ethylenediamine (EDA), which has two fewer carbons than DAB). Previously, 12 m EDA has been tested in the WWC, and was shown to have a high heat of absorption, a moderate capacity, and low absorption rates. This quarter, 6 m PZ/2 m EDA was tested using the WWC and total pressure apparatus. The measured absorption rate and CO_2 VLE of the new blend was then compared with 6 m PZ/2 m HMDA, 6 m PZ/2 m DAB, 12 m EDA, and 8 m PZ.

The molecular structures of MAPA, EDA, and PZ are shown in Table 1.

Table 1: Molecular structures of MAPA, EDA, and PZ

H$_3$C—NH ... —NH$_2$	H$_2$N— ... —NH$_2$	HN ... NH
(methylamino)propylamine (MAPA)	Ethylenediamine (EDA)	Piperazine (PZ)

Experimental Methods

The total pressure apparatus was used for high temperature VLE measurements. The equipment and experimental procedures are identical to those by Xu (2011), and the details of data analysis were described in previous reports (Rochelle, 2012).

The wetted wall column apparatus is the same as that used by Chen (2011).

Materials

The amine solvents were prepared gravimetrically. To achieve each CO_2 loading, gaseous CO_2 (99.99%, Matheson Tri-Gas) was bubbled into the solvent. The chemicals used in solvent preparation are listed in Table 1.

Table 2: Materials Used for Solvent Preparation

Chemical	Purity	Source
(methylamino)propylamine	99%	Sigma-Aldridge
Piperazine	98%	Sigma-Aldridge
Ethylenediamine	99%	Sigma-Aldridge
DDI Water	100.00%	Millipore, Direct-Q

Analytical Methods

Liquid samples for each experiment were analyzed for CO_2 content and total alkalinity. The total inorganic carbon (TIC) method was used to measure the total moles of CO_2 per unit mass of liquid sample. For each sample, TIC was performed in triplicate and the average value was reported. The cation chromatography method was used to determine total alkalinity, which is measured as the sum of the amines in each sample. The apparatus and method for both TIC and cation chromatography are identical to those used by Freeman (2011).

Safety considerations

During the WWC experiment, solvent samples are taken periodically at each experimental condition. A small syringe is used to extract the liquid sample from a sampling septum on the liquid circulation line. The sample septum is made of rubber material which can hold internal system pressure. During the sampling process, the syringe needle is inserted into the rubber septum and stays in the septum as the liquid sample fills the syringe.

In the case of high experimental temperatures, the liquid sample is hot and can burn if contacted directly. Thus, it is important to hold the syringe at the designated edges where it is safe. Typically, at high temperature conditions the WWC apparatus needs to operate with up to 60–80 psi internal pressure. At these high pressure conditions, the samples need to be extracted with extra care. The experimentalist should press the back end of the piston on the syringe at all times, in order to exert external pressure to balance the internal pressure of the WWC. When the syringe is safely inserted in the septum, the back pressure needs to be slowly released in a controlled manner for the liquid sample to fill the syringe. As the syringe is filled, the pressure on the end of the piston must be maintained to prevent the liquid leaving the system. The back pressure on the syringe must be maintained as the syringe is removed from the system.

Minor splashing of hot liquid solvent can occur during the insertion and extraction steps, which can be minimized by careful and slow handling of the syringe. If pressure is not properly exerted on the syringe, it is possible for internal system pressure to push out parts of the syringe and cause hot liquid solvent to spray out of the septum. In this case, removing all remaining parts of the syringe from the septum should stop the leak of liquid solvent. Personal protective gear should be worn at all times.

Results and discussion

CO₂ solubility

CO_2 equilibrium partial pressure ($P_{CO_2}^*$) in 8 m MAPA was measured at 100–160 ˚C and rich CO_2 loading (higher than 0.5 mol/mol alk). The high temperature results show good internal consistency and suggest a reasonable trend with CO_2 loading and temperature dependence (Figure 1). Compared with WWC results, high temperature data match low temperature VLE well at two low loadings, and show slight inconsistency around 0.5 loading (Figure 2).
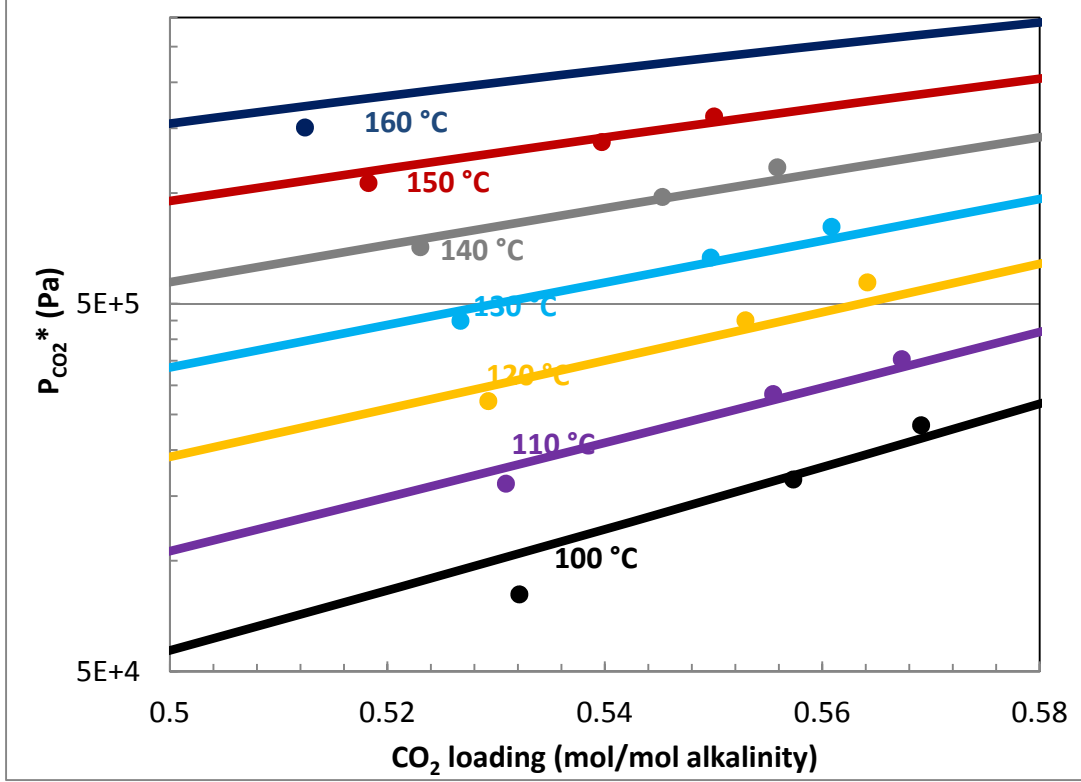
Figure 1: CO₂ solubility in 8 m MAPA at high temperature. Solid circles: total pressure results. Solid lines: 1ˢᵗ empirical model (Table 3).

The measured CO_2 partial pressure data are regressed to generate the parameters of the semi-empirical VLE model for 8 m MAPA. The form of the semi-empirical model equation is shown in Equation 1.

$$ln\left(P_{CO_2}^*\right) = a + \frac{b}{T} + c \cdot \alpha + d \cdot \alpha^2 + e \cdot \frac{\alpha}{T} + f \cdot \frac{\alpha^2}{T} \tag{1}$$

Two semi-empirical models were calculated for 8 m MAPA, the parameters of the models are summarized in Table 3. The model-predicted VLE curves are shown in Figure 2 with experimental results. The first VLE model is regressed using high temperature data and low temperature data at low loading. This model has a high R^2 value at 0.999, indicating good agreement of the experimental data. Also, the model predicts the temperature dependence of the experimental result at both low and rich loading. However, this model does not match data at rich loading and 40–80 ˚C (not included in the regression). The second semi-empirical VLE model is regressed using data at 40–100 ˚C collected by the WWC. The model can better predict experimental results at 40–80 ˚C at rich loading, but does not match high temperature data. A semi-empirical model was not calculated using all VLE data because the model result is not physically realistic.
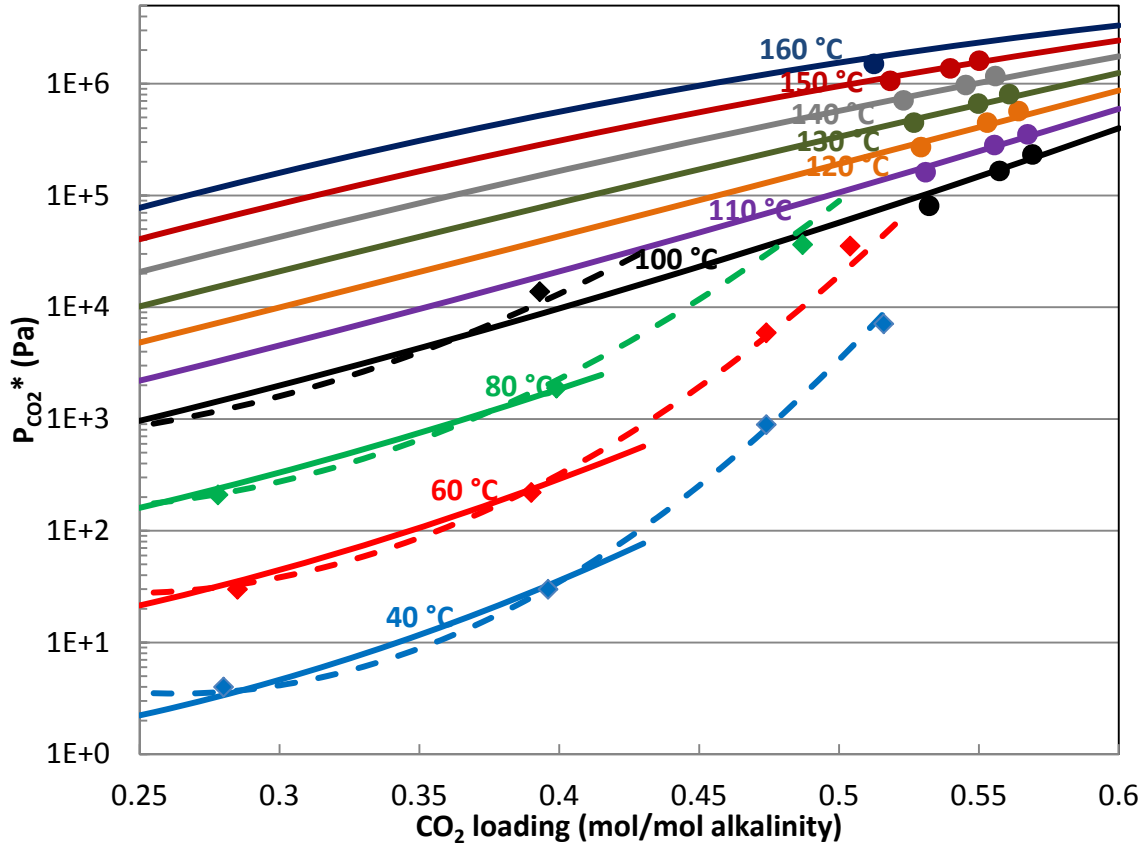
4

Figure 2: CO₂ solubility in 8 m MAPA. Diamond: WWC (Chen, 2011). Circles: total pressure. Solid lines: 1ˢᵗ empirical model. Dashed line: 2ⁿᵈ empirical model (Table 3).

Table 3: Parameter values of two semi-empirical VLE models (Equation 1) for 8 m MAPA

	1ˢᵗ		2ⁿᵈ	
	Value	Std. Err	Value	Std. Err
a	24.2	12.0	0	NA
b	-7587.8	4154.7	3028	661
c	93.4	57.3	210	21
d	-144.7	66.9	-271	49
e	-31274.5	20010.6	-85700	7666
f	57360.1	23609.6	123113	16476
R^2	0.999		0.999	
Data used	Total pressure and WWC results at two low loadings		WWC only	
Data #	26		12	

The inconsistencies between the two models are due to the inconsistency in the experimental data. At loadings close to 0.5 mol/mol alk, the WWC measurements are significantly higher than the values suggested by high temperature results. Experimentally, accurately measuring CO_2 loading at rich loadings can be difficult and slightly affect the quality of data. Physically, at around 0.5 CO_2 loading, carbamate forming species, free MAPA and MAPA carbamate, are mostly consumed. As a result, the CO_2 solubility of the solvent reduces significantly faster than at lower loadings. Due to its simple mathematical form, the semi-empirical model cannot describe the physical change in VLE around 0.5 loading and low temperature while maintaining good fit with data at other conditions.

The semi-empirical models are used to predict the operating lean and rich loading of 8 m MAPA, which correspond to P_{CO2}* of 0.5 and 5 kPa at 40 ˚C. The cyclic capacity (ΔC_{solv}) of the solvent is calculated using Equation 2.

$$\Delta C_{solv} = \frac{(\alpha_{rich} - \alpha_{rich}) \cdot mol\ alk}{kg(H_2O + amine)} \tag{2}$$

The calculated lean/rich loadings and ΔC_{solv} of 8 m MAPA are summarized in Table 4. The results of the two models are very different from each other. The first model predicts lean/rich loadings that are much higher than the second model (approximately 0.06 mol/mol alk). Also, the first model predicts a ΔC_{solv} more than 50% higher than the second. This is because of the uncertainties in the shape of the VLE curve at 40 ˚C (Figure 2). The loadings and ΔC_{solv} calculated by the second model should be used since this model better match the available experimental data at conditions critical to these properties.

Table 4: Capacity, -H$_{abs}$, and operating loading range of 8 m MAPA predicted using two empirical models (Table 3).

	1st	2nd	
α_{lean} (mol/mol alk)	0.494	**0.464**	
α_{rich} (mol/mol alk)	0.562	**0.507**	
ΔC_{solv} (mol/kg solv)	0.63	**0.40**	
-H$_{abs}$ at α_{lean} (kJ/mol)	75	85	**81***
-H$_{abs}$ at α_{mid}(kJ/mol)	67	80	**77***

*Calculated using the first model at loadings calculated by the second model

The heat of absorption of CO_2 in 8 m MAPA is calculated as the temperature dependence of the CO_2 VLE using in Equation 3.

$$-\Delta H_{abs} = R \cdot \frac{d(\ln(P_{CO_2})}{d(1/T)}\bigg|_{P,x} = R \cdot (b + e \cdot \alpha + f \cdot \alpha^2) \tag{3}$$

The ΔH_{abs} of a solvent is a function of CO_2 loading, and not dependent on temperature. Also, the calculation of ΔH_{abs} depends on the semi-empirical model. The ΔH_{abs} calculated using two models for 8 m MAPA are summarized in Table 4 and plotted in Figure 3. Since ΔH_{abs} decreases with an increase in CO_2 loading, the first model calculates a lower ΔH_{abs} than the second model mostly due to the higher loadings suggested by the first model. The ΔH_{abs} predicted by the two models are similar, as shown in Figure 3. The second model (WWC only) predicts slightly higher ΔH_{abs} at low loadings and lower ΔH_{abs} at rich loadings. However, the differences between the two models are within 5 kJ/mol at the operating condition. The ΔH_{abs} of

8 m MAPA should be calculated using the first model, since it is regressed using more data and from a greater temperature and loading range. Typically, the ΔH_{abs} of a solvent is reported at its lean loading and mid-loading ($P_{CO_2}^*$ at 1.5 kPa). In the case of 8 m MAPA, these loadings are to be calculated using the second model. The ΔH_{abs} calculated by a combination of the two models is slightly lower than the first model and much higher than the second.

The $P_{CO_2}^*$ experimental data at high temperature are summarized in Table 5.
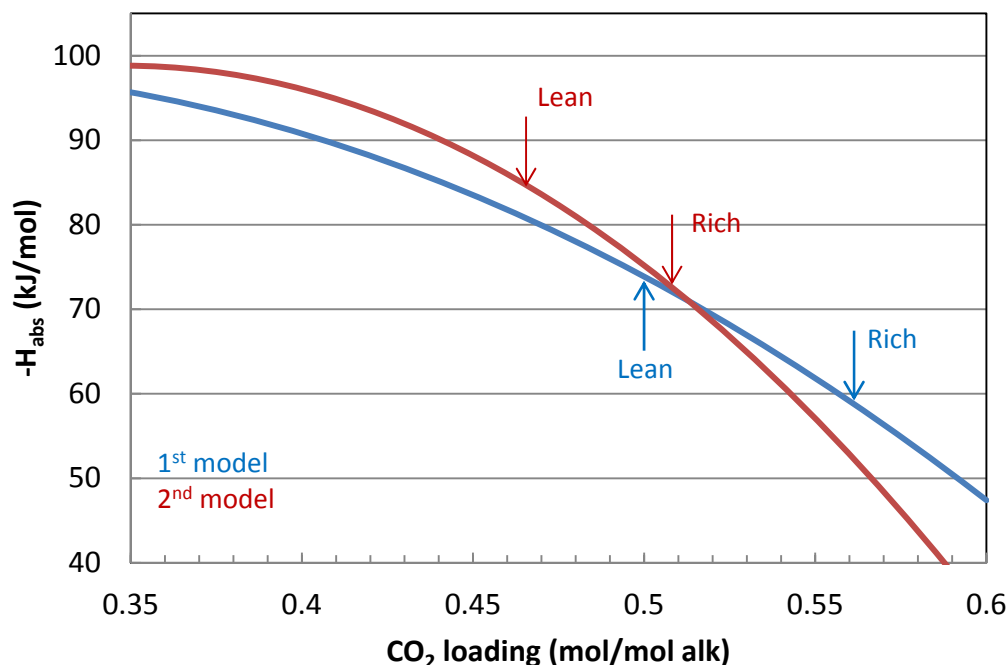
Figure 3: CO_2 heat of absorption in 8 m MAPA predicted by two empirical models (Table 3)

Table 5: $P_{CO_2}^*$ for 8 m MAPA at high temperature

T	CO_2 ldg	$P_{CO_2}^*$	P_{meas}	P_{total}
˚C	mol/mol alk		kPa	
100	0.532	81	298	170
100	0.557	166	390	255
100	0.569	234	451	322
110	0.531	162	412	287
110	0.555	284	543	409
110	0.567	353	629	478
120	0.529	272	580	445
120	0.553	450	766	624
120	0.564	571	880	745
130	0.527	449	817	685
130	0.550	667	1044	903

7

130	0.561	809	1203	1044
140	0.523	712	1167	1028
140	0.545	976	1438	1291
140	0.556	1174	1642	1489
150	0.518	1064	1621	1479
150	0.540	1375	1941	1790
150	0.550	1614	2185	2029
160	0.512	1507	2191	2046

The $P_{CO_2}*$ in 6 m PZ/2 m EDA was measured at 40–100 ˚C using the WWC, and at 100–160 ˚C using the total pressure apparatus at loading across the operating range. A total of 40 experimental points were collected and plotted in Figure 4. The experimental data are regressed using Equation 2 to generate a semi-empirical VLE model for the solvent. The parameters of the model are summarized in Table 6, and the model results are plotted also in Figure 4. The WWC and total pressure results for this blend agree well with each other. The semi-empirical model matches experimental data well, and has a high R^2 value at 0.998.
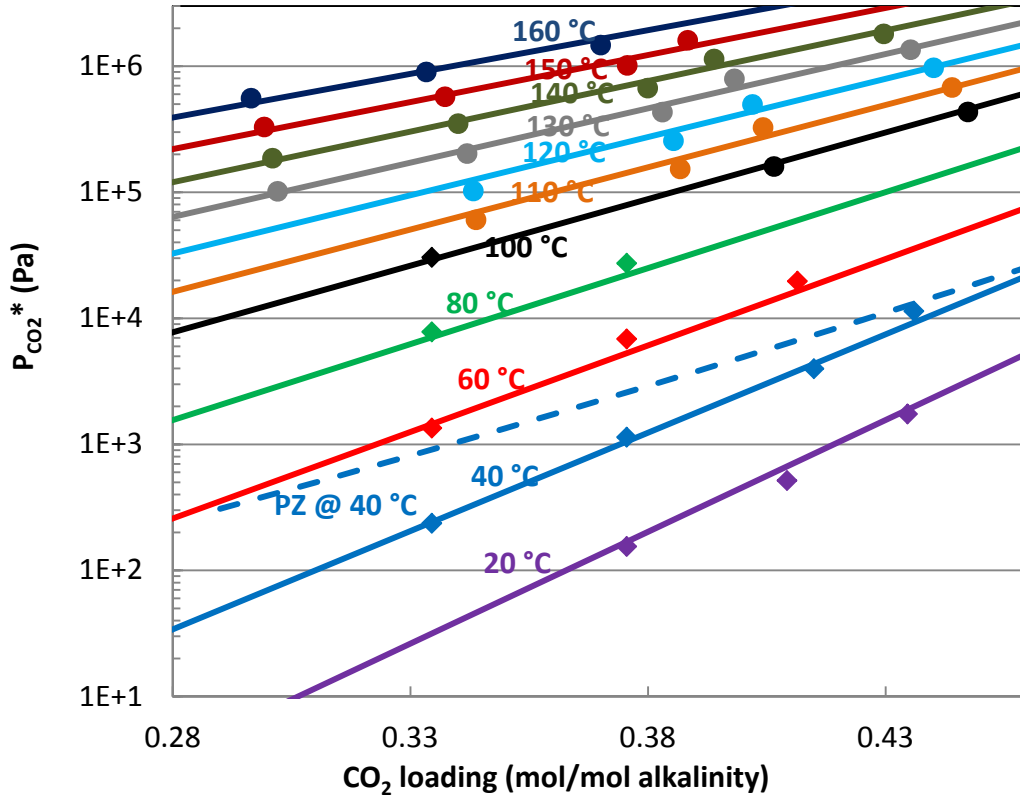
Figure 4: CO₂ solubility in 6 m PZ/2 m EDA. Diamond: WWC. Circles: total pressure. Solid lines: empirical model (Table 6). Dashed line: empirical model of 8 m PZ (Xu, 2011).

The operating lean/rich loadings, ΔC_{solv}, and ΔH_{abs} for 6 m PZ/2 m EDA are calculated using the semi-empirical model and compared with 6 m PZ/2 m HMDA, 6 m PZ/2 m DAB, 12 m EDA, 8 m PZ, and 7 m MEA in Table 7. At 40 ˚C, 6 m PZ/2 m EDA has a similar VLE curve to 6 m PZ/2 m DAB. As a result, the two solvents have similar lean/rich loadings and ΔC_{solv}. 6 m PZ/2

m EDA has ΔC_{solv} of 0.63 mol CO_2/kg solv, which is higher than 6 m PZ/2 m HMDA and 7 m MEA, but lower than 8 m PZ and 12 m EDA. The temperature dependence of CO_2 VLE in 6 m PZ/2 m EDA is more significant than 8 m PZ, which results in higher ΔH_{abs} for the blend at a higher loading than 8 m PZ. The ΔH_{abs} for 6 m PZ/2 m EDA is competitive with 7 m MEA at low loadings, and similar to 8 m PZ and other PZ blends at mid-loading.

Table 6: Parameter values of the semi-empirical VLE model (Equation 1) of 6 m PZ/2 m EDA

	Value	Std. Err
a	47.4	1.7
b	-16889	642
c	-36.2	4.3
d	/	/
e	22575	1654
f	/	/
R^2	0.998	
Data #	40	

Absorption rates

The absorption rates of 6 m PZ/2 m EDA were tested in the WWC at 40–100 ˚C and operating loadings. The liquid film mass transfer coefficient (k_g'), which is a property of the solvent and inversely proportional to the amount of packing required in the absorber, was calculated from the experimental data. The calculated k_g' for the blend is plotted in Figure 5, and compared to 8 m PZ, 7 m MEA, and 12 m EDA at 40 ˚C. The k_g' for the blend shows little temperature dependence at 20–60 ˚C. At 60–100 ˚C, the temperature dependence of k_g' is significant even at low loading, which is slightly unusual among other solvents. The strong temperature dependence at high temperature suggests the diffusion of species in the solvent becomes limiting in the mass transfer process at these conditions. At 40 ˚C, the absorption rate of 6 m PZ/2 m EDA is competitive with 8 m PZ, and much higher than 12 m EDA and 7 m MEA at all loadings tested. This suggests the absorbing species in the blend is mostly PZ at the experimental conditions. The viscosity of the blend, which will be measured during the next quarter, could offer additional explanations for the measured k_g' behavior.

To predict the absorption rate performance of the solvent in a real process, the average rate of the operation lean/rich loading is approximated for an isothermal absorber at 40 ˚C using Equation 4.

$$k'_{g\,avg} = \frac{Flux_{CO_2,LM}}{(P_{CO_2}-P^*_{CO_2})_{LM}} = \frac{(Flux_{CO_2,top}-Flux_{CO_2,bottom})/Ln(Flux_{CO_2,top}/Flux_{CO_2,bottom})}{(1.2\ kPa-0.5\ kPa)-(1.2\ kPa-5kPa)/Ln(\frac{1.2\ kPa-0.5\ kPa}{1.2\ kPa-5kPa})} \quad (4)$$

The calculated k_g'$_{avg}$ for 6 m PZ/2 m EDA is summarized in Table 7.
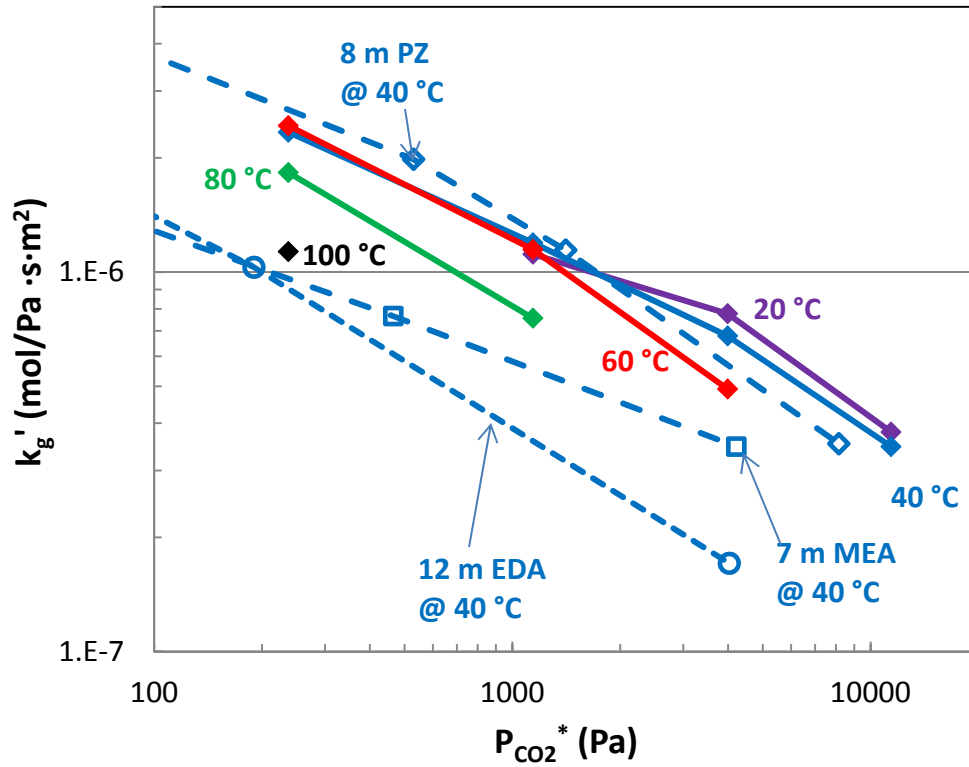
Figure 5: Absorption rate of 6 m/PZ 2 m EDA. Empty diamonds: 8 m PZ. Empty squares: 7 m MEA (Dugas, 2009). Empty circles: 12 m EDA (Chen, 2011).

The measured P_{CO2}^* and k_g' for 6 m PZ 2 m EDA are summarized in Table 8 and 9.

Table 7: Predicted performance parameters of 6 m PZ/2 m EDA

	$k_g'_{avg}$ X10^7 mol/Pa s m^2	$\alpha_{lean/rich}$ mol/mol alk	Capacity mol/kg solv	$-\Delta H_{abs}$ α_{lean}	α_{mid}
6 m PZ/2 m EDA	8.6	0.35/0.42	0.63	74	68
6 m PZ/2 m HMDA	4.9	0.37/0.43	0.55	75	68
6 m PZ/2 m DAB	7.1	0.34/0.41	0.68	69	63
8 m PZ	8.5	0.31/0.40	0.86	71	67
12 m EDA	2.5	0.44 / 0.5	0.78	83*	81*
7 m MEA	4.3	0.43/0.53	0.5	76	72

*Calculated from low temperature WWC data only, which usually slightly over predict ΔH_{abs}

Table 8: P_{CO2}^* and k_g' measurement for 6 m PZ/2 m EDA at low temperature

T	ldg	P_{CO2}^*	k_g'
°C	mol/mol	kPa	$\times 10^7$ mol/Pa s m^2
20	0.376	0.16	11.2
20	0.409	0.52	7.8
20	0.435	1.74	3.8
40	0.335	0.24	23.4
40	0.376	1.14	11.9
40	0.415	3.99	6.8
40	0.436	11.40	3.5
60	0.335	1.35	24.3
60	0.376	6.86	11.5
60	0.411	19.74	4.9
80	0.335	7.82	18.3
80	0.376	27.31	7.6
100	0.335	30.43	11.3

Table 9: P_{CO2}^* measurement for 6 m PZ/2 m EDA at high temperature

T	ldg	P_{CO2}	P_{meas}	P_{total}	T	ldg	P_{CO2}^*	P_{meas}	P_{total}
°C	mol/mol	kPa	kPa	kPa	°C	mol/mol	kPa	kPa	kPa
100	0.388	74	283	162	130	0.383	433	797	669
100	0.406	160	376	249	130	0.398	796	1143	1032
100	0.447	435	652	523	130	0.435	1352	1718	1588
110	0.344	61	309	186	140	0.301	187	642	503
110	0.387	153	400	279	140	0.340	350	802	666
110	0.404	327	557	452	140	0.380	672	1120	988
110	0.444	678	928	804	140	0.394	1144	1586	1459
120	0.303	42	351	216	140	0.430	1810	2263	2125
120	0.343	102	409	276	150	0.299	330	889	746
120	0.385	257	557	430	150	0.337	574	1130	990
120	0.402	498	805	671	150	0.376	1016	1567	1432
120	0.440	973	1282	1146	150	0.388	1608	2153	2023
130	0.302	102	472	338	160	0.296	558	1246	1100
130	0.342	203	568	439	160	0.333	900	1583	1441
					160	0.370	1474	2152	2014

Conclusions

The high temperature P_{CO2}^* result for 8 m MAPA matches low temperature data at low loading. The new heat of absorption calculated for 8 m MAPA is 81 kJ/mol at lean loading and 77 kJ/mol at mid-loading, which are both higher than 7 m MEA.

6 m PZ/2 m EDA has a capacity of 0.63 mol CO_2/kg solv, which is about 25% lower than that of 8 m PZ but 25% higher than 7 m MEA. The heat of absorption of the blend is 75 kJ/mol at lean

loading, which is competitive with 7 m MEA, and it is 68 kJ/mol at the mid-loading condition, which is similar to 8 m PZ and 4 kJ less than 7 m MEA. The blend has a high absorption rate across the operating range, with a $k_g'_{avg}$ of 8.6 $\times 10^7$ mol/Pa·s·m^2, which is competitive with 8 m PZ, and approximately twice that of 7 m MEA.

Future Work

Other PZ blends using N-(2-hydroxyethyl)piperazine (HEP) and 2 piperidine ethanol (2-PE), and other amine blends will be tested in the WWC and total pressure apparatus in the next quarter.

References

Chen X, Closmann F, Rochelle GT. "Accurate screening of amines by the wetted wall column." *Energy Proc*. 2011;4:101–108.

Dugas RE. *Carbon dioxide absorption, desorption, and diffusion in aqueous piperazine and monoethanolamine*. The University of Texas at Austin. Ph.D. Dissertation. 2009.

Freeman SA. *Thermal degradation and oxidation of aqueous piperazine for carbon dioxide capture*. The University of Texas at Austin. Ph.D. Dissertation. 2011.

Rochelle GT et al. "CO$_2$ Capture by Aqueous Absorption, First Quarterly Progress Report 2012." Luminant Carbon Management Program. The University of Texas at Austin. 2012.

Xu Q. *Thermodynamics of CO$_2$ loaded aqueous amines*. The University of Texas at Austin. Ph.D. Dissertation. 2011.

Aqueous piperazine/aminoethylpiperazine for CO_2 Capture

Quarterly Report for October 1 – December 31, 2012

by Yang Du

Supported by the Luminant Carbon Management Program

McKetta Department of Chemical Engineering

The University of Texas at Austin

January 31, 2013

Abstract

A model accurately predicting thermodynamic and kinetic properties for CO_2 absorption in aqueous amine solutions is essential for simulation and design of such CO_2 capture process. In this quarter, a rigorous thermodynamic model has been developed for the PZ-AEP-H_2O-CO_2 system in Aspen Plus$^{®}$ using the Electrolyte Nonrandom Two-Liquid (e-NRTL) activity coefficient model. Unavailable thermodynamic parameters of AEP related species, including AEP, $AEPH^+$, $AEP(H^+)_2$, $AEPCOO^-$, $AEP(COO^-)_2$, $H^+AEPCOO^-$ and $H^+AEP(COO^-)_2$, were estimated by built-in models in Aspen Plus$^{®}$, or by referring to corresponding PZ-related species as the starting point, and then sequential regressions were applied using related experimental data. The vapor-liquid equilibrium (VLE) data for AEP-H_2O-CO_2 were used to determine the standard-state properties (free energy of formation and heat of formation) of the AEP-related species. After that, the VLE data for PZ-AEP-H_2O-CO_2 were used to identify the e-NRTL interaction parameters for the molecule-electrolyte binaries. The heat capacity and the species concentrations for PZ-AEP-H_2O-CO_2 were predicted using this model as validation.

Introduction

Amine scrubbing has shown the most promise for effective capture of CO_2 from coal-fired flue gas. Piperazine/N-(2-aminoethyl) piperazine (PZ/AEP) was investigated in this study as a novel solvent for CO_2 capture. In previous reports, we have confirmed that PZ/AEP has a larger solid solubility window than concentrated PZ, slightly lower CO_2 absorption capacity, but comparable resistance to degradation, CO_2 absorption rate and viscosity, which indicates PZ/AEP is a superior solvent for CO_2 capture by absorption/stripping.

To properly simulate and design the CO_2 capture process using PZ/AEP, it is a prerequisite to develop a rigorous thermodynamic model which can accurately predict the thermodynamic properties, specifically vapor-liquid equilibrium (VLE), calorimetric properties, and chemical reaction equilibrium.

In this quarter, a rigorous thermodynamic model has been developed for PZ-AEP-H_2O-CO_2 in Aspen Plus$^{®}$ using the Electrolyte Nonrandom Two-Liquid (e-NRTL) activity coefficient model, based on the Independence model for concentrated PZ established by Frailie (Rochelle, 2012).

1

PZ-AEP-H₂O-CO₂ Thermodynamic Model

Reference State used in this Model

There are mainly two different activity coefficient conventions used in modeling. Although each convention is a combination of different reference states for different components, both conventions define the activity coefficients of water, Henry's components, and ions as unity at infinite dilution, which indicates a symmetric reference state for water,

$$r_w \to 1 \text{ as } x_w \to 1$$

and an asymmetric reference state for molecular solute and ions.

$$r_i \to 1 \text{ as } x_i \to 0$$

However, the convention 1 (also called symmetric convention) considers molecular components, other than water and Henry's components (e.g., amine) as solvent, and thus assigns an activity coefficient of one at pure solvent (symmetric reference state); whereas the convention 2 (also called asymmetric convention) considers them as molecular solute, and thus assigns an activity coefficient of one to infinite dilution (asymmetric reference state). In Aspen Plus®, GAMMA (molar basis) is the parameter used for convention 1, while GXTRUE (molar basis) is used for convention 2.

Previous investigators (Austgen, 1989; Posey, 1996; Bishnoi, 2000; Cullinane, 2005; Hilliard, 2008) of amine-CO₂-water models treated amine as a solvent and considered zwitterion as an ion with extremely small charge. For better prediction and convenience, later modelers (Plaza, 2011; Chen, 2011; Frailie, 2012), treated amine as Henry's component and consider zwitterion as molecular solute with no net charge. Table 1 compares the reference state of different components used in early models and in the current model.

Table 1: Comparison of the reference state of different components used in early models and in the current model

Species	Early version		Current version	
	Sort	Reference state	Sort	Reference State
H₂O	solvent	symmetric	solvent	symmetric
CO₂	molecular solute	asymmetric	molecular solute	asymmetric
Amine	solvent	symmetric	molecular solute	asymmetric
Zwitterion	ion	asymmetric	molecular Solute	asymmetric
ion	ion	asymmetric	ion	asymmetric

All molecular solutes and ions are treated with asymmetric reference state, while all solvents are treated with symmetric reference state.

Speciation and Chemical Equilibrium

As this PZ-AEP-H₂O-CO₂ model is developed based on the Independence model for PZ-H₂O-CO₂ established by Frailie (Rochelle, 2012), AEP-related species and corresponding chemical equilibrium reactions need to be set in Aspen Plus®. The following AEP-related species and equilibrium reactions are taken into account in this study.

Table 2: AEP-related species considered in this model

Species	Alias	Charge state
AEP	C6H15N3	0
$H^+AEPCOO^-$	C7H15N3O2	0
$AEPH^+$	C6H16N3	+1
$AEP(H^+)_2$	C6H17N3	+2
$AEPCOO^-$	C7H14N3O2	-1
$AEP(COO^-)_2$	C8H13N3O4	-2
$H^+AEP(COO^-)_2$	C8H13N3O4	-1

Table 3: AEP-related equilibrium reactions considered in this model

Rxn No.	Stoichiometry
1	$AEPH^+ \longleftrightarrow AEP + H^+$
2	$AEP + HCO_3^- \longleftrightarrow AEPCOO^- + H_2O$
3	$AEPCOO^- + HCO_3^- \longleftrightarrow AEP(COO^-)_2 + H_2O$
4	$H^+AEPCOO^- \longleftrightarrow AEPCOO- + H^+$
5	$AEP(H^+)_2 \longleftrightarrow AEPH^+ + H^+$
6	$H^+AEP(COO^-)_2 \longleftrightarrow AEP(COO^-)_2 + H+$
7	$H^+AEP(COO^-)_2 + H_2O \longleftrightarrow H^+AEPCOO^- + HCO_3^-$

Estimation of Unavailable Parameters

To accurately predict thermodynamic properties, a set of parameters need to be input into Aspen Plus®, including $\Delta_f G_i^{ig}$, $\Delta_f H_i^{ig}$ and Cp_i^{ig} for all molecular components, $\Delta_f G_i^{\infty,aq}$, $\Delta_f H_i^{\infty,aq}$ and $Cp_i^{\infty, aq}$ for all ionic components, and Henry's constant for Henry's components, as well as binary parameters for molecule-electrolyte. Although not all the parameters are available in the Aspen Plus® database, various ways can be used to determine or estimate their values. In our model, $\Delta_f G_i^{ig}$ and $\Delta_f H_i^{ig}$ of AEP were estimated by Aspen Plus® using the Benson method by providing structure information of AEP. For the Henry's constant for AEP, values were calculated from the volatility measurement of AEP by Nguyen (Rochelle, 2012) (Figure 1).
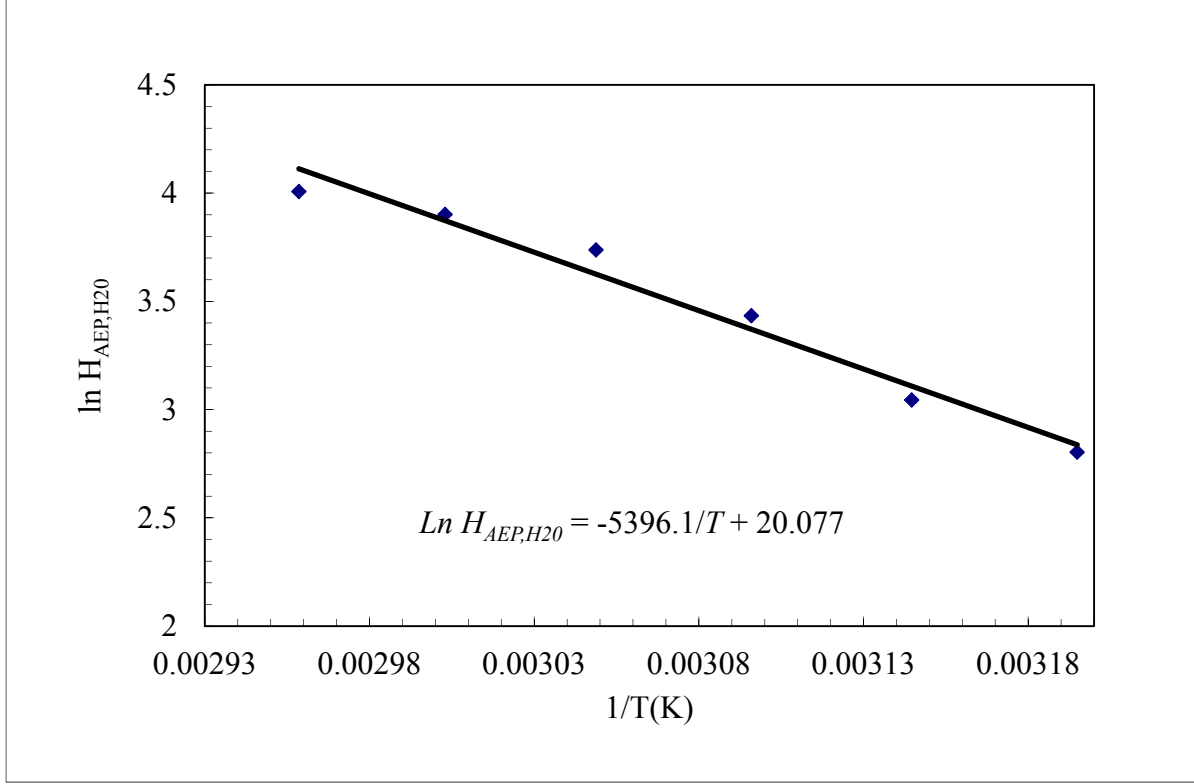
Figure 1: Henry's constant for AEP as a function of T from 40 °C to 65 °C

As modeled as Henry's components, $\Delta_f G_i^{\infty, aq}$ and $\Delta_f H_i^{\infty, aq}$ of AEP can be calculated from the following equations.

$$\Delta_f G_i^{\infty,aq} = \Delta_f G_i^{ig} + RT \ln(\frac{H_{i, H2O}}{P^{ref}}) \qquad (1)$$

$$\Delta_f H_i^{\infty,aq} = \Delta_f H_i^{ig} + R \frac{\partial \ln H_{i, H2O}}{\partial (1/T)} \qquad (2)$$

where $H_{i, H2O}$ is the Henry's constant of solute i in water and P^{ref} is the reference pressure of 1 bar.

$\Delta_f H_i^{\infty, aq}$ of $AEPH^+$ and $AEP(H^+)_2$ was calculated from the protonation reactions of $AEPH^+$ and $AEP(H^+)_2$ measured by Pagano (1961).

$AEPH^+ \leftrightarrow AEP + H^+$, $\qquad\qquad$ log $K_{m,1} = 9.538$ and $\Delta_r H_1 = -48.56$ kJ/mol at 25 °C

$AEP(H^+)_2 \leftrightarrow AEPH^+ + H^+$, $\qquad$ log $K_{m,2} = 8.453$ and $\Delta_r H_2 = -42.70$ kJ/mol at 25 °C
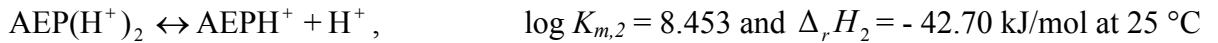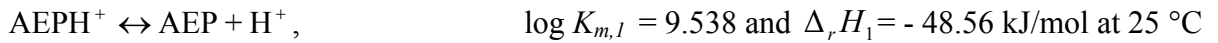
$\Delta_f H_{AEPH+}^{\infty,aq} = \Delta_f H_{AEP}^{\infty,aq} + \Delta_r H_1$

$\Delta_f H_{AEP(H+)2}^{\infty,aq} = \Delta_f H_{AEPH+}^{\infty,aq} + \Delta_f H_2$

$\Delta_f G_{AEPH+}^{\infty,aq} = \Delta_f G_{AEP}^{\infty,aq} + \Delta_r G_1 = \Delta_f G_{AEP}^{\infty,aq} - RT\ln K_{x,1}$

$$\Delta_f G^{\infty,aq}_{AEP(H+)2} = \Delta_f G^{\infty,aq}_{AEPH+} + \Delta_r G_2 = \Delta_f G^{\infty,aq}_{AEP} - RT\ln K_{x,2}$$

where $\Delta_r H_1$ and $\Delta_r H_2$ are the heat of reactions, $K_{x,1}$ and $K_{x,2}$ are protonation constants on a mole fraction basis, and $K_{m,1}$ and $K_{m,2}$ are molality-based protonation constants. The conversion from molality scale to molar scale can be found in Hilliard (2008).

$\Delta_f G^{\infty,\,aq}_i$ and $\Delta_f H^{\infty,\,aq}_i$ of carbamate AEP species were estimated based on the assumption that the difference between related AEP species is the same as the difference between related PZ species. For example, we can assume:

$$\Delta_f H^{\infty,aq}_{AEPcoo-} - \Delta_f H^{\infty,aq}_{AEPH+} = \Delta_f H^{\infty,aq}_{PZcoo-} - \Delta_f H^{\infty,aq}_{PZH+},$$

and

$$\Delta_f H^{\infty,aq}_{AEP(coo-)2} - \Delta_f H^{\infty,aq}_{AEPcoo-} = \Delta_f H^{\infty,aq}_{PZ(coo-)2} - \Delta_f H^{\infty,aq}_{PZcoo-}.$$

The initial values for free energy and heat of formation of AEP species have been summarized in Table 4.

Table 4: Initial values for free energy and heat of formation of AEP species (kJ/mol)

Species	$\Delta_f G^{ig}_i$	$\Delta_f H^{ig}_i$	$\Delta_f G^{\infty,\,aq}_i$	$\Delta_f H^{\infty,\,aq}_i$
AEP	304.61	21.20	280.93	-23.66
$H^+AEPCOO^-$	-78.54	-491.22	____	
$AEPH^+$			216.54	-72.22
$AEP(H^+)_2$			168.30	-114.92
$AEPCOO^-$		____	-84.47	-465.14
$AEP(COO^-)_2$			-439.38	-925.24
$H^+AEP(COO^-)_2$			-433.44	-951.32

Cp^{ig}_i and $Cp^{\infty,\,aq}_i$ of AEP species were assumed to be the same as PZ species based on mass scale. e-NRTL binary parameters for AEP species were also assumed to be the same as PZ species. For example, the GMELCC-1 of ($AEPH^+$, $AEPCOO^-$)/H_2O and (PZH^+, $AEPCOO^-$)/H_2O are assumed to be the same as that of (PZH^+, $PZCOO^-$)/H_2O

Sequential Regression

After getting the above initial value of parameters as a starting point, sequential regression using experimental data was applied to obtain the optimum value of these parameters for accurate prediction of thermodynamic properties.

AEP/H₂O/CO₂ Regression

The VLE for 6 m loaded AEP solutions between 40 °C and 100 °C was initially regressed by adjusting the $\Delta_f G^{\infty,\,aq}_i$ and $\Delta_f H^{\infty,\,aq}_i$ of $AEPCOO^-$, $AEP(COO^-)_2$ and $H^+AEP(COO^-)_2$, and $\Delta_f G^{ig}_i$ and $\Delta_f H^{ig}_i$ of $H^+AEPCOO^-$. After regression, although the experimental data can be predicted by the model, the large standard error of regressed value of $\Delta_f G^{\infty,\,aq}_i$ and $\Delta_f H^{\infty,\,aq}_i$ of $AEP(COO^-)_2$,

and $\Delta_f H_i^{\infty, aq}$ of $H^+AEP(COO^-)_2$ indicates these parameters do not have a significant effect on the prediction of VLE of 6 m AEP. Therefore, these three parameters were excluded from the final regression. The prediction of VLE of 6 m loaded AEP is shown in Figure 2 and the regressed parameters and standard error are summarized in Table 5.
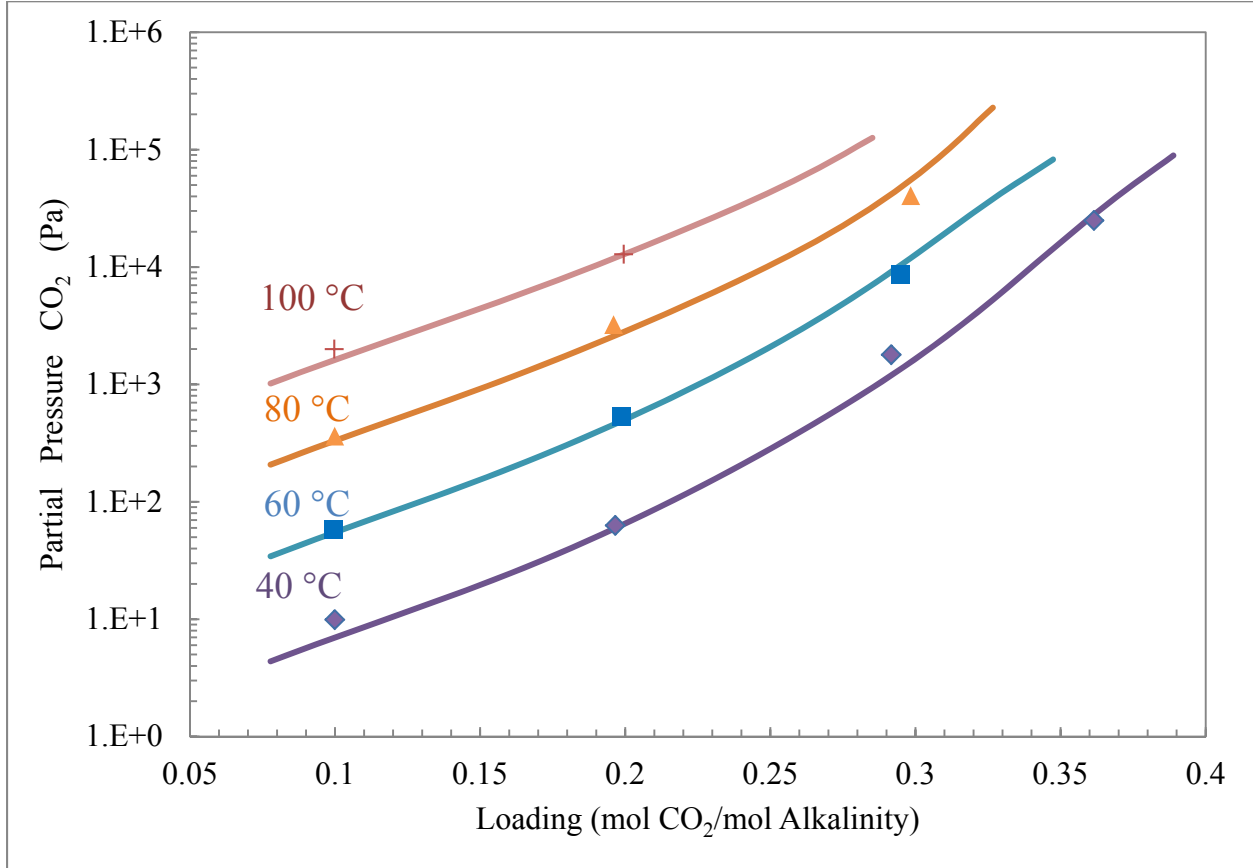
Figure 2: Experimental measurement (points) (Chen, 2011) and Aspen Plus® predictions (lines) for VLE of loaded 6 m AEP solution between 40 °C and 100 °C.

Table 5. The regressed parameters and standard error

Species	Parameter	Initial value	Regressed value	Standard error
$H^+AEPCOO^-$	$\Delta_f G_i^{ig}$	-78.54	-85.88	0.42
	$\Delta_f H_i^{ig}$	-491.22	-504.44	2.76
$AEPCOO^-$	$\Delta_f G_i^{\infty, aq}$	-84.47	-89.19	0.69
	$\Delta_f H_i^{\infty, aq}$	-465.14	-473.42	5.07
$H^+AEP(COO^-)_2$	$\Delta_f G_i^{\infty, aq}$	-433.44	-494.08	0.91

PZ/AEP/H₂O/CO₂ Regression

With the parameters obtained in the AEP/H₂O/CO₂ regression, VLE of 5 m PZ/2 m AEP can be adequately predicted by this model without adjusting any other parameters (Figure 3).
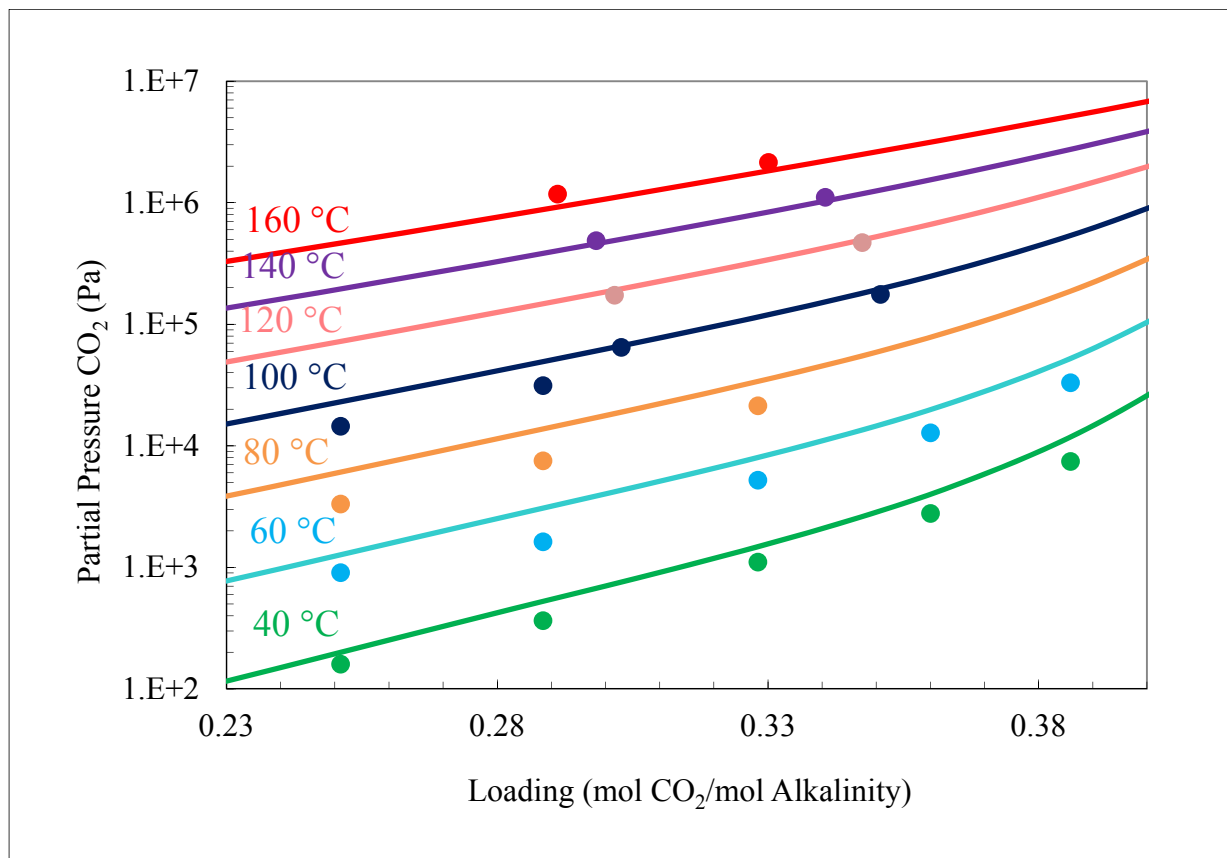
Figure 3: Comparison of Aspen Plus® predictions (lines) and experimental data (points) for loaded 6 m AEP between 40 °C and 160 °C

A better prediction can be obtained by adjusting the e-NRTL binary parameters (Figure 4), and the regressed values are summarized in Table 6.
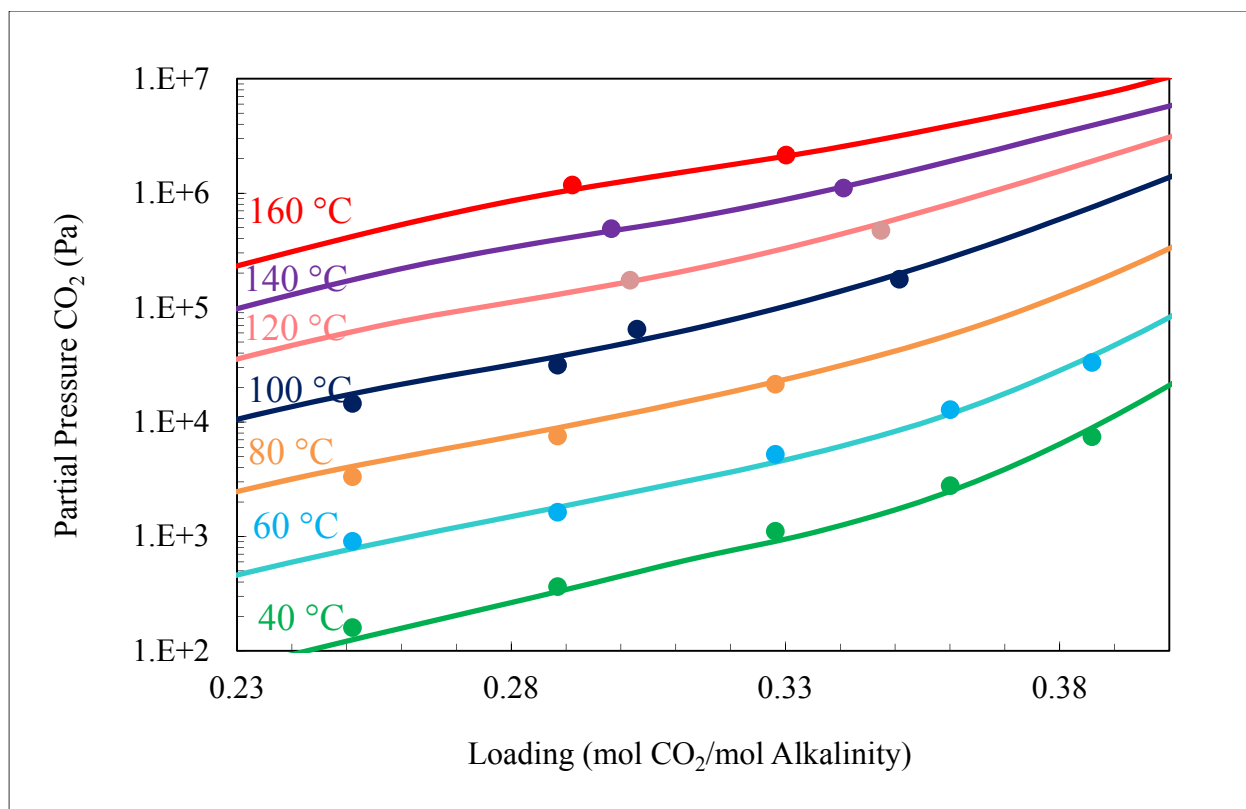
Figure 4: Comparison of Aspen Plus® predictions (lines) and experimental data (points) for loaded 6 m AEP between 40 °C and 160 °C, after regression.

Table 6: PZ/AEP/H₂O/CO₂ Regression Results

Parameter	Component i	Component j	Value	Standard deviation
GMELCC/1	(AEPH+,PZCOO-)	H2O	0	0
GMELCC/1	(AEPH+,PZCOO-2)	H2O	-6.46	4.88
GMELCC/1	(PZH+,AEPCOO-)	H2O	-2.86	0.29
GMELCC/1	(PZH+,HAEPCOO)	H2O	-1.02	8.34
GMELCC/1	(AEPH+2,PZCOO-)	H2O	-3.21	2.54
GMELCC/1	(AEPH+2,PZCOO-2)	H2O	-6.56	3.52
GMELCC/1	(AEPH+2,PZCOO-)	HPZCOO	-8.91	4.27
GMELCC/1	(AEPH+2,PZCOO-2)	HPZCOO	-10.54	8.03
GMELCC/1	(PZH+,PZCOO-2)	HAEPCOO	-8.28	0.72
GMELCC/1	(AEPH+2,AEPCOO-)	HPZCOO	-11.21	1.91
GMELCC/1	(PZH+,AEPCOO-)	HPZCOO	-8.56	0.40

Validation of the Thermodynamic Model

As no experimental data are available at the moment for the speciation and heat capacity of AEP or PZ/AEP, we can only roughly validate this model by examining the behaviors of these predicted properties as a function of loading or temperature.

8

Speciation Validation

The predicted speciation of 6 m AEP as a function of loading at 40 °C is given in Figure 5.
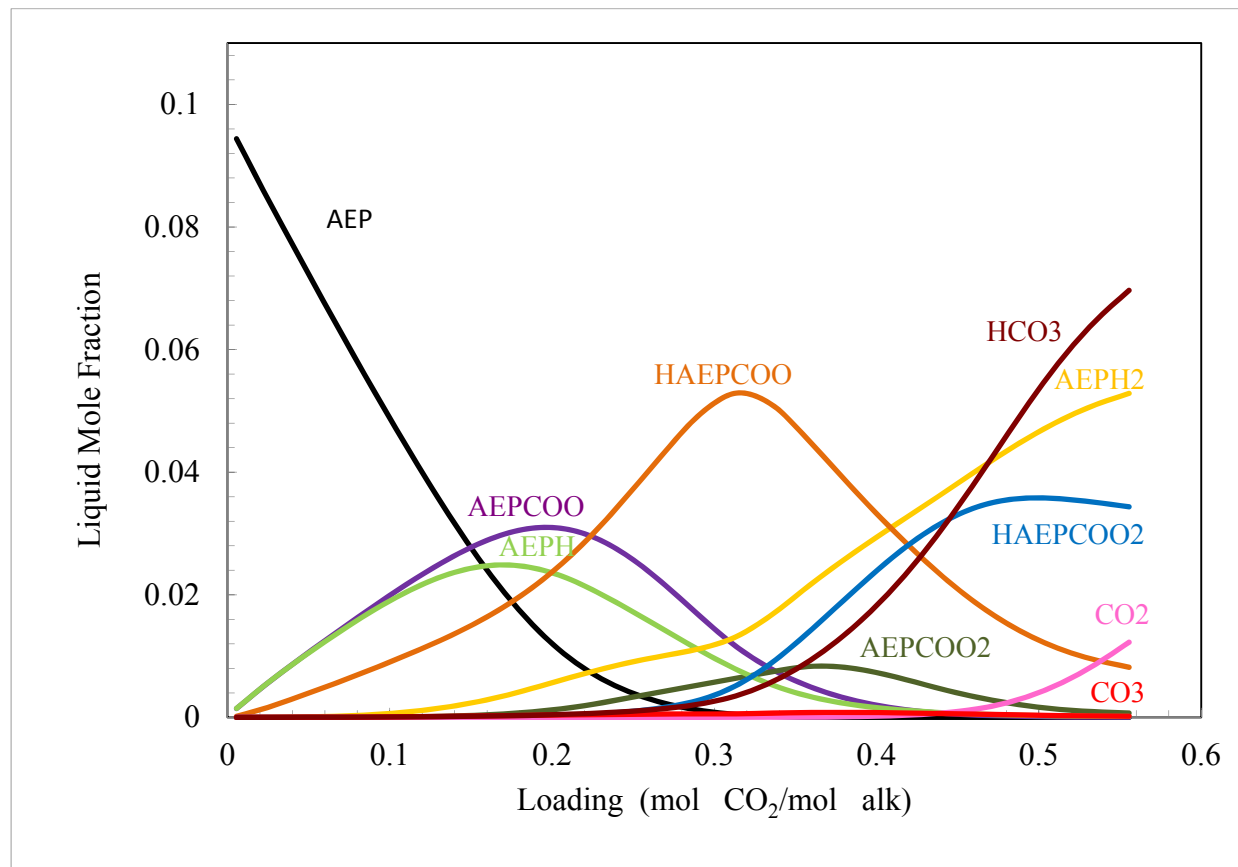
Figure 5: Prediction of speciation of 6 m AEP as a function of loading at 40 °C.

As can be seen in Figure 5, at very lean loading (0–0.05) AEP is the dominant species in the solution. With the increase in loading, AEP decreases sharply while $AEPH^+$, $AEPCOO^-$ and $H^+AEPCOO^-$ play a more significant role. At very high loading (0.35–0.5), AEP, $AEPH^+$ and $AEPCOO^-$ all disappear, with HCO_3^-, $AEP(H^+)_2$ and $H^+AEP(COO^-)_2$ as dominant species. This relative abundance of these species and their trend with loading is similar to that for corresponding PZ species (Frailie, 2012).

Heat Capacity Validation
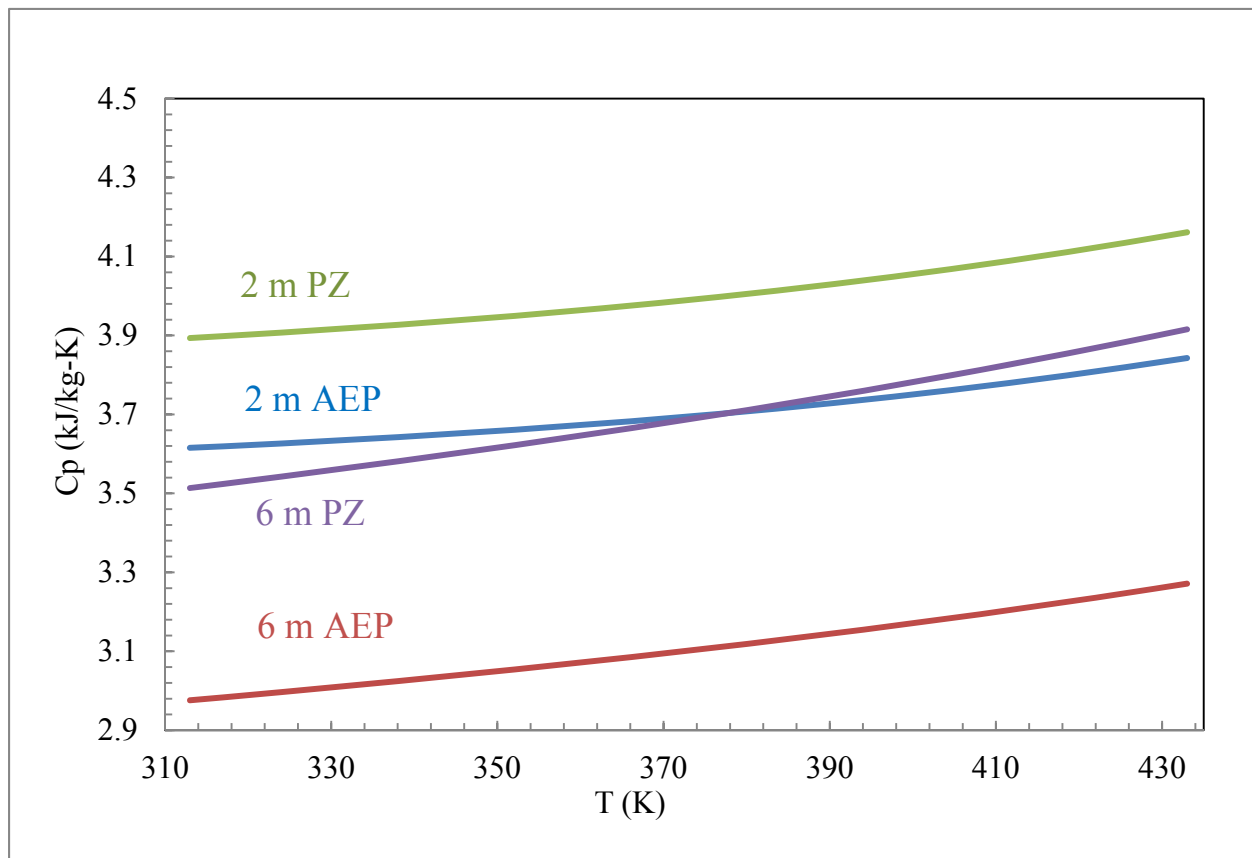
Figure 6: Prediction of heat capacity of 6 m AEP as a function of T.
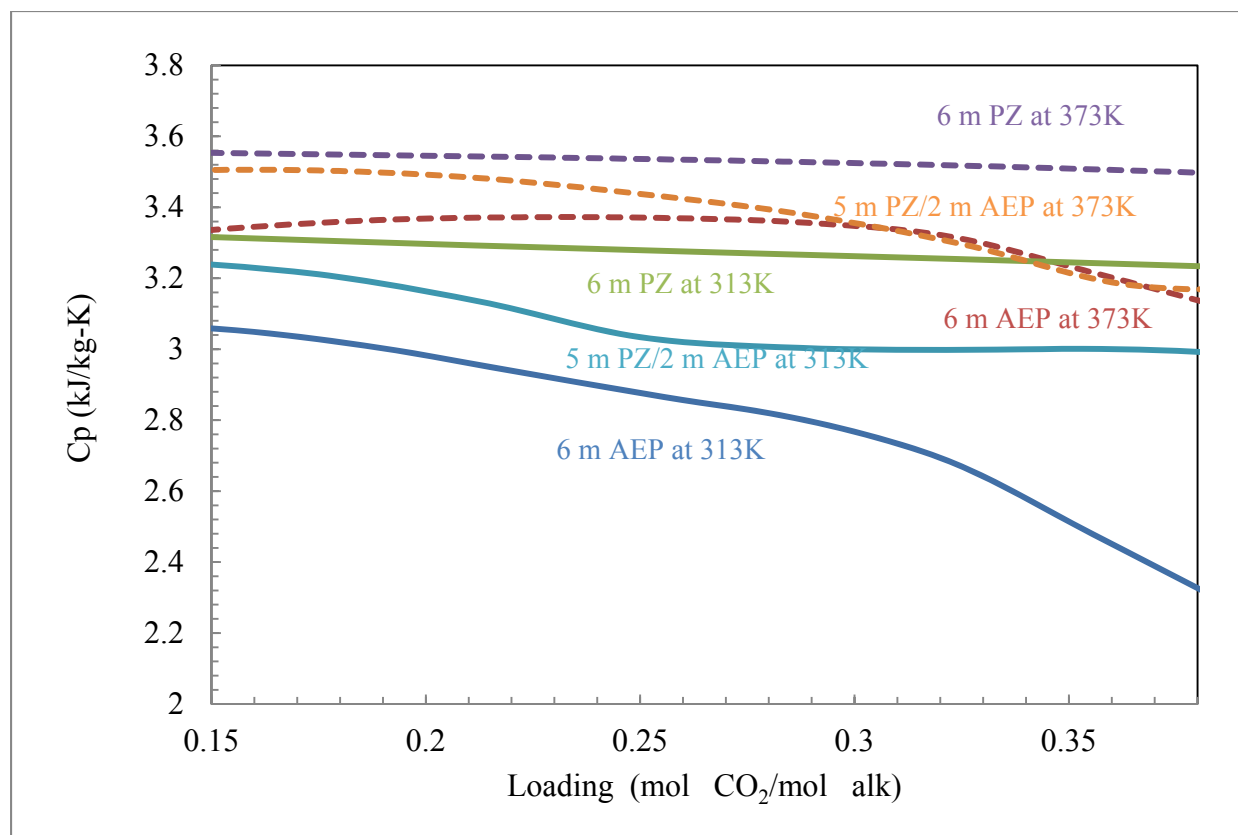
Figure 7: Prediction of heat capacity of AEP and PZ/AEP as a function of loading

Conclusions

1. A rigorous thermodynamic model has been preliminarily developed for the PZ-AEP-H_2O-CO_2 system in Aspen Plus[®] using the Electrolyte Nonrandom Two-Liquid (e-NRTL) activity coefficient model.
2. This model can accurately predict VLE of 6 m AEP and 5 m PZ/2 m AEP at practical loading and temperature range.
3. This model can predict reasonable behavior of speciation and heat capacity of AEP and PZ/AEP as a function of loading and temperature.

Future Work

Volatility measurement for AEP and PZ/AEP, which has started in this quarter, will be finished in next quarter. Volatility data will be incorporated into the current thermodynamic model and then a kinetic model will be established based on it.

References.

Austgen, DM. *A Model of Vapor-Liquid Equilibria for Acid Gas-Alkanolamine-Water Systems*. The University of Texas at Austin. Ph.D. Dissertation. 1989.

Bishnoi S. *Carbon Dioxide Absorption and Solution Equilibrium in Piperazine Activated Methyldiethanolamine*. The University of Texas at Austin. Ph.D. Dissertation. 2000.

Chen X. *Carbon dioxide thermodynamics, kinetics, and mass transfer in aqueous piperazine derivatives and other amines*. The University of Texas at Austin. Ph.D. Dissertation. 2011.

Cullinane JT. *Thermodynamics and Kinetics of Aqueous Piperazine with Potassium Carbonate for Carbon Dioxide Absorption*. The University of Texas at Austin. Ph.D. Dissertation. 2005.

Hilliard MD. *A Predictive Thermodynamic Model for an Aqueous Blend of Potassium Carbonate, Piperazine, and Monoethanolamine for Carbon Dioxide Capture from Flue Gas*. The University of Texas at Austin. Ph.D. Dissertation. 2008.

Pagano JM., Goldberg DE. Fernelius WC. A Thermodynamic study of homopiperazine, piperazine, and N-(2-aminoethyl)-piperazine and their complexes with copper(II) ion. *J Phys Chem*. 1961;65:1062–1064.

Plaza JM. *Modeling of Carbon Dioxide Absorption using Aqueous Monoethanolamine, Piperazine and Promoted Potassium Carbonate*. The University of Texas at Austin. Ph.D. Dissertation. 2011.

Posey, ML. *Thermodynamic Model for Acid Gas Loaded Aqueous Alkanolamine Solutions*. The University of Texas at Austin. Ph.D. Dissertation. 1996.

Rochelle GT, et al. "CO_2 Capture by Aqueous Absorption, Third Quarterly Progress Report 2012." Luminant Carbon Management Program. The University of Texas at Austin. 2012.

Advanced Absorber and Stripper Configurations

Abstract

The goal of this study is to evaluate the performance of an absorber/stripper operation that utilizes MDEA/PZ. Before analyzing unit operations and process configurations, thermodynamic, hydraulic, and kinetic properties for the blended amine must be satisfactorily regressed in Aspen Plus®. The approach used in this study is first to construct separate MDEA and PZ models that can later be reconciled via cross parameters to model accurately the MDEA/PZ blended amine. During the past quarter a rate-based absorber model was constructed for both intercooled and non-intercooled cases. Adding intercooling improved solvent capacity by as much as 80% for 5 m MDEA/5 m PZ, but it requires the use of twice as much packing. Another absorber modification that was tested was the use of higher solvent flowrates, which have the potential to reduce packing volumes by 25 to 30% while only decreasing solvent capacity by 8 to 11%. Using the rich solutions generated by the absorber models, four stripper configurations were evaluated: (1) simple stripper, (2) interheated stripper, (3) two-stage flash with warm rich bypass, and (4) two-stage flash with warm rich bypass and a low temperature adiabatic flash. All results were generated using the Independence model. All three advanced configurations reduced the equivalent work relative to the simple stripper, but a techno-economic analysis is needed to determine the optimum configuration. This report is an expansion of the presentation given at GHGT-11, delivering new data concerning operating conditions, process efficiencies, and interactions between process modifications.

Introduction

The removal of CO_2 from process gases using alkanolamine absorption/stripping has been extensively studied for several solvents and solvent blends. An advantage of using blends is that the addition of certain solvents can enhance the overall performance of the CO_2 removal system. A disadvantage of using blends is that they are very complex compared to a single solvent, thus making them much more difficult to model.

This study will focus on a blended amine solvent containing piperazine (PZ) and methyldiethanolamine (MDEA). Previous studies have shown that this particular blend has the potential to combine the high capacity of MDEA with the attractive kinetics of PZ (Bishnoi, 2000). These studies have supplied a rudimentary Aspen Plus®-based model for an absorber with MDEA/PZ. The previous work recommended that more kinetic and thermodynamic data should be acquired for the MDEA/PZ blend before the model can be significantly improved.

Three researchers in the Rochelle lab have been acquiring these data, which are being incorporated into the model. One of the major goals of this study will be to improve the supplied Aspen Plus® absorber model with up-to-date thermodynamic and kinetic data. Another major goal will be to make improvements to the MDEA and PZ thermodynamic models, which should simplify the construction of the blended amine model.

Methods and Discussion

During the past quarter novel absorber and stripper configurations were designed and evaluated for 8 m PZ, 7 m MDEA/2 m PZ, and 5 m MDEA/5 m PZ. What follows is a description of those novel configurations as well as the results of the evaluations.

Rate-Based Absorber

The rich solutions used for the stripper modeling were generated using a rate-based absorber model in Aspen Plus®. The column was split into three sections of equal height with a pumparound extracting 75% of the solvent from the bottom of the second section, cooling it to 40 °C, and feeding the solvent back into the top of the second section. All three sections were set to be the same height, but they did not have the same packing. The top and bottom sections used Mellapak 250X and the middle section used Mellapak 125X. The column diameter was set to 80% flood in the second section, and the total column height is such that 90% of the CO_2 is removed using liquid flow rates corresponding to 1.1 and 1.2 times the minimum. Figure 1 gives a process flow diagram for the intercooled absorber.
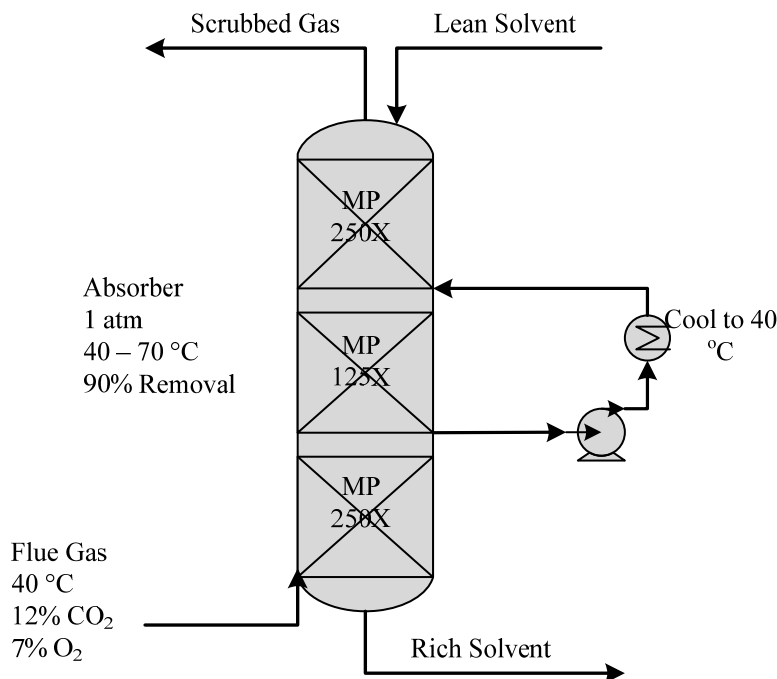
Figure 1: Process flow diagram for intercooled absorber.

Using this convention 8 m PZ, 7 m MDEA/2 m PZ, and 5 m MDEA/5 m PZ were tested over a wide lean loading range to determine solvent capacity. Figure 2 reports solvent capacity for both the intercooled and non-intercooled absorber when the liquid flow rate is set to 1.1 times the minimum.

2
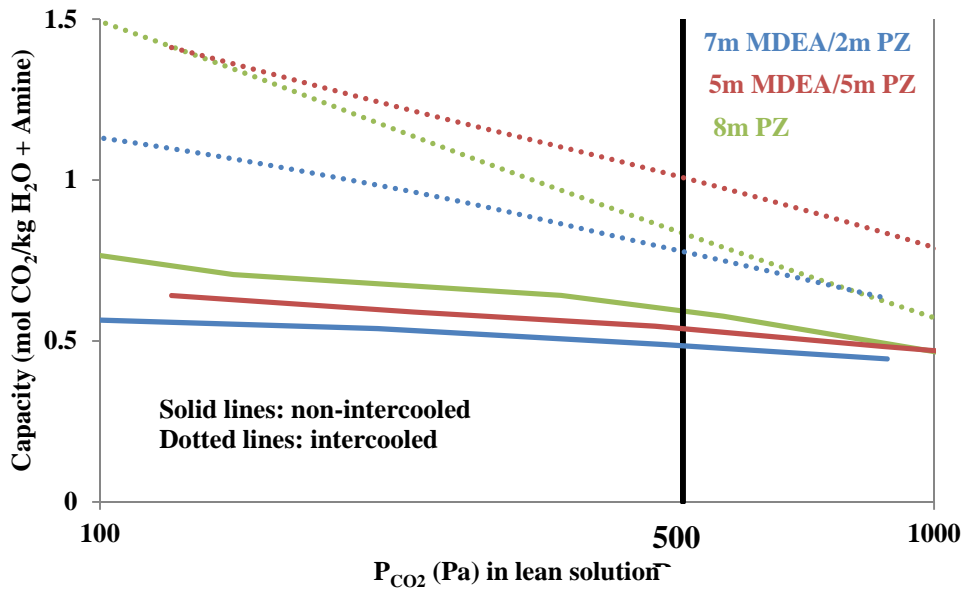
Figure 2: Capacity as a function of lean partial pressure of CO_2 for 8 m PZ, 7 m MDEA/2 m PZ, and 5 m MDEA/5 m PZ at 40 ^{o}C in an intercooled and non-intercooled absorber when the flow rate is 1.1 times the minimum.

Intercooling improves solvent capacity for every amine. The most marked improvement was observed for 5 m MDEA/5 m PZ, which experienced an 80% increase in capacity at the nominal lean loading of 500 Pa. However, this comes with added capital cost. The intercooled absorber must be approximately 3x the size of the non-intercooled absorber. The column heights are summarized in Table 1.

Table 1: Absorber height corresponding to 90% removal at 40 ^{o}C for 8 m PZ, 7 m MDEA/2 m PZ, and 5 m MDEA/5 m PZ with an equilibrium partial pressure of 500 Pa in the lean solvent and a solvent flow rate of 1.1 times the minimum

Amine	Non-Intercooled Height (m)	Intercooled Height (m)
8 m PZ	12	18
7 m MDEA/2 m PZ	15	30
5 m MDEA/5 m PZ	13	27

Increasing the solvent flow rate to 1.2 times the minimum will decrease the column height, but it also decreases solvent capacity. Table 2 compares the column heights and capacities for 8 m PZ, 7 m MDEA/2 m PZ, and 5 m MDEA/5 m PZ in intercooled absorbers.

Table 2: Intercooled absorber height and solvent capacity at 40 °C for 8 m PZ, 7 m
MDEA/2 m PZ, and 5 m MDEA/5 m PZ with an equilibrium partial pressure of 500 Pa in
the lean solvent and solvent flow rates of 1.1 and 1.2 times the minimum

Table 2: Intercooled absorber height and solvent capacity at 40 °C for 8 m PZ, 7 m MDEA/2 m PZ, and 5 m MDEA/5 m PZ with an equilibrium partial pressure of 500 Pa in the lean solvent and solvent flow rates of 1.1 and 1.2 times the minimum

	1.1 x Minimum L/G		1.2 x Minimum L/G	
Solvent	**Absorber Height (m)**	**Capacity (mol CO_2/mol alk)**	**Absorber Height (m)**	**Capacity (mol CO_2/mol alk)**
8 m PZ	18	0.84	14	0.75
7 m MDEA/2 m PZ	30	0.82	21	0.73
5 m MDEA/5 m PZ	27	0.97	20	0.88

Increasing the solvent flow rate to 1.2 times the minimum decreases column height between 25 and 30% and decreases solvent capacity by 8 to 11%. A techno-economic analysis is required to determine which solvent flow rate yields a lower cost of mitigation.

Advanced Stripper Configurations

Interheated Stripper

The first advanced stripper configuration is the interheated stripper, which can be found in Figure 3. The interheated stripper recycles heat from the rich solution leaving the bottom of the stripper back into the middle of the column, thus reducing the amount of heat exchanged in the main cross-exchanger and lowering the temperature of the rich solvent entering the top of the stripper. Two and a half meters of Mellapak 250X packing is included above and below the point where solvent is removed and returned for interheating. A lower temperature at the top of the stripper will reduce the energy losses associated with steam generation. The cross-exchanger associated with the interheating is specified to have a 5 °C LMTD, whereas the main cross-exchanger is designed for a 5 °C cold-side approach. The reboiler temperature was set to 150 °C and 120 °C for 8 m PZ and 120 °C for 7 m MDEA/2 m PZ and 5 m MDEA/5 m PZ.
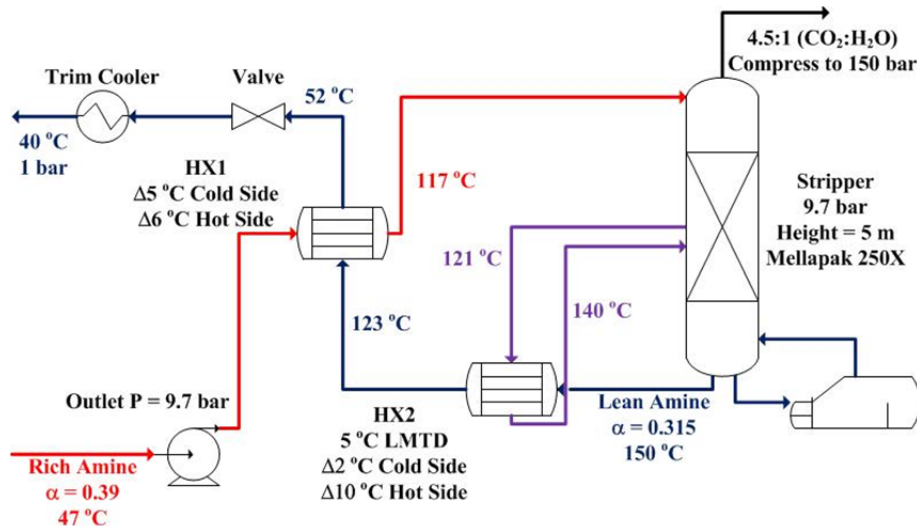
Figure 3: Process flow diagram for interheated stripper with 8 m PZ regenerated at 150 °C

Two-Stage Flash (2SF) with Warm Rich Bypass (WRB)

Just as with the interheated stripper, the 2SF with CRB cools the exiting vapor to minimize steam losses. Anywhere from 5–30% of the solvent is removed after passing through a cross-exchanger, where it was heated by the lean amine. The 70–95% that is not bypassed goes directly into another cross-exchanger, where it is again heated by the lean amine before being fed into a heated high pressure flash vessel. Half of the cooler amine removed before the second cross-exchanger is sprayed into the top of the vessel and passes through 1 foot (~0.3 m) of packing. The other half is sent to the low pressure flash vessel. The first cross-exchanger is designed with a 5 ^{o}C cold-side approach, and the second cross-exchanger is designed with a 5 ^{o}C LMTD. Both flash tanks are heated to the same temperature. For 8 m PZ they are heated to 150 ^{o}C, and for the MDEA PZ blends they are heated to 120 ^{o}C. This configuration can be found in Figure 4. The optimum case had a 7.5% bypass, with 5% going to the low pressure flash and 2.5% going to the high pressure flash. At the top of each flash tank is 1.5 ft (~0.46 m) of Mellapak 500Y packing. The pressure of the high pressure flash was fixed at 1.5 times that of the low pressure flash.
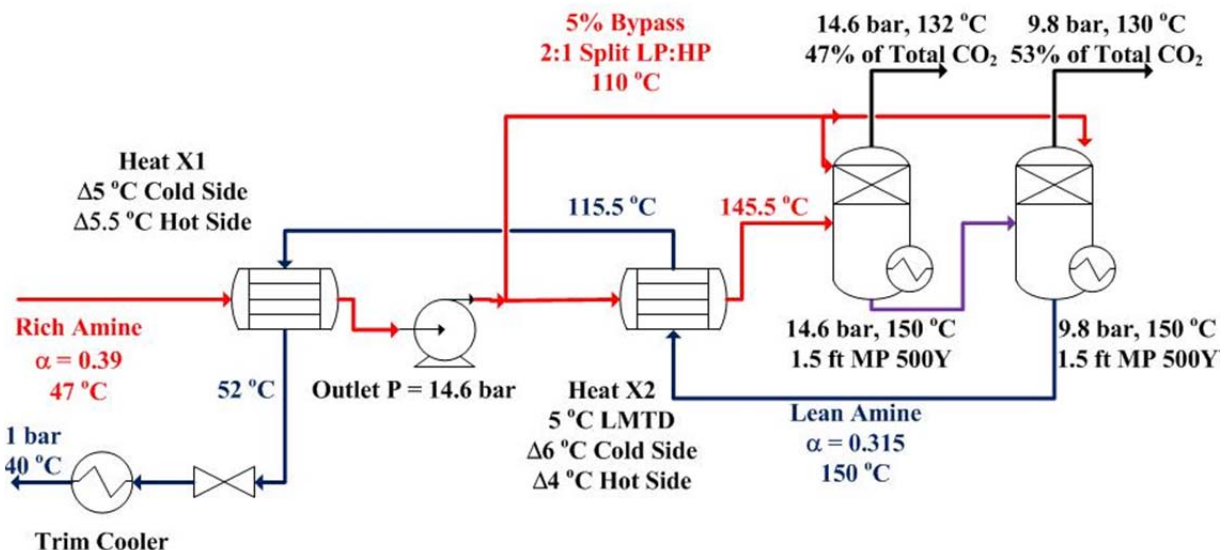
Figure 4: Process flow diagram for 2SF with CRB with 8 m PZ regenerated at 150 ^{o}C

2SF with WRB and a Low Temperature Flash (LTF)

This configuration is very similar to the one in the previous section, except it has an additional low temperature adiabatic flash immediately after the first cross-exchanger (Figure 5). This flash serves two purposes: (1) it makes the process more reversible by removing the CO_2 in more steps, and (2) it removes any entrained oxygen before introducing the solvent to the higher temperature flash vessels. The same temperature and pressure constraints applied to the 2SF with CRB were applied to this configuration. For 8 m PZ the flash tanks were held at 150 ^{o}C, and for 7 m MDEA/2 m PZ and 5 m MDEA/5 m PZ they were held at 120 ^{o}C. The pressure of the high pressure flash was fixed to be 1.5 times that of the low pressure flash. A total of 7.5% of the solvent was bypassed with 5% going to the low pressure flash and 2.5% going to the high pressure flash. At the top of each flash tank is 1.5 ft of Mellapak 500Y.

1 bar, 80.8 ^{o}C
8% of Total CO_2

5% Bypass
2:1 Split LP:HP
81.4 ^{o}C

14.6 bar, 108 ^{o}C
50% of Total CO_2

9.8 bar, 110 ^{o}C
42% of Total CO_2

Heat X1
Δ5 ^{o}C Cold Side
Δ6.6 ^{o}C Hot Side

87.4 ^{o}C

Rich Amine
$\alpha = 0.39$
47 ^{o}C

52 ^{o}C

14.6 bar, 150 ^{o}C
1.5 ft MP 500Y

9.8 bar, 150 ^{o}C
1.5 ft MP 500Y

1 bar
40 ^{o}C

Heat X2
5 ^{o}C LMTD
Δ6 ^{o}C Cold Side
Δ4 ^{o}C Hot Side

Lean Amine
$\alpha = 0.315$
150 ^{o}C

Trim Cooler

LT Flash
1 bar
80.8 ^{o}C

Outlet P = 14.6 bar
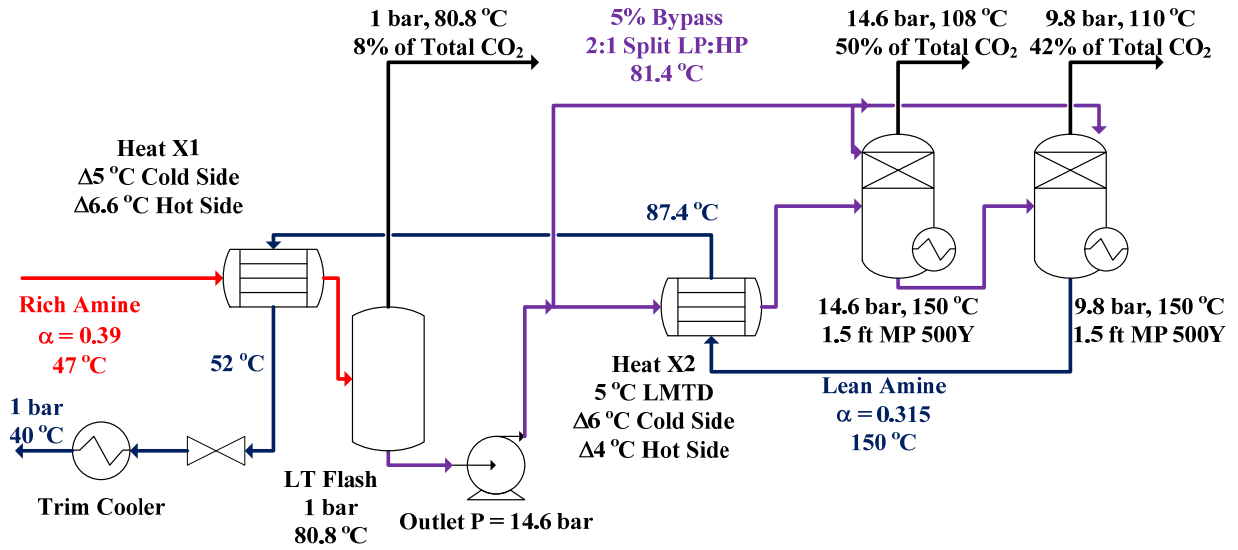
Figure 5: Process flow diagram for 2SF with CRB and LTF for oxygen removal with 8 m PZ regenerated at 150 ^{o}C

Comparing Configurations

Table 3 reports the equivalent work in kJ/mol CO_2 for each amine using the three advanced stripper configurations as well as the simple stripper.

Table 3: W_{EQ} (kJ/mol CO_2) for 8 m PZ, 7 m MDEA/2 m PZ, and 5 m MDEA/5 m PZ with an intercooled absorber and a simple stripper (SS), interheated stripper (IH), two-stage flash with WRB (2SF/WRB), or two-stage flash with WRB and LT flash (2SF/WRB/LTF) assuming a 500 Pa lean loading equilibrium P_{CO2}.

Amine	SS	IH	2SF/WRB	2SF/WRB/LTF
8 m PZ (150 ^{o}C)	33.3	31.0	31.3	31.1
8 m PZ (120 ^{o}C)	33.4	31.3	31.7	31.4
7 m MDEA/2 m PZ	34.6	32.1	32.2	32.0
5 m MDEA/5 m PZ	32.6	31.6	30.5	30.4

Equation 1 was used to calculate equivalent work, and Equations 2 and 3 were used to calculate compressor work.

$$W_{eq} = \sum_{i=1}^{n_{reboilers}} 0.75 Q_i \left(\frac{T_i + 5K - T_{\sin k}}{T_i + 5K} \right) + W_{pumps} + W_{comps} \tag{1}$$

6

$$W_{comps}\left(kJ/mol\ CO_2\right)=4.572\log\left(\frac{148}{P_{in}\left(atm\right)}\right)-4.096 \qquad P_{in}\leq 4.5atm \qquad (2)$$

$$W_{comps}\left(kJ/mol\ CO_2\right)=4.023\log\left(\frac{148}{P_{in}\left(atm\right)}\right)-2.181 \qquad P_{in}>4.5atm \qquad (3)$$

In Equation 1, Q_i is the reboiler duty, T_{sink} is 313 K, and T_i is the reboiler temperature. In Equations 2 and 3, P_{in} is the total pressure of the stream being fed into the compressor. Adding interheating to the stripper reduces the equivalent work by 1–2.5 kJ/mol CO_2. This improvement may be attributed to the reduced steam losses. Table 4 reports the steam losses for the three solvents with a simple stripper and an interheated stripper.

Table 4: Relative molar quantities of CO_2 and H_2O in the product streams of a simple stripper (SS) and interheated stripper (IHS) for 8 m PZ, 7 m MDEA/2 m PZ, and 5 m MDEA/5 m PZ when using a lean loading corresponding to a 500 Pa equilibrium partial pressure of CO_2.

Amine	SS molar ratio of CO_2:H_2O	IHS molar ratio of CO_2:H_2O
8 m PZ (150 ^{o}C)	2.2	4.5
8 m PZ (120 ^{o}C)	1.6	2.8
7 m MDEA/2 m PZ	1.7	3.1
5 m MDEA/5 m PZ	2.1	3.1

The greater the change in CO_2:H_2O the greater the reduction in W_{EQ}. Adding the adiabatic LTF does not significantly impact the equivalent work of the 2SF with CRB configurations. The LTF impacts process performance in two ways: (1) improving process reversibility by removing CO_2 in more steps and (2) decreasing process efficiency by requiring more mechanical compression for the CO_2 removed in the LTF. These results suggest that the effects offset each other, and, if there is significant concern surrounding oxidative degradation of the amine, the LTF is a feasible process modification.

Conclusions

- Increasing the solvent flow rate from 1.1 times the minimum L/G to 1.2 times the minimum L/G decreases absorber height by 25 to 30% and decreases capacity by 8 to 11%.
- The interheated stripper reduces W_{EQ} by reducing steam losses in the stripper.
- Increasing the regeneration temperature from 120 ^{o}C to 150 ^{o}C for 8 m PZ improves W_{EQ} for all configurations, but the improvement is on the order of 0.1–0.3 kJ/mol CO_2.
- Adding a low temperature adiabatic flash to the two-stage flash with warm rich bypass has a negligible effect on process performance.

Future Work

The remainder of this study will focus on process design and optimization. The effect of absorber temperature on process performance will be determined for 8 m PZ, 7 m MDEA/2 m PZ, and 5 m MDEA/5 m PZ. Novel stripper configurations will be developed and evaluated using the recently updated thermodynamic, hydraulic, and kinetic model. All work will be performed with the intention of graduating in Spring 2013.

References

Bishnoi S. *Carbon Dioxide Absorption and Solution Equilibrium in Piperazine Activated Methyldiethanolamine*. The University of Texas at Austin. Ph.D. Dissertation. 2000.

Cullinane JT. *Thermodynamics and Kinetics of Aqueous Piperazine with Potassium Carbonate for Carbon Dioxide Absorption*. The University of Texas at Austin. Ph.D. Dissertation. 2005.

Ko JJ, Li MH. Kinetics of absorption of carbon dioxide into solutions of N-methyldiethanolamine + water. *Chem Eng Sci*. 2000;55:4139–4147.

Plaza JM. *Modeling of Carbon Dioxide Absorption using Aqueous Monoethanolamine, Piperazine and Promoted Potassium Carbonate*. The University of Texas at Austin. Ph.D. Dissertation. 2011.

Novel Absorber Intercooling Configurations

Abstract

A modeling study was initiated to evaluate 3 intercooling design configurations ("in-and-out" intercooling, recycle intercooling, recycle intercooling with bypass) for 3 CO_2 flue gas concentrations corresponding to potential capture applications (natural gas combined cycle (4% CO_2), coal-fired power plant (12–14% CO_2), and cement/steel/industrial (>20% CO_2). During the past quarter, preliminary analysis of the natural gas combined cycle application was completed. Results for a constant rich loading analysis at low recycle rates (0.5 to 2 $L_{Recycle}/G$) indicate that the recycle with bypass is significantly better than the simple recycle design (up to 47% packing reduction) and provides benefits over in-and-out intercooling (up to 13% packing reduction). At higher recycle rates (> 2 $L_{Recycle}/G$), the simple recycle and bypass become indistinguishable, and no longer justifies the use of a bypass. At the maximum recycle rate considered in this work (8 $L_{Recycle}/G$), and at a constant rich loading, the simple recycle design results in a 46% packing reduction compared to the intercooling design. The simple recycle design shows improvements in both rich loading and packing requirements when compared to in-and-out intercooling as the recycle rate is increased, though diminishing returns occur with the incremental recycle rate increases. Therefore, recycle intercooling designs show improvement over in-and-out intercooling over the full range of recycle rates (bypass design at low rates, simple design at high rates). Economic analysis is required to determine plausible operating points and potential optimum operating conditions for the recycle intercooling configurations.

The natural gas application design cases for TOTAL have been completed, including equipment and stream tables. All results and data will be included in a report to be completed in the early part of 2013.

Introduction

During the past quarter, an intercooling comparison summary was initiated including 3 intercooling designs (in-and-out, simple recycle, recycle with bypass) at 3 CO_2 concentrations (NGCC = 4.1%, coal = 13.5%, cement/steel = >20%). The work is an extension of the initial development of the recycle intercooling design as part of previous natural gas absorber modeling (Rochelle et al., 2012b) and seeks to confirm and quantify the benefits of the recycle intercooling design. Preliminary results have been generated for the NGCC scenario and are presented in this report.

1

Absorber Intercooling Design Comparison Study

Previous work (Rochelle et al., 2012b) with natural gas combined cycle (NGCC) applications introduced the concept of recycle intercooling and included preliminary sensitivity results for recycle process parameters (e.g., solvent recycle rate and packing height). Recycle intercooling was implemented as a potential improvement over the "in-and-out" intercooling concepts studied and developed in detail by Plaza for coal applications (Plaza, 2011). The expected improvement with recycle intercooling was, in part, due to the additional benefit of cooling the gas as well as the solvent in a well-mixed section. However, the previous analyses did not directly compare recycle intercooling to the in-and-out design and did not consider different CO_2 concentrations (capture applications).   In the past quarter, a rigorous comparison study was initiated with intercooling comparison for NGCC applications. Table 1 includes NGCC flue gas conditions. Table 2 summarizes equipment design parameters used in the NGCC intercooling comparison.

Table 1: Natural Gas Capture Application, Flue Gas Conditions

Gas Conditions		
Gas Feed Rate	114,000	kg-mol/hr
	3,230,000	kg/hr
Temperature	106	°C
Pressure	0.1	MPa
Composition (Mole %)		
CO_2	4.0%	
H_2O	8.7%	
N_2	74.3%	
O_2	12.1%	
Data from NETL Case 13 (NETL, 2010)		

Table 2: Intercooling Comparison Study: Equipment and Process Design Summary

Equipment and Process Design Parameters		
CO_2 Removal	90%	
Lean Loading (mols CO_2/ mols alkalinity)	0.25	
Flue Gas CO_2 Concentration (mol%)	4%, 14%, >20%	
Recycle Rate ($L_{recycle}$/G)	0.5–8	
Maximum Approach to Flooding	70%	
Packing (No Solvent Recycle in Section)**	MP 250X	
Packing (Solvent Recycle in Section)**	0.5 $L_{Recycle}$/G:	MP 250X
	1 $L_{Recycle}$/G:	MP 250X

2 $L_{Recycle}$/G:	MP 2X
3 $L_{Recycle}$/G:	MP 170X
5 $L_{Recycle}$/G:	MP 125X
8 $L_{Recycle}$/G:	MP 64X

**Coarse Packing required to meet flooding criteria in packing section with solvent recycle. Packing type varied to approximate identical flooding profiles in each case.

Table 2 includes the range of recycle rates evaluated in this study (defined in the table as liquid rate in the recycle relative to the overall gas rate in the column). In addition, the table reflects an important design choice regarding packing. MP 250X is the standard packing used in all cases in packing sections without recycled solvent. However, in the cases *with solvent recycle* (around the middle of 3 sections of packing), the maximum approach to flooding is reached in the recycle section due to high liquid rates compared to the rest of the column. Instead of increasing the column diameter with increasing recycle liquid rate, coarse packing was used to minimize pressure drop and flooding with limited change to column diameter from case to case. By using a nearly constant column diameter, the sections *outside* of the recycle maintain a nearly constant liquid rate per wetted perimeter (or superficial velocity). This superficial velocity is correlated to mass transfer performance via the Reynolds number dependence of liquid side mass transfer coefficients. If the superficial velocity in the top and bottom sections of packing dropped significantly from case to case (as the diameter of the column increased), the mass transfer performance of the column would deteriorate and offset the benefit of recycle intercooling.

Figure 1 through **Error! Reference source not found.** are PFDs for the intercooling configurations considered in the study and reflect the packing configuration described in the preceding paragraph.
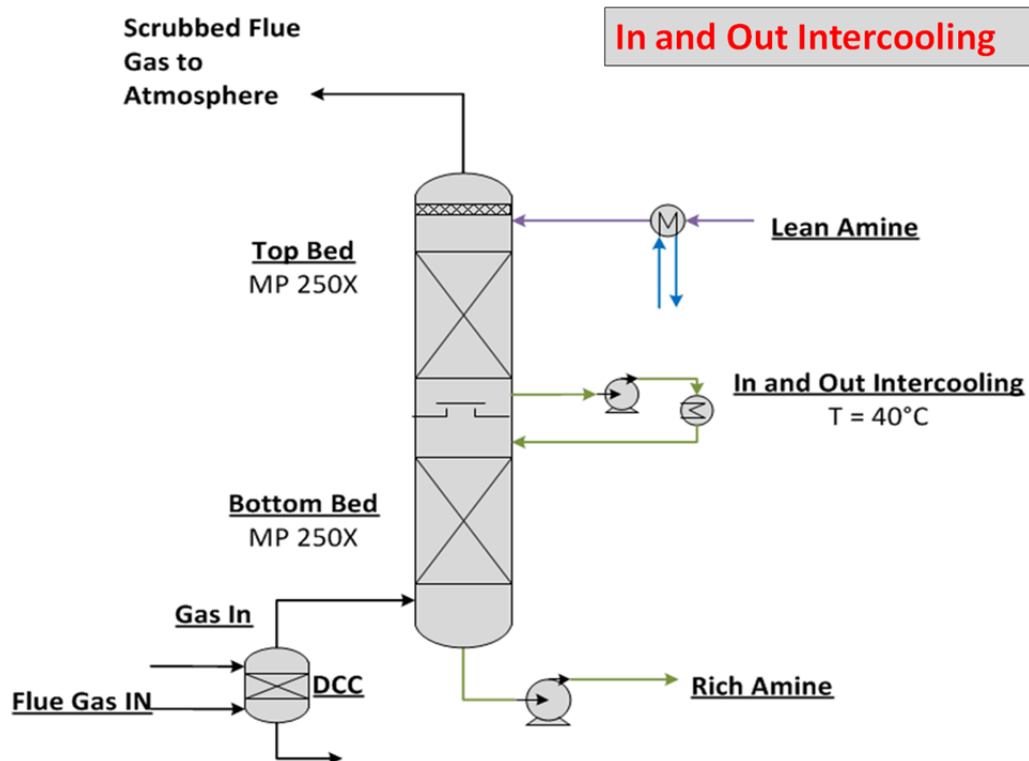
Figure 1: Absorber PFD for In-and-out Intercooling Design. Two equal sections of packing (MP 250X) are used with liquid draw-off, cooling, and return between the packed sections. The solvent is cooled to 40 °C before returning to the column.
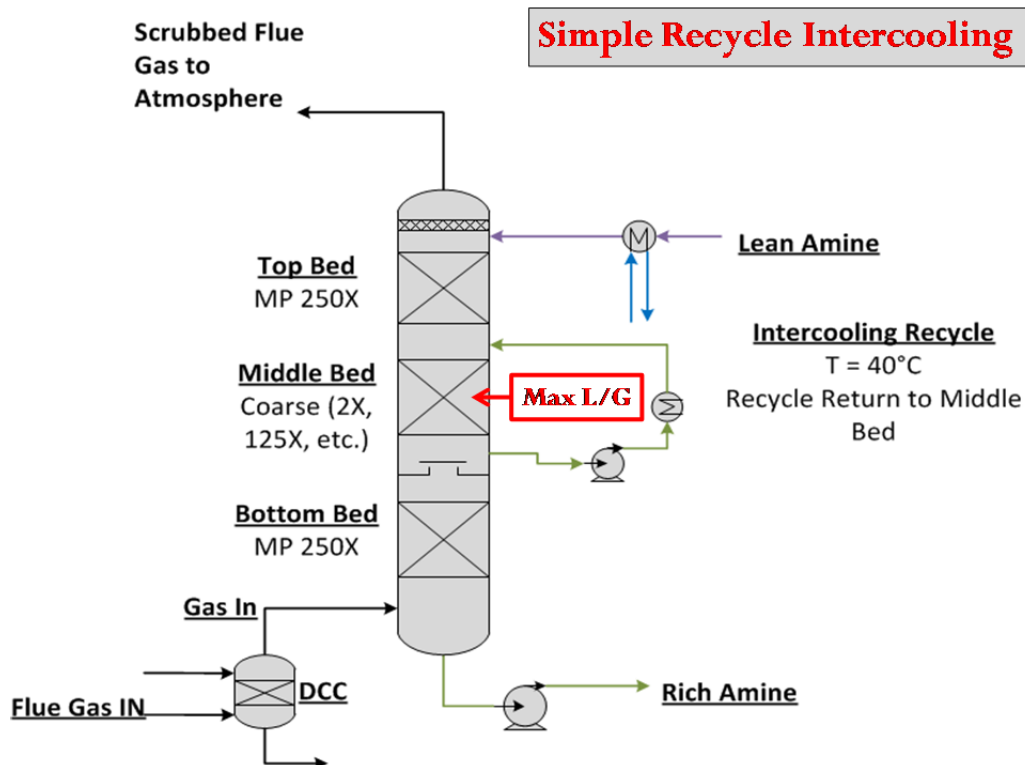
Figure 2: Absorber PFD for Simple Recycle Intercooling Design. Three packing sections are used, with the packing height of each section optimized for each design case to minimize total packing area. MP-250X is used in the top and bottom section and various coarse structured packing is used in the middle (recycle section) to maintain 70% max approach to flood. Solvent is drawn off the bottom of the middle section, cooled, and returned to the top of the middle section of packing at 40 °C.
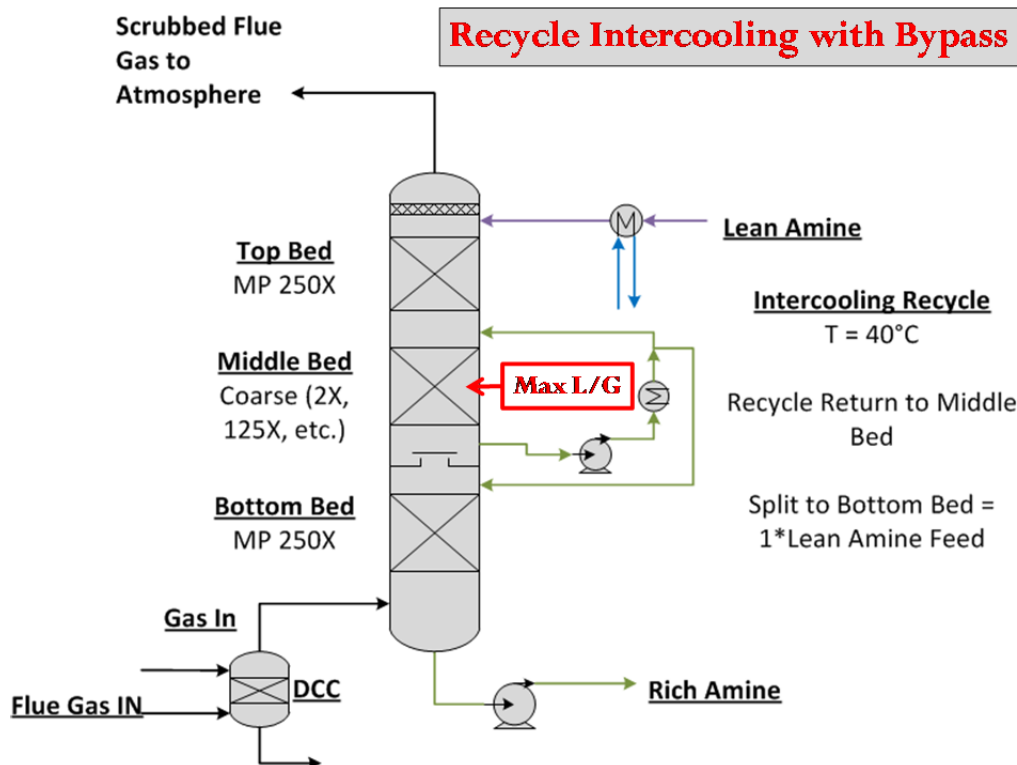
Figure 3: Absorber PFD for Recycle Intercooling with Bypass Design. Three packing sections are used, with the packing height of each section optimized for each design case to minimize total packing area. MP-250X is used in the top and bottom section and various coarse structured packing is used in the middle (recycle section) to maintain 70% max approach to flood. Solvent is drawn off the bottom of the middle section and cooled to 40 °C. A portion of the solvent is sent directly to the bottom section of the column (equal to the nominal liquid feed rate of the column) while the remaining liquid is recycled to the top of the middle section.

As mentioned, the recycle design is expected to more effectively cool the gas (particularly important in the NGCC cases with high gas rates or relatively low L/G ratios). In addition, the recycle is expected to provide some additional benefit due to a high liquid rate per wetted perimeter. The draw-back of the recycle design is the mixing of the solvent on the recycle section. The driving forces of the column are reduced by mixing a richer solvent with lean solvent entering the middle section of the column. In addition, the temperature leaving the recycle section will be higher than 40 °C, diminishing the benefits of intercooling realized in the bottom section of the column. The bypass design was developed to address the latter shortcoming of the simple recycle design. By splitting a portion of the recycled solvent after cooling and sending it to the bottom section directly, the solvent entering the bottom of the column is 40 °C, and the full benefit of intercooling in the bottom section should be achieved.

Methodology

Two approaches were used to compare the intercooling designs. First, the simple recycle design was compared to the in-and-out intercooling design and a case with no intercooling at an

operating point of 1.2*minimum liquid flow rate for each case (all achieving 90% CO_2 removal). This approach allows comparison of the designs at a common operating point; the packing requirement and energy performance (as reflected in the rich loading) can be compared for all designs. However, this method requires interpretation or weighting of the capital cost benefits (packing) and the energy benefits (rich loading) on a common basis to provide an absolute comparison of designs.

The second approach involved comparison of intercooling designs at a common rich loading. By fixing the rich loading (and, in conjunction with the 90% removal requirement, fixing the absolute solvent rate), the packing requirements of each design could be compared directly without consideration of energy performance implications.

In both approaches, the recycle intercooling designs were designed to minimize the total packing requirement in the column for every case that was run. This was accomplished by optimizing the packing split between the three sections in the column. As in previous work, the packing split optimization was incorporated into the Aspen Plus® simulation as an objective function of the following form:

$$Min \left[A_{Cross-Section} * (a_{p,top} * h_{top} + a_{p,middle} * h_{middle} + a_{p,middle} * h_{middle}) \right] \tag{1}$$

$$Subject\ to: Max\ Flood \leq 70\%, CO_2 Removal = 90\%$$

Where:
   a_p = Specific area of packing (m^2/m^3);
   $h_{section}$ = Specific area of packing (m^2/m^3);
   $A_{Cross-Section}$= Cross-sectional area of column (m^2).

Result

Figure 4 and 5 provide a comparison of the simple recycle intercooling design to both in-and-out intercooling and a baseline of no intercooling.

7
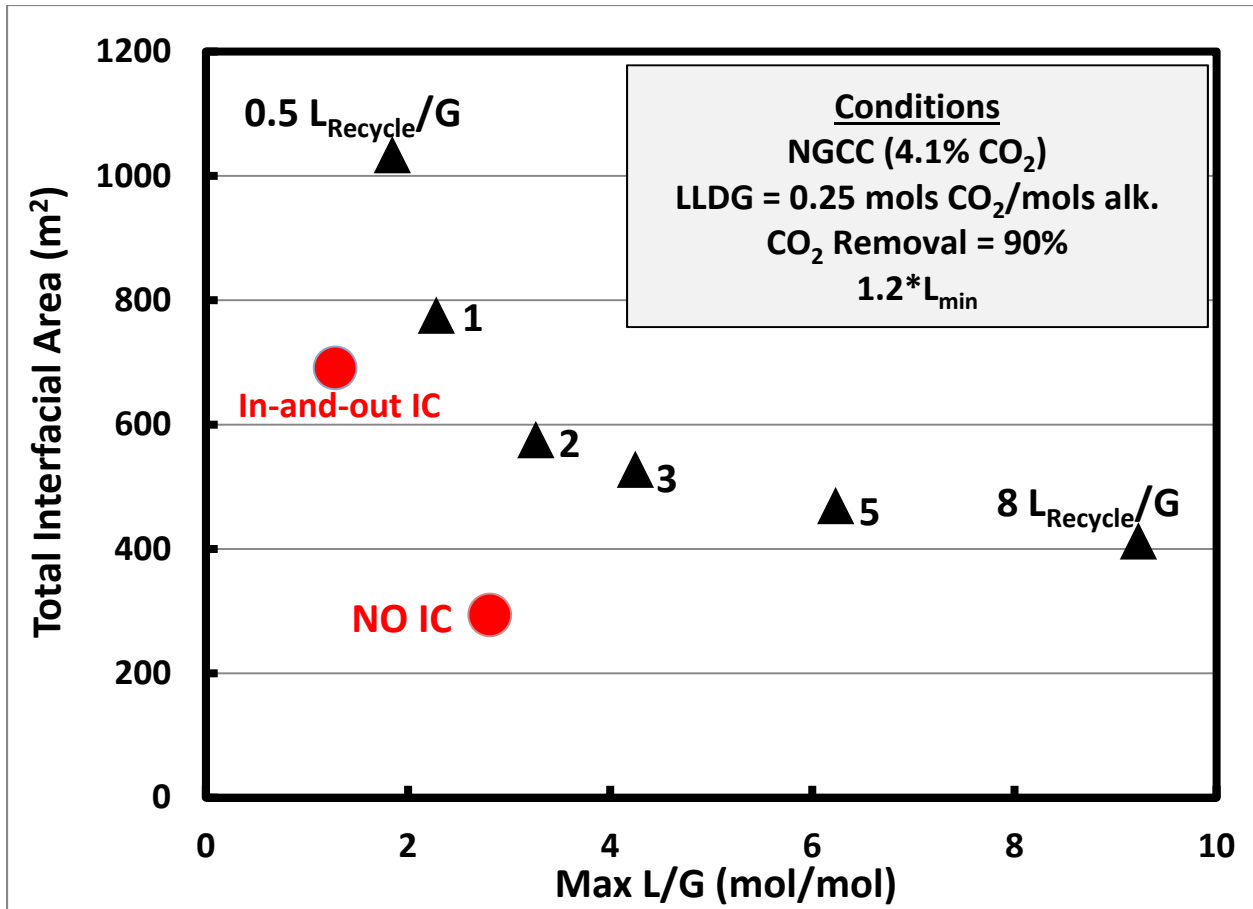
Figure 4: Intercooling configuration comparison in terms of total packing requirement: simple recycle intercooling, in-and-out intercooling, and no intercooling. For cases without recycle, the maximum L/G corresponds to the nominal feed L/G. For the recycle cases, this corresponds to the L/G in the recycle section (feed L + recycle L). Recycle intercooling simulated at a series of recycle solvent flow rates (and corresponding max L/G).
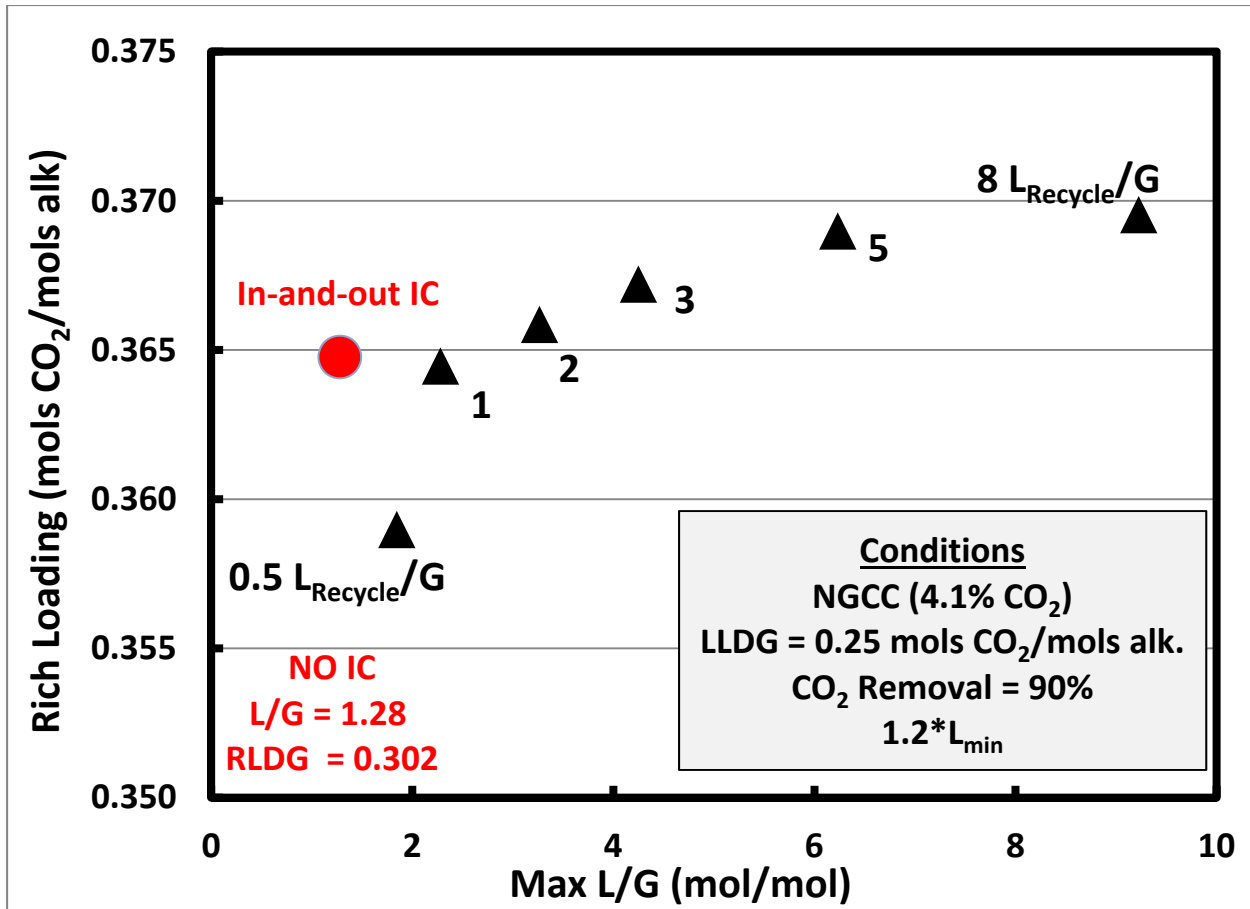
Figure 5: Intercooling configuration comparison in terms of rich loading achieved: simple recycle intercooling, in-and-out intercooling, and no intercooling. For cases without recycle, the maximum L/G corresponds to the nominal feed L/G. For the recycle cases, this corresponds to the L/G in the recycle section (feed L + recycle L). Recycle intercooling simulated at a series of recycle solvent flow rates (and corresponding max L/G). No intercooling point is out of the scope of the chart; raw data included for comparison.

The preceding figures should be used together when evaluating the designs. For example, Figure 4 indicates that a design without intercooling will provide the lowest packing requirement; however, the high liquid rate required leads to a rich loading (Figure 5: 0.302 mols CO_2/mols alkalinity) that is impractical from an energy and stripping performance perspective.

More importantly, the chart highlights the minimum recycle rate required for the simple recycle design to become competitive with the in-and-out intercooling design. In terms of both packing requirement and rich loading, a recycle rate of 1 L/G is required (max L/G = 2.28) to make the recycle design comparable to in-and-out intercooling. Given the additional cost associated with the recycle design (pumping liquid around the middle section of packing, potentially larger intercooling equipment, etc.), a higher recycle rate would be needed to justify the recycle design. As both figures show, the higher recycle rates provide both reduced packing requirements and improved rich loading performance. However, the benefits show diminishing returns with incremental increases in recycle rate, and when considered with costs associated with higher

9

recycle rates, indicate potential for an optimal recycle rate somewhere above 1 L/G but below the 8 L/G value simulated here.

To compare the configurations on a common basis, Figure 6 compares all 3 intercooling designs (now including the recycle with bypass design) at a constant rich loading of 0.365 mols CO_2/mols alkalinity (constant L/G of 1.28 mol/mol). The fixed rich loading corresponds to that achieved by in-and-out intercooling at 1.2*minimum liquid rate.
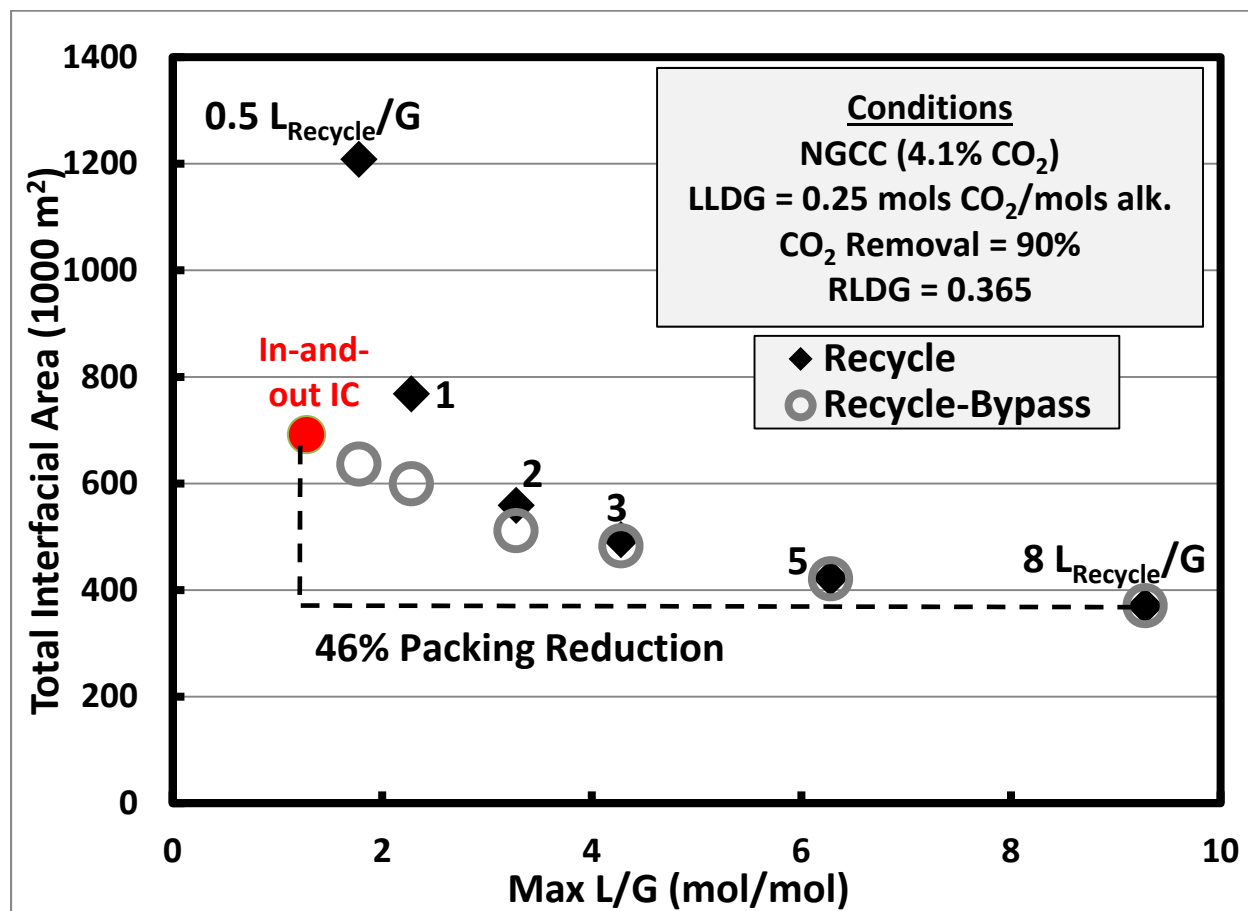
Figure 6: Intercooling configuration comparison at constant rich loading (solvent rate) in terms of total interfacial area: simple recycle intercooling, recycle with bypass, and in-and-out intercooling. For cases without recycle, the maximum L/G corresponds to the nominal feed L/G. For the recycle cases, this corresponds to the L/G in the recycle section (feed L + recycle L). Recycle intercooling simulated at a series of recycle solvent flow rates (and corresponding max L/G).

As in the previous figures, simple recycle intercooling must utilize a recycle rate greater than 1 $L_{Recycle}$/G to be competitive with the in-and-out intercooling design. At a recycle rate of 8 $L_{Recycle}$/G, the maximum packing reduction of 46% is achieved compared to in-and-out intercooling. However, the implementation of the recycle with bypass (sending 40 °C solvent to the bottom section of the column and maintaining intercooling benefit) shows drastic improvements at the low recycle rates. At a recycle rate of 0.5 $L_{Recycle}$/G, the implementation of

bypass reduces the packing requirement by 47% compared to the simple recycle case and by 8% compared to the in-and-out recycle intercooling case. The benefit of recycling solvent is effectively combined with the intercooling benefit realized with the standard in-and-out design. A similar improvement is seen at a recycle rate of 1 $L_{Recycle}/G$; however, beyond this rate, the benefit of the bypass design is marginal and eventually the bypass and simple recycle designs become indistinguishable. At higher solvent recycle rates, the temperature of the solvent leaving the recycle section is lower and lower, approaching 40 °C; therefore, the bypass is providing less benefit compared to the simple recycle case of sending the solvent directly to the bottom section of the column. This is illustrated in Figure 7.
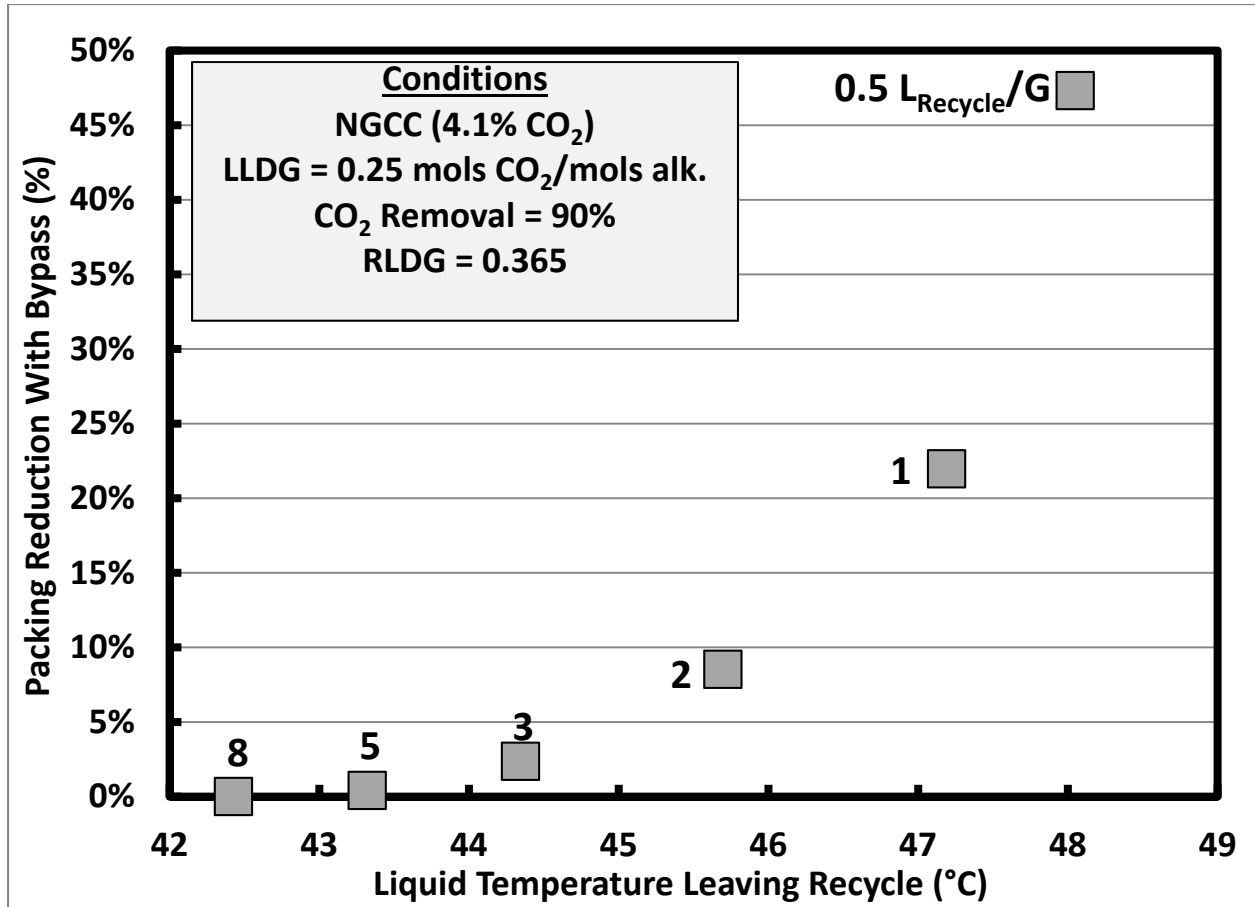
Figure 7: The benefit of recycle intercooling with bypass compared to simple recycle intercooling as a function of the solvent recycle rate and corresponding temperature leaving the recycle section.

As expected, at higher recycle rates the temperature leaving the recycle drops; the temperature is as low as 42.4 °C at the highest recycle rate of 8 $L_{Recycle}/G$. With the drop in temperature leaving the recycle, the benefit of the bypass design compared to the recycle design is diminished. By a recycle rate of 3 $L_{Recycle}/G$ (temperature leaving recycle = 44.3 °C), the benefit is less than 5% reduction in packing.

The preliminary results of the NGCC application intercooling comparison revealed the operating range in which recycle intercooling may be beneficial. At low recycle rates (0.5–2 $L_{Recycle}/G$), the bypass design must be implemented to realize benefits when compared to in-and-out intercooling. Beyond a recycle rate of 2 $L_{Recycle}/G$, the simple recycle design should be used since the benefit of the bypass design is lost. However, at higher recycle rates, benefits (reduced packing and higher rich loadings) show diminishing returns, so an optimal rate likely exists for simple recycle. With a range of potentially feasible recycle intercooling designs identified, future work will include economic analyses to validate and confirm the benefits of the recycle intercooling designs.

Conclusions

Comparison of 3 intercooling configurations for NGCC applications (4.1% CO_2) resulted in the following:

- When compared at an operating point of $1.2*L_{minimum}$, the simple recycle intercooling design provides benefits (reduced packing requirement, increased rich loading) over in-and-out intercooling at recycle rates above ~ 1 $L_{Recycle}/G$.
- When compared at constant rich loading (0.365 mols CO_2/mols alkalinity), recycle with bypass resulted in the lowest packing requirements at low recycle rates (0.5 to 2 $L_{Recycle}/G$). The bypass intercooling reduced packing requirements by 47% over simple recycle and by 8% over in-and-out intercooling when operated at 0.5 $L_{Recycle}/G$.
- At higher recycle rates (>2 $L_{Recycle}/G$), the bypass and simple recycle design are indistinguishable. At a recycle rate of 8 $L_{Recycle}/G$, a packing reduction of 46% compared to in-and-out intercooling is achieved with either recycle design.
- The bypass configuration should be used at low recycle rates (0.5 to 2 $L_{Recycle}/G$) while the simple recycle design should be used for high recycle rates (>2 $L_{Recycle}/G$). Economic analysis is needed to determine the operating point which maximizes benefits over standard in-and-out intercooling design.

Future Work

The NGCC intercooling comparison will be expanded to include preliminary economic analysis to identify operating points where recycle intercooling provides benefits over in-and-out intercooling. In addition, the full comparative analysis will be extended to coal and cement/steel applications to represent higher CO_2 concentration sources. Finally, new absorber designs will be developed based on the results of the intercooling comparison analysis.

References

National Energy Technology Laboratory. *Cost and Performance Baseline for Fossil Energy Plants Volume 1: Bituminous Coal and Natural Gas to Electricity.* Washington D.C.: U.S. Department of Energy, 2010.

Plaza JM. *Modeling of Carbon Dioxide Absorption using Aqueous Monoethanolamine, Piperazine, and Promoted Potassium Carbonate.* The University of Texas at Austin. Ph.D. Dissertation. 2011.

Rochelle GT et al. "CO_2 Capture by Aqueous Absorption, First Quarterly Progress Report 2012." Luminant Carbon Management Program. The University of Texas at Austin. 2012a.

Rochelle GT et al. "CO_2 Capture by Aqueous Absorption, Second Quarterly Progress Report 2012." Luminant Carbon Management Program. The University of Texas at Austin. 2012b.

Rochelle GT et al. "CO_2 Capture by Aqueous Absorption, Third Quarterly Progress Report 2012." Luminant Carbon Management Program. The University of Texas at Austin. 2012c.

Stripper Modeling and Optimization

Quarterly Report for October 1 – December 31, 2012

by Yu-Jeng Lin

Supported by the Luminant Carbon Management Program

McKetta Department of Chemical Engineering

The University of Texas at Austin

January 31, 2013

Abstract

In this work, alternative stripper configurations have been modeled and optimized using Aspen Plus®. Equivalent work is used as indicator of energy performance instead of only heat duty. Two configurations are investigated, a simple stripper with cold rich bypass and a simple stripper with rich exchanger bypass.

In the simple stripper with cold rich bypass, stripping steam heat is recovered using a bypass of rich solvent around the cross exchanger to the top of the stripper. Optimization of packing height has been done using 0.30 lean loading with 7.5% bypass. Rich packing height affects energy equivalent work more significantly than lean packing. By varying the rich packing from no packing to 1.0 meter, 12.7% energy savings can be realized. However, the energy improvement of increased packing height is less than 1%.

In the simple stripper with rich exchanger bypass, a cross exchanger is applied to recover heat from hot stripped vapor using cold rich solvent. Optimum bypass is obtained at 6.5% with 29.6 (kJ/mol CO_2) equivalent work.

Introduction

For post-combustion CO_2 capture, steam usage for lean solvent regeneration in the stripper and CO_2 compression work are the main contributions to the energy requirement of the process. Implementing CO_2 capture incurs 20~30% penalty of electricity output for typical coal-fired power plant (Rochelle, 2009). Alternative stripper configurations could improve capture efficiency significantly compared to a simple stripper. Also, solvent selection only can be made after applying to optimum stripper operating conditions.

Several previous studies have been done to improve equivalent work by introducing alternative stripper configurations. Oyenekan (2007) proposed matrix, internal exchange, multi-pressure and flashing feed stripper configurations. The best performance case was obtained in matrix with MDEA/PZ giving 22% of energy savings over the simple stripper. Van Wagener (2011) emphasized the importance of increasing process reversibility by introducing more complex configurations including multi-stage flash, cold rich bypass and interheated column. Van Wagener showed that interheated column with 8 m PZ has the best energy improvement.

1

To provide potential process flowsheet improving capture efficiency, stripper modeling and optimization of novel configurations have been done using Aspen Plus® software.

Methods

In this work, two configurations are studied:

1. Simple stripper with cold rich bypass.

2. Simple stripper with rich exchanger bypass.

Simple Stripper with Cold Rich Bypass

Figure 1 is the flowsheet of a simple stripper with cold rich bypass. Cold rich solvent from the absorber is heated in the main heat exchanger by hot lean solvent. To mitigate water flashing at the top of stripper due to high temperature, part of the cold rich solvent is drawn and sent to top of stripper without being heated by the main exchanger. There are two sections of packing in stripper, lean packing at the top and rich packing at the bottom. Hot rich solvent is fed into the stripper between lean and rich packing.

Specifications

The following are the process specifications used in simulations of this configuration:

- Process modeling tool: Aspen Plus® v7.3
- Thermodynamic model: Independence model developed in-house
- Solvent: 8 m PZ
- Packing type: Mellapak standard 500Y
- Rich loading: 0.4 (mol CO_2/mol alkalinity)
- Rich solvent temperature: 40 ^{o}C
- Main exchanger: 5 ^{o}C LMTD approach
- Reboiler temperature: 150 ^{o}C
- Pump efficiency: 72%
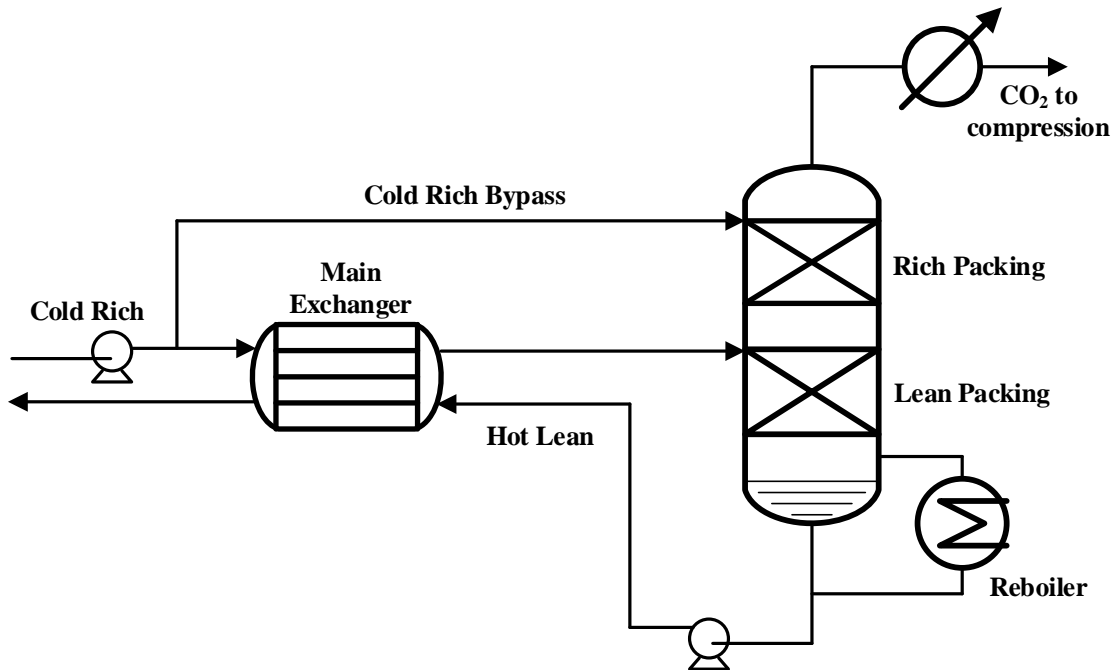
Figure 1: Simple stripper with cold rich bypass flowsheet

Simple Stripper with Rich Exchanger Bypass

Figure 2 is the flowsheet of a simple stripper with rich exchanger bypass. In this configuration, a cross exchanger is applied to recover heat from stripped vapor. Part of the cold rich solvent is drawn to the rich exchanger instead of the main exchanger. Sensible heat and latent heat of water in stripped vapor can be partly recovered by implementing this heat integration.

Specifications

The following are the process specifications used in simulations of this configuration:

- Process modeling tool: Aspen Plus® v7.3
- Thermodynamic model: Independence model developed in house
- Solvent: 8 m PZ
- Packing type: Mellapak standard 500Y
- Rich loading: 0.4 (mol CO_2/mol alkalinity)
- Rich solvent temperature: 40 ^{o}C
- Main exchanger: 5 ^{o}C LMTD approach
- Reboiler temperature: 150 ^{o}C
- Pump efficiency: 72%
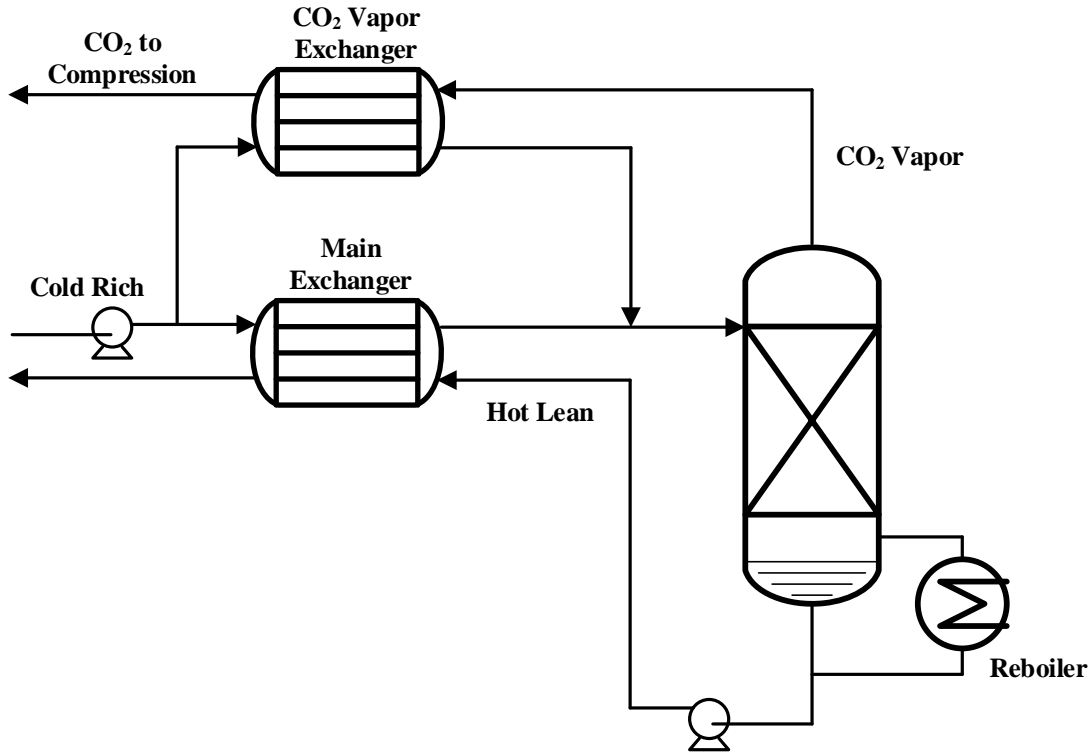
Figure 2: Simple stripper with rich exchanger bypass.

Equivalent Work Calculation

To evaluate energy requirement, instead of only using heat duty, equivalent work is more comprehensive for energy requirement estimation. As Equation 1 shows, equivalent work consists of pump work, compression work, and heat work. The pump is required to move the solvent from the absorber to the pressure and height of the stripper. Heat work is obtained from heat duty by Equation 2. The work-heat transfer efficiency is set to a typical value of 75%.

$$W_{eq}\left(\frac{kJ}{mol\ CO_2}\right) = W_{Heat} + W_{pump} + W_{comp} \tag{1}$$

$$W_{Heat} = \eta \left(\frac{T_{source} + \Delta T - T_{sink}}{T_{source} + \Delta T}\right) Q_{reb} \tag{2}$$

Compression work is calculated by Equation 3 as a function of suction pressure to a discharge pressure of 150 bar.

$$W_{comp}\left(\frac{kJ}{mol\ CO_2}\right) = \begin{cases} 4.572\ln\left(\frac{150}{P_{in}}\right) - 4.096 & P_{in} \leq 4.56\ bar \\ 4.023\ln\left(\frac{150}{P_{in}}\right) - 2.181 & P_{in} > 4.56\ bar \end{cases} \tag{3}$$

Results and Discussion

Simple Stripper with Cold Rich Bypass

In this configuration, part of the cold rich solvent is used to mitigate water vapor flashing at the top of the stripper. By bypassing 5~15% of the cold rich solvent, stripping steam can be condensed in the stripper. The stripper needs extra packing for cold liquid contacting with hot vapor. However, the sensitivity of rich packing height and lean packing height is unknown. Van Wagener (2011) found that the case with 0.30 lean loading and 7.5% bypass has the best energy performance in a simple stripper with cold rich bypass configuration. Therefore, this case is chosen as the base case for simulating different rich and lean packing heights.

Figure 3 gives energy performance at 1.0 m lean packing height as a function of rich packing height. The benefit of increasing rich packing diminishes and converges to near 31 kJ/mol CO_2. From the stripper temperature profile shown in Figure 4, temperature at the top decreases with increasing rich packing height which gives effective heat transfer area. Also, lean packing height is varied with fixed rich packing height at 1.0 meter, as Figure 5 shows. However, the effect of lean packing height is much less than rich packing height. Only 0.1 meter rich packing is needed to give equivalent work of 31 kJ/mol CO_2.
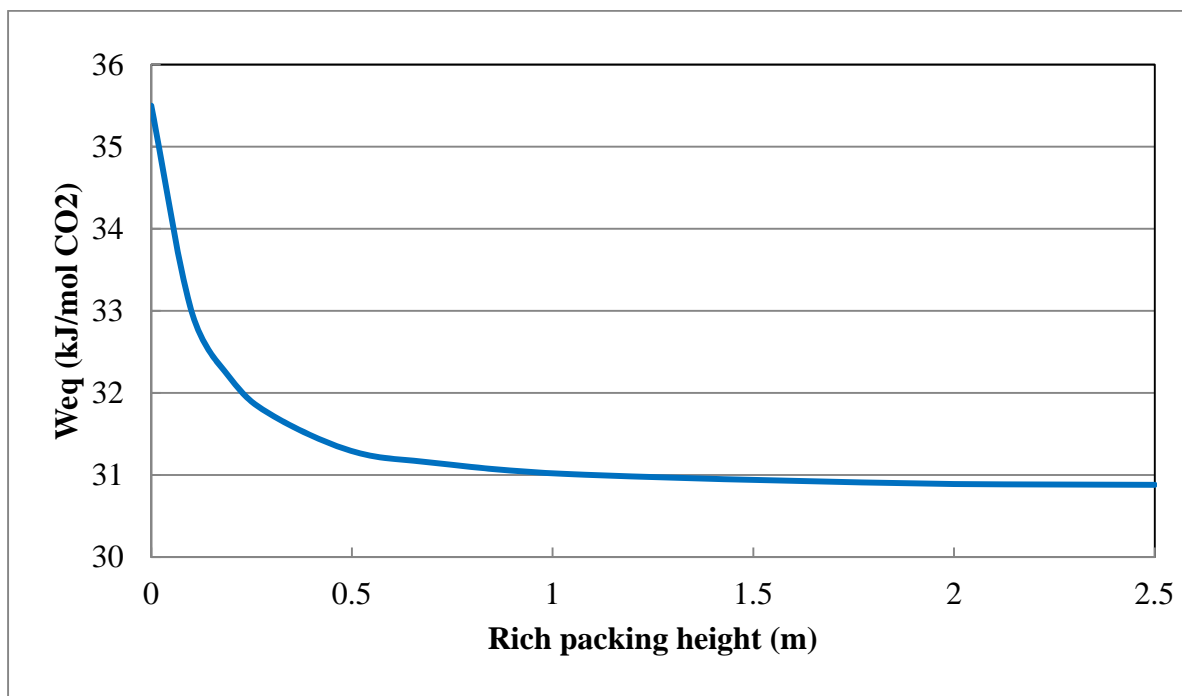
Figure 3: Relationship between equivalent work and rich packing height. Lean packing height is 1.0 meter. 0.30 lean loading with 7.5% bypass.
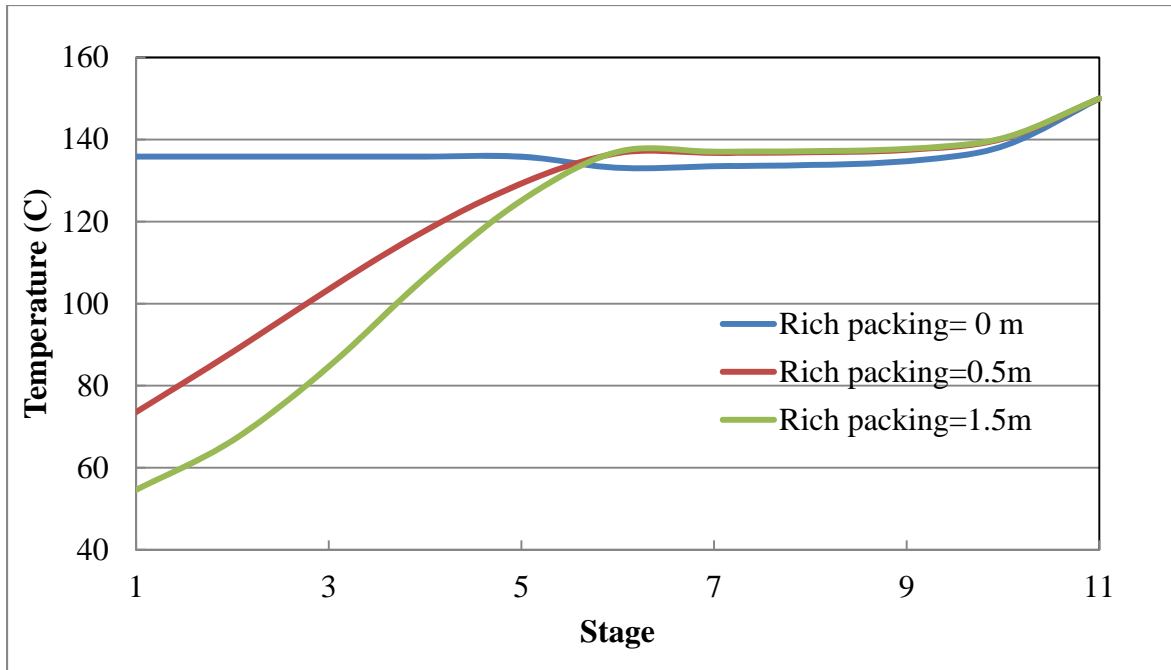
Figure 4: Temperature profile of stripper when rich packing height is varied.
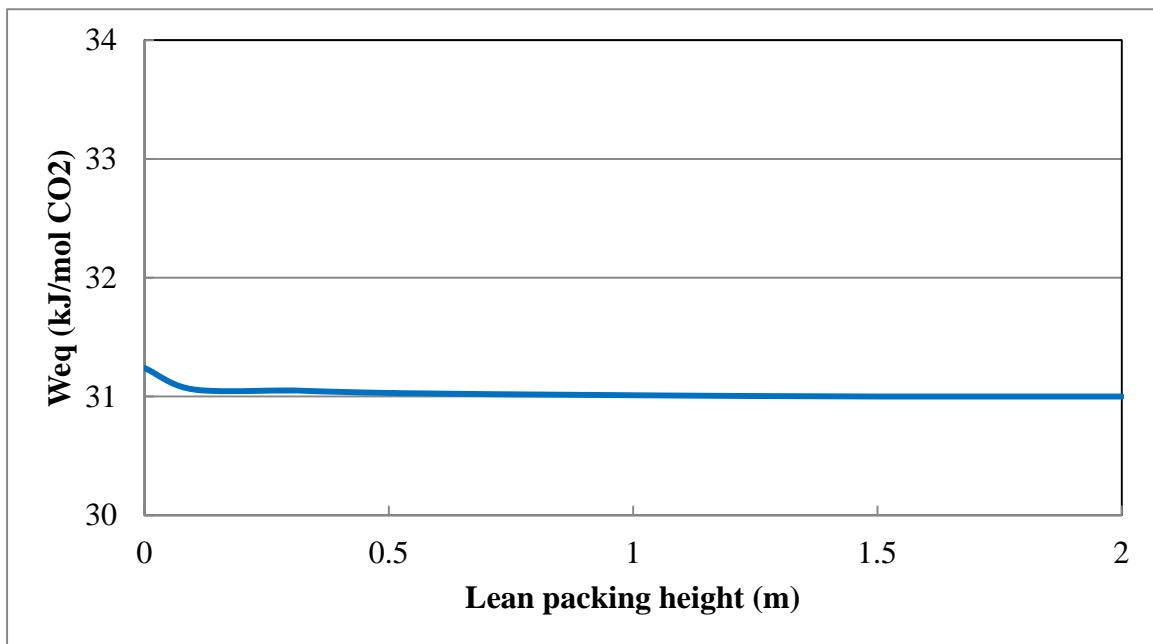
Figure 5: Relationship between equivalent work and lean packing height. Rich packing height is 1.0 meter. 0.30 lean loading with 7.5% bypass.

Simple Stripper with Rich Exchanger Bypass

In this configuration, instead of sending hot CO_2 vapor to the condenser where vapor is usually condensed to 40 ^{o}C by cooling water before entering the compression stage, waste heat is recovered using a cross exchanger. As in previous cases, 0.30 lean loading is chosen as the base case. By varying bypass from 5% to 10%, the temperature approach limitation is shifted from the hot side to the cold side. Table 1 shows that the lowest equivalent work (29.6(kJ/mol CO_2) is obtained at 6.5% bypass when either cold side or hot side temperature approach is 1.0 ^{o}C for each case maximizing heat recovered. When more heat from CO_2 vapor is effectively recovered, mixed rich solvent temperature becomes higher, that is, less sensible heat is needed in the reboiler to heat to 150 ^{o}C.

Table 1: Energy performance of rich exchanger bypass configuration with varied bypassing rate

Bypass (%)	Hot side temperature approach (^{o}C)	Cold side temperature approach (^{o}C)	Mixed rich solvent temperature (^{o}C)	Weq (kJ/mol CO_2)
5	1	41.4	145.8	29.89
6.5	3.2	1	146.2	29.59
7.5	11.8	1	145.6	30.11
10	34.3	1	143.5	31.84

Conclusions

1. In the simple stripper with cold rich bypass, rich packing height affects energy equivalent work more significantly than lean packing.

2. By varying rich packing from no packing to 1.0 meter, 12.7% energy savings can be achieved, however, the effect of increasing lean packing height is less than 1% improvement.

3. In a simple stripper with rich exchanger bypass configuration, optimum bypass is 6.5% giving 29.6 (kJ/mol CO_2) equivalent work.

Future Work

1. Simple stripper with water recovery case will be investigated to see if any benefit could be obtained using condensing water.

2. 20 ^{o}C LMTD in the CO_2 vapor exchanger will be used to evaluate energy performance giving a standard criterion for choosing optimum bypass and exchanger design.

References

Oyenekan BA. *Modeling of Strippers for CO$_2$ Capture by Aqueous Amines*. The University of Texas at Austin. Ph.D. Dissertation. 2007.

Rochelle GT. "Amine scrubbing for CO$_2$ capture". *Science.* 2009; 325,1652–4.

Van Wagener DH. *Stripper Modeling for CO$_2$ Removal Using Monoethanolamine and Piperazine Solvents.* The University of Texas at Austin. Ph.D. Dissertation. 2011.

Measurement of Effective Packing Area and

Mass Transfer Coefficients

Abstract

In this quarter, liquid film and gas film mass transfer coefficients models including the influence of corrugation angle and packing nominal size were developed. A new concept, mixing points density (M), was introduced to represent the impact of corrugation angle and nominal size on mass transfer.

Mixing points are the turning points where liquid and gas flows change directions, mix with each other, and create turbulence. Intensive mass transfer between liquid and gas phase happens at the mixing points. Structured packing with a lower corrugation angle has larger $k_{L/G}$ because it has more mixing points than packing with a higher corrugation angle at the same packed height.

To quantify the mixing point density in packing, packing geometric structures were studied. Structured packings are composed of corrugated metal sheets crossing with each other. The crossing points are the mixing points, which divide structured packings into hundreds of small square pyramids. The number of mixing points per m^3 equals to the number of square pyramids per m^3 multiplied by the number of mixing points per pyramid. Thus, mixing points density (M) for structured packing can be calculated by the equation: $M = \dfrac{6}{B * h * B \tan \theta}$

Random packings are composed of hundreds of small packing pieces. The mixing points are the turning points at each piece. The number of mixing points per m^3 equals the number of packing pieces per m^3 (ρ_0) multiplied by the number of mixing points per piece (M_0). Thus, mixing points density (M) for random packing can be calculated by the equation:

$$M = \rho_0 * M_0 = \frac{a_P * M_0}{a_0}.$$

Preliminary mass transfer models are developed based on three factors influencing mass transfer: the liquid/gas superficial velocity ($u_{L/G}$), the packing size (a_P), and the mixing points density (M). Through data regression, the experimental constant and the exponents for each factor can be calculated. The mass transfer models are:

For structured packing:

$$k_L = 0.024 * u_L^{0.71} M^{0.38} a_P^{-1.46}$$

$$k_G = 13.2 * u_G^{0.53} M^{0.44} a_P^{-2.19}$$

For random packing:

$$k_L = C_1 * u_L^{0.71} M^{0.25}, \quad C_1 = 4.5E - 5$$

$$k_G = C_2 * u_G^{0.88} M^{0.81}, \quad C_2 = 2.95E - 7$$

Introduction

Packing is widely used in distillation, stripping, and gas-scrubbing processes because of its relatively low pressure drop, good mass transfer efficiency, and ease of installation. Packing is being investigated for post-combustion carbon capture for these reasons. In the CO_2 capture process, absorber performance depends on the effective mass transfer area of the packing (a_e), stripper performance depends on liquid film mass transfer coefficient (k_L), and the gas cooler and water wash performance depends on gas film mass transfer coefficient (k_G). This research is focused on the measurement of these important fundamental parameters and construction of mechanistic design models. The mass transfer models considering the influence of corrugation angle and packing nominal size were developed this quarter.

Experiment and Results

Corrugation angle effect on mass transfer coefficient

The corrugation angle effect is determined by comparing structured packing with similar geometry except for corrugation angle. Figures 1 and 2 give samples of how corrugation angle influences liquid film and gas film mass transfer coefficients. For both k_L and k_G, increasing corrugation angle will have a negative effect. This phenomenon can be interpreted by the flow mechanism in corrugated metal sheets shown in Figure 3.
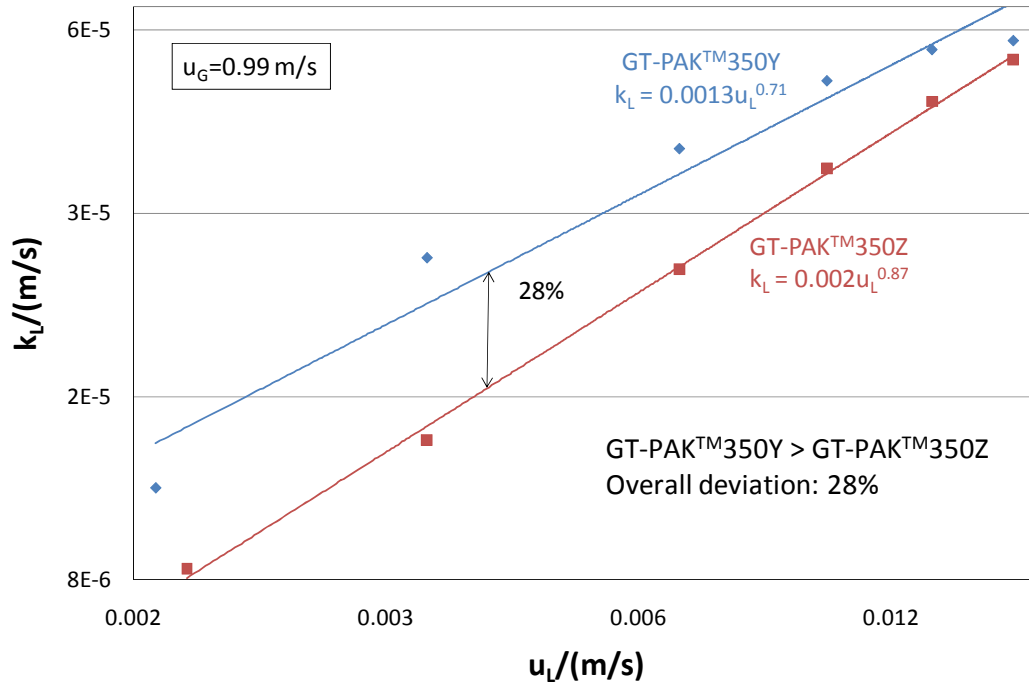
Figure 1: k_L comparison of GT-PAK^{TM} 350Y and GT-PAK^{TM} 350Z
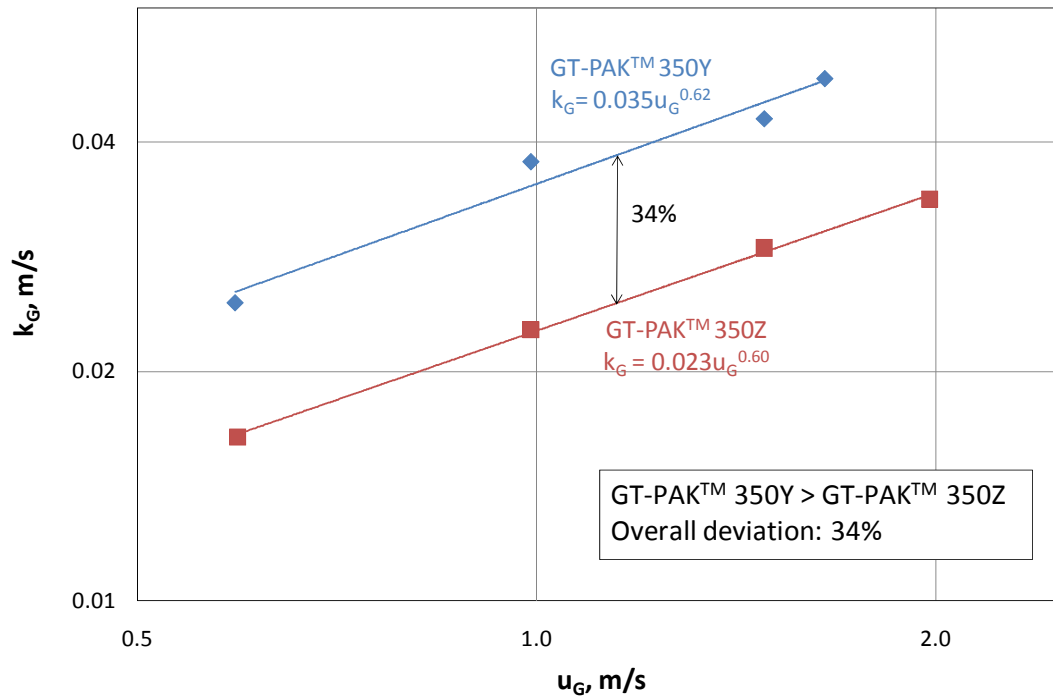
Figure 2: k_G comparison of GT-PAK^{TM} 350Y and GT-PAK^{TM} 350Z
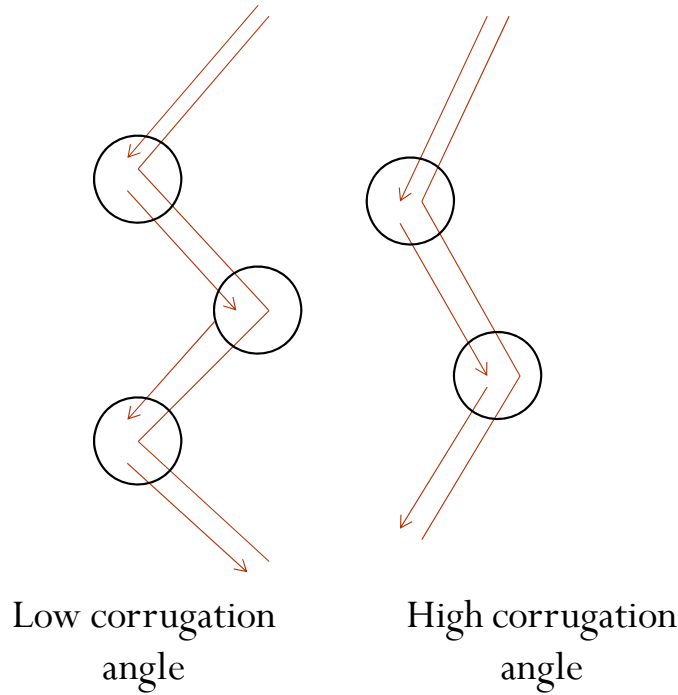
Figure 3: Liquid flow along corrugated metal sheets

Structured packing is composed of corrugated metal sheets. Liquid flow inside the packing can be seen as flowing along these corrugated sheets. At the joint points of metal sheets (marked by circles in Figure 3), flows mix with each other, change directions, and create turbulence. Thus, these mixing points are believed to be the key points for mass transfer in structured packing. In packing with a lower corrugation angle, there will be more mixing points than packing with a higher corrugation angle at the same packed height, which means liquid and gas flows mix with each other more often, change direction more frequently, and create more turbulence. Therefore, the phenomenon that lower corrugation angle packing has a higher k_G and k_L can be explained.

Mixing points density in structured packing

To quantify the number of mixing points inside structured packing, packing geometric structures are studied. Figure 4 shows the lateral view of a structured packing with a corrugation angle θ. From the lateral view, the corrugated metal sheets can be seen as bunches of parallel lines with a tilt angle θ to the horizontal line. In the structured packing, each corrugated metal sheet contacts with the one next to it. In the lateral view, it is expressed by the parallel lines crossing with another set of reversed parallel lines. The crossed corrugated metal sheets form hundreds of square pyramids, which are the triangles in the lateral view. The mixing points are the vertices of the triangles, which are marked in black circles in the lateral view. The bottom of the triangle is the channel base B, and the height of the triangle is $\frac{B}{2}\tan\theta$.

4
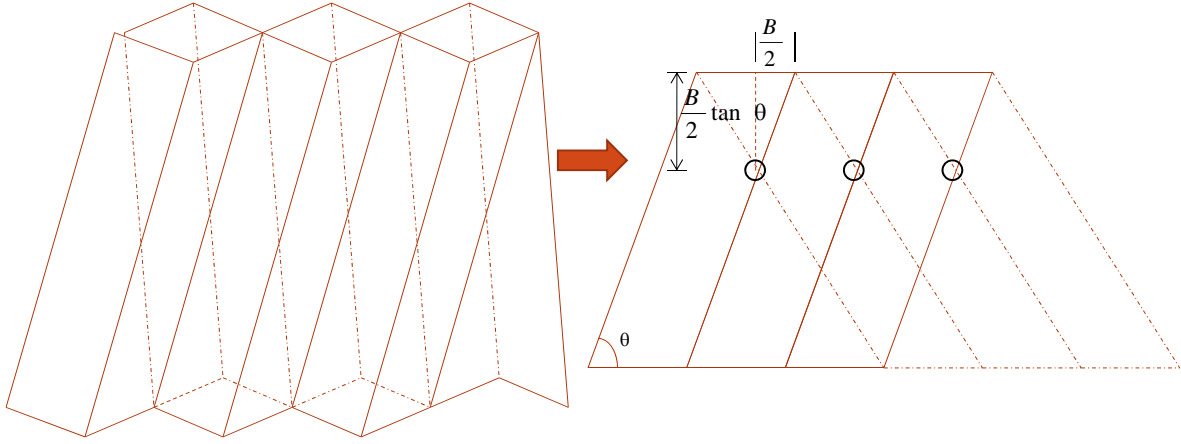
Figure 4: Lateral view of a structured packing with a corrugation angle θ

The square pyramids formed by the crossed metal sheets can be better seen from the top view of the packing (Figure 5). The height of the square pyramid is $\frac{B}{2}\tan\theta$, the bottom area of the pyramid is B*h. The volume of the square pyramid is $\frac{1}{6}B*h*B\tan\theta$. Thus, the number of square pyramids per m^3 volume is $\frac{6}{B*h*B\tan\theta}$. Each pyramid has five mixing points; however, each pyramid is also sharing mixing points with other four adjacent pyramids. Thus, the number of mixing points per pyramid is 5/5. The total number of mixing points per m^3 (M) = the number of square pyramids per m^3 * the number of mixing points per pyramid = $\frac{6}{B*h*B\tan\theta}$.
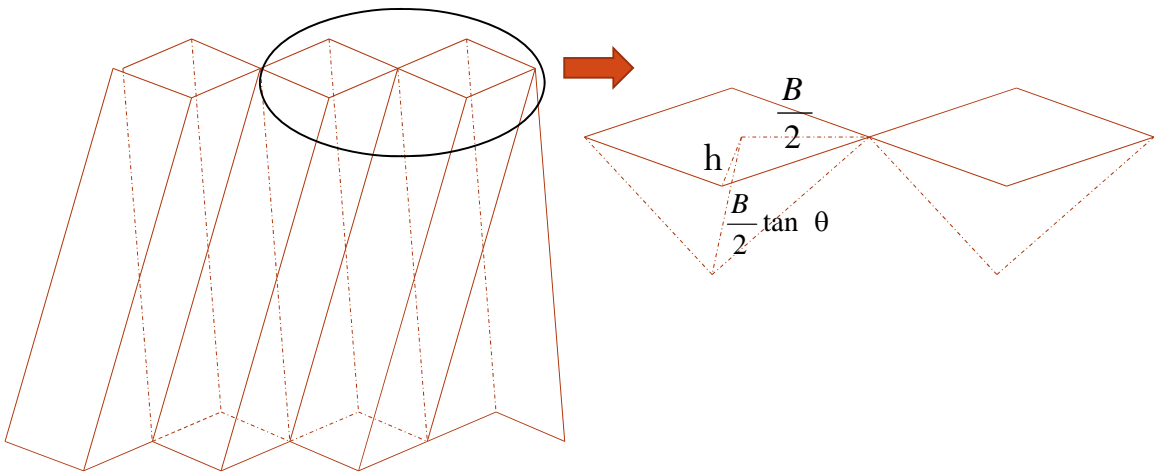
Figure 5: Top view of a structured packing with a corrugation angle θ

Preliminary k_L and k_G models for structured packing

To develop mass transfer models predicting k_G and k_L, three factors are considered: the liquid/gas superficial velocity ($u_{L/G}$), the packing size (a_p), and the mixing points density (M). M is the number of mixing points per m^3, which can be calculated by the equation:

$$M = \frac{6}{B * h * B \tan \theta} \tag{1}$$

where B is the channel base, m;

      h is the crimp height, m;

      and θ is the corrugation angle.

Thus, $k_{L/G}$ can be written as a function of these three factors:

$$k_{L/G} = f(u_{L/G}, M, a_P) \tag{2}$$

Taking a natural logarithm of both sides, Equation 2 can be written as:

$$\ln(k_{L/G}) = C + m \ln(u_{L/G}) + n \ln(M) + k \ln(a_P) \tag{3}$$

Through data regression, the experimental constant C and the exponents for each factor can be calculated. Finally, the k_L and k_G models for structured packing are developed:

$$k_L = 0.024 * u_L^{0.71} M^{0.38} a_P^{-1.46} \tag{4}$$

$$k_G = 13.2 * u_G^{0.53} M^{0.44} a_P^{-2.19} \tag{5}$$

The comparison between experimental data and values predicted by preliminary k_L and k_G models are shown in Figures 6 and 7. The deviation between $k_{L, \text{experiment}}$ and $k_{L, \text{model}}$ is 17% while the deviation between $k_{G, \text{experiment}}$ and $k_{G, \text{model}}$ is 4.9%.
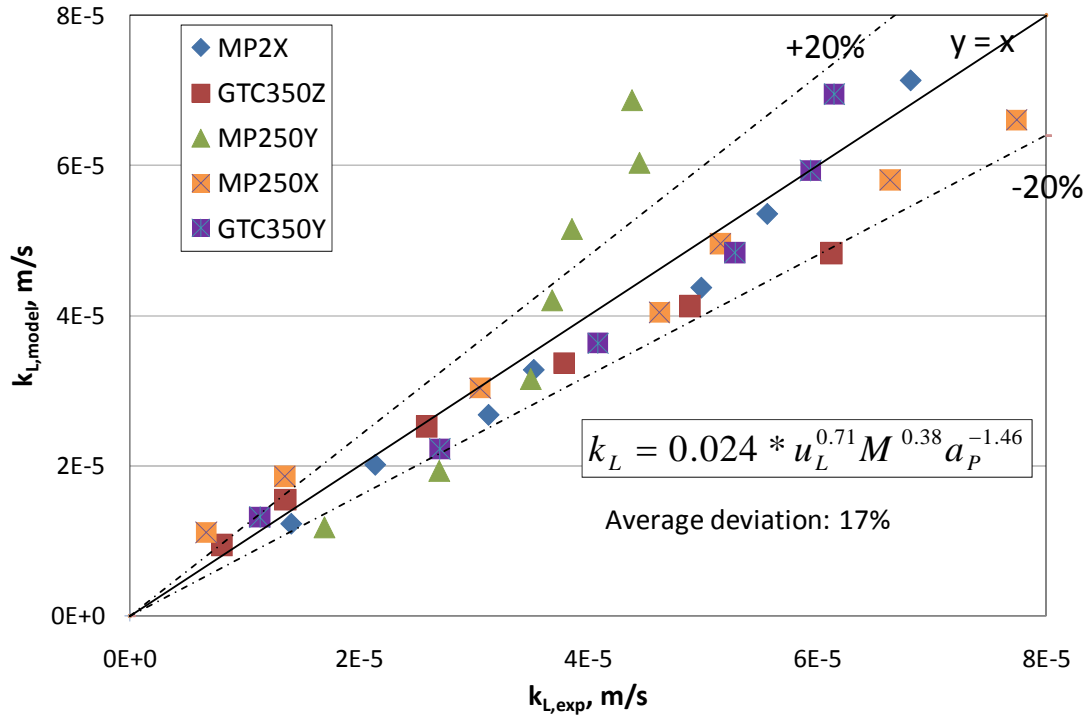
Figure 6: Comparison between experimental data and k_L model for structured packing

The equation shown in the figure:

$$k_L = 0.024 * u_L^{0.71} M^{0.38} a_P^{-1.46}$$

Average deviation: 17%
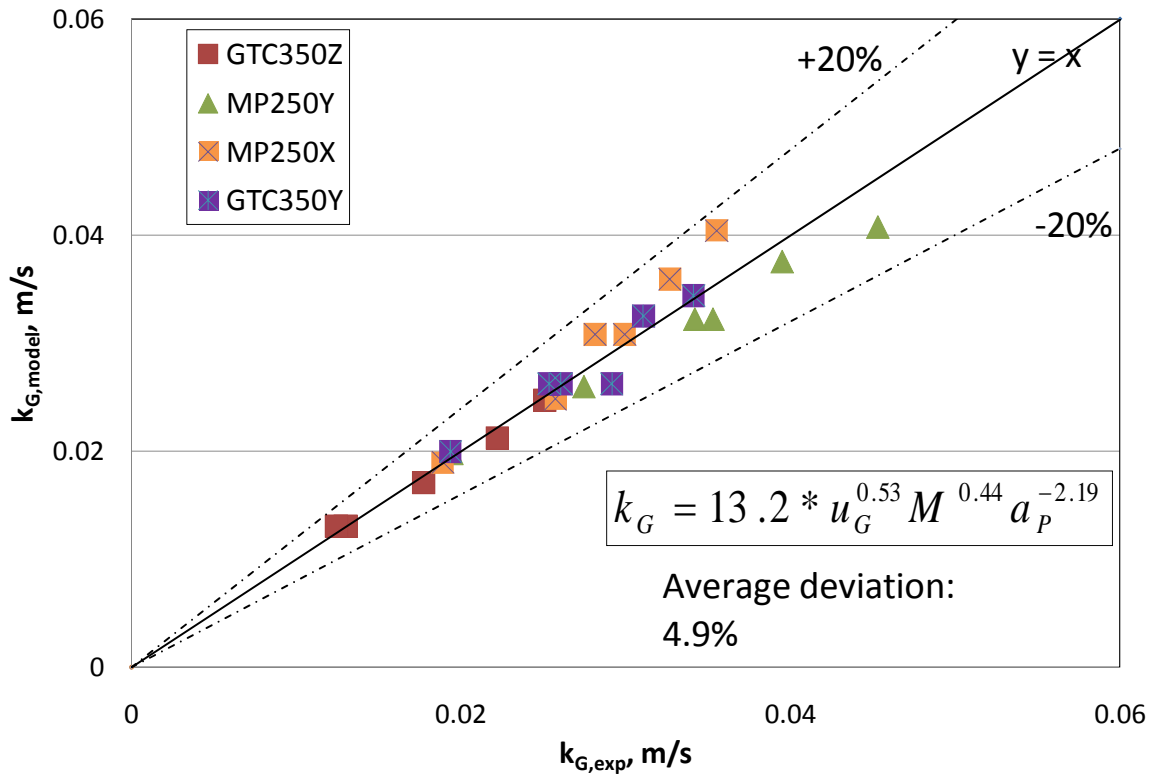
Figure 7: Comparison between experimental data and k_G model for structured packing

The equation shown in the figure:

$$k_G = 13.2 * u_G^{0.53} M^{0.44} a_P^{-2.19}$$

Average deviation: 4.9%

Nominal size effect on mass transfer coefficient

For random packing, the nominal size effect is explored by comparing random packing in the same family (Raschig Super Ring family) which have similar geometric structures but different sizes. For both k_L and k_G, increasing packing nominal size will cause a decrease in mass transfer coefficients. Like structured packing, this tendency can be explained by the flow mechanism in random packing pieces shown in Figure 8.

Large nominal size packing

Small nominal size packing
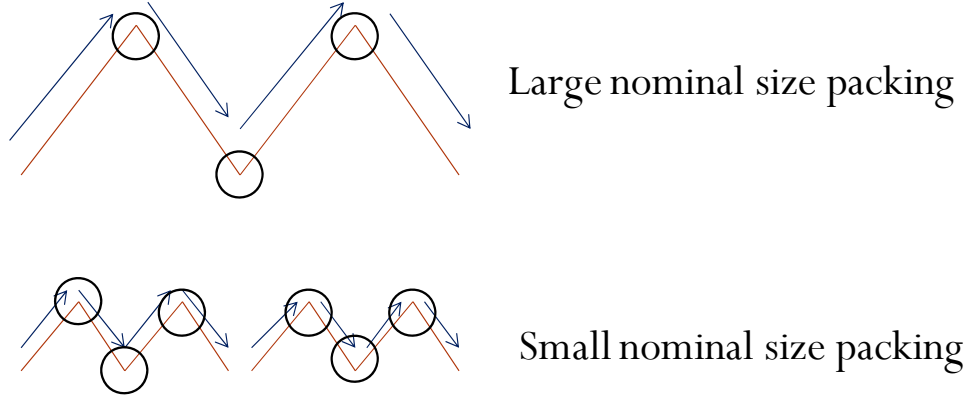
Figure 8: Liquid flow along random packing pieces

Random packing is composed of hundreds of small packing pieces. Liquid flow inside random packing can be seen as flowing along these small pieces. At the turning points of packing pieces (marked by circles in Figure 8), liquid flow mixes with each other, changes directions, and creates turbulence. Thus, these turning points are believed to be the key points for mass transfer in random packing. In packing with a smaller nominal size, there will be more turning points than packing with a larger nominal size at the same packed height. Therefore, packing with a smaller nominal size will have larger k_L and k_G than packing with larger nominal size.

Mixing points density in random packing

Like structured packing, a factor representing mixing points density is defined. M is the total number of mixing points per m^3 in random packings. According to definition, M can be calculated by Equation 6:

Mixing points/m^3 (M)= number of packing pieces/m^3 (ρ_0)*mixing points per piece (M_0)   (6)

The packing density (number of packing pieces/m^3, ρ_0) can be calculated from the packing total area a_P.

$$Packing\ total\ area\ a_P (m^2/m^3) = \frac{total\ number\ of\ packing\ pieces * area\ of\ one\ packing\ piece}{packed\ volume\ V}$$

(7)

$$total\ number\ of\ packing\ pieces = number\ of\ packing\ pieces/m^3 (\rho_0) * packed\ volume\ V \quad (8)$$

Combining Equations 7 and 8:

$$a_P \ (m^2 / m^3) = \frac{number\ of\ packing\ pieces\ /\ m^3(\rho_0) * volume\ V * area\ of\ one\ piece\ (a_0)}{packed\ volume\ V} \qquad (9)$$

Thus, the packing density can be calculated:

$$number\ of\ packing\ pieces\ /\ m^3\ \rho_0 = \frac{packing\ total\ area\ a_P}{area\ of\ one\ piece\ a_0} \qquad (10)$$

Finally, the mixing points density (M) can be calculated by combining Equations 6 and 10:

$$M = \rho_0 * M_0 = \frac{a_P * M_0}{a_0} \qquad (11)$$

Table 1 lists the number of mixing points density (M), packing density (ρ_0), area of one packing piece (a_0), and total area (a_P) for the random packings studied in this work.

Table 1: Random packing parameters

	RSR#0.3	RSR#0.5	RSR#0.7
Nominal size (mm)	15	20	25
Number pieces/m^3, ρ_0	180,000	145,000	45,500
Total area (m^2/m^3), a_P	315	250	180
Mixing points per piece, M_0	12	8	12
Area of one packing piece (cm^2), a_0	17.5	17.24	39.56
Mixing points/m^3, M	2,160,000	1,160,000	546,000

Preliminary k_L and k_G models for random packing

To develop mass transfer models predicting k_G and k_L, the mixing points density (M) as well as liquid/gas superficial velocity ($u_{L/G}$) are considered. Models for random packing do not consider packing total area (a_P) separately because it is already included in the mixing points density factor (M). The mixing points density is the number of mixing points per m^3, which can be calculated by Equation 11.

Thus, $k_{L/G}$ can be written as a function of M and $u_{L/G}$:

$$k_{L/G} = f(u_{L/G}, M) \qquad (12)$$

Taking a natural logarithm of both sides, Equation 12 can be written as:

$$\ln(k_{L/G}) = C + m\ln(u_{L/G}) + n\ln(M) \qquad (13)$$

Through data regression, the experimental constant C and the exponents for each factor can be calculated. Finally, the k_L and k_G models for random packings are developed:

$$k_L = C_1 * u_L^{0.71} M^{0.25}, \ C_1 = 4.5E - 5 \qquad (14)$$

$$k_G = C_2 * u_G^{0.88} M^{0.81}, \ C_2 = 2.95E - 7 \qquad (15)$$

For random packing, the comparison between experimental data and values predicted by preliminary k_L and k_G models is shown in Figures 9 and 10. The deviation between $k_{L, experiment}$ and $k_{L, model}$ is 15% while the deviation between $k_{G, experiment}$ and $k_{G, model}$ is 5%.
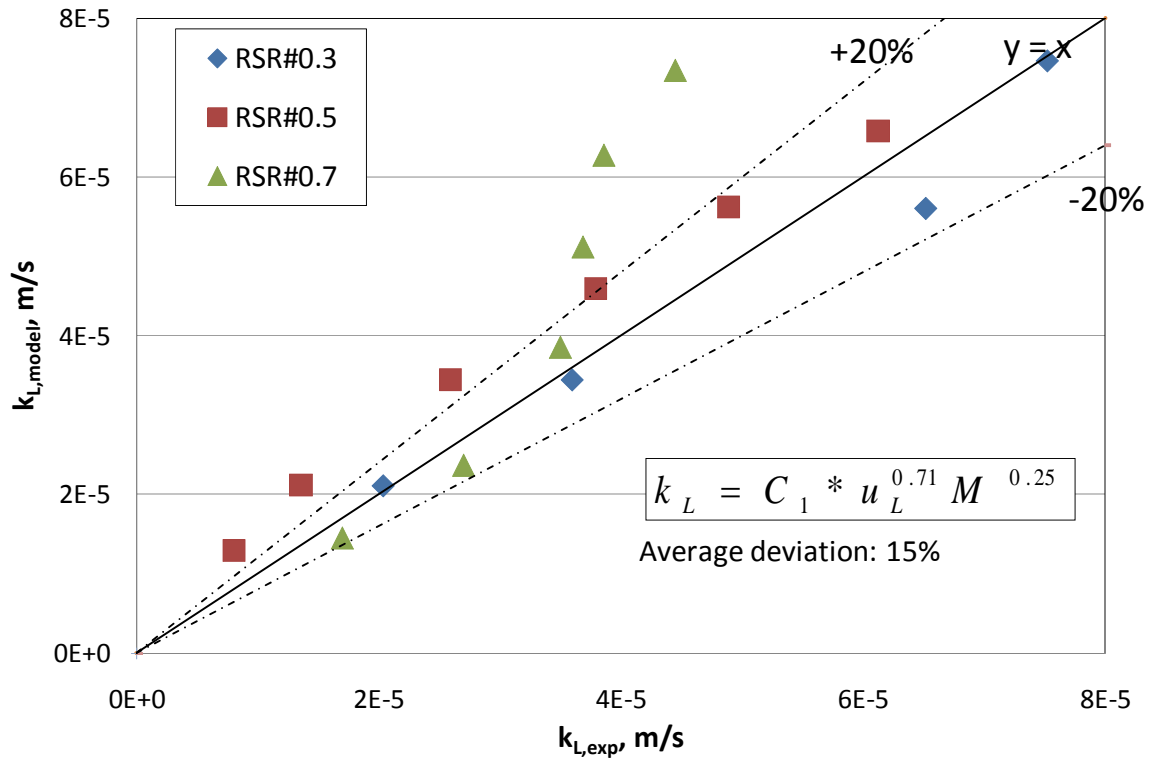
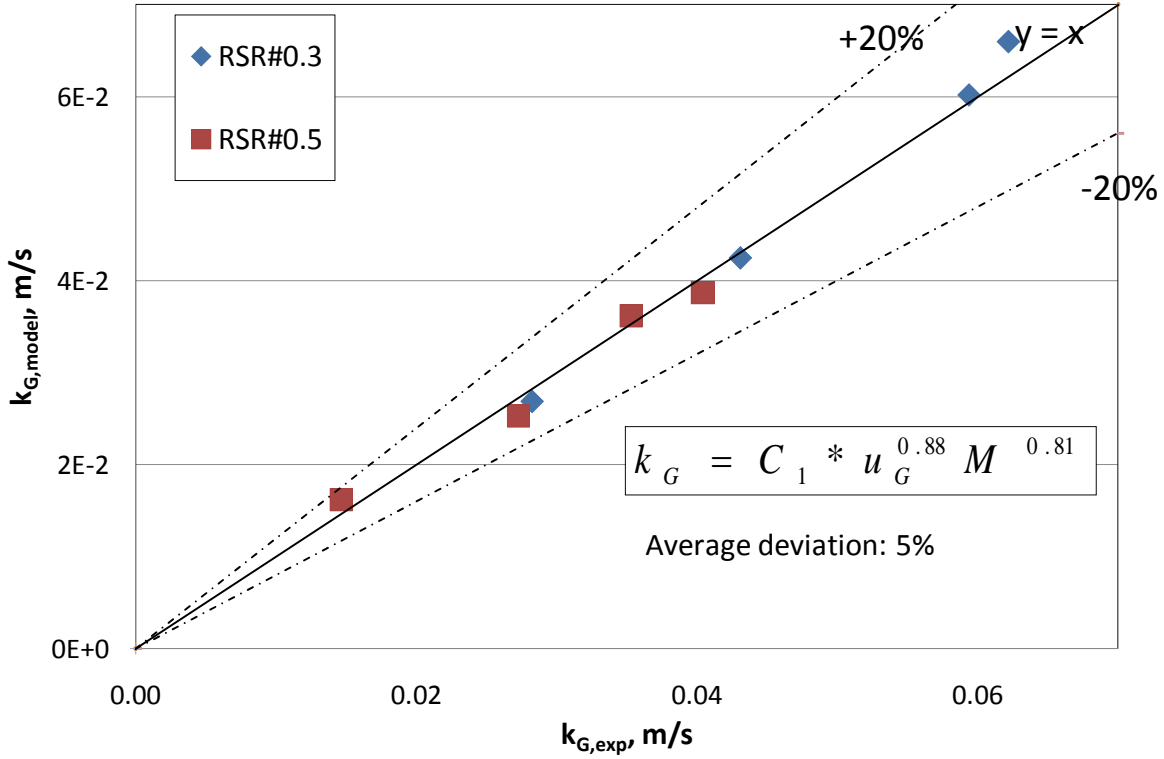**Figure 9: Comparison between experimental data and k_L model for random packing**

Figure 10: Comparison between experimental data and k_G model for random packing

Conclusions

In this quarter, work has focused on developing mass transfer models including a new concept: mixing points density (M).

1. Mixing points are the turning points where flows change directions, mix with each other, and create turbulence. Mixing points contribute directly to mass transfer.

2. Structured packing with a lower corrugation angle has larger $k_{L/G}$ because it has more mixing points.

3. For structured packing, mixing points density can be calculated by the equation:
$$M = \frac{6}{B * h * B \tan \theta}$$

4. Random packing with a smaller nominal size has larger $k_{L/G}$ because it has more mixing points.

5. For random packing, mixing points density can be calculated by the equation:
$$M = \rho_0 * M_0 = \frac{a_P * M_0}{a_0}$$

6. k_L and k_G models considering mixing points density (M), liquid/gas superficial velocity ($u_{L/G}$), and packing size (a_P) are developed:

$$k_{L/G} = C_1 * u_{L/G}^m M^n a_P^k \tag{16}$$

11

The parameters and deviation for k_G and k_L models are summarized in Table 2.

Table 2: Summary of mass transfer model

	C_1	m	n	k	Deviation
k_L, structured packing	0.024	0.71	0.38	-1.46	17%
k_G, structured packing	13.2	0.53	0.44	-2.19	4.9%
k_L, random packing	4.49E-5	0.71	0.25	N/A	15%
k_G, random packing	2.95E-7	0.88	0.81	N/A	5%

Future Work

Next quarter, GT-PAK^{TM} 500Y, a 500 m^2/m^3 total area packing with a 45-degree corrugation angle will be measured. More Raschig Super Rings, such as RSR#0.1 or RSR#1, may also be measured to expand our random packing database. k_G measurements for some previous packings will be repeated with the new SO_2 sampling system.

Work on developing fundamental k_G and k_L models for novel packings will be continued.

Lab Safety issues

1. Steel reinforced gloves are required to prevent being cut when handling sheet metal structured packings.

2. Chemical resistant lab gloves are required when handling a strong base such as NaOH used in effective area measurement, and toxic chemical such as toluene in k_L measurement. After runs, NaOH should be neutralized before draining.

3. Gas mask with respirator is required when changing SO_2 bottles.

References

Raschig GMBH Jaeger Products, INC. PALL-RING Product Bulletin 350.

Raschig GMBH Jaeger Products, INC. Raschig Super-Ring Product Bulletin 250.

Report of Raschig Super-Ring No. 0.3 Test. Fractionation Research, INC.

Report of Raschig Super-Ring No. 0.7 Test. Fractionation Research, INC.

Rochelle GT et al. "CO_2 Capture by Aqueous Absorption, Third Quarterly Progress Report 2012." Luminant Carbon Management Program. The University of Texas at Austin. 2012.

Stripper Modeling and Pilot Plant Configurations

Quarterly Report for October 1 – December 31, 2012

by Tarun Madan

Supported by the Luminant Carbon Management Program

McKetta Department of Chemical Engineering

The University of Texas at Austin

January 31, 2013

Abstract

Stripper complexity is an important tool in minimizing the energy penalty of amine scrubbing. Different stripper and flash configurations can be optimized for energy consumption by identifying and changing the various degrees of freedom. A new configuration of 'Advanced Flash Stripper' was studied in this quarter. This configuration recovers the waste heat of stripping steam more reversibly by using a combination of cold, warm, and rich bypass. Complex advanced flash configurations, corresponding to warm bypass, cold and hot bypass, and cold, warm, and rich bypass had equivalent work values of 31.4, 30.3, and 29.7 kJ/mol CO_2 using the Independence solvent model for 8 m PZ in Aspen Plus®.

Alternate pilot plant configurations based on the advanced flash stripper were also modeled. Best performance of 29.0 kJ/mol CO_2 was achieved using heat recovery by warm rich bypass and heat exchange between cold rich and hot CO_2 streams.

Introduction

Stripper complexity and advanced stripper configurations have been studied in the past to minimize the energy requirement of amine scrubbing for post-combustion carbon capture. Increasing the reversibility of the process using advanced configurations improves the energy performance. This complexity can be increased by using recycles, better heat recovery, splits, multiple pressure stages, and other features (Leites et al., 2003). For post-combustion CO_2 capture with 8 m PZ, Oyenekan (2007) and Van Wagener (2012) have evaluated advanced configurations including multi-stage flash, cold rich bypass, and interheated stripper. These configurations were investigated using Aspen Plus® with thermodynamic models developed using experimental data. For 8 m PZ, equivalent work of 30.5–35.3 kJ/mol CO_2 has been reported for different configurations.

A new configuration of the 'Advanced Flash Stripper,' which recovers waste stripping steam heat more reversibly using combinations of warm, cold, and hot rich bypass, was studied in this quarter. Based on this advanced flash stripper, pilot plant cases were modeled to identify configurations.

Methods and Discussion

Advanced Flash Stripper

This configuration has various complexities associated with combinations of warm, cold, and hot bypass. The following combinations were modeled.

1. Warm rich bypass (Advanced Flash 1, AF1)
2. Cold and hot rich bypass (Advanced Flash 2, AF2)
3. Cold, warm and hot rich bypass (Advanced Flash 3, AF3)

The following modeling and design specifications were held constant in all the configurations.

1. Process modeling software – Aspen Plus®
2. Solvent – 8 m piperazine (PZ)
3. Solvent model – Independence
4. Rich loading – 0.4 mol/mol(alk)
5. Cross exchanger – LMTD of 5 °C
6. Packing – Mellapak 250X (3 m for AF1, 5 m for AF2 and AF3)

Equivalent work for each case was calculated using the following equation.

$$W_{eq}\left(\frac{kJ}{mol\ CO_2}\right) = 0.75\left(\frac{T_{source} + \Delta T - T_{sink}}{T_{source} + \Delta T}\right)Q_{reb} + Q_{pump} + Q_{comp}$$

$$Q_{reb} = Reboiler\ Duty;\ \ Q_{pump} = Pump\ Work;\ \ Q_{comp} = Compressor\ Work.$$

Figures 1 to 3 show the process flow diagram of these three configurations in increasing complexity of the Advanced Flash.
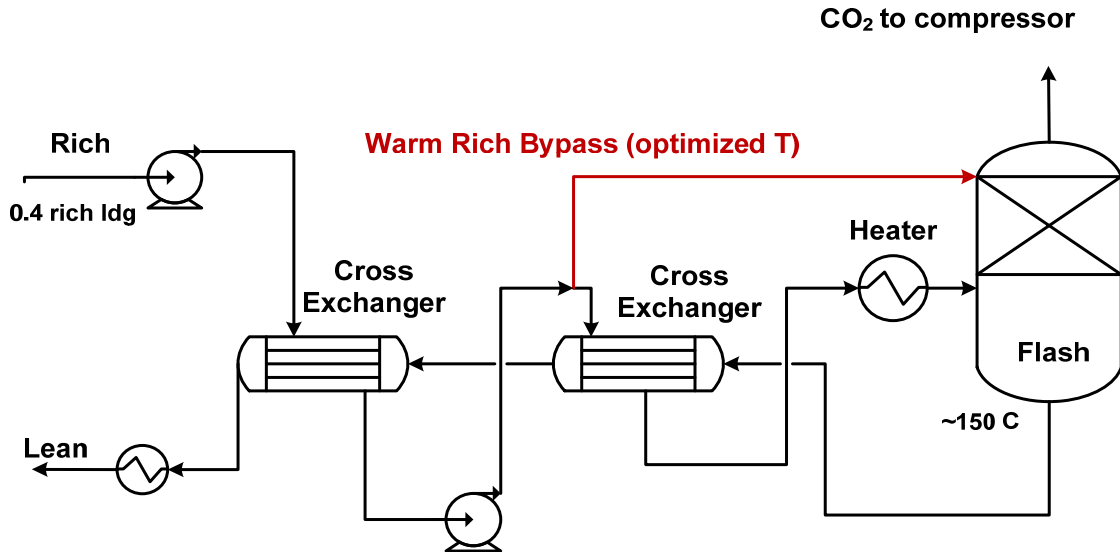
Figure 1: Flash with warm rich bypass (Advanced Flash 1, 2 m Mellapak 250X packing, 8 m PZ, 5 °C LMTD Cross exchanger)

Advanced Flash 2 uses a combination of cold and hot rich bypass to recover the waste heat of stripping steam in the flash. Advanced Flash 3 has a combination of cold, warm, and hot rich bypass as shown in Figure 3.
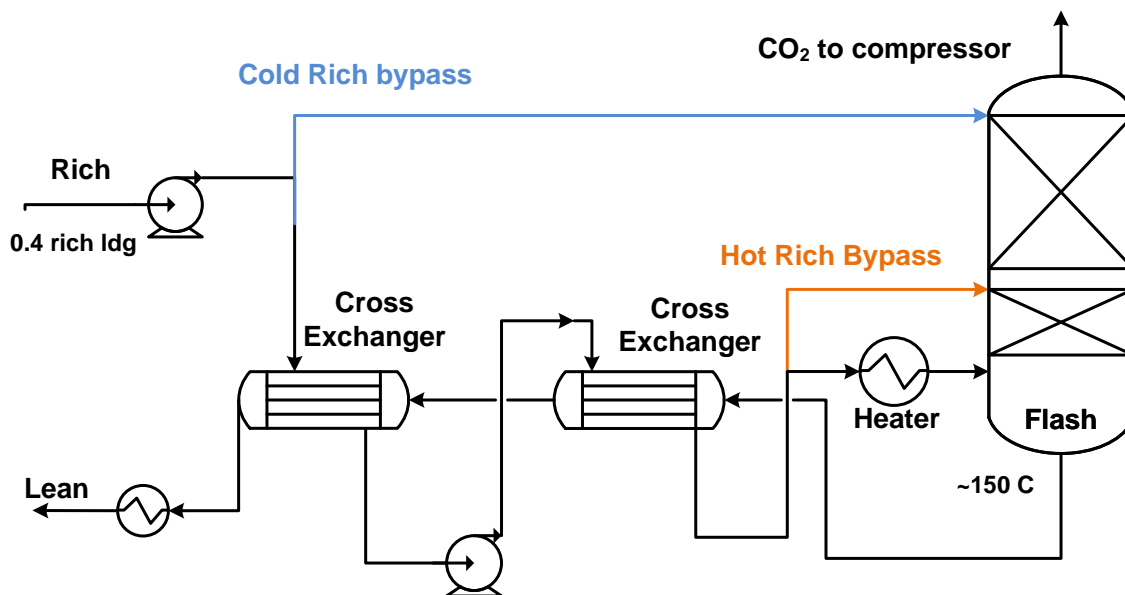
Figure 2: Flash with hot and cold rich bypass (Advanced Flash 2, Mellapak 250X packing, 8 m PZ, 5 °C LMTD Cross exchanger)
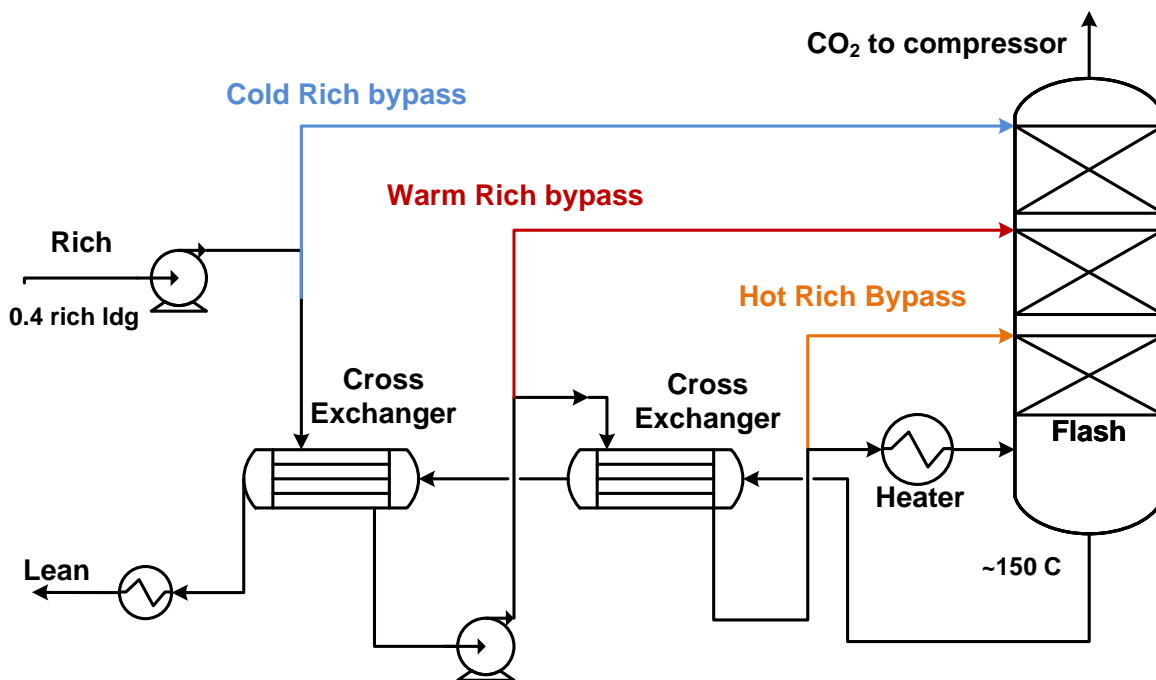
Figure 3: Flash with hot, warm and cold rich bypass (Advanced Flash 3, Mellapak 250X packing, 8 m PZ, 5 °C LMTD Cross exchanger)

Pilot Plant Configurations

Pilot plant configurations based on the advanced flash stripper concept were modeled with the following changes over the base design.

1. Flashing allowed in the cross exchanger design.
2. Heat Recovery from hot CO_2 using a rich bypass exchange with a 15 °C LMTD heat exchanger instead of cold rich bypass (to minimize packing requirement).
3. Fixed total amount of packing (5 m Mellapak 250X).
4. Other specifications: 8m PZ, 0.4 rich ldg, 0.29/0.27 lean ldg, 150 °C stripping T.

The resulting configurations are shown in Figures 4 to 8.
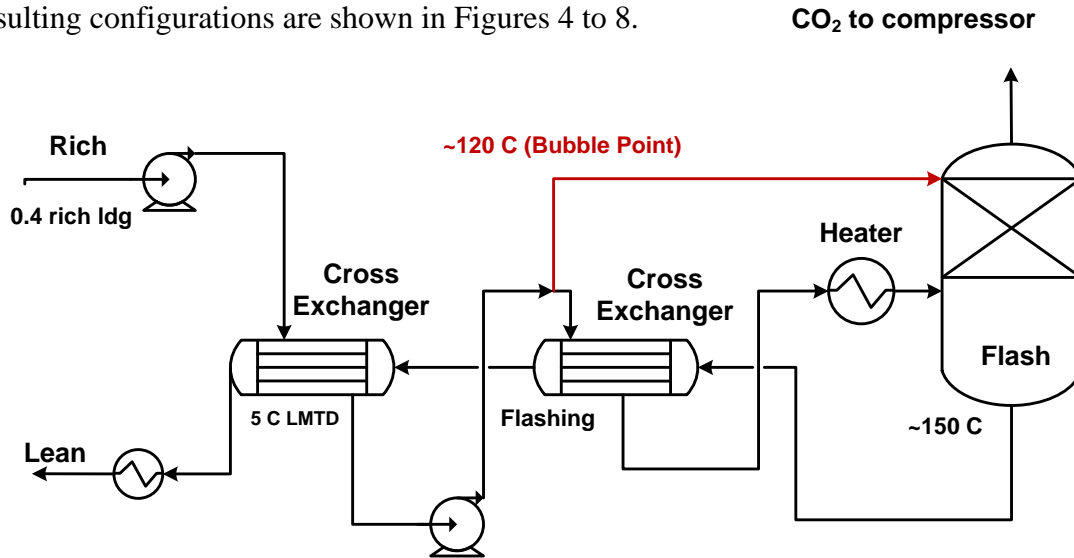
Figure 4: Warm Rich bypass at rich liquid bubble point
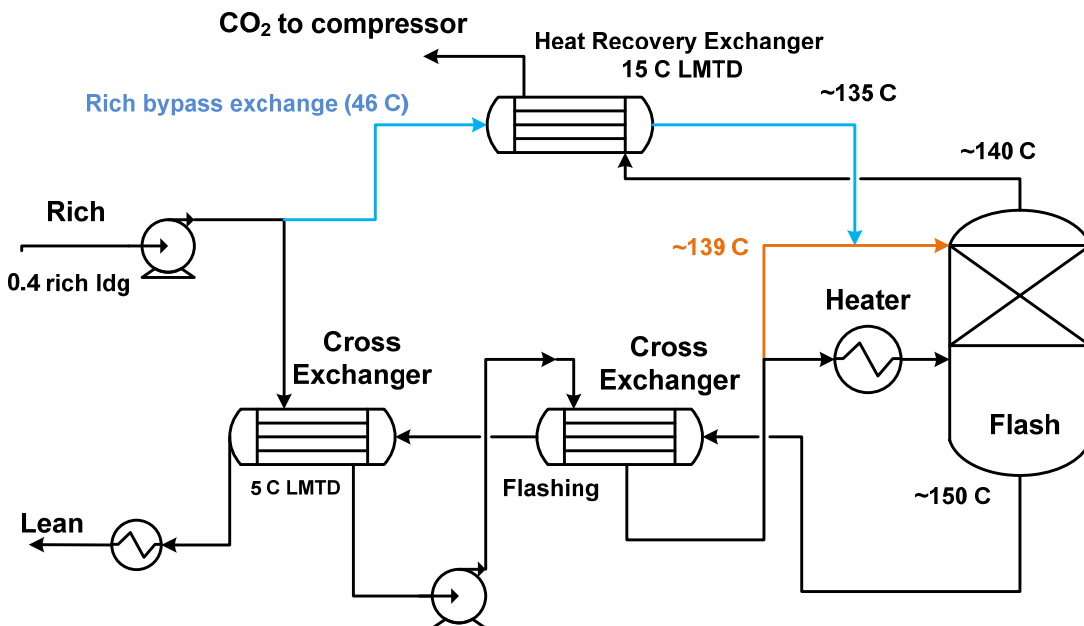
Figure 5: Single stage flash with rich bypass exchange and hot bypass

4

Figure 6: Single flash with rich bypass exchange and warm bypass

Figure 7: Single flash with rich bypass exchange, warm bypass (at bubble point), and hot bypass
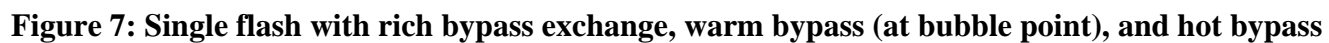
A combination of hot and warm bypass was also tested with vapor recycle in which vapor from partially heated solvent is sent to flash directly as shown in Figure 8.
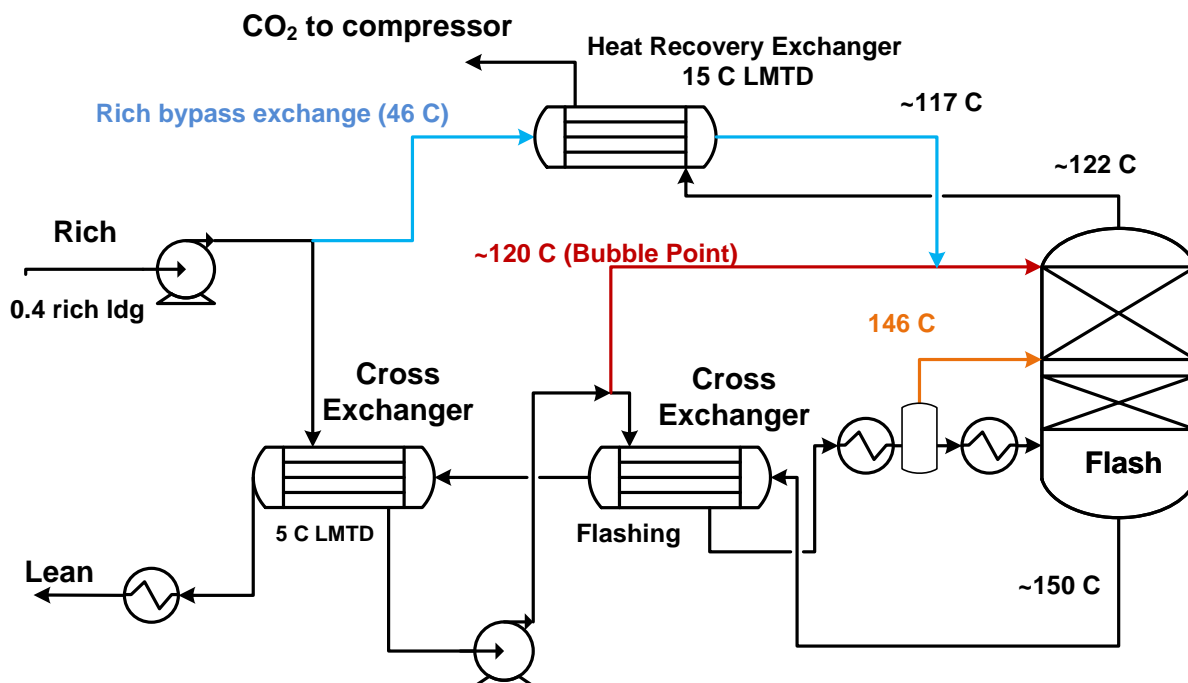
Figure 8: Advanced Flash with vapor recycle

Results

Advanced Flash Stripper

Figure 9 compares the equivalent work values for various complex configurations of the Advanced Flash and Simple Stripper over a range of lean loadings.

Table 1 shows the improvement of the advanced flash compared with the base case of the simple stripper.
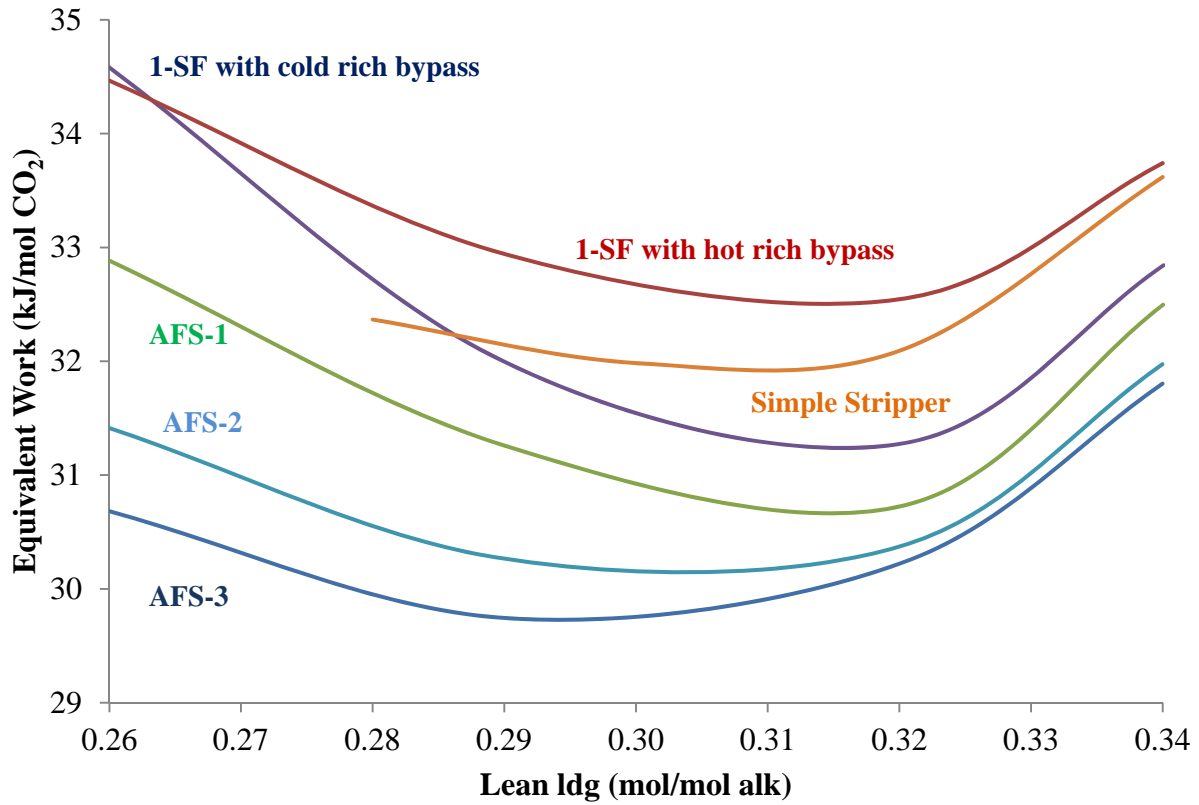
Figure 9: Equivalent work of various stripper configurations for a range of lean loading (Independence model, 8 m PZ, 5 °C LMTD cross exchanger, 150 °C stripping T, compression to 150 bar, 3 m packing for AF1, 5 m packing AF2 and AF3)

Table 1: Improvement of equivalent work for different stripper configurations compared to base case of simple stripper (8 m PZ, 5 °C LMTD cross exchanger, 150 °C stripping T, compression to 150 bar)

Configuration	Equivalent Work (kJ/mol CO_2)	Improvement over base case
Simple Stripper (Fawkes)	32.6	-
Interheated Stripper (Fawkes)	30.0	-
Simple Stripper (Independence, Base case)	32.1	-
Advanced Flash 1	31.4	2.2%
Advanced Flash 2	30.3	5.6%
Advanced Flash 3	29.7	7.5%

Pilot Plant Configurations

Table 2 shows the result of pilot plant configuration options at lean loading values of 0.29 and 0.27.

Table 2: Equivalent work for pilot plant cases at lean loading of 0.29 and 0.27 (8 m PZ, 5 °C LMTD cross exchanger, 150 °C stripping T, compression to 150 bar, 5 m Mellapak 250X)

Configuration	Equivalent Work @0.29 lean ldg (kJ/mol CO_2)	Equivalent Work @0.27 lean ldg (kJ/mol CO_2)
Advanced Flash with rich bypass exchange	30.6	31.2
Advanced Flash with warm bypass	30.1	30.2
Advanced Flash with rich bypass exchange and hot bypass	30.0	30.3
Advanced Flash with rich bypass exchange and warm bypass	29.0	29.2
Advanced Flash with rich bypass exchange, warm bypass and hot bypass	29.0	29.1
Advanced Flash with vapor recycle	29.0	29.1

Conclusions

1. The Advanced Flash Stripper with cold, warm, and hot bypass and excess packing provides an equivalent work value of 29.7 kJ/mol (7.5% improvement) with 8 m PZ.

2. A pilot plant configuration with rich exchange bypass and warm rich bypass should provide an equivalent work of 29.0 kJ/mol.

References

Leites IL, Sama DA, Lior N. "The theory and practice of energy saving in the chemical industry: some methods for reducing the thermodynamic irreversibility in chemical technology processes." *Energy*, Volume 28, Issue 1, January 2003; 55–97.

Oyenekan B. *Modeling of Strippers for CO_2 Capture by Aqueous Amines*. The University of Texas at Austin. Ph.D. Dissertation. 2007.

Rochelle GT et al. "CO_2 Capture by Aqueous Absorption, First Quarterly Progress Report 2012." Luminant Carbon Management Program. The University of Texas at Austin. 2012.

Van Wagener DH. *Stripper Modeling for CO_2 Removal Using Monoethanolamine and Piperazine Solvents.* The University of Texas at Austin. Ph.D. Dissertation. 2011.

Thermodynamic Models for 4 m 2MPZ/4 m PZ and 8 m 2MPZ

by Brent Sherman

Supported by the Luminant Carbon Management Program

McKetta Department of Chemical Engineering

The University of Texas at Austin

January 31, 2013

Abstract

A non-rigorous model for 4 m 2MPZ/4 m PZ was made by modifying $\Delta_f H^{\infty,aq}_{PZCOO^-}$ in the rigorous 8 m PZ model. This model does not include 2MPZ or its derivative species, and so PZ and its derivatives serve as pseudocomponents. Still, this non-rigorous thermodynamic model gives acceptable performance. A kinetic model was begun, but not completed owing to a shift in focus to the rigorous 8 m 2MPZ model. The current version (V0.0) improves upon the prior version by stripping the model down to just 2MPZ in addition to changing the chemistry set and viscosity subroutine to conform to current standards, specifically the elimination of proton and hydroxide ions and use of the modified Weiland equation. In examining this rigorous model for weaknesses, a ~5 kJ/mol discrepancy at high loadings between calculating the heat of absorption via calorimetry and via Lewis-and-Randall (formerly Gibbs-Helmholtz) was uncovered. All recent and under development models have been centralized, assigned a version number, and a metadata file to ensure consistency among present and future modelers.

Introduction

The overarching goal of this project is to develop a generic amine model and to use this model to systematically investigate the impact of amine properties on process performance. Subordinate goals include developing more models, developing new modeling methods, and ensuring consistency across models.

A generic amine model would allow for more rapid amine solvent screening. There are currently models for sundry piperazine (PZ) blends, including PZ with methyl diethanolamine (MDEA), 2-methylpiperazine (2MPZ), 2-amino-2-methyl-1-proponol (AMP), and aminoethylpiperazine (AEP). All of these blends broaden the solid solubility window of PZ while minimally compromising its beneficial properties. Each of these models represents a substantial investment of man hours, and so I seek to streamline this process. Furthermore, a different model maker has crafted each aforementioned model. Without a system for version control, tracking changes between versions will become increasingly problematic.

Immediate work focused on a non-rigorous 4 m 2MPZ/4 m PZ model, a rigorous 8 m 2MPZ model, and version control.

Modeling Methods

Non-Rigorous 4 m 2MPZ/4 m PZ

This model was created by modeling the blend as 8 m PZ in the Independence model. In effect, PZ and its derivative species are pseudocomponents, which is why this a non-rigorous model. Neither 2MPZ nor any of its derivative species were added to the model. As the blend has very similar properties to straight 8 m PZ, slightly modifying the existing model should create an acceptable blend model.

There are drawbacks inherent to this approach. For one, the model will not extrapolate amine concentration, making modeling of water wash and thermal reclaimer conditions infeasible. For another, the speciation is unclear. As there are no 2MPZ species in the model, the set of PZ species must represent both PZ and 2MPZ. This makes it difficult to determine what the catalyzing base is for kinetics.

In order to match the vapor-liquid equilibrium data, 2MPZ VLE data were initially regressed using the Data Regression System. However, this led to unsatisfactory results. Starting instead with the previously regressed PZ values for the parameters in Table 1 and applying small manual tweaks to just a few parameters made the model represent the VLE data (Figure 2).

Table 1: To match 8 m 2MPZ, these parameters were explored for HCO_3^-, $CO3^{2-}$, PZ, $PZ(COO^-)_2$, $PZCOO^-$, PZH^+, PZH^{+2}, HPZCOO.

Parameter	Symbol
DGAQFM	$\Delta_f G_k^{\infty,aq}$
DGAQHG	$\Delta \bar{G}_f^o$
DGFORM	$\Delta_f G_w$
DHAQFM	$\Delta_f H_k^{\infty,aq}$
DHAQHG	$\Delta \bar{H}_f^o$

After verifying the model thermodynamics, the hydraulics must be regressed prior to kinetic modeling. While the density of the blend and straight PZ are very similar, their viscosity is very different. For this reason, density was not regressed, but viscosity was regressed using Equation 1, which is modified from Weiland (Weiland et al., 1998).

$$\mu_{pure} = \mu_{H_2O} \exp \left\{ \frac{[\Omega \{(A\Omega + B)T + C\Omega + D\}][(E\Omega + FT + H)\alpha + 1]}{T^2} \right\} \tag{1}$$

The results of kinetic modeling were unsatisfactory despite seven different runs using the DataFit tool. This may result from representing each WWC experiment as six parallel measurements (Chen, 2011). Kinetic modeling techniques will be explored further in the pure 2MPZ model.

Rigorous 8 m 2MPZ

Returning to this model with more sophisticated techniques as well as a better understanding of thermodynamic and kinetic modeling necessitated recreating the model from the original framework (Chen, 2011). The original model will be referred to as 2MPZ version α, while my

2

model is 2MPZ Version 0.0. α is based on a Fawkes model, and so it contains many parameters, reactions, and associated code blocks necessary for modeling PZ/MDEA. To isolate problems, these parts − the chemistry reactions, the subroutine code, the analysis blocks, etc. − were eliminated. Then, the default chemistry set was stripped down to agree with our current methods, namely not modeling the proton and hydroxide ions. These ions are not modeled owing to their insignificantly low concentration throughout operating conditions.

Table 2: The chemistry blocks of the two models differ in the presence of proton and hydroxide ions.

2MPZ Version α	2MPZ V0.0
2MPZ + HCO3- ↔ 2MPZCOO + H2O	2 2MPZ + CO2 ↔ 2MPZCOO + 2MPZH+
	2 2MPZCOO + CO2 ↔
H2MPZCOO ↔ 2MPZCOO + H+	2MPZCOO2 + H2MPZCOO
2MPZCOO + HCO3- ↔ 2MPZCOO2 +	2MPZCOO + CO2 + H2O ↔
H2O	HCO3- + H2MPZCOO
	2MPZ + H2MPZCOO ↔ 2MPZH+ +
2MPZH+ ↔ 2MPZ + H+	2MPZCOO
H2O ↔ H+ + OH-	2MPZCOO + HCO3- ↔ CO3-- + H2MPZCOO
CO2 + H2O ↔ H+ + HCO3-	
HCO3- ↔ H+ + CO3--	

To ensure that these changes did not harm the model, the validation was repeated. The model was verified as thermodynamically sound. This process showed a large discrepancy between the calorimetric and Lewis-and-Randall (formerly referred to as the Gibbs-Helmholtz) methods for calculating heat of absorption. The latter method uses Equation 2), while the former uses Equation 3. Prior work reduced the difference between the two by eliminating the inconsistency between thermodynamic properties and equilibrium constants, yet a discrepancy persists (Rochelle et al., 2011).

$$\Delta H_{abs} = -R \frac{d \left(\ln f^*_{CO_2} \right)}{d \left(1/T \right)} \tag{2}$$

$$\Delta H_{abs} = \frac{Q}{\dot{n}_{CO_2}} \tag{3}$$

where Q is the net-duty of the flash block, and $\dot{n}_{CO_2}$ is the molar flow rate of gaseous CO_2. The heat of absorption is calculated by sending a loaded solvent stream and a gaseous CO_2 stream to a flash block for a bubble point calculation.

Once the review was complete, hydraulic regression began. The viscosity subroutine used a different equation (Freeman, 2011: Equation 4.3). While this was functional, having all models use the same set of equations will allow easy comparison of the significance of parameters across amine systems, so the viscosity data were fit with Equation 1.

Version Control

Last quarter, version control for the uncompiled source code for all Fortran subroutines was implemented. This took advantage of the dynamic linker option in Aspen Plus® to centralize all Fortran subroutines. This quarter, version control for the binary model files (*.bkp) was implemented by centralizing all recent models with a focus on those under active development.

- 2MPZ (Chen, 2011; Rochelle et al., 2013)
- 2MPZ/PZ (this report)
- AMP/PZ (Rochelle et al., 2012)
- KPZ (Hilliard, 2008)

- MEA (Phoenix, Model A, Model B) (Plaza, 2011; Xu, 2011)
- PZ & MDEA/PZ (Fawkes, Independence) (Frailie, Plaza, Van Wagener, & Rochelle, 2011)
- AEP/PZ (Rochelle et al, 2013)

Each model has an associated metadata file detailing its creation history and changes between versions.

Results and Discussion

Non-Rigorous 4 m 2MPZ/4 m PZ

A thermodynamic model in good agreement with the experimental data was obtained by adjusting $\Delta_f H^{\infty,aq}_{PZCOO^-}$ from -4.99E+08 to -4.80E+08 $J/kmol$. The results are shown below in Figures 1–5.
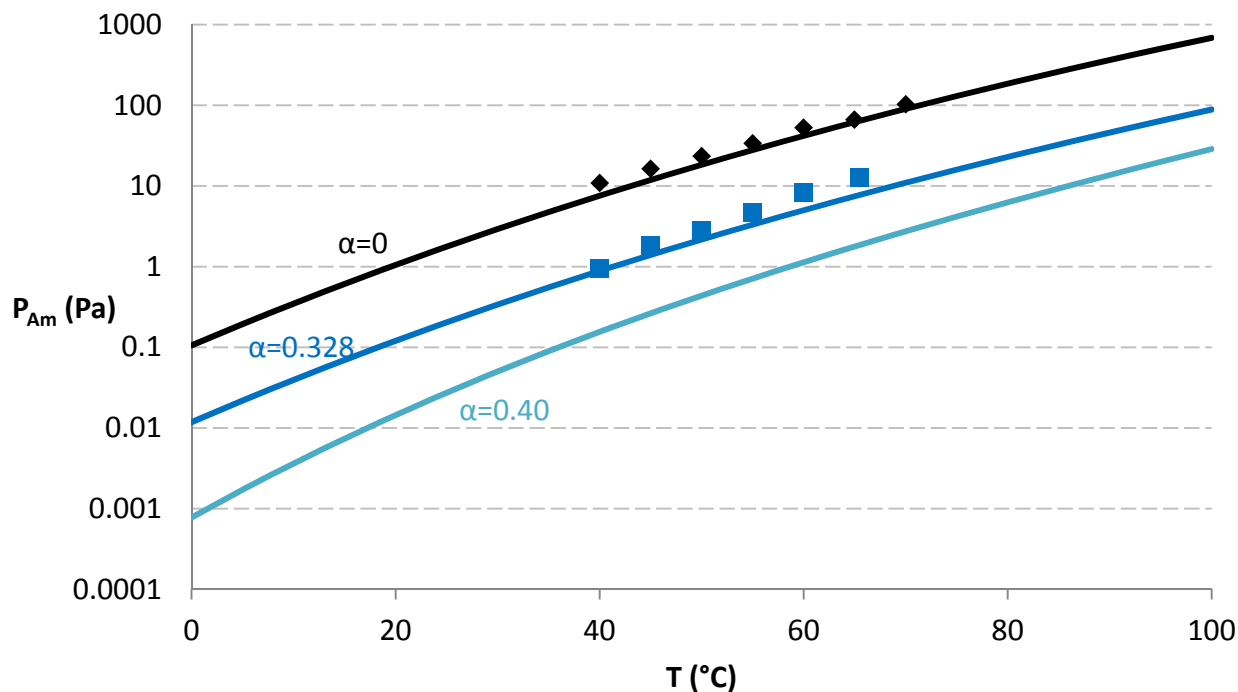
Figure 1: Loaded amine volatility of 4 m 2MPZ/4 m PZ. Points are data (Nguyen, 2011); lines are model predictions.

4
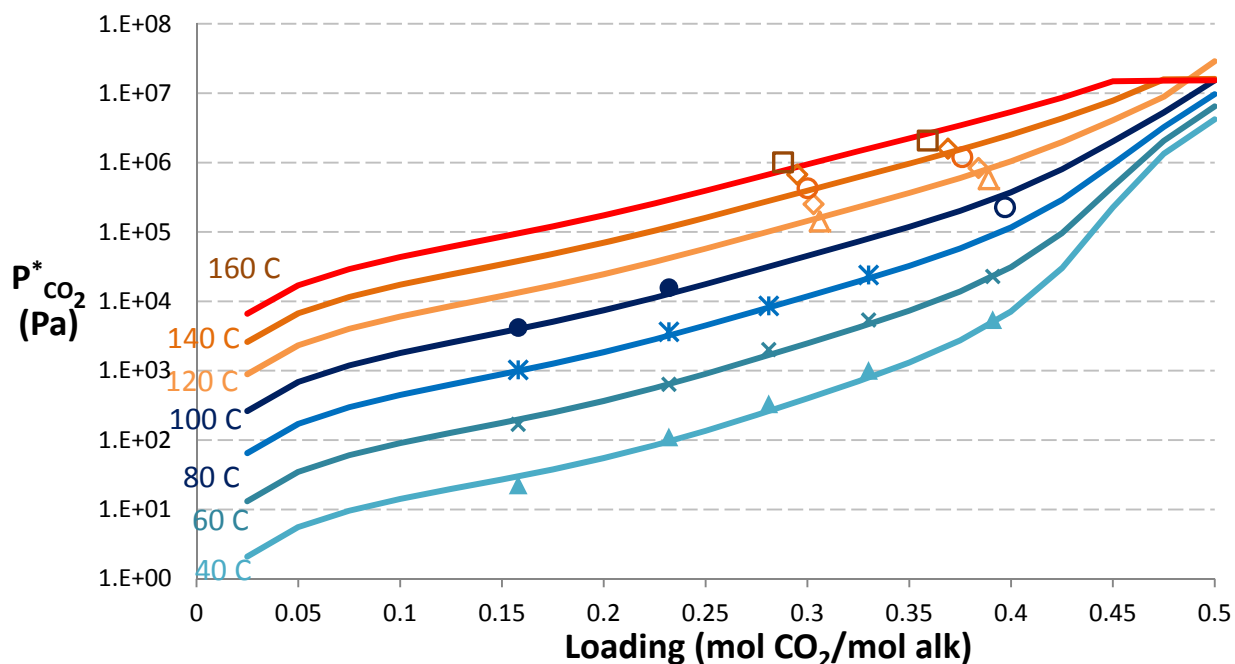
Figure 2: VLE for 4 m 2MPZ/4 m PZ. The experimental data are well fit by manually changing $\Delta_f H^{\infty,aq}_{PZCOO^-}$**. Lines are the model; filled points WWC data (Chen, 2011); empty points total pressure (Xu, 2011).**
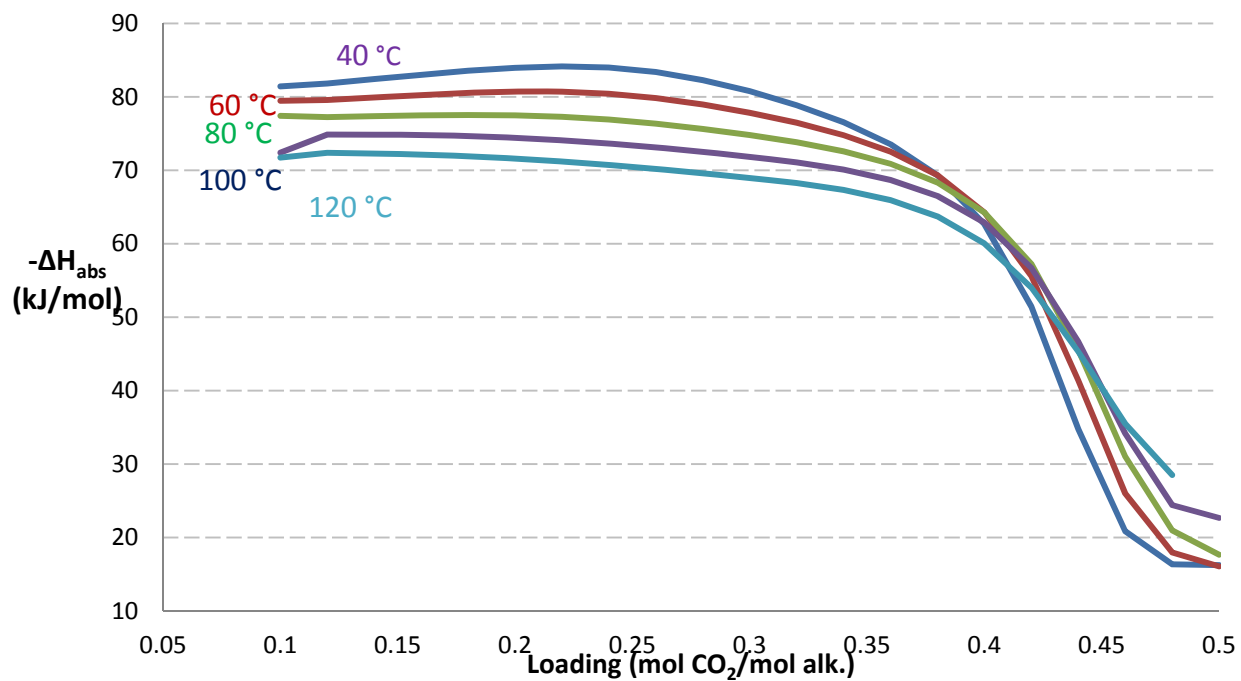
Figure 3: Heat of absorption of 4 m 2MPZ/4 m PZ calculated using Equation 2. The inflection is poorly defined and the higher loadings are muddy, but the curves are reasonable.
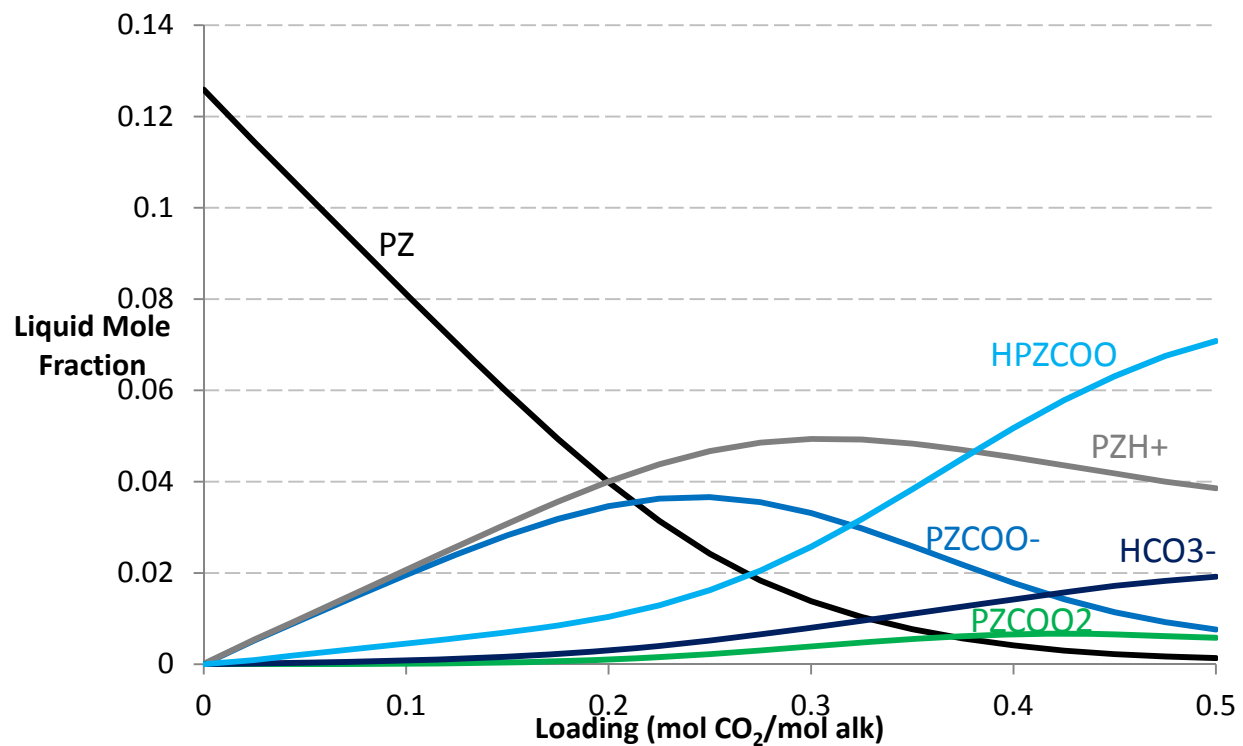
Figure 4: Non-rigorous speciation 4 m 2MPZ/4 m PZ at 40 °C. As expected, more bicarbonate forms due to the hindered 2MPZ than in the pure PZ system, as seen in Figure 5.
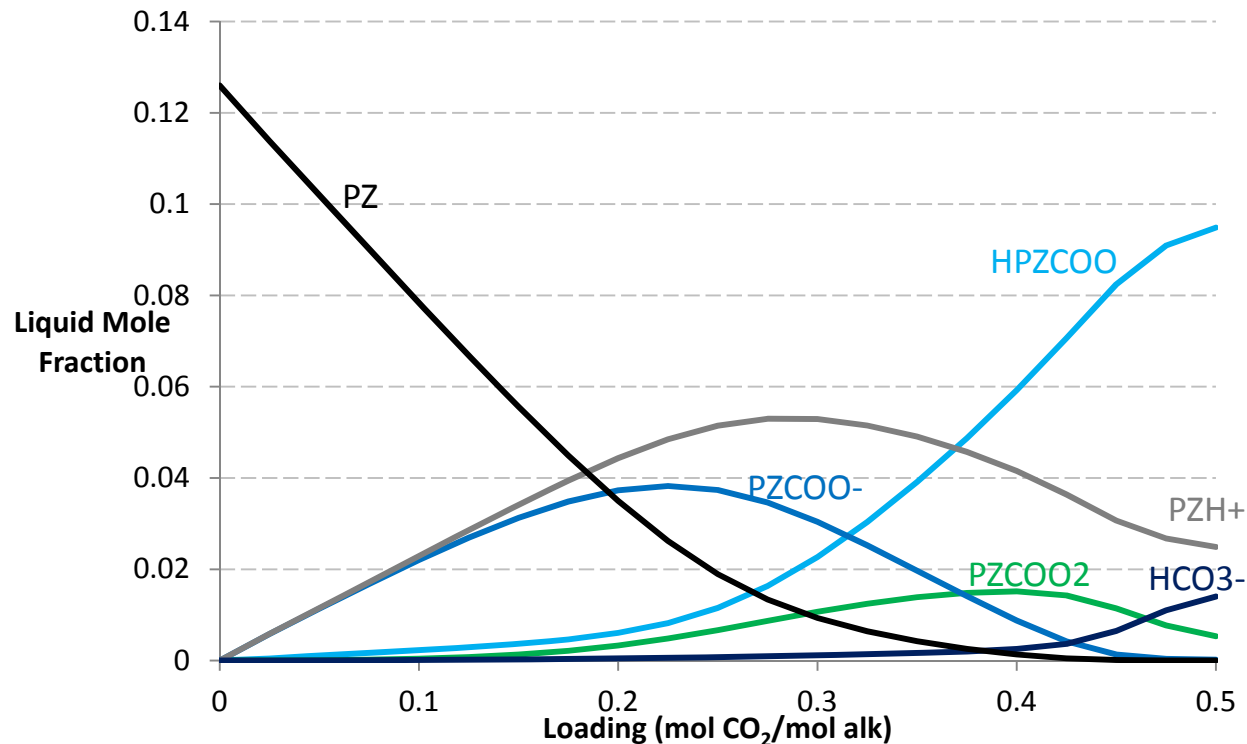
Figure 5: Speciation of 8 m PZ at 40 °C from Independence. The solid solubility limit is exceeded above 0.45 loading.

An intermediary step between the thermodynamic and kinetic models is regression of the hydraulics. Whereas density is not critically important to kinetics, and the two amines have similar densities, that hydraulic parameter was calculated as straight 8 m PZ. Contrariwise, the viscosity of the blend differs substantially from that of pure PZ, so the parameters of Equation 1 were changed to the values in Table 3.

Table 3: Viscosity parameters of Equation 1 for 4 m 2MPZ/4 m PZ and 8 m 2MPZ.

Parameter	4 m 2MPZ/4 m PZ	8 m 2MPZ
A	2.56E+03	4.85E+02
B	7.64E+02	1.52E+03
C	1.00E+00	2.07E+00
D	4.01E+00	5.13E+00
E	-3.46E+01	-4.38E+00
F	3.03E-03	-1.05E-02
H	1.45E+01	7.16E+00
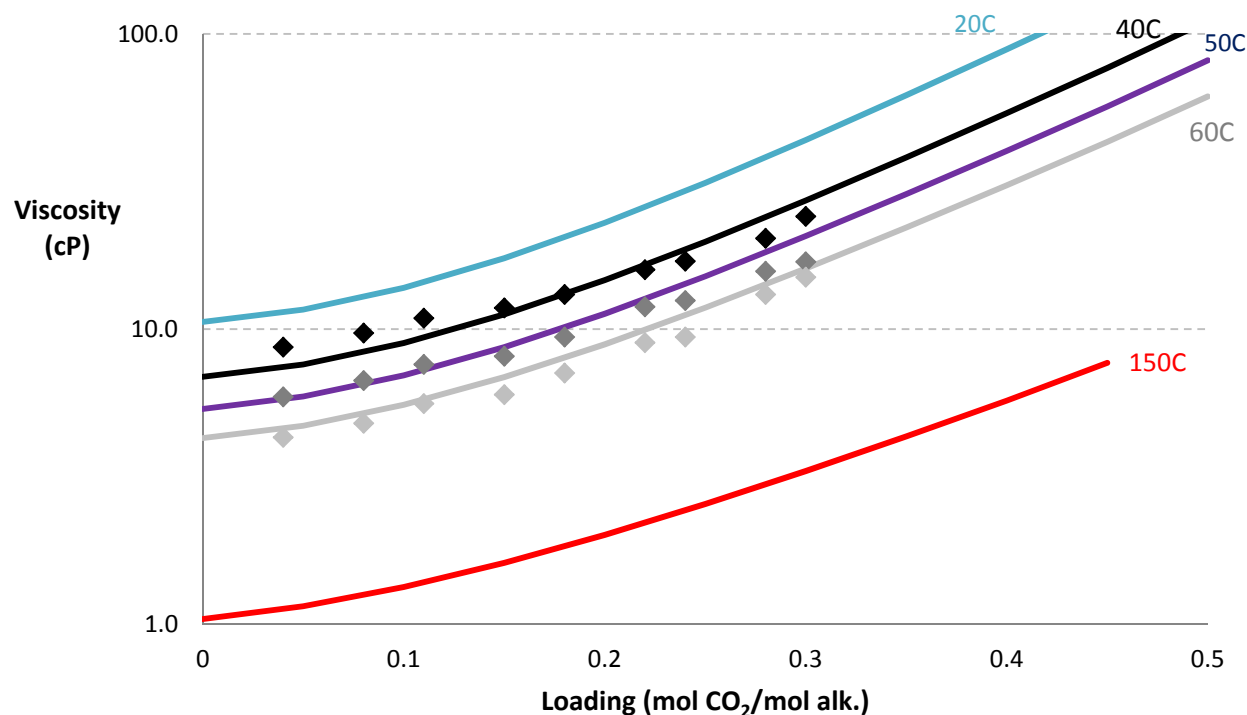
Figure 6: Viscosity of 4 m 2MPZ/4 m PZ. Lines are the model; points are data (Chen, 2011).

The kinetic model failed to match the experimental flux within ±20%. There was no clear trend in the disagreement with regards to loading, temperature, or magnitude of flux.

Rigorous 8 m 2MPZ Model

Despite removal of protons and hydroxide ions and changing the chemistry reaction set, the thermodynamic model shows just as good agreement as shown elsewhere (Chen, 2011). This confirms the insignificance of those ions, and their elimination should aid convergence. While verifying the heat of absorption, the two different methods outlined previously were compared. The results are shown in Figures 7–9. It is suspected that the deviation above a loading of 0.25 mol CO_2/mol alk. is due to the zwitterion becoming a significant species.
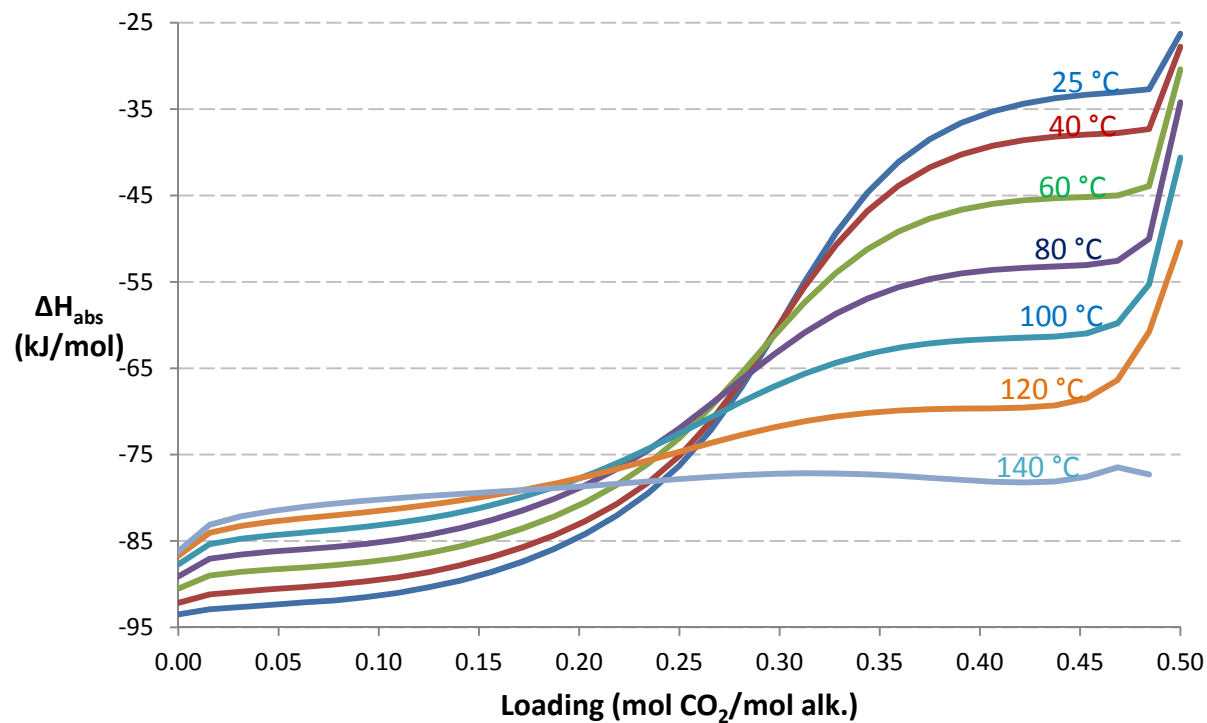
Figure 7: Heat of absorption of 8 m 2MPZ calculated from Equation 2.
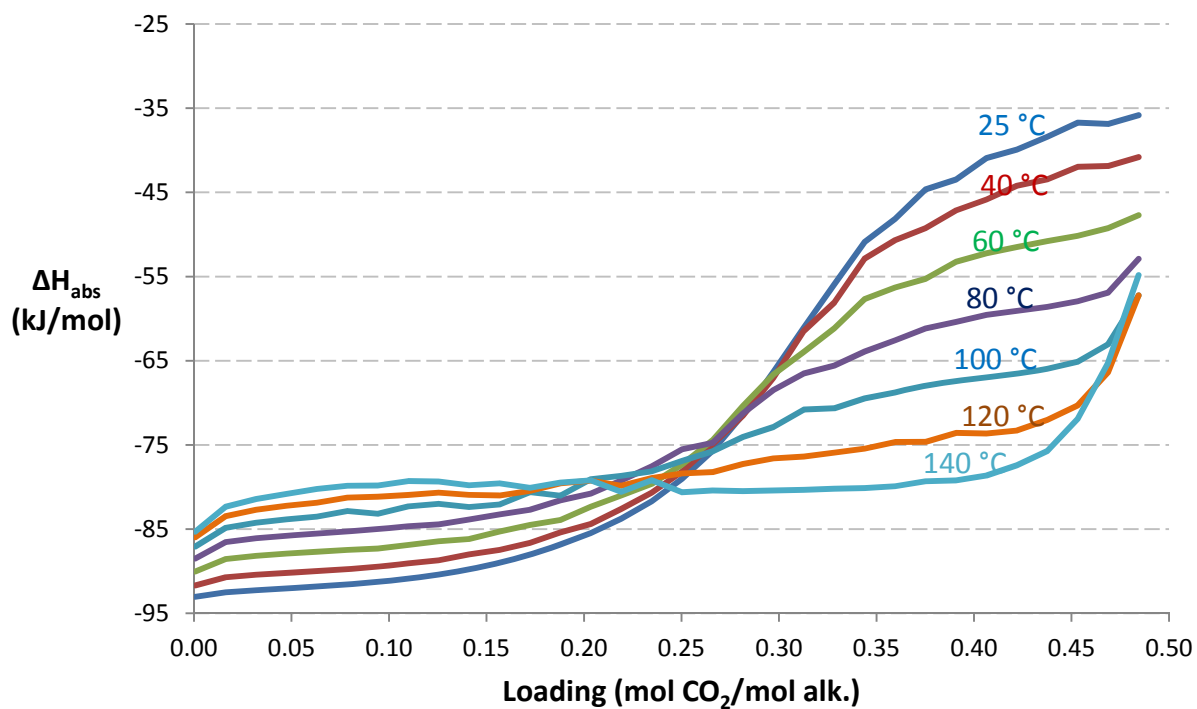
Figure 8: Heat of absorption of 8 m 2MPZ calculated from Equation 3. The disagreement between the two methods occurs above a loading of 0.25 (compare Figure 9).
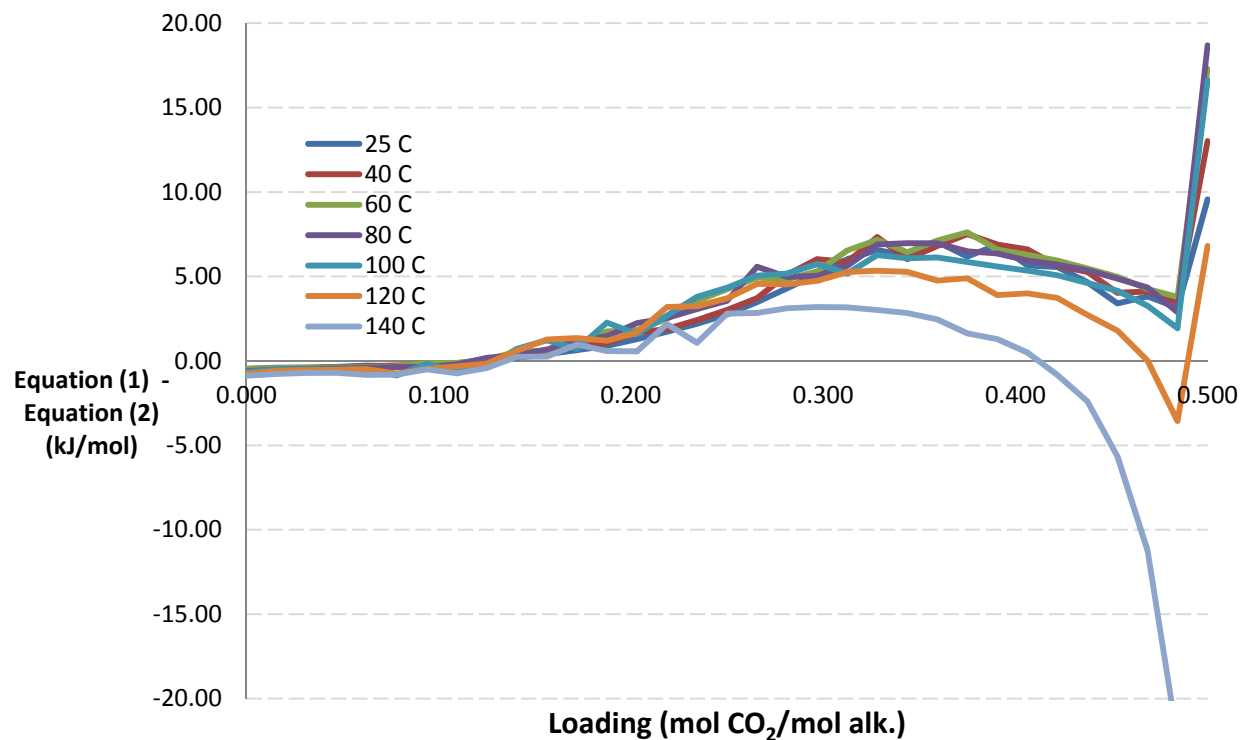
Figure 9: The absolute difference between the two heat of absorption calculations. They agree well until a loading of 0.25 mol CO_2/mol alk., where the zwitterion becomes significant.

With a sound thermodynamic model, the hydraulics are regressed prior to kinetic modeling. The viscosity fit using Equation 1 with parameters from Table 3 is shown in Figure 10.
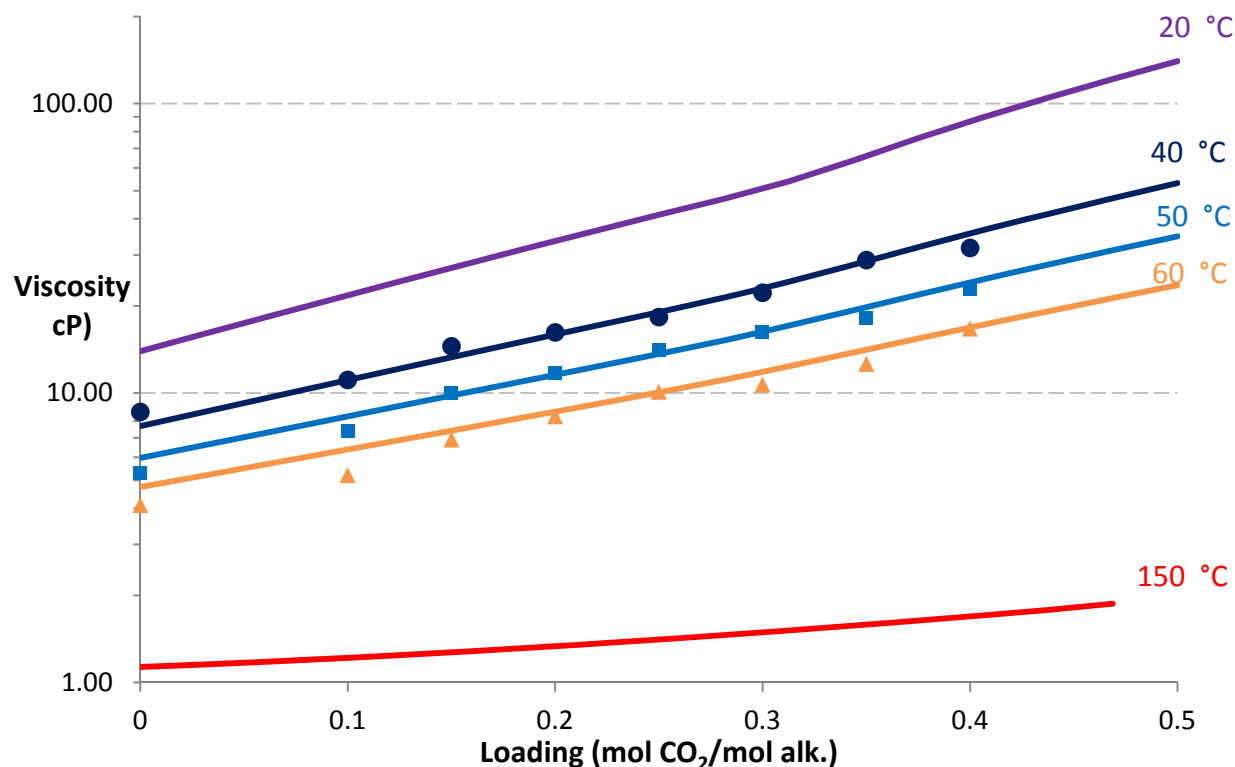
Figure 10: Viscosity of 8 m 2MPZ. Lines are the model; points are data (Chen, 2011).

Version Control

All Aspen Plus® models of interest were centralized into a single repository and assigned version numbers and a metadata file. This repository is key to ensuring consistency among the models. The implementation of this system brings us in line with the best practices currently used in software development.

Conclusions

1. A non-rigorous 4 m 2MPZ/4 m PZ thermodynamic model was made by modifying one parameter of the rigorous 8 m PZ model.
2. The rigorous 8 m 2MPZ model V0.0 improves on the old model by eliminating the proton and hydroxide ions and reducing the model to only 8 m 2MPZ.
3. There is a discrepancy between calculating heat of absorption from VLE and from calorimetry (Equations 2 and 3) particularly where the zwitterion species becomes significant.
4. All recently active models have been centralized and assigned version numbers and metafiles to track development. This will ensure consistency across present and future modelers.

Future Work

Next quarter work will focus on the creation of a kinetic 2MPZ model. This process will explore multiple kinetic modeling methods and compare their end results to determine the best practice. Once this is complete, focus will shift to the 4 m 2MPZ/4 m PZ model, which also needs a kinetic model. Other projects include improving version control, finding the root of the heat of absorption discrepancy, and solid solubility studies for various systems of 2MPZ/PZ.

References

Chen X. *Carbon Dioxide Thermodynamics, Kinetics, and Mass Transfer in Aqueous Piperazine Derivatives and Other Amines*. The University of Texas at Austin. Ph.D. Dissertation. 2011.

Frailie PT, Plaza JM, Van Wagener DH, Rochelle GT. "Modeling Piperazine Thermodynamics." *Energy Proc.* 2011;4:35–42.

Freeman SA. *Thermal Degradation and Oxidation of Aqueous Piperazine for Carbon Dioxide Capture*. The University of Texas at Austin. Ph.D. Dissertation. 2011.

Hilliard MD. *A Predictive Thermodynamic Model for an Aqueous Blend of Potassium Carbonate, Piperazine, and Monoethanolamine for Carbon Dioxide*. The University of Texas at Austin. Ph.D. Dissertation. 2008.

Nguyen T. Personal communication. 2011.

Plaza JM. *Modeling of Carbon Dioxide Absorption using Aqueous Monoethanolamine, Piperazine and Promoted Potassium Carbonate*. The University of Texas at Austin. Ph.D. Dissertation. 2011.

Rochelle GT et al. "CO_2 Capture by Aqueous Absorption, First Quarterly Progress Report 2011." Luminant Carbon Management Program. The University of Texas at Austin. 2011.

Rochelle GT et al. "CO_2 Capture by Aqueous Absorption, Second Quarterly Progress Report 2012." Luminant Carbon Management Program. The University of Texas at Austin. 2012.

Rochelle GT et al. "CO_2 Capture by Aqueous Absorption, Fourth Quarterly Progress Report 2012." Luminant Carbon Management Program. The University of Texas at Austin. 2013.

Weiland RH, Dingman JC, Cronin DB, Browning GJ. "Density and Viscosity of Some Partially Carbonated Aqueous Alkanolamine Solutions and Their Blends." *J Chem Eng Data.* 1998;43(3):378–382.

Xu Q. *Thermodynamics of CO_2 Loaded Aqueous Amines*. University of Texas at Austin. Ph.D. Dissertation. 2011.

Equation-Based Representations of Mass Transfer, Heat Transfer, and Reaction Kinetics in Gas/Liquid Contactors

Quarterly Report for October 1 – December 31, 2012

by Matthew S. Walters

Supported by the Luminant Carbon Management Program

McKetta Department of Chemical Engineering

The University of Texas at Austin

January 31, 2013

Abstract

Previously developed models of gas/liquid contactors used in amine scrubbing have been analyzed for accuracy and practicality based on their representations of mass transfer, heat transfer, and reaction kinetics. It is recommended that the continuity equation approach be used to represent mass and heat transfer in a continuous packed bed, but discontinuous sections of the bed, including liquid feed points, intercooling sections, and interheating sections, be treated as a well-mixed segment. Two-film theory assuming binary diffusion should be used to avoid the estimation of multiple binary diffusion coefficients needed in the Maxwell-Stefan formulation. In the liquid phase, it is valid to assume that the internal energy holdup of a segment is equal to enthalpy holdup, but this is not valid for the compressible vapor phase. The liquid film mass transfer coefficient can be experimentally determined in a wetted wall column, so this is the most advantageous representation of reaction kinetics in the absorber. Additional parameter uncertainty is introduced when an enhancement factor is used as an alternative representation of reaction kinetics. These recommendations will be used when implementing a gas/liquid contactor model in gPROMS$^{®}$ for an amine scrubbing system.

Introduction

Equation-based models, in contrast to closed-source process simulators, provide a transparent set of physically significant relations with explicit expressions describing system parameters. An equation-based model may be advantageous for a process in the development stage like amine scrubbing where the solvent and operating conditions will likely change between initial pilot plant testing and commercial scale implementation. Several similar, yet unique approaches have been applied to the equation-based modeling of gas/liquid contactors used in amine scrubbing. The most notable research in this area has taken place at the Norwegian University of Science and Technology (Kvamsdal et al., 2009), Cranfield University (Lawal et al., 2009), and the University of Texas at Austin (Ziaii, 2012). The goal of this work is to understand the underlying theory and assumptions used in previously developed models, compile the most useful components of these models, and implement a new plantwide amine scrubbing simulator in gPROMS$^{®}$, an advanced process modeling platform. This report provides a thorough examination of how mass transfer, heat transfer, and reaction kinetics have been previously represented, and attempts to examine the advantages and shortcomings of each method in order

1

to better understand the applicability of the model. A final model for an absorber and stripper will be proposed for implementation in gPROMS® using piperazine solvent.

Representing Mass and Heat Transfer

Mass and heat transfer are the foundations of an equation-based model for a gas/liquid contactor. Based on the laws of conservation of mass and conservation of energy, dynamic equations can be written that describe the state of the system. This section examines various ways of representing the laws of conservation and associated driving forces when modeling an amine scrubbing system.

Discrete versus Continuous Representation

First, consider the case where a continuous packed bed is treated as a series of well-mixed segments using ordinary differential equations (ODEs). This is the method used by Ziaii for amine scrubbing, and it is also commonly seen in reactive distillation literature (Taylor and Krishna, 2000; Peng et al., 2003). Each segment is treated as two phases, and conservation equations can be applied to each phase. Performing a mass balance on a discrete, well-mixed phase is relatively straightforward, as shown in Equation 1, which states that the change in mass of phase j in a given segment is equal to the flow of mass in and mass out of the segment plus the interphase flux.

$$\frac{dM_i^j}{dt} = \sum_{k=1}^K \dot{M}_{i,k}^j + a \cdot V^j \cdot N_i \tag{1}$$

An energy balance for a discrete control volume is a direct result of the First Law of Thermodynamics, which is shown for an open system in Equation 2 (Sandler, 2006).

$$\frac{d}{dt}\left\{ U^j + M^j \left(\frac{v^2}{2} + \Psi \right) \right\} = \sum_{k=1}^K \dot{M}_k^j \left(\hat{H} + \frac{v^2}{2} + \Psi \right)_k + \dot{Q} + \dot{W} \tag{2}$$

In a gas/liquid contactor, changes in kinetic and potential energy are negligible and can therefore be ignored. Although liquid can perform work on the gas through holdup volume changes, the associated work from this is expected to be small compared to other energy flows and is also neglected. Equation 2 can then be simplified to Equation 3, which states that the change in energy is equal to the flow of enthalpy in and enthalpy out of the segment (including interphase flux) plus heat added to the system. In the case of two phase flow in a separation column, heat is added in the form of convection between the gas and liquid and convection to the ambient surroundings. Heat of reaction is accounted for in the enthalpy definitions.

$$\frac{dU^j}{dt} = \sum_{k=1}^K (\dot{M}^j \hat{H})_k + \dot{Q} \tag{3}$$

Using the discrete approach shown in Equations 1 and 3 for a series of small segments, the continuous solution can be approximated. As the number of well-mixed segments goes to infinity, the solution approaches the continuous case. The appropriate number of segments needed to represent a column is usually selected by sequentially adding more segments until a system parameter, such as reboiler heat duty or product mole fraction, approaches a constant value for a given set of operating conditions within some error tolerance. Figure 1 shows a simple case where the number of segments needed to represent the column is grossly underestimated, leading to significant loss of information in the column temperature profile. Failure to include an adequate number of segments will lead to unrealistic simulation results.
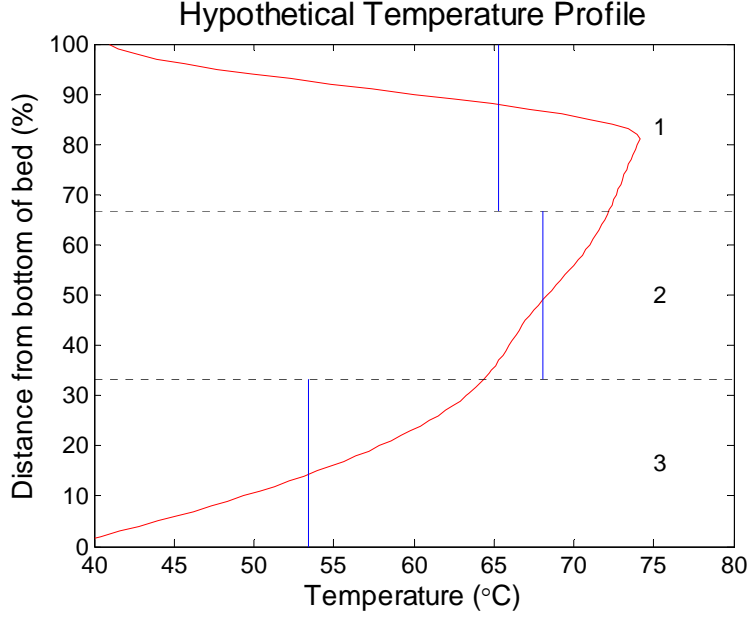
Figure 1: Example showing that a column represented as three well-mixed segments (blue) has a significant loss of information relative to the true temperature profile (red).

Kvamsdal and Lawal used the continuous approach where partial differential equations (PDEs) can be used to represent heat and mass transfer. The continuity equation is shown in generic form for either heat or mass transfer in Equation 4, where f refers to either concentration (for mass transfer) or energy (for heat transfer), $\mathbf{j}$ is the total flux vector, and s is a source or sink term.

$$\frac{\partial f}{\partial t} + \nabla \cdot \boldsymbol{j} = \text{s} \tag{4}$$

For a separation column, flux by diffusion or conduction along the axis of the column is negligible compared to bulk flow; therefore only the advective component of the total flux term is significant. The source/sink term for mass transfer is interphase flux and for heat transfer is heat of reaction or vaporization, convection between the gas and liquid, and convection to the ambient surroundings. Equation 4 can thus be written as Equation 5 for mass transfer and Equation 6 for heat transfer. The heat of reaction and vaporization terms in Equation 6 only apply to the liquid phase.

$$\frac{\partial c_i^j}{\partial t} + \nabla \cdot \left(\boldsymbol{u}^j c_i^j \right) = \text{a} \cdot \text{V} \cdot N_i \tag{5}$$

$$\frac{\partial U^j}{\partial t} + \nabla \cdot \left(\boldsymbol{u}^j H^j \right) = \text{H}_r + H_v + \dot{Q} \tag{6}$$

Equations 5 and 6 represent continuous contact between a plug flow liquid and a plug flow gas. Plug flow is expected in commercial columns with structured packing greater than approximately three meters in height (Ellenberger and Krishna, 1999), so this is probably an accurate representation.

3

Two-Film Theory

All equation-based models that have been developed use two-film theory to describe the driving force behind mass transfer, although the theory has been executed in different ways. Kvamsdal calculates flux using the driving force between the bulk gas and bulk liquid, shown in Equation 7. Ziaii calculates flux in the absorber equivalently to Equation 7, but in the stripper the driving force for CO_2 flux is the difference between the equilibrium concentration at the bulk liquid and the interface, shown in Equation 8. K_{tot} is the mass transfer coefficient of the overall gas and liquid film resistance, discussed later.

$$N_i = K_{tot,i}(P_i^{BL*} - P_i^{BV*}) \tag{7}$$

$$N_{CO_2} = k_l([CO_2]_T^{BL} - [CO_2]_T^I) \tag{8}$$

There are n-1 independent expressions for flux, where n is the number of components. However, in the dilute limit the binary fluxes become independent since the convective term in Equation 9 is approximately equal to zero. Kvamsdal and Ziaii assumed the concentration of CO_2 in the gas is small in the absorber due to a large amount of N_2 compared to CO_2 in the flue gas and use Equation 7 independently for both water and CO_2.

$$N_{CO_2} = D_{CO_2}\frac{dy_{CO_2}}{dz} + y_{CO_2}(N_{CO_2} + N_{H_2O}) \approx D_{CO_2}\frac{dy_{CO_2}}{dz}, when\ y_{CO_2} \ll 1 \tag{9}$$

In the stripper, Ziaii used Equation 10, which is a direct result of the full form of Equation 9, to relate the flux of water to the flux of CO_2 since the dilute limit assumption is not valid under stripper conditions.

$$N_{CO_2} + N_{H_2O} = k_l \ln\left(\frac{\frac{N_{CO_2}}{N_{CO_2}+N_{H_2O}}-y_{CO_2}^b}{\frac{N_{CO_2}}{N_{CO_2}+N_{H_2O}}-y_{CO_2}^I}\right) \tag{10}$$

Lawal used the Maxwell-Stefan Equations for multicomponent mass transfer to calculate flux, including resistance in both the vapor and liquid phases. Equation 11 shows the Maxwell-Stefan formulation, which is applied to both the vapor and liquid films.

$$C^j \frac{\partial y_i^j}{\partial z} = \sum_{m=1}^n \left(\frac{y_i^j N_m - y_m^j N_i}{D_{i,m}}\right) \tag{11}$$

There are n-1 independent equations, along with the conditions that the sum of the component fluxes must equal the total flux and the sum of the mole fractions must equal unity.

Internal Energy versus Enthalpy

Some researchers have written an enthalpy time derivative in the energy balance, rather than an internal energy time derivative, as derived in this report from the First Law of Thermodynamics (Ziaii, 2012; Kvamsdal et al., 2009). The definition of enthalpy is given in Equation 12, and its differential form is in Equation 13.

$$H = U + PV \tag{12}$$

$$\frac{dH}{dt} = \frac{dU}{dt} + V\frac{dP}{dt} + P\frac{dV}{dt} \tag{13}$$

Neglecting the PV work term in Equation 13 and substituting Equation 3 for the internal energy time derivative gives Equation 14.

4

$$\frac{dH^j}{dt} = \sum_{k=1}^{K}(\dot{M}^j\hat{H})_k + \dot{Q} + V\frac{dP}{dt} \tag{14}$$

This result shows that in general $\frac{dU^j}{dt} \neq \frac{dH^j}{dt}$, and the two expressions differ by the term $V\frac{dP}{dt}$. For liquids, which are approximately incompressible, Cp ≈ Cv and thus $\frac{dP}{dt} \approx 0$. Because of this observation, it is valid to assume that U = H for the liquid phase. For the compressible vapor phase, this assumption is questionable, as Cp = Cv + R for an ideal gas. It is expected that assuming enthalpy and internal energy are equal for a gas may introduce error into the model. As a reference, making this assumption for saturated water at 9.5 bar and 178 °C gives a 0.14% error but making this assumption for saturated steam at the same conditions gives a 7.5% error.

It is not obvious what effect assuming internal energy and enthalpy are equal has upon the simulation results. Because the vapor dynamics are expected to be much faster than the liquid dynamics and the holdup of the vapor is much less than the liquid, it may be reasonable to assume the vapor is approximately in steady state, so the $\frac{dU^j}{dt}$ and $\frac{dM_i^j}{dt}$ terms are approximately equal to zero. This approach was used by Lawal.

Representing Reaction Kinetics

Chemical kinetics can become important in the absorption of CO_2 at low temperatures, which specifically applies to the absorber. Lawal has ignored reaction kinetics, and assumed equilibrium is attained everywhere. Other more sophisticated approaches have been applied to addressing reaction kinetics, discussed below.

Enhancement Factor

Kvamsdal has represented reaction kinetics in terms of an enhancement factor, which is used in the calculation of the total mass transfer coefficient, shown in Equation 15, where H is the Henry's Law constant and E is the enhancement factor. The enhancement factor is calculated using Equation 16, where k_r is the rate of reaction for CO_2 with aqueous MEA, $[MEA]^{BL}$ is the liquid concentration of free MEA in solution, and D_{CO2} is the diffusivity of CO_2 in aqueous MEA solution. The enhancement factor determines how much mass transfer in the liquid film is enhanced as a result of reaction kinetics.

$$\frac{1}{K_{tot}} = \left(\frac{1}{k_g}\right) + \left(\frac{H_{CO_2}}{k_l E_{CO_2}}\right) \tag{15}$$

$$E_{CO_2} = \frac{\sqrt{k_r[MEA]^{BL}D_{CO_2}}}{k_l} \tag{16}$$

Liquid Film Mass Transfer Coefficient

Ziaii has alternatively represented kinetics implicitly in a liquid film mass transfer coefficient, $k_g{}'$. In this case, the total mass transfer coefficient is calculated using Equation 17, where the liquid film mass transfer coefficient is defined in Equation 18.

$$\frac{1}{K_{tot}} = \left(\frac{1}{k_g}\right) + \left(\frac{1}{k_g'}\right) \tag{17}$$

$$\frac{1}{k_g'} = \left(\frac{1}{k_g''}\right) + \left(\frac{H_{CO_2}}{k_l}\right) \tag{18}$$

5

Equation 18 shows how the liquid film mass transfer coefficient can be divided into kinetic and physical mass transfer resistances, but in practice the overall parameter is determined experimentally for a specific solvent using a wetted wall column.

Discussion

From a simulation time and convergence standpoint, representing mass transfer as discrete, well-mixed segments is probably advantageous since only ODEs are used. While the continuous case presents greater accuracy than the discrete case, it also has potential for greater difficulty in coming to a solution. MATLAB®, for example, cannot solve PDEs and the equations must be discretized prior to implementation using a collocation method. Other advanced solvers that can handle PDEs may have initialization and convergence issues. However, convergence difficulties have been observed in the discrete case as well, and using the incorrect number of segments can introduce error to the simulation. Reboilers, flash tanks, and condensers cannot be modeled using the continuous plug flow representation, and are better suited for the discrete well-mixed phase approach. It also may be advantageous to use the discrete approach for an intercooled absorber, interheated stripper, or multifeed stripper where a continuous liquid film is not an appropriate representation. In future work, the continuous representation for the continuous sections of packed beds and the discrete representation discontinuous sections of packed beds, as well as for reboilers, tanks, and condensers, will be used.

The Maxwell-Stefan formulation for multicomponent mass transfer is more accurate than assuming binary diffusion. However, estimating binary diffusion coefficients among all species for both the liquid and gas films will undoubtedly be challenging. It is therefore recommended that in the absorber a partial pressure driving force between the bulk liquid and bulk gas be used. In the high temperature stripper, which is liquid film controlled, it is recommended that an equilibrium concentration driving force between the bulk liquid and interfacial liquid be used.

Enhancement factors are probably not the best way to account for reaction kinetics because they require an algebraic expression for the reaction rate constant, the liquid film mass transfer coefficient, and the diffusivity of CO_2, as well as the Henry's Law constant when applied in the overall resistance equation. It also requires the model to calculate the free amine concentration. This method is complicated and significant parameter uncertainty will be introduced. Additionally, it is unnecessary to calculate the enhancement factor explicitly since the physical liquid film mass transfer coefficient, $k_{l,CO2}$, which is a function of the apparatus, cancels out when Equation 16 is substituted into Equation 15. k_g', on the other hand, is just one experimentally determined parameter that lumps both physical and kinetic mass transfer resistances. Due to the greater uncertainty in the enhancement factor approach, k_g' will be used to represent reaction kinetics in the low temperature absorber.

Conclusions

- A continuous gas/liquid contactor can be represented as either a discrete series of well-mixed segments or as a continuous plug flow regime through the continuity equation.
- Rate-based mass transfer can be represented using two-film theory, assuming either binary diffusion or multicomponent diffusion with the Maxwell-Steffan formulation.
- Internal energy is the correct dynamic variable to use in an energy balance, although this can safely be approximated as enthalpy for liquids.

- Reaction kinetics can be represented using an enhancement factor, which requires expressions for the reaction rate constant, diffusivity of CO_2, liquid film mass transfer coefficient, and Henry's Law constant, or using kg', which is experimentally determined.

Future Work

- Implement previously developed two-stage flash MATLAB® model (Walters et al., 2012) in gPROMS®.
- Model an absorber in gPROMS® using the continuity equation for mass and heat conservation, the liquid film mass transfer coefficient to represent reaction kinetics, and bulk liquid and vapor partial pressure driving forces.
- Model a stripper in gPROMS® using the continuity equation for mass and heat conservation and bulk liquid and interfacial liquid concentration driving forces.
- Validate model using available pilot plant data.

Notation

a	specific area of packing
c	concentration
D	binary diffusion coefficient
E_{CO2}	enhancement factor
H	enthalpy
$\hat{H}$	specific enthalpy
H_{CO2}	Henry's law constant
k_g	gas film mass transfer coefficient
k_g'	liquid film mass transfer coefficient
k_g''	pseudo first-order liquid film mass transfer coefficient
k_l	liquid film physical mass transfer coefficient
k_r	reaction rate constant
K	total number of streams into and out of a segment
K_{tot}	overall mass transfer coefficient
M	total mass in a segment
$\dot{M}$	mass flow rate
n	total number of components
N	flux
P	pressure
$\dot{Q}$	heat flow
t	time

U	internal energy
v	velocity
V	volume of segment
$\dot{W}$	work
y	mole fraction
Greek	
Ψ	potential energy
Subscripts	
i	component
k	stream number
r	reaction
v	vaporization
Superscripts	
BL	bulk liquid
BV	bulk vapor
I	interface
j	phase (liquid or gas)
T	total
*	equilibrium partial pressure

References

Ellenberger J, Krishna R. "Counter-current operation of structured catalytically packed distillation columns: pressure drop, holdup and mixing." *Chem Eng Sci*. 1999;54:1339–1345.

Kvamsdal HM, Jakobsen JP, Hoff KA. "Dynamic modeling and simulation of a CO_2 absorber column for post-combustion CO_2 capture." *Chem Eng Process: Process Intensif*. 2009;48:135–144.

Lawal A, Wang M, Stephenson P, Koumpouras G, Yeung H. "Dynamic modeling of CO_2 absorption for post combustion capture in coal-fired power plants." *Fuel*. 2009;88:2455–2462.

Peng J, Edgar TF, Eldridge RB. "Dynamic rate-based and equilibrium models for a packed reactive distillation column." *Chem Eng Sci*. 2003;58:2671–2680.

Sandler SI. *Chemical, Biochemical, and Engineering Thermodynamics, 4th Ed*. Hoboken, NJ, John Wiley & Sons. 2006.

Taylor R, Krishna R. "Modelling reactive distillation." *Chem Eng Sci*. 2000;55:5183–5229.

Walters MS, Dunia RH, Edgar TF, Rochelle GT. "Two-stage flash for CO_2 regeneration: dynamic modeling and pilot plant validation". Presented at GHGT-11, Kyoto, Japan, November 18–22, 2012.

Ziaii S. *Dynamic Modeling, Optimization, and Control of Monoethanolamine Scrubbing for CO_2 Capture*. The University of Texas at Austin. Ph.D. Dissertation. 2012.

Thermal Degradation of Activated Tertiary Amine Blends for Carbon Capture from Coal Combustion and Gas Treating

Abstract

The thermal degradation of activated tertiary amine solvents has been studied this quarter. The thermal degradation of triethanolamine (TEA), dimethylaminoethanol (DMAE), methyldiethanolamine (MDEA), diethylaminoethanol (DEAE), dimethylaminopropanol (DMAP), dimethylaminobutanol (DMAB), ethyldiethanolamine (EDEA), and 2-[2-(Dimethylamino)ethoxy]ethanol (DMAEE) activated by piperazine (PZ) was studied. The thermal degradation of MDEA activated by hexamethylenediamine (HMDA) and 2-(2-aminoethoxy)ethylamine (BAE) was also studied. The solvent composition was as follows for each amine system: 5 m tertiary amine/5 m activator with an initial loading of 0.225 mol CO_2/mol alkalinity. Degradation was studied at 135–175 $^{\circ}$C. A first-order rate model with respect to parent amine concentration was used to estimate thermal degradation rates.

Tertiary amine pKa does not appear to influence thermal degradation rates of the tertiary amine; however, the structure of the tertiary amine does appear to have a strong effect on thermal degradation. S_N2 attack of hydroxyethyl groups is the slowest, followed by ethyl groups and then by methyl groups in PZ-activated tertiary amine solvents. Intermediate secondary amine breakdown products of the tertiary amine can rapidly react with the amine activator and accelerate the loss of the activator if the breakdown product contains a hydroxyethyl functional group.

At 150 $^{\circ}$C and with an initial concentration of 5 m tertiary amine/5 m PZ, thermal degradation was quantified for the following amines: TEA (5.81E-4 1/h), MDEA (1.17E-3 1/h), EDEA (7.15E-4 1/h), DMAE (1.50E-3 1/h), DMAP (8.63E-4 1/h), DMAB (8.08E-3 1/h), DMAEE (1.22E-3 1/h). PZ has a higher thermal degradation rate (50–150%) than the tertiary amines in PZ-activated solutions containing DEA, DMAE, MDEA, EDEA, and DEAE, suggesting that reactive intermediate degradation products are responsible for the loss of PZ. However, PZ loss is nearly identical in magnitude to the tertiary amine loss in PZ-activated DMAP and DMAEE, suggesting that the intermediate breakdown product is relatively stable.

HMDA and BAE have thermal degradation rates of about a quarter and a half, respectively, of PZ when used to activate MDEA. HMDA and BAE also have higher rates of thermal

degradation than MDEA, suggesting that the reactive intermediates of thermal degradation degrade the activator. PZ-activated DMAB has a loss rate about an order of magnitude greater than other tertiary amines, suggesting that another reaction mechanism is responsible for degradation in addition to S_N2 substitution.

Introduction and Motivation

Brief Literature Review

Activated tertiary amine solvents find extensive use in removing acid gases from natural gas and synthesis gas sources; they also offer competitive energy performance compared to concentrated PZ when used to capture CO_2 from coal-derived flue gas. The work presented in this report will focus on understanding the thermal degradation characteristics of activated-tertiary amine solvents as functions of tertiary amine structure and activator type. Stable tertiary amine solvent blends could serve as drop-in replacements for MDEA/PZ in natural gas or synthesis gas treating applications especially if the acid gas is to be sequestered and used for EOR purposes.

Literature studies suggest that tertiary amines and activated tertiary amines degrade via an S_N2 pathway (Namjoshi, 2012). A free nitrogen on either the amine activator or the tertiary amine can attack a protonated tertiary amine. This scheme is presented in Figure 1.
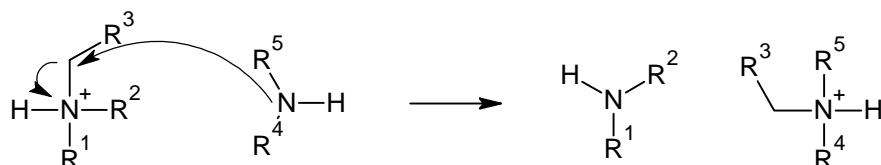
Figure 1: Thermal degradation in tertiary amine solvents is initiated by S_N2-type mechanisms where a free amino group attacks a substituent group on a protonated tertiary amine.

Byproducts of the initial thermal degradation step include a secondary amine and, depending on the attacking species, either a secondary amine, tertiary amine, or quaternary amine. These intermediate breakdown products can be reactive intermediates: tertiary and quaternary amines can undergo S_N2 substitution reactions, and secondary amines capable of forming oxazolidinones can react rapidly with either a secondary or primary amine, which includes the parent amine activator used in the tertiary amine blends. An example of the amine-oxazolidinone reaction is presented in Figures 2 and 3; this reaction is generally similar to the amine synthesis reactions presented in the first and second quarter (Rochelle, 2012).
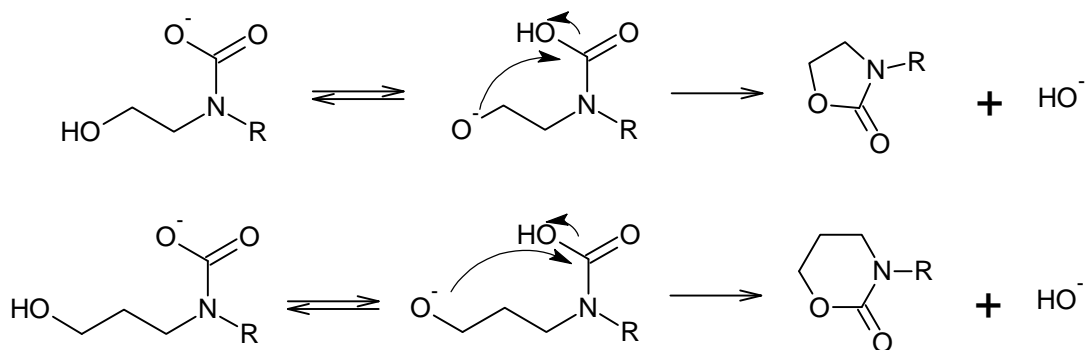
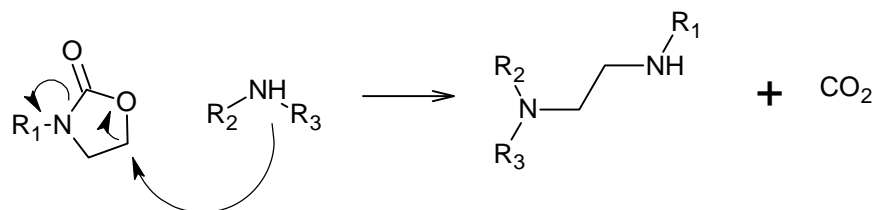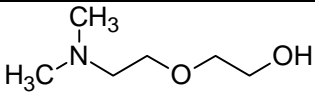**Figure 2: Scheme showing oxazolidinone formation via primary and secondary amine carbamates.**
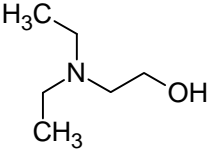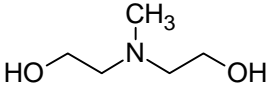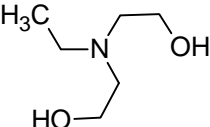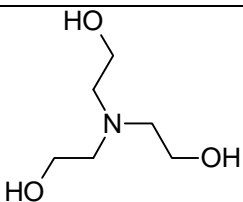

Figure 3: Scheme showing reaction between a free primary or secondary amine and an oxazolidinone to form substituted polyamines.

Amines Tested

Table 1 lists the amines that were tested for this study.

Table 1: List of amines (names, structure, abbreviated names) tested this quarter

Amine Name	Abbreviation	Structure	Role
Piperazine	PZ		Activator
Hexamethylenediamine	HMDA		Activator
2-(2-Aminoethoxy)ethylamine	BAE		Activator
Dimethylaminoethanol	DMAE		Tertiary Amine
Dimethylaminopropanol	DMAP		Tertiary Amine
Dimethylaminobutanol	DMAB		Tertiary Amine

2-[2-(Dimethylamino)ethoxy]ethanol	DMAEE		Tertiary Amine
Diethylaminoethanol	DEAE		Tertiary Amine
Methyldiethanolamine	MDEA		Tertiary Amine
Ethyldiethanolamine	EDEA		Tertiary Amine
Triethanolamine	TEA		Tertiary Amine

Experimental Methods

Samples were prepared gravimetrically. CO_2 was sparged into the solution and measured gravimetrically. Approximately 4 ml of loaded amine solution was placed in 3/8" Swagelok® stainless steel cylinders with a 4.5 ml capacity. The cylinders were sealed and placed in forced convection ovens at set temperatures and removed periodically for analysis. Cation chromatography (Dionex ICS-2100) was used to analyze for parent amine and degradation byproduct; the separation was carried out using a Dionex CS17 column. These methods are described in previous quarterly reports and dissertations (Freeman, 2011) and will not be described in detail here.

All amine solvents were prepared with identical starting concentrations: 5 m tertiary amine/5 m activator with an initial CO_2 loading of 0.225 mol CO_2/mol alkalinity.

Safety Aspects

The existing half-inch Swagelok® stainless steel cylinders previously used for thermal degradation work (including synthesis and nitrosamine studies) have now been retired; 3/8" Swagelok® stainless steel cylinders are exclusively being used. The 3/8" cylinders have given excellent service with no failures over hundreds of analyzed samples. Cylinders will be proactively retired after 10 uses.
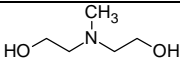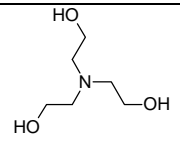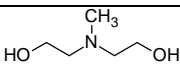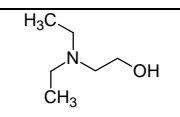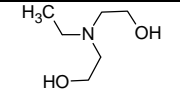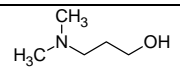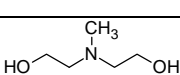
Results & Analysis

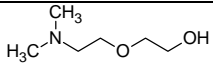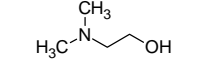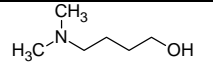### First-Order Rate Models and Arrhenius Temperature Dependency

First-order rate models with respect to parent amine concentration were used to estimate thermal degradation rates. These models match the experimental data well and the results from these models can be used to correlate effects of structure and other properties with the rate of degradation. The Arrhenius relationship was used to estimate the activation energy of thermal degradation.

Results Summary

Table 2 summarizes the thermal degradation results for the various amines tested. Figures 4 through 8 summarize the data graphically and correlate thermal degradation with structure and pKa.

Table 2: Thermal degradation of various amines tested at initial concentrations of 5 m Activator/5 m tertiary amine at an initial loading of 0.225 mol CO_2/mol alkalinity

Tertiary Amine/ Activator	Tertiary amine structure	Tert Am. pKa	T (^{o}C)	Degradation k_1 (hr^{-1})		Activation energy (kJ/mol)	
				Tertiary Amine	PZ	Tertiary Amine	Acti-vator
MDEA/HMDA		8.5	150	2.93E-4	7.01E-4		
TEA/PZ		7.8	175	1.16E-2	2.37E-2	168	189
			150	5.81E-4	9.95E-4		
			135	1.45E-4	1.66E-4		
MDEA/BAE		8.5	150	6.22E-4	1.08E-3		
DEAE/PZ		10.0	175	7.98E-3	1.05E-2	158	153
			150	6.56E-4	9.27E-4		
EDEA/PZ		8.7	150	7.15E-4	1.2E-3		
DMAP/PZ			175	7.64E-3	8.91E-3	138	142
			150	8.63E-4	9.30E-4		
MDEA/PZ		8.5	175	1.03E-2	2.48E-2	137	139

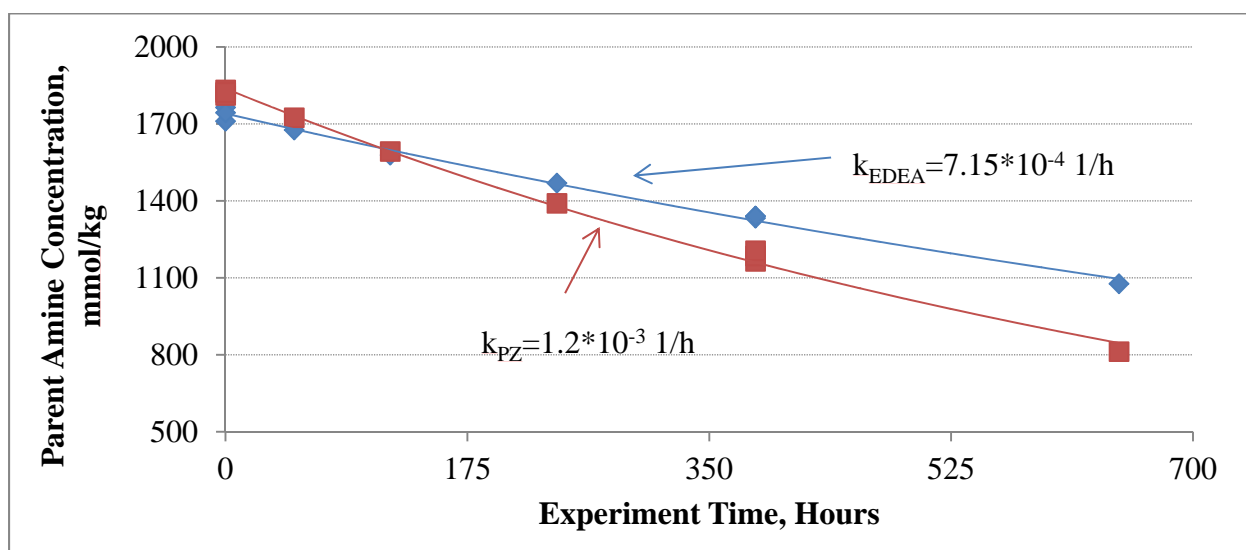|			150	1.17E-3	2.76E-3		
			135	2.61E-4	6.33E-4		
DMAEE/PZ	(structure)		150	1.22E-3	1.09E-3		
DMAE/PZ	(structure)	9.4	175	1.13E-2	1.70E-2	127	129
			150	1.50E-3	2.22E-3		
			135	3.23E-4	6.16E-4		
DMAB/PZ	(structure)		150	8.08E-3	5.48E-3		

Figure 4: Thermal degradation of 5 m PZ/5 m EDEA at 150 °C with an initial loading of 0.225 mol CO_2/mol alkalinity, showing that first-order kinetics can accurately model thermal degradation.

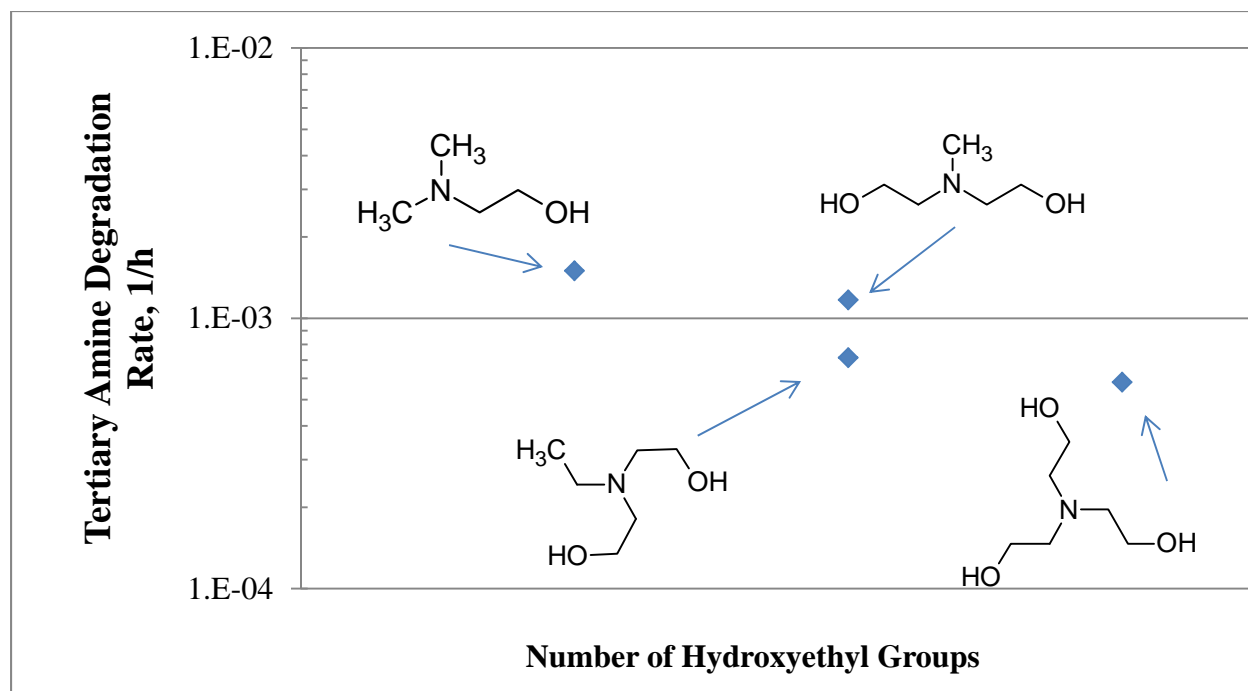In the figure: $k_{EDEA}=7.15*10^{-4}$ 1/h and $k_{PZ}=1.2*10^{-3}$ 1/h.

Figure 5: Comparison of thermal degradation of tertiary ethanolamines as a function of structure, demonstrating that methyl groups are preferentially attacked over ethyl and hydroxyethyl groups. Conditions: 5 m PZ/5 m tertiary amine, 150 $^{\circ}$C, initial loading of 0.225 mol CO_2/mol alkalinity
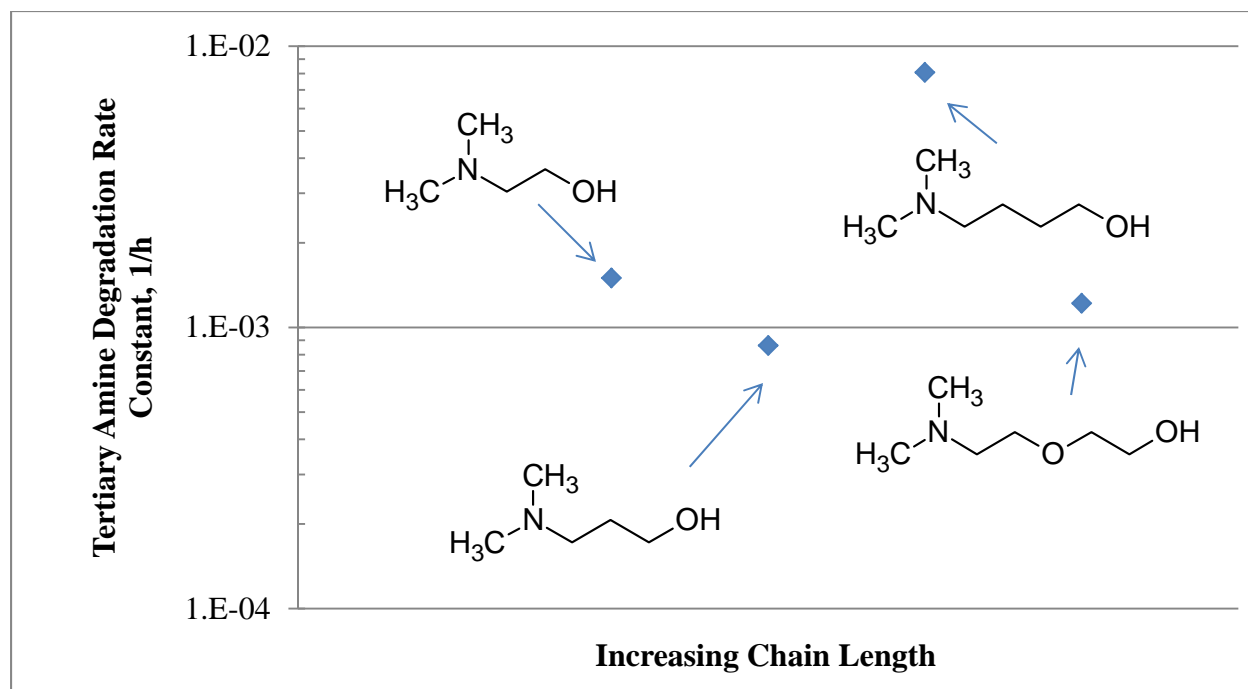
Figure 6: Comparison of thermal degradation of tertiary dimethylamines as a function of structure, demonstrating that DMAB degrades via another mechanism. Conditions: 5 m PZ/5 m tertiary amine, 150 $^{\circ}$C, initial loading of 0.225 mol CO_2/mol alkalinity.
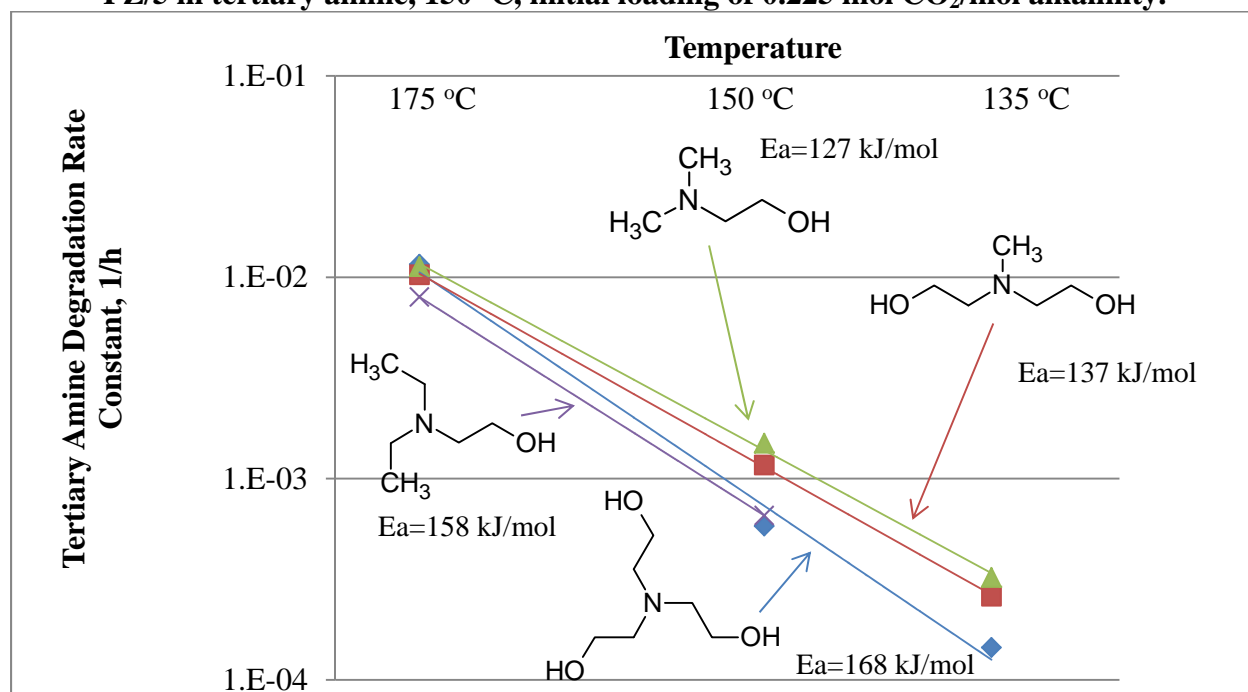

Figure 7: Comparison of thermal degradation activation energy of activated tertiary amines as a function of structure, demonstrating that activation energy increases as degradation rate decreases. Conditions: 5 m PZ/5 m Tertiary Amine, initial loading of 0.225 mol CO_2/mol alkalinity.
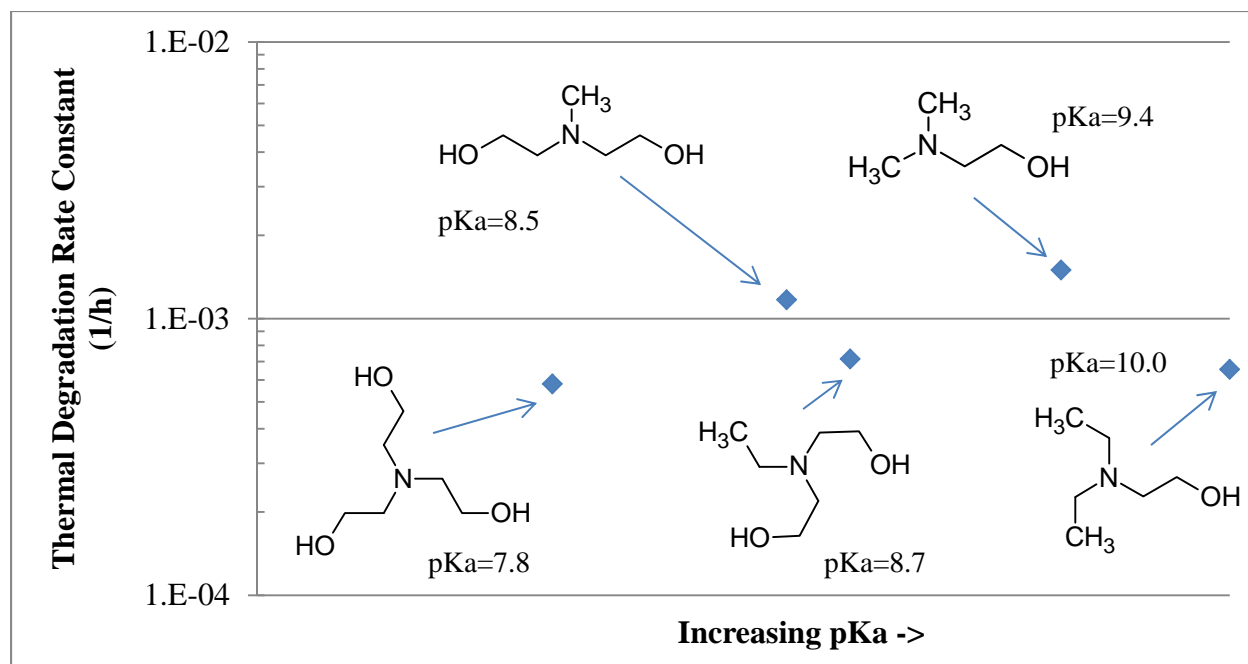
Figure 8: Comparison of thermal degradation of tertiary amines as a function of pKa, demonstrating that degradation is a strong function of structure and not correlated with pKa. Conditions: 5 m PZ/5 m tertiary amine, 150 $^{\circ}$C, initial loading of 0.225 mol CO_2/mol alkalinity.

Role of Structure on Activation Energy and Thermal Degradation Rate

Methyl Groups versus Ethyl Groups versus Hydroxyethyl Groups. Tertiary amines with ethyl groups and no methyl groups, such as DEAE and EDEA, have lower thermal degradation rates and appear to have higher activation energies relative to tertiary amines with methyl groups and no ethyl groups, such as DMAE, DMAP, and MDEA. TEA, which only has hydroxyethyl groups, has a significantly higher activation energy of thermal degradation when compared to DMAE, DMAP, and MDEA.

Tertiary amine activators. Both HMDA and BAE had lower rates of degradation compared to PZ when used to activate MDEA. Both HMDA and BAE have higher pKa values than PZ; therefore, tertiary amines activated with either HMDA or BAE will have higher concentrations of activator in the protonated and carbamate forms and a reduced concentration of the protonated tertiary amine relative to MDEA activated by PZ. This might result in the lower rate of thermal degradation as it is initiated by S_N2 attack of protonated tertiary amine by a free amine.
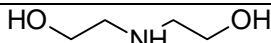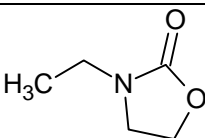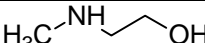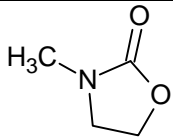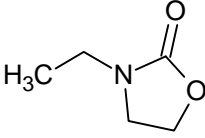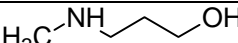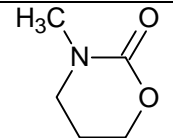
Relationship of Thermal Degradation Rates with Tertiary Amine pKa. Activated tertiary amine solvents consisting of a tertiary amine with a high pKa value will have a higher concentration of protonated tertiary amine relative to an activated tertiary amine solvent consisting of a low pKa tertiary amine; in the absence of structural effects, high pKa tertiary amines would degrade more quickly than low pKa tertiary amines. This was not observed to be the case in PZ-activated tertiary amine solvents: EDEA, which has a pKa of 8.7, and DEAE, which has a pKa of 9.9, degrade more slowly than MDEA, which has a pKa of 8.5.

9

Role of Structure of Intermediate Breakdown Products: Autocatalytic Degradation

Any tertiary amine with a hydroxyethyl or hydroxypropyl functional group(s) will likely form an oxazolidinone-forming amine as its initial secondary amine byproduct. The oxazolidinone formed from this amine can then rapidly react with other primary or secondary amines, which includes the tertiary amine activator. This can lead to increased amine loss rate of the activator relative to the tertiary amine.

The initial thermal degradation byproducts of PZ-activated MDEA, DMAE, and DEAE solvents include diethylaminoethanol (DEA), methylaminoethanol (MAE), and ethylaminoethanol (EAE), respectively; 1MPZ was formed as the byproduct. DEA is also suspected to be an intermediate byproduct of activated TEA. The structures of these amines are shown in Table 3. These secondary amine byproducts have at least one hydroxyethyl substituent group. The concentrations of these secondary amines appeared to be constant throughout the run, suggesting that they are reactive intermediates in thermal degradation. The initial thermal degradation byproduct of activated DMAP includes methylaminopropanol (MAP), which appears to accumulate throughout the degradation run at 150 ^{o}C. These data are shown in Figure 4.

Table 3: List of Intermediate Thermal Degradation Products in Activated Tertiary Amine Degradation

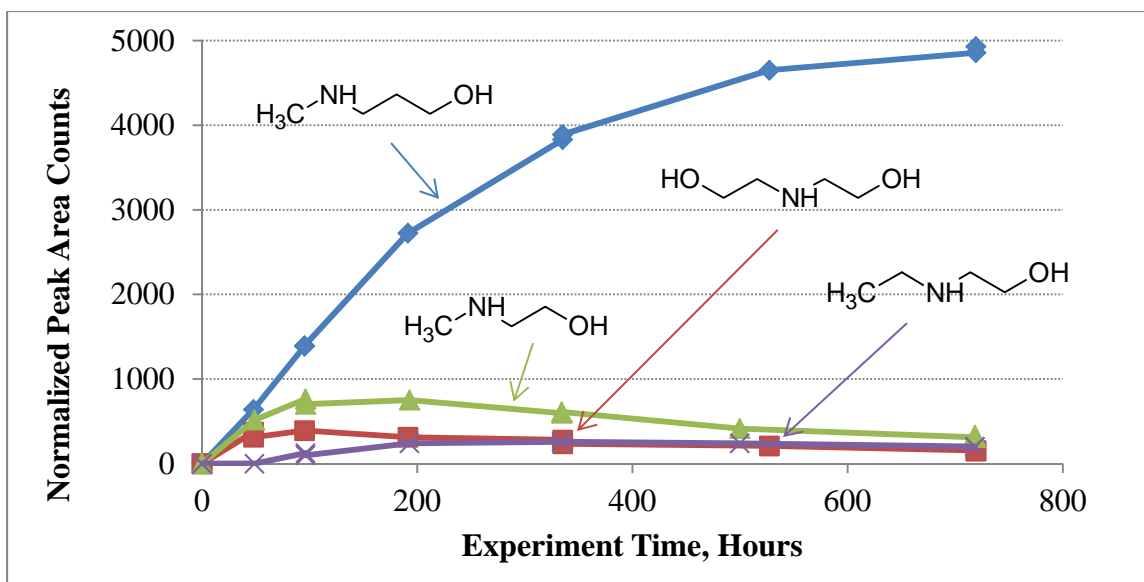| Amine Name	Abbreviation	Amine Structure	Amine Oxazolidinone Structure	Parent Tertiary Amine
Diethanolamine	DEA			MDEA, TEA
Methylaminoethanol	MAE			MDEA, DMAE
Ethylaminoethanol	EAE			DEAE
Methylaminopropanol	MAP			DMAP

Figure 4: Plot of normalized (by dilution factor) area of intermediate degradation products seen in PZ-activated DMAP, MDEA, DMAE, and DEAE degradation. MAE, EAE, and DEA are reactive intermediates whereas MAP is not.

PZ degradation rates are 50–150% greater than the tertiary amine in activated MDEA, DMAE, DEAE, and TEA blends; similar behavior was observed in HMDA- and BAE-activated MDEA. In contrast, the PZ degradation rate is about 10% greater than the tertiary amine degradation rate in the activated DMAP blend. The discrepancy in rates suggests that the oxazolidinone-forming amine intermediate in activated MDEA, DMAE, DEAE, and TEA solvents rapidly reacts with the amine activator. Similar phenomena were observed in the amine synthesis experiments, where it was found that oxazolidinone-forming primary amines with hindered hydroxyethyl groups (e.g., AMP or MIPA) or with hydroxypropyl substituent groups reacted with PZ at 25% the rate of MEA, which has an unhindered hydroxyethyl substituent group (Rochelle, 2011).

Alternate Thermal Degradation Pathways – Tertiary Amine Hydrolysis

DMAB activated by PZ was observed to thermally degrade at a rate approximately an order of magnitude greater than other tertiary amines at 150 $^\circ$C. The rate of PZ degradation is less than DMAB. It is postulated that this behavior is due to the hydrolysis of free DMAB, producing an unstable quaternary amine with a five-membered hetrocyclic backbone. This quaternary amine can, like the protonated DMAB, be attacked by the parent amines present in the solvent. This mechanism is shown in Figure 5.
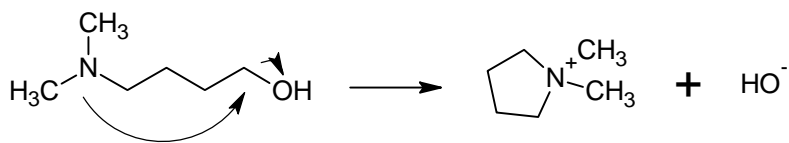

Figure 5: Hydrolysis of DMAB, forming water and a quaternary amine

Like DMAB, DMAEE could also undergo a hydrolysis step, forming a quaternary amine. However, PZ-activated DMAEE degradation rates were comparable in magnitude to other

11

tertiary amines such as DMAP and MDEA, and it is likely that the rates of amine hydrolysis are significantly slower than via a S_N2 pathway for DMAEE. Raw chromatography data also suggested that methylaminoethoxyethanol accumulated in degraded samples, which is identical to the behavior observed in PZ-activated DMAP degradation.

In primary diamine degradation it was observed that 1,4-diaminobutane (DAB) degrades about an order of magnitude faster than BAE; these amines have analogous structures to DMAB and DMAEE, respectively. DAB degrades by a ring closing mechanism to form pyrrolidine. The ratio of thermal degradation rates of DAB and BAE is roughly similar to the ratio of thermal degradation rates of DMAB and DMAEE (Namjoshi 2013).

Conclusions

1. At 150 ^{o}C and with an initial concentration of 5 m tertiary amine/5 m PZ, thermal degradation was quantified for the following amines: TEA (5.81E-4 1/h), MDEA (1.17E-3 1/h), EDEA (7.15E-4 1/h), DMAE (1.50E-3 1/h), DMAP (8.63E-4 1/h), DMAB (8.08E-3 1/h), DMAEE (1.22E-3 1/h)
2. PZ has a higher thermal degradation rate (50–150%) than the tertiary amines in PZ-activated solutions containing DEA, DMAE, MDEA, EDEA, and DEAE, suggesting that reactive intermediate degradation products are responsible for the loss of PZ.
3. PZ loss is nearly identical in magnitude to the tertiary amine loss in PZ-activated DMAP and DMAEE, suggesting that the intermediate breakdown product is relatively stable.
4. HMDA and BAE have thermal degradation rates of about a quarter and about a half, respectively, of PZ when used to activate MDEA. HMDA and BAE also have higher rates of thermal degradation than MDEA, suggesting that the reactive intermediates of thermal degradation degrade the activator.
5. PZ-activated DMAB has a loss rate about an order of magnitude greater than other tertiary amines, suggesting that another reaction mechanism is responsible for degradation in addition to S_N2 substitution.
6. Tertiary amine pKa does not appear to influence thermal degradation rates of the tertiary amine.
7. The structure of the tertiary amine appears to have a strong effect on thermal degradation. S_N2 attack of hydroxyethyl groups is the slowest, followed by ethyl groups and then by methyl groups in PZ-activated tertiary amine solvents.
8. Intermediate secondary amine breakdown products of the tertiary amine can rapidly react with the amine activator and accelerate the loss of the activator if the breakdown product contains a hydroxyethyl functional group.

References

Freeman SA. *Thermal Degradation and Oxidation of Aqueous Piperazine for Carbon Dioxide Capture.* The University of Texas at Austin. Ph.D. Dissertation. 2011.

Namjoshi O. *Thermal Degradation of Activated Tertiary Amine Solvents for Carbon Capture and Gas Treating Applications.* The University of Texas at Austin. PhD. Proposal. 2012.

Namjoshi O, Le L, Du Y, Rochelle GT. Thermal degradation of piperazine blends with diamines. Presented at *GHGT-11.* Kyoto, Japan, November 18-22, 2012.

Rochelle GT et al. "CO_2 Capture by Aqueous Absorption, Second Quarterly Progress Report 2012." Luminant Carbon Management Program. The University of Texas at Austin. 2012.

Oxidation of Amines with High Temperature Cycling

Abstract

Screening of CO_2 capture amine solvents for oxidative stability was carried out by cycling the amine to stripper temperatures in the presence of dissolved oxygen (DO). Performance of each amine solvent was assessed using four metrics: amine loss, DO uptake, ammonia production, and total formate production. To cycling systems, the integrated solvent degradation apparatus (ISDA) and high temperature cycling system (HTCS) were used in this evaluation.

Oxidative stability was found to be in the order: 2-amino-2-methyl-1-propanol (AMP) > (PZ) and PZ+2-methyl-piperazine (2MPZ) > methyl-diethanolamine (MDEA) and MDEA+PZ > monoethanolamine (MEA). MEA is the only amine susceptible to oxidation at low temperature; these results provide differentiation among the other oxidatively stable amines.

These four indicators of amine oxidation showed good agreement, with the exception of MDEA. MDEA, MDEA+PZ, and MEA showed similar levels of total formate production and amine loss in the ISDA, however DO uptake in the ISDA and amine loss in the HTCS were both higher for MEA. No ammonia production was observed from MDEA, however formaldehyde and acetaldehyde were observed in the gas phase.

Introduction

Low temperature oxidation occurs in the absorber as a result of oxygen in the flue gas. Previous studies have shown that a variety of amines are stable to oxidation at low temperature. These include all tertiary amines, many six-membered ring amines, and some hindered amines (Table 1)

Table 1: Summary of amine oxidation screening work at low temperature

Evidence of significant oxidation at absorber conditions	Ref.	Resistant to oxidation at absorber conditions	Ref.
Monoethanolamine	[5]	All tertiary amines	[1]
Ethylendiamine	[6]	Piperazine	[13]
1,2-diamino-propane	[6]	1-methyl-piperazine	[9]
Bis-aminoethyl-ether	[7]	2-methyl-piperazine	[7]
Diethanolamine	[5,8]	2-amino-2-methyl-1-propanol	[7]
Methyl-aminoethanol	[8]	3-amino-2-methyl-2-propanol	[1]
2-ethoxy-aminoethyl-ether	[9]	Aminoethyl morpholine	[1]
3-methylamino-1-propanol	[10]	3-amino-propanol	[12]
1-amino-2-propanol	[12]	Potassium β-alaninate	[12]
aminoethyl-piperazine	[7]	Potassium α-alaninate	[1]
Potassium taurinate	[9]	Potassium prolinate	[11]
Potasssium sarcosinate	[11]		
Potassium glycinate	[9]		
Potassium taurinate	[9]		

In a real system, the amine is cycled between the low temperature, aerobic environment of the absorber, and the high temperature, anaerobic environment of the stripper. Very little work has studied amine oxidation with representative high temperature cycling. In cycling systems, oxygen dissolves into the solution in the absorber, and reacts in the high temperature zone. In an absorber/stripper system, dissolved oxygen is removed from the solvent when it enters the stripper.

Closmann (2011) conducted high temperature oxidation of MDEA, PZ, and MDEA+PZ in a cycling apparatus up to 125 ºC. The results indicated that the amount of degradation increased when the amine was cycled to higher temperatures, and that PZ was more stable than MDEA to high temperature oxidation. Closmann concluded that the kinetics of oxygen uptake were sufficiently slow to be a function of the high temperature, in other words only part of the dissolved oxygen was consumed with each pass, and the amount depended on the temperature of the system.

The objective of this work is to provide a more complete picture of degradation with high temperature cycling, in particular by testing more amines, at higher temperatures, and by measuring dissolved oxygen uptake.

Experimental Methods

Experimental Methods

High temperature oxidation was carried out in two cycling apparatuses. These were the high temperature cycling system (HTCS) and the integrated solvent degradation apparatus (ISDA). The HTCS used air in the oxidative reactor, had an operational pressure limit of 200 psig, and could analyze the gas phase for degradation products. The ISDA used oxygen in the oxidative reactor, had an operational pressure limit of 80 psig, and could analyze for dissolved oxygen.

Both apparatuses used a solvent circulation rate of 200 mL/min with a 350 mL hold-up in the oxidative reactor. These apparatuses have been described in greater detail previously (Voice, 2012).

Analytical Methods

Amine concentration and total formate were determined using cation and anion chromatography, respectively. Fourier-transform infrared spectroscopy was used for ammonia and aldehyde analysis in the gas phase. A Rosemount Analytical 499ADO was used for dissolved oxygen (DO) analysis in the liquid phase. The kinetics of DO uptake were determined by measuring the concentration of DO before and after the high temperature zone of the reactor. Further details of the analytical methods used in this method are discussed elsewhere.

- Cation chromatography (Davis, 2009)
- Anion chromatography (Sexton, 2008)
- FTIR (Voice, 2012)

Results

Formate production was measured in the ISDA for various amine solutions cycling from 55 to 120 °C. MDEA, MDEA+PZ, and MEA showed similar levels of formate production, whereas PZ and AMP showed resistance to oxidation. Of the solvents studied, AMP offered the most resistance at 120 °C (Figure 1).
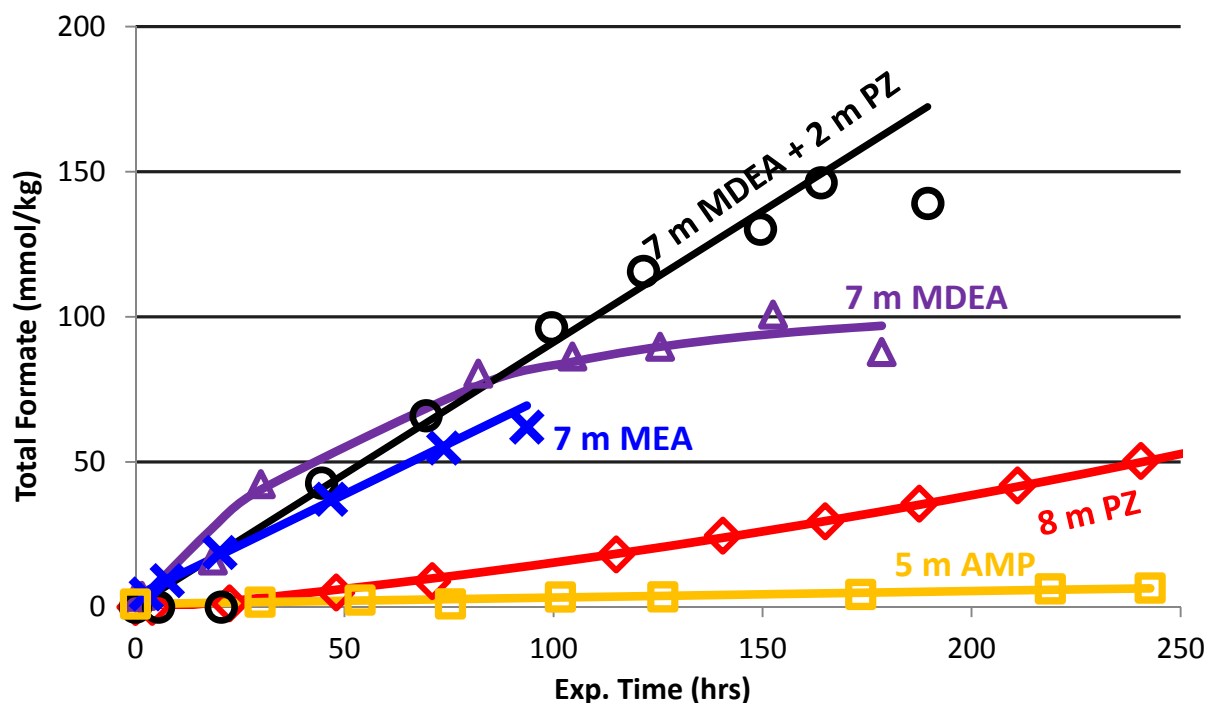
Figure 1: Formate production in amine solutions in the ISDA. Cycling from 55 °C to 120 °C at 200 mL/min with 0.4 mM Fe, 0.1 mM Ni, and 0.05 mM Cr. Agitation at 1400 RPM in the oxidative reactor.

3

Dissolved oxygen uptake was measured in the ISDA. Uptake was fastest in 7 m MEA and slowest in AMP (Figure 2). These data agree with data showing relative amine stability in the presence of oxygen both at high and low temperature using other indicators (ammonia production, formate production, and amine loss).
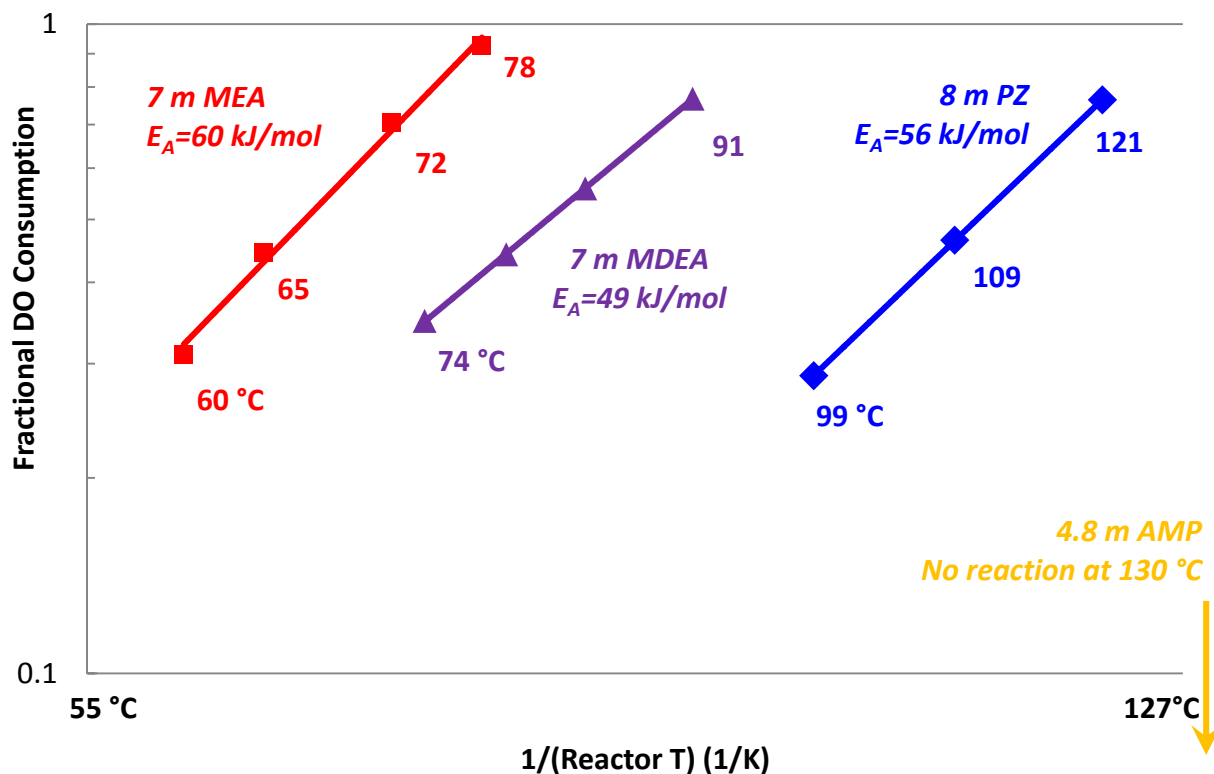
Figure 2: Dissolved oxygen uptake for amine solutions in the ISDA. Conditions: oxidative reactor at 40 °C, 200 mL/min circulation rate, 0.13 L hold-up at high temperature.
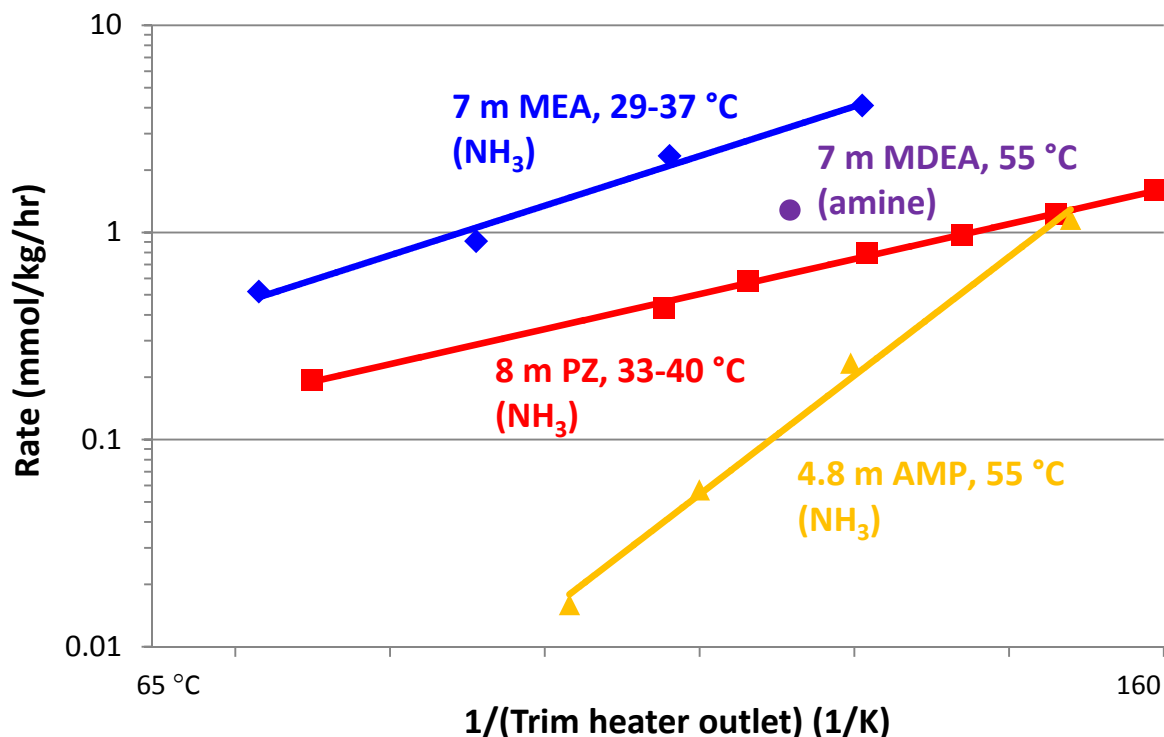
Figure 3: Ammonia production and amine loss rates for various amines in the HTCS. Ammonia rates were determined at steady state for each temperature. The temperature of the oxidation reactor is shown for each amine. Circulation at 200 mL/min in the presence of Fe, Mn, Ni, Cr. Oxidation reactor with air and 1% CO_2 (AMP), 0.5% CO_2 (PZ, 4/4blend, MEA), or 2% CO_2 (MDEA).

Oxidation of amines in the HTCS was estimated at various trim heater temperatures using ammonia production as an indicator of oxidation (Figure 3). Amine loss rates were measured for PZ, AMP, and MDEA over a two-week period. NH_3 was a good indicator of oxidation for PZ. AMP has the highest activation energy for oxidation. MDEA did not produce any ammonia, however formaldehyde and acetaldehyde were observed.

Oxidation of 4 m PZ + 4 m 2MPZ (4/4 blend) was a function of the oxidative reactor temperature (Figure 4). A temperature-controlled trim cooler was used with the 4/4 blend to tightly control the oxidative reactor temperature; this was not used with 8 m PZ.
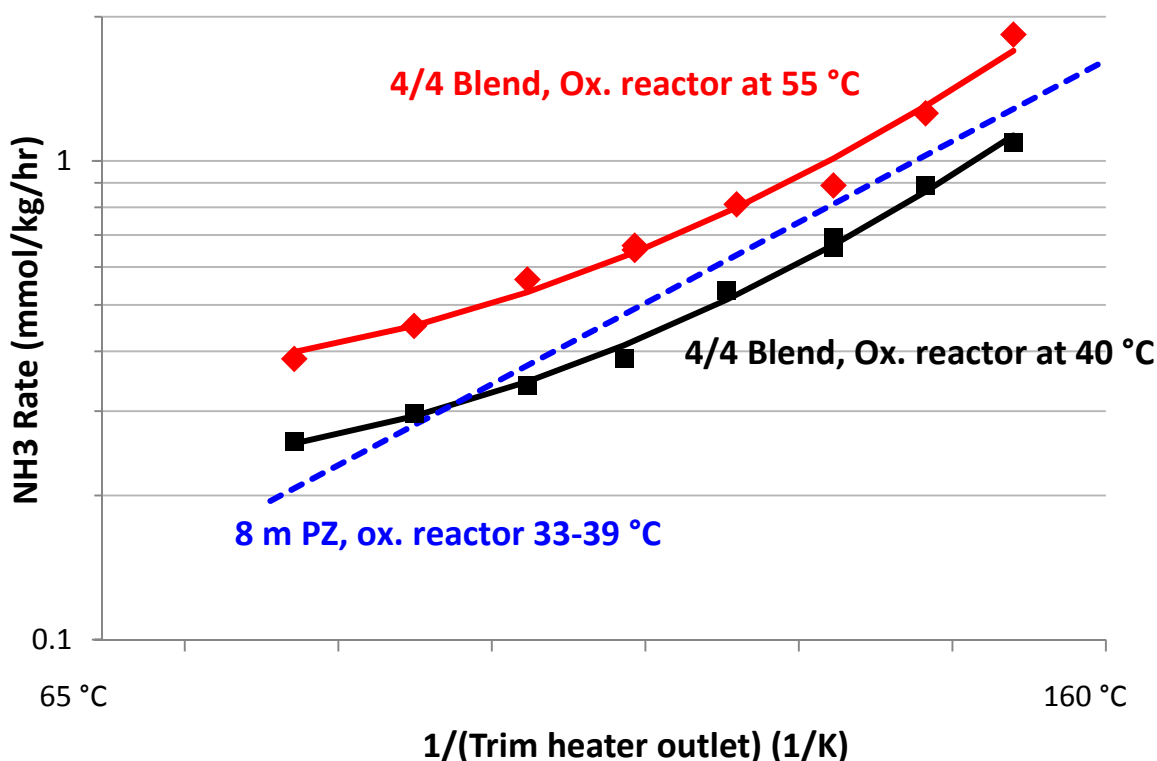
Figure 4: Oxidation of 4 m PZ + 4 m 2MPZ in the HTCS with the oxidation reactor at 40 or 55 °C. Circulation at 200 mL/min with 0.4 mM Fe, 0.1 mM Ni, 0.05 mM Cr, and 0.1 mM Mn. Oxidation reactor with 0.5% CO_2 in air.

A summary of amine oxidation screening experiments in the HTCS is shown below in Table 2. Amine loss was difficult to measure precisely due to small changes in concentration and convolution with water concentration. Ammonia production matched amine loss within the error of the measurement for PZ and the 4/4 blend. AMP had significantly greater amine loss than ammonia production.

Table 1: Summary of ammonia and amine loss rates for various amines degraded in the HTCS for two weeks in the presence of air

Solvent	Conditions: ox. Rxr. T (°C) / high T (°C), CO_2 (%)	Max NH_3 rate	Amine loss rate	Lost amine recovered as NH_3 at final (%)	NH_3 rate at 120 °C from regression (ox. Rxr. T.)	High T for 2% loss/wk (°C)
7 m MEA	30-36 / 120, 0.5 %	4.10	--	--	3.24 (~40)	75
7 m MDEA	55 / 120, 2 %	0	1.3 ± 0.3	0	1.28 (55)	--
8 m PZ	40 / 160, 0.5 %	1.86	1.3 ± 0.5	80	0.51 (35)	119
4 m PZ + 4 m 2MPZ	40 / 150, 0.5 %	1.59	1.5 ± 0.5	50	0.54 (40)	115
					0.80 (55)	95
4.8 m AMP	55 / 150, 1 %	1.17	10.7 ± 0.9	16	0.12 (55)	109

Other data for cycling experiments are shown below in Figures 5–8.
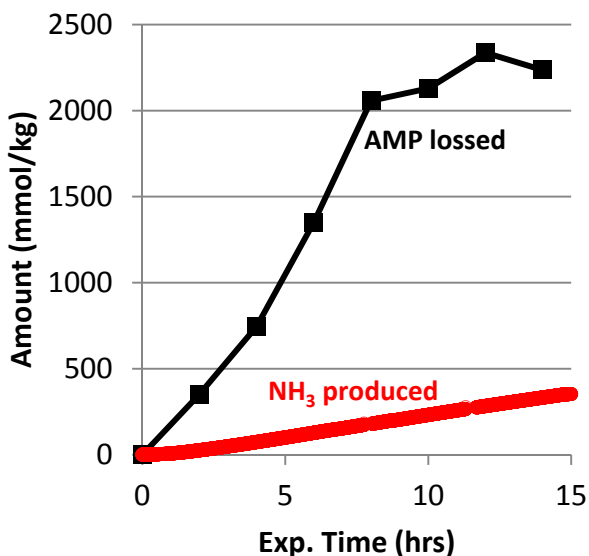
Figure 5: Amine loss and NH₃ production for 4.8 m AMP in the HTCS. Cycling from 55 to 150 °C at 200 mL/min with 0.4 mM Fe, 0.1 mM Ni, 0.05 mM Cr, 0.1 mM Mn. Oxidation reactor with 1% CO₂ in air.
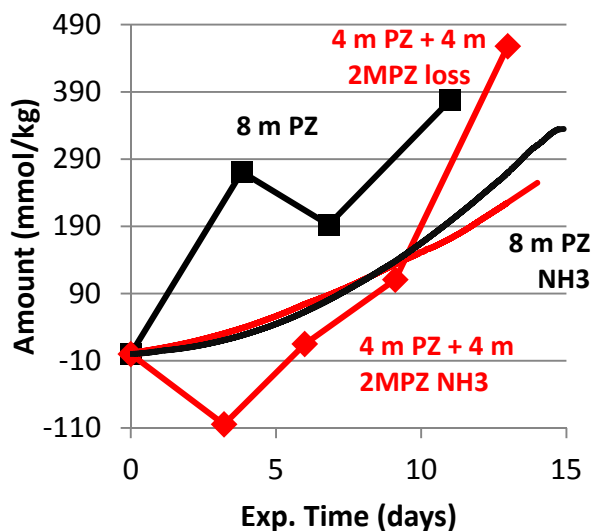
Figure 6: Amine loss and NH3 production for 8 m PZ and 4 m PZ + 4 m 2MPZ in the HTCS. Cycling from 40 to 150 °C (4/4blend) or 160 °C (PZ) at 200 mL/min with 0.4 mM Fe, 0.1 mM Ni, 0.05 mM Cr, 0.1 mM Mn. Oxidation reactor with 0.5 % CO₂.

Figure 7: Amine loss and alkalinity loss for 7 m MDEA in the HTCS and ISDA. Cycling from 55 to 120 °C at 200 mL/min with 0.4 mM Fe, 0.1 mM Ni, 0.05 mM Cr, 0.1 mM Mn (HTCS only). Oxidation reactor with 2% CO₂ in air (HTCS) or oxygen (ISDA)

Figure 8: Products formed from oxidation of 7 m MDEA in the HTCS. Cycling from 55 to 120 °C at 200 mL/min with 0.4 mM Fe, 0.1 mM Ni, 0.05 mM Cr, 0.1 mM Mn. Oxidation reactor with 2% CO₂ in air (HTCS).
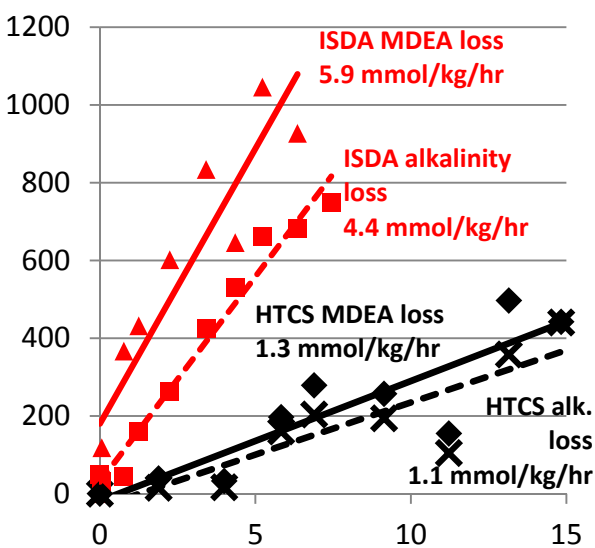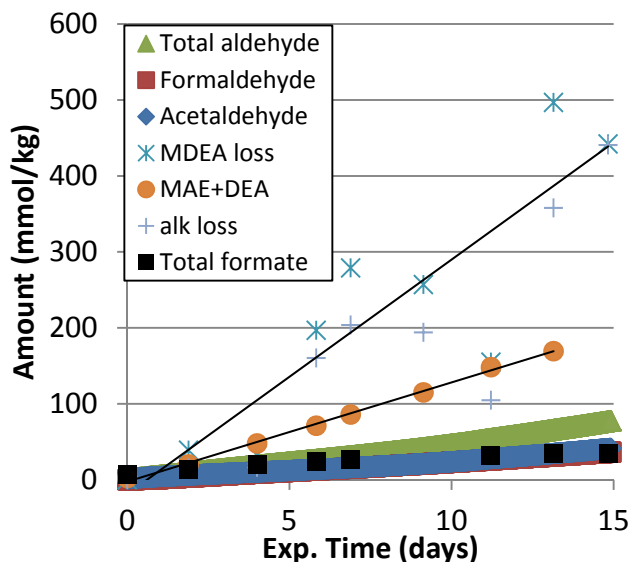
7

Discussion

Prior to this work, oxidation in cycling systems was thought to be caused by the presence of dissolved oxygen, which reacted in the high temperature part of the cycling system. In a real system, this would correspond to the cross exchanger and pipe leading to the top of the stripper prior to flashing off dissolved oxygen.

This work demonstrates that this explanation is too simple in several respects. First, the oxygen uptake measurements and HTCS data show that oxidation continues to increase with greater stripper temperatures beyond the point where all dissolved oxygen has been consumed. Second, the absolute oxidation rates are significantly higher than the rate of oxygen cycling, indicating that either the oxygen stoichiometry (moles oxygen consumed per mole amine degraded) is a function of temperature, or that other oxygen carriers are involved (e.g., oxidized metals, peroxides). Third, the oxidation rate increases with higher oxidative reactor temperatures. If oxidation were only occurring from dissolved oxygen, lower oxidation rates would be expected from higher oxidative reactor temperatures due to lower oxygen solubility. These results show that higher oxidative reactor temperatures act synergistically with high temperature cycling, increasing oxidation either by increasing the concentration of oxygen carriers, or because oxidation occurs both in the high and low temperature parts of the system only when the amine is cycling to high temperature.

Conclusions

Conclusions from this work are as follows

- All amines found to be stable to oxidation at low temperature oxidized at high temperatures. Amine stability was in the order of AMP > PZ = PZ+2MPZ > MDEA = MDEA+PZ >= MEA.
- Dissolved oxygen uptake can be used as an indicator of oxidative stability at high temperature.
- Oxidation continued after all dissolved oxygen was consumed; no plateau was observed for high temperature oxidation up to 160 °C.
- AMP was the most resistant to oxidation at 120 °C but increased most rapidly at higher temperatures
- Ammonia production can be used as an absolute indicator of oxidation for MEA, PZ, and 2MPZ, and as a relative indicator for AMP oxidation.
- Oxidized MDEA did not produce any gas phase ammonia; acetaldehyde and formaldehyde were produced.
- Oxidation of MDEA with high temperature cycling was first-order in oxygen concentration in the oxidative reactor
- Oxidation of 4 m PZ + 4 m 2MPZ increased with higher oxidative reactor temperatures

Future Work

A two-week experiment will be performed to determine the amount of MEA converted to ammonia during high temperature oxidation.

8

References

Closmann F. *Oxidation and thermal degradation of methyldiethanolamine/piperazine in CO$_2$ capture*. The University of Texas at Austin. Ph.D. Dissertation. 2011.

Davis, JD. *Thermal Degradation of Aqueous Amines Used for Carbon Dioxide Capture*. The University of Texas at Austin. Ph.D. Dissertation. 2009.

Sexton AJ. *Amine Oxidation in CO$_2$ Capture Processes*. The University of Texas at Austin. Ph.D. Dissertation. 2008.

Voice AK, Rochelle GT. "Oxidative degradation of amines with high temperature cycling." Accepted to *Energy Proc.* 2013.

Aerosol and Volatile Control in CO$_2$ Capture

Abstract

In this quarter, a concentric-tube particle growth column was designed in more detail. Droplet growth will be measured under varying operating conditions representative of CO$_2$ capture in an amine scrubbing system. The miniature absorber column will have an inner diameter of 1.5 inches with a packed height of up to 6 feet. The gas rate will vary from 25–125 LPM. The solvent rate will vary from 0.05–1.00 GPM corresponding to an L/G range of 6–30 mol/mol under all gas flow rates. A heating jacket along the length of the packed section using externally-circulated oil will maintain isothermal conditions (40 °C) during absorption and provide heat (80 °C) for stripping.

Seed particles will be generated by either salt nuclei from a Brechtel Manufacturing Inc. model 9200 Aerosol Generation System or by injecting vaporized H$_2$SO$_4$ using a syringe pump connected to a heated injection port. Particle count and size will be measured in-situ using a Phase Doppler Particle Analyzer (PDPA). Droplet content will also be measured using in-situ swirl-tubes and inertial impactors connected to an FTIR analyzer. The FTIR will quantify the content and composition of droplets not collected on the upstream gas-particle separators.

Goals for next quarter include continued design and construction of the aerosol growth chamber.

Introduction

Volatile emissions are a primary concern for CO$_2$ capture plants using amine scrubbers. Emissions constitute increased economic expense through solvent loss as well as being a source of potentially hazardous environmental pollutants. Compounds found in treated flue gas include contaminants from thermal degradation and oxidation as well as combustion byproducts. Degradation and reaction products have a wide range of toxicity and biodegradation characteristics which potentially represent unacceptable emissions; as a result, recent work has focused on estimating volatile losses and assessing their toxicological impact.

Volatile emissions can be reduced through the use of an absorber column using recycled water as a solvent, called a water wash. Design considerations for water wash systems include liquid distribution methods to adequately wet packing with low liquid rates, and balancing water in the absorber/stripper system by adjusting the total volatile concentration in the wash water. Water

wash columns have relatively flat efficiency profiles, meaning the removal efficiency is not a strong function of either the gas or liquid flow rates or the operating temperature.

Emissions with Aerosols

Recent pilot plant measurements have shown that normal water wash columns are ineffective at controlling volatile loss of amine and other pollutants due to the presence of aerosols. In 2011, MHI presented pilot test results for both KS-1[TM] and MEA which showed that emissions were proportional to inlet SO_3 concentration (MHI, 2012). Amine levels out of the wash section were 0.4–23.2 ppmv and 0.8–67.5 ppmv for KS-1[TM] and MEA, respectively, for 0–3 ppmv inlet SO_3. Aerosols were visually present at the direct contact cooler (DCC) and wash outlets. At the Maasvlakte pilot plant, TNO and SINTEF jointly tested a 30 wt % MEA CO_2 capture unit with a downstream water wash complete with online gas and aerosol phase sampling (TNO, 2012; SINTEF, 2012). Excessive emissions were observed; aerosols, not physical entrainment, were responsible for the increase. Lithium and rubidium carbonate (Li_2CO_3, Rb_2CO_3) tracers in the solvent and wash loops verified negligible entrainment. A Brownian demister unit (BDU) was installed downstream of the wash section which reduced emissions to previously simulated levels, indicating the bulk of emissions were contained in the droplet phase. Mean droplet diameters (d_{Drop}) were measured using light extinction coefficients and ranged between 0.76 and 7.88 μm at the BDU inlet and 0.2–1.74 μm at the outlet. The quality of the inlet flue gas and the absolute temperature of the absorber influenced the emission rate. More recently, a baseline study using MEA at the National Carbon Capture Center (NCCC) in Wilsonville, Alabama saw higher amine emissions than expected (NCCC, 2012). The number of absorber beds (2–3), intercoolers (0–2), and inlet SO_3 concentration (1.8 and 3.2 ppmv) were varied as part of a parametric test on emission rate. Their work concluded that carry-over was proportional to inlet SO_3 and also to the concentration of MEA in the wash water. Emissions were inversely related to absorber temperature. In all studies, aerosols increased emissions roughly 1–2 orders of magnitude.

It is clear from pilot plant observations and emission studies that removing aerosols is a key part of reducing possible releases from amine-based CO_2 capture plants. The failure of conventional wash columns and the potential financial impact of particle collectors necessitate fundamental research to identify more practical means of controlling emissions for large scale processes. Understanding interconnectivities of the bulk CO_2 removal process operating conditions and aerosol dynamics can provide the necessary insight required to either design or operate a system with the intention of suppressing droplet growth; or conversely, to condition aerosols for easier removal.

Aerosol Column Experiment

Designing equipment for particle removal requires proper characterization of the inlet size distribution; however, existing data for droplet sizes out of CO_2 absorber columns is limited. The only direct measurement of droplet diameters is the TNO/SINTEF project at the Maasvlakte power plant (TNO, 2012; SINTEF, 2012). In that study, the mean particle diameter at the inlet and exit of the BDU was calculated using light extinction coefficients from in-situ fog analyzers and mass balance data from collected condensate in the BDU catch. Nearly all aerosolized amine was removed in the BDU indicating that the majority of particles were above the cut-diameter (90% removal for < 1 μm) of the filter element. Additional experimental measurement

2

and modeling are required to determine the proper design and placement of mitigation equipment such that cost and impact on the CO_2 capture system is minimized.

An aerosol growth model has been utilized to investigate mechanisms of droplet growth for aqueous, amine-laden particles in CO_2 absorption columns fitted with downstream wash towers. However, transport processes described therein are complicated and assumptions must be made to allow numerical approximation. The relative length scales of transfer processes for aerosols and bulk absorption differ by several orders of magnitude. Further, transport of various components is thought to occur according to certain limitations, i.e., H_2O and PZ are gas-film controlled whereas CO_2 is controlled by reaction kinetics; it is unclear if these assumptions hold for a spherical system with fast moving boundary. The stiffness of the current formulation of the differential processes combined with narrow working ranges of correlations used to describe thermodynamics makes simulations of submicron particles intractable. Results from particle simulations may be extrapolated down to the submicron region; however, potential error is likely because of continuum-kinetic length-scale effects and other modeling assumptions. Due to modeling uncertainties, experimental measurement to validate or further refine the aerosol model is warranted.

Column Design

A concentric-tube, glass-jacketed column has been designed to measure particle growth exposed to varying gas compositions characteristic of an absorber or water wash. The chamber will contain up to 6 ft of packing inside a 1.5" inner diameter glass-jacketed tube. The column can accommodate random (>315 m^2/m^3) and structured (500 m^2/m^3) packing. The packing approximates gas-side mass transfer present in large scale absorber columns. Oil will be circulated in the tubing annulus to maintain isothermal conditions. Aerosols from a La-Mer-Sinclair-type generation system will be injected into a carrier gas (25–125 LPM) introduced at the bottom of the packing. A spray nozzle at the column top will bring in solvent (0.05–1.00 GPM) which will counter-currently contact the aerosol laden gas. CO_2 can be removed up to 90% under high L/G conditions. A large L/G will also prevent temperature bulging. The gas phase composition inside the packed section will be controlled by the circulating solvent composition and an upstream gas mixer with mass flow controllers. Figure 1 shows a simplified process flow diagram for the aerosol growth experiment.

Aerosol Generation

Aerosols will be generated in a Brechtel Manufacturing Inc. (BMI) model 9200 Aerosol Generation System by atomizing a liquid solution containing latex spheres or dissolved salt delivered by a syringe pump into a high pressure gas stream. Particle count is controlled by the syringe speed. Atomized material is sent to a drying chamber where solvent is vaporized leaving behind only dissolved substance. Use of Polystyrene Latex (PSL) spheres or other dimensionally uniform objects allows creation of mono-disperse particulate. Aqueous aerosols can also be generated; however, controlling the distribution breadth is more difficult.

Aerosols will also be generated by injecting vaporized H_2SO_4 into the gas stream using a syringe pump. The H_2SO_4 will recondense in the gas to form small nuclei, similar to those found in FGD scrubbers. The acid delivery system will be a scaled version of the apparatus used to calibrate liquid components on the FTIR system described in Sexton (2008).

Particle concentration will be low enough to avoid coagulation and Brownian collection.
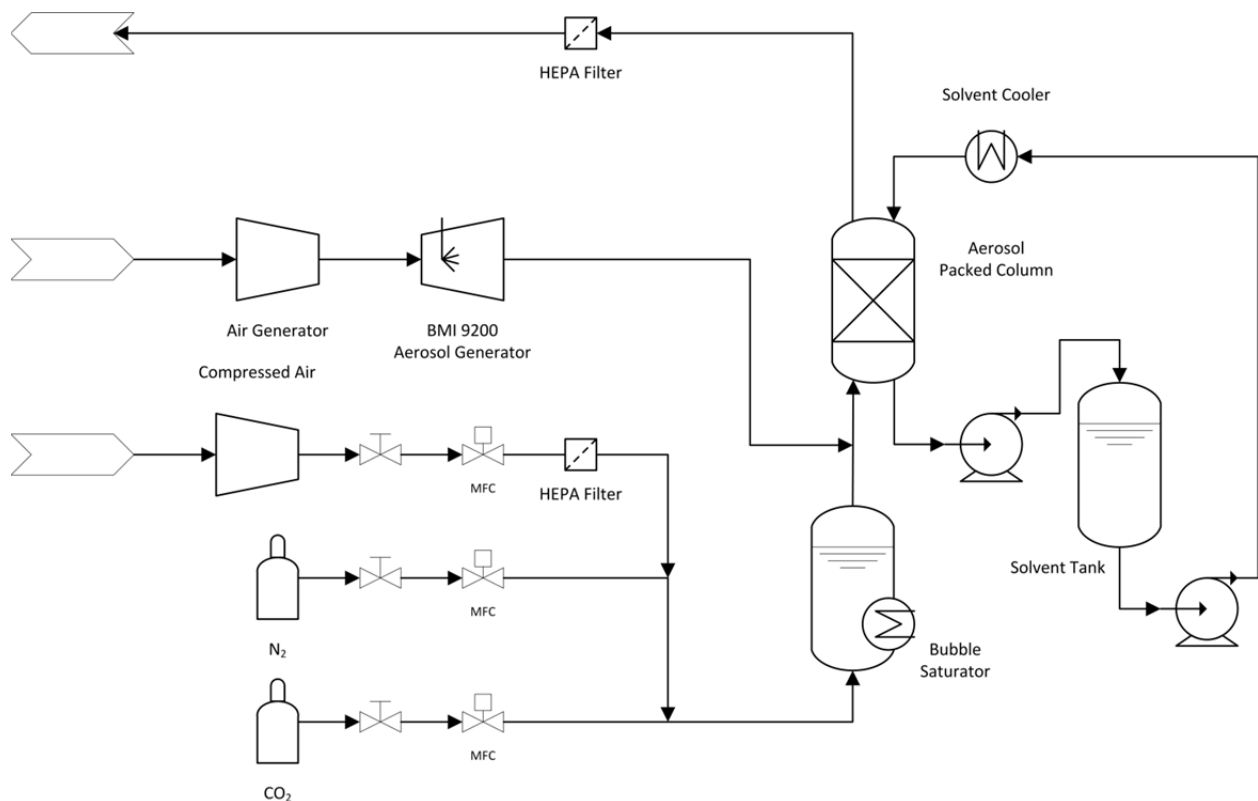
Figure 1: Aerosol growth experiment process flow diagram

Aerosol Analysis

In-situ measurement of aqueous aerosols is critical. The combination of sampling losses and gas quality changes during sampling and analysis can significantly distort the measured particle distribution. Analysis equipment must be maintained at the temperature of the flue gas; however, many particle counters/sizers have a maximum operating temperature of about 40 °C at 98% non-condensing relative humidity. Most aerosol analyzers are designed for low humidity, ambient particle sampling. Further, internal acceleration of gases during measurement can change the relative humidity leading to particle shrinkage or growth. PSL define this calibration would not capture these effects. Therefore, particle distributions will be measured in-situ by two methods: by interferometry (phase doppler) and size-cut total analysis using FTIR.

PDPA is a differential technique for measuring particle distributions and velocity. Flux of particles through a small, well-defined sample volume in a gas stream eliminates coincidence effects present in integral measurements which rely on reproducing extinction of light using Mie Theory and assuming a particle distribution. A phase doppler-type analyzer will be used to measure the particle distribution before and after the packed section in the aerosol growth column. Viewing windows into the gas ducts and stabilized railing for the transmitter and receiver are all that is required.

A second method for particle analysis will be to size-select aerosols in-situ before total analysis in a hot-gas FTIR system. The particle separators will be sized to take the full gas flow, thereby eliminating isokinetic sampling error. A series of gas-particle separators with different cut diameters will be used in conjunction with an FTIR to produce a cumulative distribution of mass

4

represented as aerosols. The accumulated liquid from captured aerosols will be sampled for composition.

Future Work

Goals for next quarter include continued design and initial construction of an aerosol growth chamber. Experiments will be run to validate the aerosol growth model coded into MATLAB$^{®}$. H_2O absorption into salt-core aerosols will represent a baseline modeling and experimental exercise. Generation and growth measurement of H_2O/CO_2/amine aerosols will be investigated.

References

Mitsubishi Heavy Industries (MHI). (August 16, 2011). "Amine Emission Control Technology of KM CDR Process^{TM}." Presented at the Amine Workshop in Palo Alto, California.

National Carbon Capture Center (NCCC). (July 10, 2012). "National Carbon Capture Center: Post Combustion." Presented at the 2012 NETL CO_2 Capture Technology Meeting.

Netherlands Organization for Applied Scientific Research (TNO). "Emission Reducing Technologies Aerosols." Presented at UTCCS-1, University of Texas at Austin, January 25, 2012.

Sexton AJ. *Amine Oxidation in CO_2 Capture Processes.* The University of Texas at Austin. Ph.D. Dissertation. 2008.

SINTEF. (January 25, 2012). "Emission Studies at the Maasvlakte CO_2 Capture Pilot Plant." Presented at UTCCS-1, University of Texas at Austin, January 25, 2012.

Amine Degradation in Pilot Plants

Abstract

In this quarter, a method for detecting formaldehyde and other aldehydes and ketones in degraded solvent was developed. The method consists of reacting 2,4-dinitrophenylhydrazine (DNPH) with degraded solvent to produce an aldehyde-DNPH derivative that can be separated and detected by HPLC with UV. DNPH reacts selectively with aldehydes and ketones, and does not react with alcohols, carboxylic acids, amino acids, amides, or carbamates. Testing previously-collected pilot plant samples, insubstantial amounts of formaldehyde were detected. However, a significant amount of DNPH reacted with the degraded samples, equivalent to 75 mmol/kg of aldehyde in the degraded SRP PZ sample and 130 mmol/kg in the degraded PP2 MEA sample. This indicates the presence of an unidentified significant degradation product that is likely an aldehyde or ketone.

PZ was shown to react with hydrogen peroxide. Total formate accounted for 10% of the total degradation observed. This is an identical ratio to that observed in previous oxidation experiments, indicating that oxidation almost certainly occurs along a radical peroxide pathway. Adding hydrogen peroxide may be an easy way to rapidly simulate oxidation in future experiments.

2.7 mmol/kg of MNPZ was measured at the end of the OE25 batch PZ oxidation experiment. This accounts for 0.1% of the oxidation observed in the experiment.

Introduction

Piperazine (PZ) has shown promise as a solvent for carbon dioxide capture, with greater capacity, absorption rate, and thermal and oxidative stability than the baseline monoethanolamine (MEA) solvent. However, PZ degradation has not yet been as thoroughly characterized as MEA, with 25–40% of the mass balance still unknown.

Samples of degraded PZ solvent were collected from the Separations Research Program (SRP) pilot plant at the Pickle Research Campus in Austin, Texas, and from "Pilot Plant 2" (PP2). SRP used a synthetic flue gas mixture simulating a 0.1 MW plant, consisting of air plus 12 kPa CO_2, while PP2 used a slipstream of real flue gas from a coal-fired boiler.

Experimental Methods

DNPH Method

In order to quantify aldehydes and ketones using HPLC, solvent samples were treated with 2,4-dintrophenylhydrazine (DNPH). DNPH reacts selectively with aldehydes and ketones to produce phenylhydrazones that can be separated by reverse-phase HPLC and detected by UV absorption. The sample preparation method is as follows, as developed from Nascimento et al. (1997):

1. Dilute 0.1 to 0.2 mL of concentrated solvent in 1.4 mL DDI H_2O and 2.8 mL MeOH.

2. Add 1.0 mL of 0.4 wt % DNPH in acetonitrile (ACN) and 0.025 mL of 2 M $HClO_4$

3. Stir and let sit for 24 hours at room temperature.

Without further dilution, the sample is then injected on HPLC using an Acclaim™ Polar Advantage II C18 5 µm 120 Å 4.6 x 150 mm reverse phase column with UV detection at 365 nm, using the following methanol:10 mM ammonium carbonate buffer gradient profile flowing at 1.0 mL/min (Figure 1).
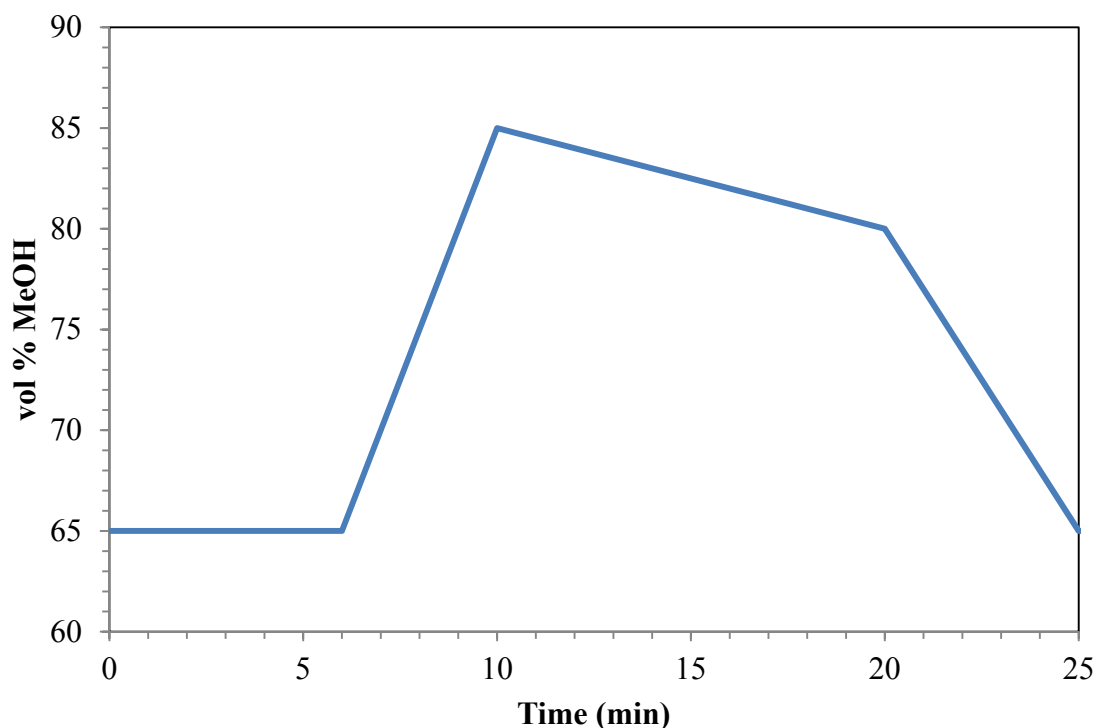
Figure 1: Methanol:10 mM $(NH_4^+)_2CO_3^{2-}$ gradient profile for DNPH HPLC method

A calibration curve was created using a 1000 ppm formaldehyde (COH_2) standard. The spectra are shown below in Figure 2, showing both the DNPH and COH_2 peaks. The formaldehyde peak increases linearly with formaldehyde added, while the DNPH peak decreases linearly, as shown in Figure 3 and Figure 4. If it is assumed that DNPH reacts stoichiometrically with aldehydes and ketones, the DNPH peak can be used to calculate a total aldehyde and ketone concentration. The limit of detection was determined to be 0.18 mmol/kg aldehyde. The DNPH method reaches

saturation limit of 3.7 mmol/kg of aldehyde in the derivatized sample being injected in HPLC, above which the DNPH is fully reacted.
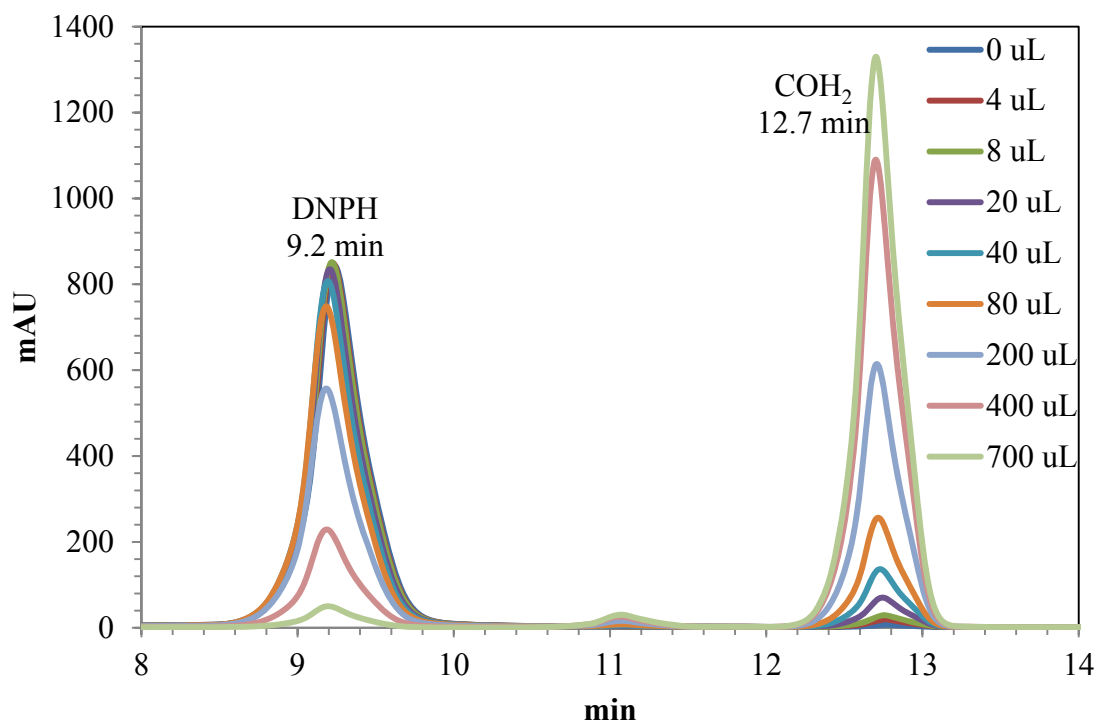
Figure 2: DNPH + 0 to 700 µL 1000 ppm COH₂ standard HPLC spectra
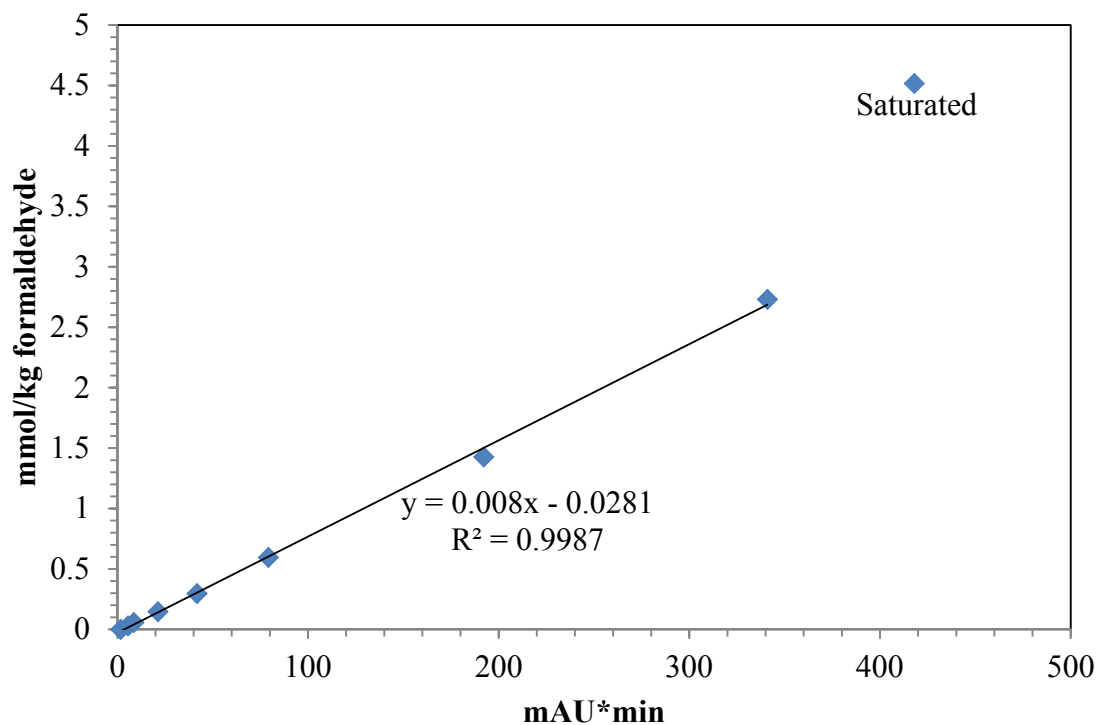
Figure 3: COH$_2$ calibration curve (peak at 12.7 minutes)
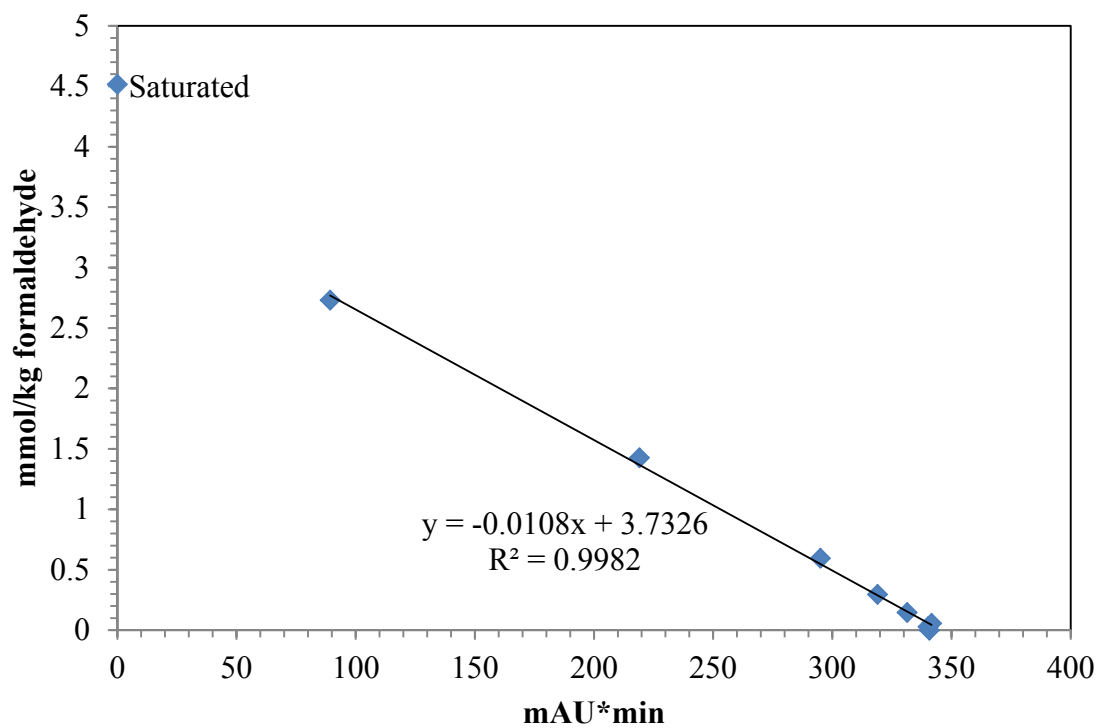
Figure 4: DNPH total aldehydes and ketones calibration curve (peak at 9.2 minutes)

Reaction of Hydrogen Peroxide with Piperazine

In a 40 mL vial, 10 g of loaded 8 m PZ was mixed with 0.005 g of 217.6 mM $FeSO_4$ (0.1 mM). 0.1 to 0.5 mL of 30 wt % H_2O_2 (100–500 mmol/kg) was then added drop-wise, and the mixture was stirred at room temperature for 15 minutes. The reaction mixture was then stored at room temperature for 24 hours before being analyzed.

Analytical Methods

Other analytical methods are discussed in previous quarterly reports.

Results and Discussion

DNPH Method for Degraded Amines

Degraded samples from 4 pilot plant campaigns were treated with DNPH and run on HPLC. 2 samples from PZ campaigns conducted at SRP and PP2 were tested, as well as 2 samples from MEA campaigns conducted at SRP and NCCC. The PZ campaign samples contained insubstantial amounts of formaldehyde. This was expected, as any significant quantity of formaldehyde will react rapidly with PZ to produce an insoluble polymer (Freeman, 2011). The SRP and NCCC MEA campaigns saw slightly greater formaldehyde accumulation, at 7.6 and 9.8 mmol/kg, respectively.

All 4 samples saw significant conversion of the DNPH added, far more than what would be expected from reaction with the formaldehyde alone. This is quantified by the "total aldehydes" measurement, which assumes that a mole of DNPH reacts stoichiometrically with one mole of aldehyde or ketone. Figure 5 shows the HPLC spectra of the degraded SRP PZ sample compared to fresh PZ, which shows the reduction in the DNPH area without a significant increase in the formaldehyde peak. The largest unidentified peak occurs at 3.2 minutes, but at this point no known degradation product has been matched to it. In addition to fresh PZ, standards of formate, N-formyl-PZ, and 2-piperazinone have been tested, but none react with DNPH. DNPH reacts selectively with aldehydes and ketones, and does not react with carboxylic acids, amino acids, amides, or carbamates.

Table 1: DNPH method results for pilot plant samples

Sample	COH_2 (mmol/kg)	Total Aldehydes (mmol/kg)
SRP (2011)	0.3	75.2
PP2 (2011)	0.5	129
SRP MEA (2009)	7.6	153
NCCC MEA (2012)	9.8	159
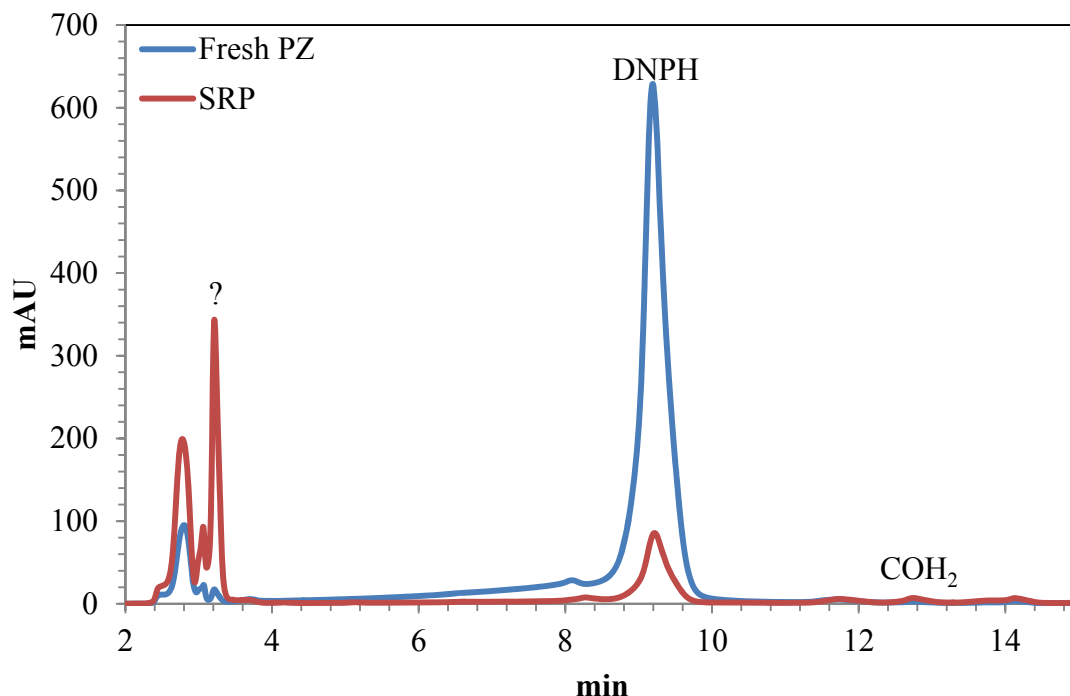
Figure 5: DNPH method HPLC spectra of fresh PZ and degraded SRP solvent

Reaction of Hydrogen Peroxide with Piperazine

Reaction of amine with peroxide radicals has been proposed as a major pathway of amine oxidation (Freeman, 2011). To test this theory, samples of fresh loaded 8 m PZ were treated with 100 and 500 mmol/kg of hydrogen peroxide (H_2O_2). Select results are shown below in Table 2. Of greatest interest, quantitative amounts of formate and nitrite were produced by the oxidation experiment. In previous oxidation experiments, formate accounted for approximately 10% of the PZ that degraded (Freeman, 2011). The 500 mmol/kg H_2O_2 experiment matches this trend, with 28 mmol/kg of total formate produced for 260 mmol/kg of PZ lost. 1.6 mmol/kg of nitrite was produced. No MNPZ was observed in HPLC, due to the experiment being conducted at room temperature. MNPZ would be expected to form at elevated temperatures.

Effervescing was observed upon the addition of hydrogen peroxide, but the volatile products were not quantified. These products most likely consist of oxygen produced from peroxide decomposition and ammonia from PZ oxidation.

Table 2: Results of PZ + H_2O_2 experiments

H_2O_2 added (mmol/kg)	PZ loss (mmol/kg)	Total formate (mmol/kg)	Nitrite (mmol/kg)
100	90	4.8	0.2
500	260	28	1.6

6

OE25 Nitrosamine Formation

OE25 was an oxidation experiment conducted by Freeman in the LGF apparatus. It simulated an extremely high PZ oxidation rate, at 70 °C and with 4 mM Cu^{2+}, and the final sample was thoroughly analyzed for degradation product characterization. However, at the time of the experiment the samples were not tested for MNPZ accumulation. A select number of samples were tested for MNPZ this previous quarter. The results are shown below in Figure 6, along with nitrite accumulation results measured at the time of the experiment 2 years ago. By the end of the experiment, 2.7 mmol/kg of MNPZ had accumulated. This represents approximately 0.1% of the 3200 mmol/kg of PZ that degraded.

The samples had been stored for approximately 2 years before being tested for MNPZ. Extrapolating from kinetic data collected at higher temperatures, the thermal degradation rate of MNPZ at room temperature should be on the order of $2.3*10^{-10}$ s^{-1} (Fine et al., 2012). At this rate, 1–2% of the MNPZ would have degraded before measurement.
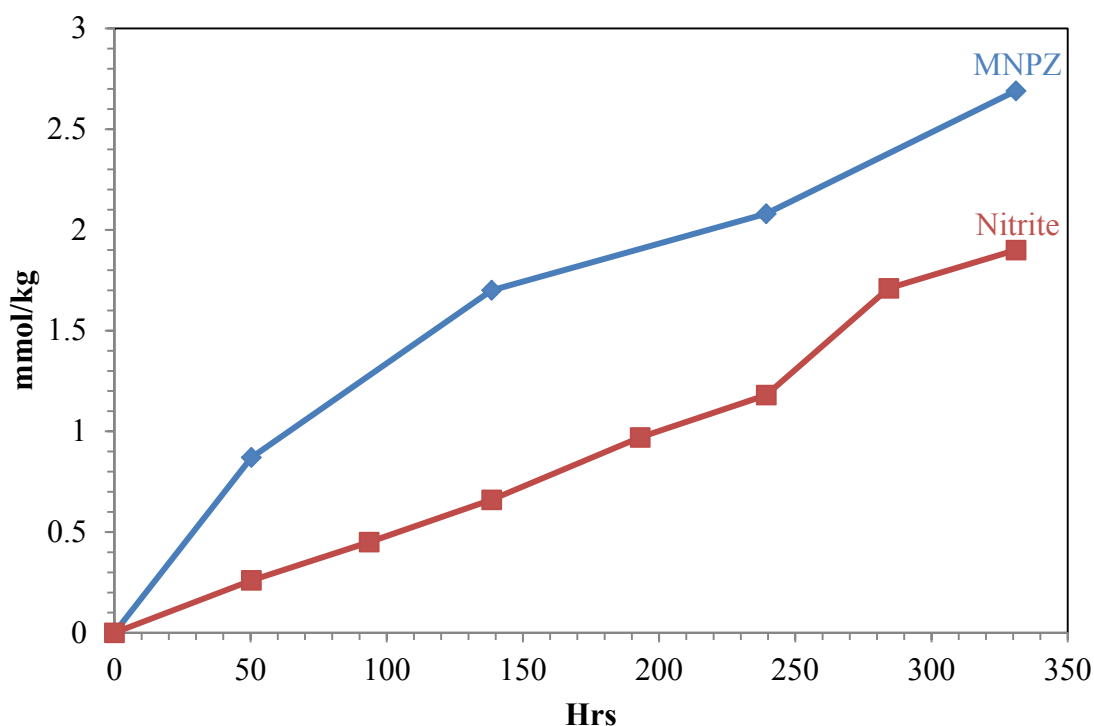
Figure 6: MNPZ and nitrite accumulation during OE25 (LGF, 8 m PZ, α = 0.3, 70 °C, 94 kPa O_2, 100 mL/min, 4 mM Cu^{2+}, 14 days (Freeman, 2011)) (nitrite analysis from Freeman, 2011)

Conclusions

Formaldehyde was not a significant degradation product for any of the pilot plant campaigns studied.

Significant degradation has occurred in the pilot plant samples in the form of currently unquantified aldehydes or ketones, as measured by the reaction of DNPH with the degraded PZ pilot plant samples.

Hydrogen peroxide can be used to rapidly oxidize PZ. The degradation products observed from peroxide oxidation are similar to those observed in other experiments, including 10% of degradation in the form of total formate.

2.7 mmol/kg of MNPZ accumulated during OE25 at 70 °C, showing that MNPZ can form from the oxidation of PZ to nitrite even without the addition of nitrite or cycling to higher temperatures. This represents 0.1% of total PZ oxidation.

Future Work

Degradation and Reclaimer Modeling and Literature Review

The University of Texas at Austin, URS, and Trimeric have been awarded a proposal to conduct a rigorous literature review of reclaimer sludge disposal by IEAGHG. In support of this, I will conduct a literature review of all published data on amine degradation as well as compiling all useful unpublished degradation data from our lab. Using kinetic and thermodynamic data, complete degradation models for MEA and PZ will be created to estimate amine loss and heat stable salt accumulation in a full-scale CO_2 post-combustion capture facility. The models will be created in Excel and will model the process in steady state. If there is sufficient time, dynamic models will be created in MATLAB, to simulate non-continuous reclaimer operation. The models will have the form of Figure 7, which divides the amine scrubbing process into 6 different degradation reactors with 2 additional separation units.

In the absorber packing, oxidation will be modeled using temperature and loading profiles exported from Aspen Plus®, and will be assumed to be plug flow. Oxygen content will be assumed to be constant at the saturation limit (mass transfer limitations will be ignored). The effect of intercooling on oxidation will be determined.

The absorber sump oxidation reactor will be modeled as a continuously-stirred tank reactor (CSTR), with the inlet rich solvent entering saturated with oxygen.

A "heated oxidation" reactor will be included in the model, to estimate plug flow oxidation of the rich amine at high temperatures in the cross exchanger and piping before the stripper.

Any remaining oxygen will be assumed to flash off upon entering the stripper. Loading and temperature profiles will be exported from Aspen Plus® to model thermal degradation in the stripper packing in plug flow conditions. Additional thermal degradation will be modeled in the stripper sump at lean solvent conditions as a CSTR. Alternative stripper configurations, such as 2-stage flash and cold-rich bypass, will be modeled.

The thermal reclaimer will take a slip-stream of lean solvent and heat it to separate the amine as a vapor from a sludge containing nonvolatile degradation products including heat stable salts. If a better VLE model cannot be developed, it will be assumed that the sludge will contain 1 mole of amine per mole of degradation product removed. The flow rate of the reclaimer feed will be set to maintain a steady state in the system, removing all degradation products formed in a single pass of solvent, including additional degradation in the reclaimer.

The recently-developed MNPZ model will be included to determine the expected steady-state values of MNPZ in the solvent and reclaimer sludge for the PZ degradation model.

Some volatile amine will be lost from the solvent in both the absorber and stripper. Amine lost in the absorber overhead will be captured by a water wash, which will be assumed to reduce

amine concentration in the flue gas to 1 ppm. The captured amine will either be returned to the lean solvent or purged. Volatile amine, water, and degradation products in the stripper overhead will be separated by the CO_2 compressor and returned to the lean solvent. Potential volatile reclaiming processes will be studied to remove volatile degradation products which would otherwise accumulate in the system.

Aerosols will be ignored.

Based on the amount of amine loss to degradation, a solvent makeup rate and cost will be calculated. The cost of treating the reclaimer sludge will be estimated. Multiple strategies for sludge treatment will be studied, including incineration, bio-treatment, and novel process concepts.

Figure 7: Degradation Model
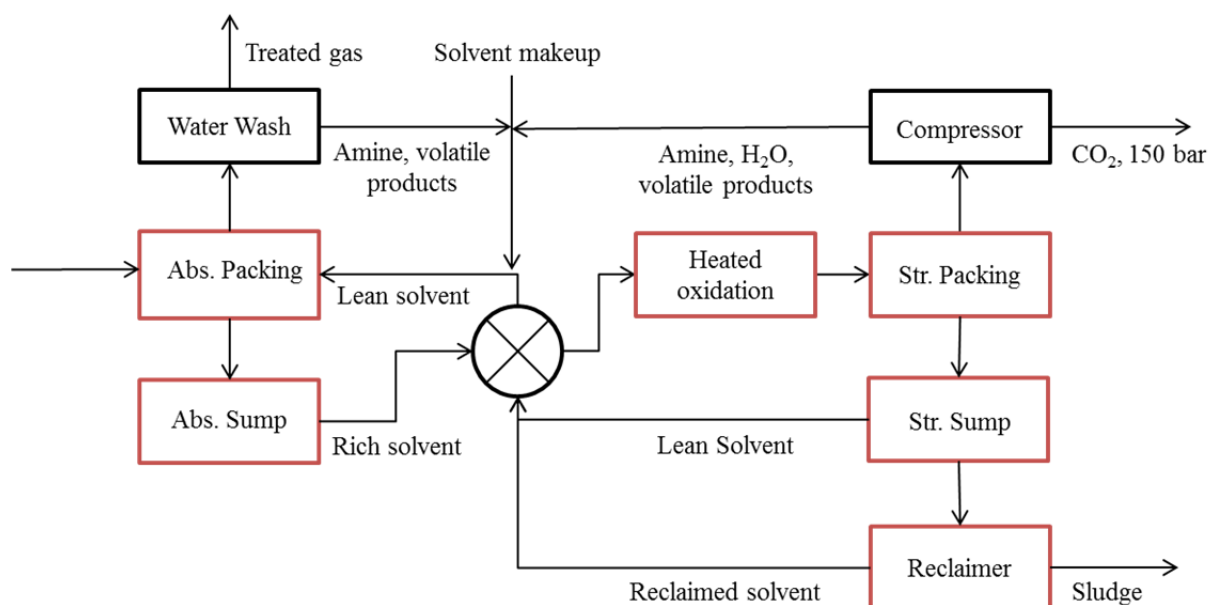
Table 3: Selected recent group degradation publications

Type of Oxidation	Paper/Dissertation
Oxidation in absorber	Sexton, 2008 (MEA); Freeman, 2011 (PZ)
Heated oxidation/cycling	Closmann, 2011; Voice et al., 2012 (MEA, PZ, MDEA/PZ)
Thermal degradation	Davis, 2009 (MEA); Freeman, 2011 (PZ)
Nitrosation	Fine et al., 2012

Other Future Work

Work is ongoing to determine the source of the "total aldehydes" observed by the DNPH method in the degraded pilot plant samples. Other standards of known and suspected degradation products still need to be tested to determine whether any react with DNPH. The HPLC method will be optimized to better separate the unidentified peaks observed early in the methanol-buffer gradient. This will ultimately help to close the PZ oxidation balance gap.

9

Pilot plant samples will be analyzed from a PZ campaign conducted at Tarong in Australia by CSIRO and from MEA campaigns conducted in Europe by OCTAVIUS.

Safety

DNPH is a very dangerous substance. In pure form, it is a flammable solid, and even the 0.4 wt % standard is diluted in acetonitrile, which is also flammable. Skin contact causes redness, itching, and pain, and ingestion can cause cyanosis. It is also potentially carcinogenic. For safety purposes, the diluted DNPH is stored in the "flammables" cabinet, and all work with it is done in a fume hood with safety glasses, gloves, and a lab coat.

References

Closmann F. *Oxidation and Thermal Degradation of Methyldiethanolamine/Piperazine in CO$_2$ Capture*. The University of Texas at Austin. Ph.D. Dissertation. 2011.

Davis JD. *Thermal Degradation of Aqueous Amines Used for Carbon Dioxide Capture*. The University of Texas at Austin. Ph.D. Dissertation. 2009.

Fine NA, Goldman MJ, Nielsen PT, Rochelle GT. "Managing n-nitrosopiperazine and dinitrosopiperazine." Presented at GHGT-11, Kyoto, Japan November 18-22, 2012.

Freeman SA. *Thermal Degradation and Oxidation of Aqueous Piperazine for Carbon Dioxide Capture*. The University of Texas at Austin. Ph.D. Dissertation. 2011.

Nascimento RF, Marques JC, Lima Neto BS, De Keukeleire D, Franco DW. "Qualitative and quantitative high-performance liquid chromatographic analysis of aldehydes in Brazilian sugar cane spirits and other distilled alcoholic beverages." *J Chromatog A*. 1997;782(1):13–23.

Sexton AJ. *Amine Oxidation in CO$_2$ Capture Processes*. The University of Texas at Austin. Ph.D. Dissertation. 2008.

Voice AK, Closmann F, Rochelle GT. "Oxidative degradation of amines with high-temperature cycling." Presented at GHGT-11, Kyoto, Japan November 18-22, 2012.

Quantification of Nitrosamines in Amine Scrubbing

Abstract

This quarter, a group analysis method was developed for the quantification of nitrosamines in amine scrubbing conditions. The total nitrosamine (TONO) method uses hydrobromic acid to selectively produce nitric oxide (NO) gas from a nitrosamine. The NO is purged from the reactor and enters a chemiluminescent NO_x analyzer, which produces a voltage proportional to the NO concentration. The area under the voltage-time curve is integrated and then calibrated with the total nitrosamine concentration. The calibration is linear across three orders of magnitude with a limit of quantification (LOQ) of 0.1 ppm nitrosamine in the amine sample. The LOQ can be easily decreased to 1 ppb by using a more sensitive NO_x analyzer.

The Necessity for the Total Nitrosamine Method

Nitrosamines as a family are carcinogenic degradation products that can be formed during CO_2 scrubbing with amines. Previously, nitrosamines with known standards have been quantified using an HPLC method with UV absorbance. However, many other degradation products will also absorb UV at the same wavelength, making separation difficult. Furthermore, many nitrosamines in amine capture have not been identified and therefore cannot be quantified using the HPLC. Finally, many pertinent nitrosamines have been identified but do not have standards. Since nitrosamines absorb UV with different efficiencies, it is impossible to quantify these nitrosamines using the HPLC method. The TONO method is group-specific to nitrosamines, so it can quantify nitrosamines in heavily degraded amine solutions. The TONO method is also quantitatively equivalent across all nitrosamines, so it can be used in tandem with the HPLC for calibration purposes.

Total Nitrosamine Method

Standard Operating Procedure

A diluted amine sample with nitrosamines is injected into a reagent of hydrobromic acid in acetic acid (AcOh) and ethyl acetate (EtAc). The hydrobromic acid denitrosates the protonated nitrosamine, forming NO as shown in Figure 1 (Biggs & Williams, 1975; Ding, Lee, & Eatough, 1998).
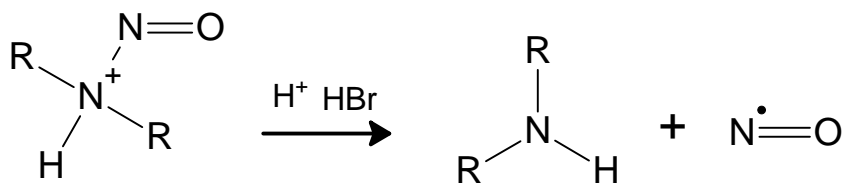
Figure 1: NO Evolution from Nitrosamine in the Presence of Hydrobromic Acid

Nitrogen gas (N$_2$) at 0.8 SLPM and 20 psig flows through a frit into a 1 in. OD glass reactor to sparge the NO (Figures 2 & 3). The reactor is filled with glass beads to provide surface area for the mass transfer of the NO into the gas phase. The diluted NO then travels to a condenser where the gas is cooled using ice water to approximately 10 °C. The cooling knocks out the majority of the EtAc that is stripped along with the NO so that the gas is unsaturated at room temperature. The gas then passes an atmospheric bypass where a small slipstream is allowed to vent. The remaining gas is at atmospheric pressure and is pulled through a Model 14 B/E Thermoelectric Chemiluminescent NO$_x$ Analyzer using a vacuum pump.

In the NO$_x$ analyzer, the NO reacts with ozone to produce electronically excited nitrogen dioxide (NO$_2$). The NO$_2$ returns to its ground state and gives off a photon at a specific wavelength. The photon hits a photomultiplier where it is converted into a voltage. The voltage is then read using Picolog to give the transient concentration of NO. The voltage-time curve is integrated and calibrated against the concentration of the nitrosamine added. Unknown concentrations of nitrosamines can then be quantified using the voltage integration and the calibration. The NO$_x$ analyzer was set to a nominal 5 ppm range but was not calibrated with a standard NO gas. The detection limit should be easily improved by a factor of 100 by using a NO$_x$ analyzer capable of ppb NO$_x$ level analysis. All tubing leading into the NO$_x$ analyzer is Teflon to prevent reaction with NO.
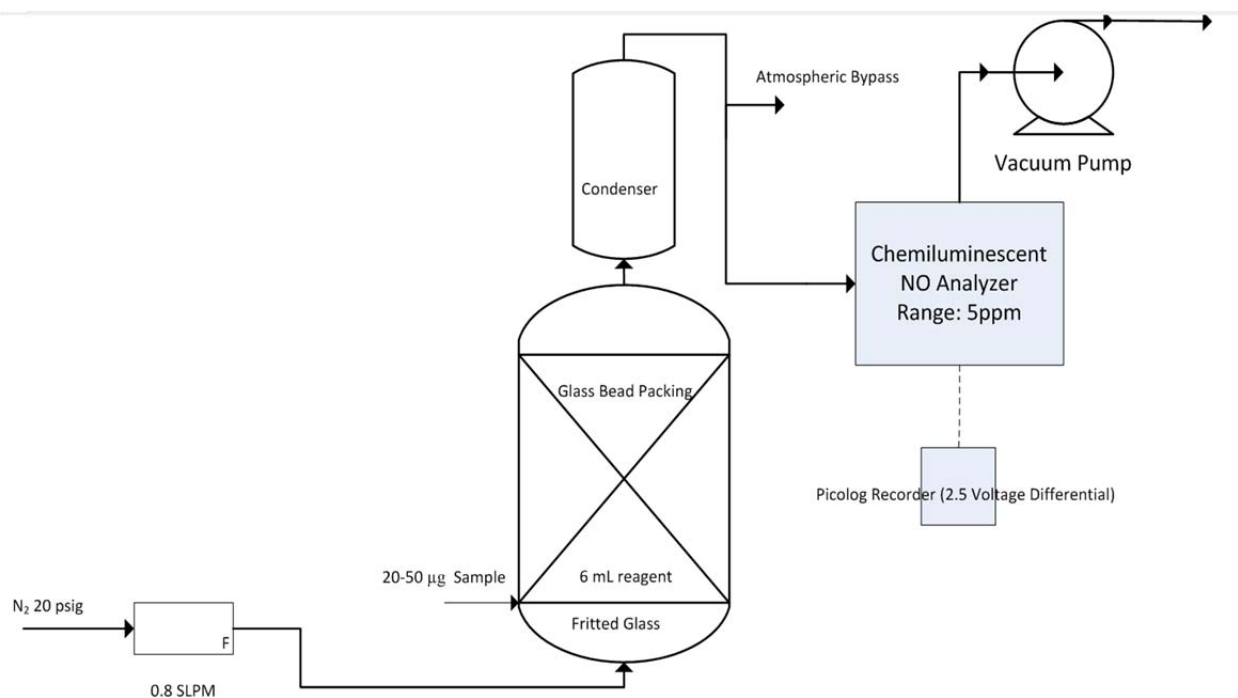
Figure 2: Process Flow Diagram for Total Nitrosamine Apparatus (Not Drawn to Scale)
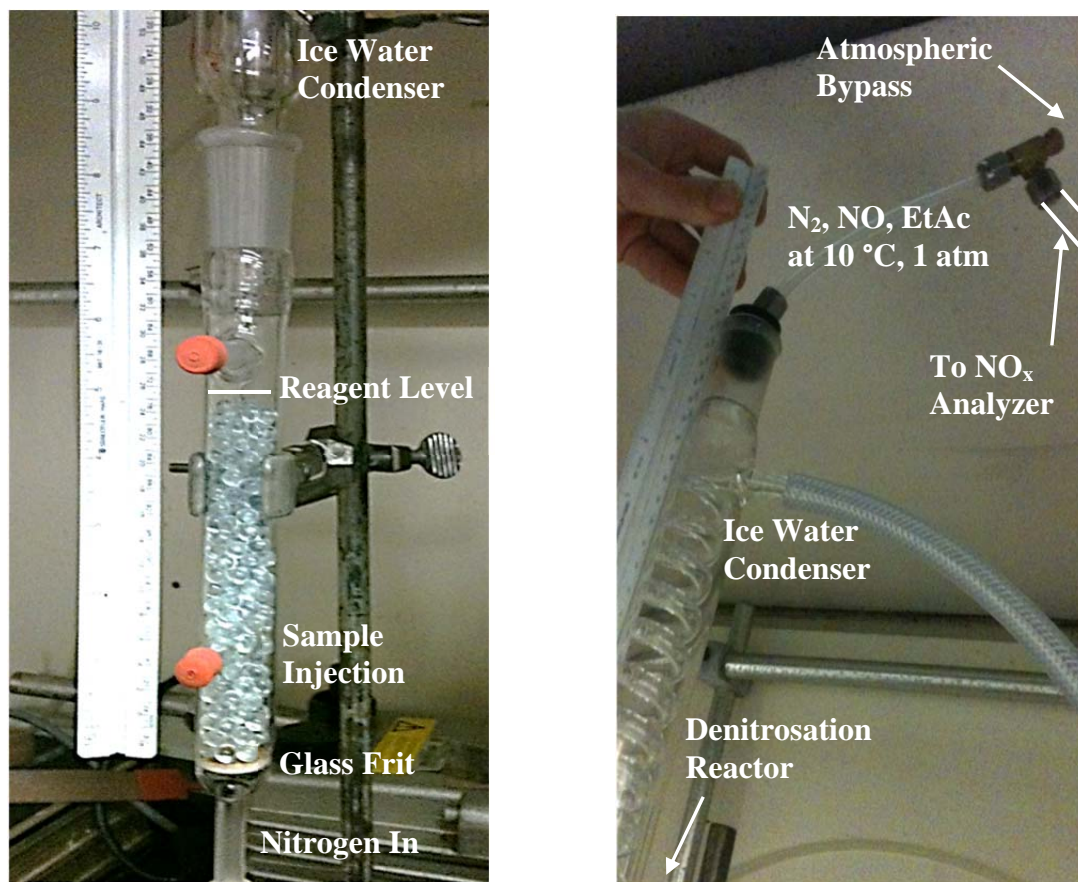
Figure 3: Images of Reactor, Condenser, and Atmospheric Bypass

Reaction Conditions

Many total nitrosamine methods rely on refluxing AcOh in EtAc at elevated temperatures or under vacuum (Dai et al., 2012; Downes, Elsey, & Walters, 1976; Frischmann, 2011). Refluxing can increase the elution rate of NO, creating sharper peaks and decreasing the limit of quantification (LOQ). However, directly sparging with N_2 from the bottom of the reactor does an adequate job of eluting NO with a peak width of approximately 5 minutes. The peak width can be further decreased by a factor of 5 by adding glass packing to the reactor to increase surface area for liquid-gas separation. At low nitrosamine concentrations the denitrosation reaction rate could be the rate limiting step for NO elution, so it might be necessary to run the reactor at higher temperatures to increase the denitrosation reaction rate. A slow denitrosation rate will manifest as a very slow return to the baseline after sample injection (Frischmann, 2011).

Water present in the hydrobromic acid solution has been shown to have a detrimental effect on the denitrosation rate at low nitrosamine concentrations (Drescher & Frank, 1978), To remove this excess water, an equimolar amount of acetic anhydride (AcAnh) was added to the reagent (Table 1). The current method at ambient conditions produces sharp peaks with a width of approximately 60–120 seconds and a complete return to the baseline (Appendix A). The total nitrosamine analysis takes approximately 3 minutes per injection and a daily set up time of 1 hour, allowing for rapid quantification of up to 100 samples over a workday.

3

Table 1: Reactor Conditions for Denitrosation and NO Sparging

Condition	Purity	Amount
Temperature	-	21 °C
Pressure	-	14.7 psig
Nitrogen	99.99%	0.8 SLPM
Ethyl Acetate	98%	12 mL
Acetic Acid	99.85%	2 mL
HBr	48% in water	0.4 mL
Acetic Anhydride	99%	0.6 mL

Sample Conditioning

The TONO method can be used to analyze nitrosamine concentration in amine solutions after sample conditioning to dilute the nitrosamine, inhibit artifactual denitrosation, and remove the water. First, the sample needs to be diluted to a nitrosamine concentration of 100 μmol/kg or around 10 ppm. Choosing the correct diluent is non-trivial since unknown nitrosamines will have different solubility limits. Furthermore, diluents similar to water might also inhibit denitrosation in the glass reactor. Acetone has proved to be a good diluent for MNPZ, DNPZ, and NDELA standards. Since acetone is very volatile, it is important to prepare the dilutions in capped vials using a syringe. Diluents can easily be tested for solubility limits by diluting to different concentrations and comparing the slopes of the calibration curves. If the slope of the more dilute sample is steeper, then there is a solubility limit at the dilution level. After dilution, the sample must be scavenged of its water to improve denitrosation rates. A stoichiometric amount of AcAnh is added to the sample to completely react with the water, forming AcOh. The sample is then mixed and allowed to sit for at least 30 minutes before injection.

TONO Method Calibration

Standards of MNPZ, DNPZ, NDELA, and NO_2^- were diluted in water and then conditioned following the above method with ethyl acetate as the diluent. Diluted samples between 10 μL and 100 μL were weighed and then injected into the reagent. The resulting curves were integrated and then calibrated against the known moles of nitrosamine in the injected samples. The calibration curves were linear over 1 order of magnitude with R^2 values above 0.99 for every case except one (Appendix B). The slopes were then arbitrarily normalized to the slope of MNPZ to give the relative analytical selectivity for each nitrosamine. Since the method is equivalent for each nitrosamine, the slopes should be statistically equivalent (Drescher & Frank, 1978; Kulshrestha, McKinstry, Fernandez, Feelisch, & Mitch, 2010). MNPZ and DNPZ had equivalent slopes when accounting for the second nitrosamine on DNPZ. NDELA had a slightly lower slope, but the NDELA standard was very old which could account for the difference. Nitrite had a very different slope, which is most likely due to solubility issues. After waiting for over an hour, the conditioned nitrite sample still contained two liquid phases.

Table 2: Comparison of Calibration Slopes

Nitrosamine	MNPZ	NDELA	DNPZ	NO$_2^-$
Slope (V·s/nmol)	1.93	1.7	1.02	2.9
Normalized to MNPZ	1.00	1.14	0.95*	0.67

Determination of TONO Detection Limit

A sample of DNPZ in water was dehydrated and diluted to 182 μmol/kg in acetone following the sample conditioning procedure. The sample was then diluted again to 1.7 μmol/kg in acetone to test the LOQ of the current method. Two injections of the concentrated sample at 30 μL and 70 μL and two injections of the dilute sample at 200 μL and 600 μL were calibrated. (Appendix C). The calibration was linear across all samples with an R^2 of 0.9996. When taking into account the dilution factor, this represents three orders of magnitude of linearity. The 200 μL injection yielded a peak approximately ten times the noise level. Extrapolating to three times the noise level gives an LOQ of approximately 0.2 nmol. A 2000 μL injection of an amine sample diluted a factor of 10 containing a nitrosamine with a MW of 100 g/mole would have a sample detection limit of approximately 0.1 ppm. The noise using the current NO$_x$ analyzer is approximately 100 times greater than it should be due to a malfunctioning refrigeration unit around the photomultiplier. A more sensitive instrument would theoretically have a detection limit of 1 ppb, which is similar to detection limits reported in literature (Ding et al., 1998; Kulshrestha et al., 2010; Pignatelli et al., 1987).

Preliminary Total Nitrosamine Results

The TONO method was used to calibrate the HPLC for the amino-ethylpiperazine nitrosamine (N-AEP). The previous HPLC method used the MNPZ calibration on a mole basis to quantify N-AEP. Using this calibration the overall yield of nitrosation was 80%, with no other products found. A sample from the N-AEP formation experiment was conditioned using ethyl acetate and run through the TONO apparatus with varying injection amounts. The calibration was linear with an R^2 of 0.996 (Appendix B); the concentration in the sample was determined by varying the calibration slope to match the calibration slope of MNPZ. Using the TONO method, the overall yield to N-AEP from nitrite was 96%. Thus, the primary amine on AEP did not scavenge any of the nitrite as previously hypothesized. The HPLC method can now be calibrated for N-AEP using the concentration determined from the TONO method.

Safety

The MSDSs were read and understood for all chemicals used in the total nitrosamine experiment. AcOH and HBr were stored in the acid cabinet; EtAc and AcAnh were stored in the flammable chemical cabinet. EtAc and AcOH are both volatile and were only used in the hood. The handling of concentrated nitrosamine standards was minimized by using diluted stock solutions. The NO$_x$ analyzer outlet gas was vented into the hood.

Conclusions

- A total nitrosamine method using denitrosation of the nitrosamine with HBr was developed.
- Gas sparging through the bottom of the reactor and adding glass beads decreased peak width.
- Adding acetic anhydride to the denitrosating agent scavenges the water from HBr and eliminates baseline drift.
- Total peak width is less than 2 minutes, allowing for rapid quantification.
- The diluent for samples must be carefully selected to dilute across all nitrosamines in the sample.
- Acetic anhydride should be added to the samples before analysis to scavenge any water.
- The method is quantitative across the three nitrosamine standards tested.
- The calibration curve is linear through 3 orders of magnitude and passes through zero.
- The detection limit is around 0.1 ppm but could improve to 1 ppb with a more sensitive analyzer.
- N-AEP was calibrated using the TONO
- The yield of N-AEP formation from nitrite is unity; the primary amine did not scavenge any nitrite.

Updated Scope of Dissertation

- NO_2 absorption into sulfite solutions
- NO_2 absorption into amine solutions
- Nitrite formation through amine oxidation
- Nitrosamine formation under absorber and stripper conditions
- Nitrosamine thermal decomposition under stripper conditions
- Nitrosamine volatility under thermal reclaimer conditions
- Nitrosamine thermal decomposition under reclaimer liquid-phase conditions
- Nitrosamine UV decomposition under reclaimer gas-phase conditions
- Nitrosamine concentrations under cycling conditions

References

Biggs, I., & Williams, D. "Kinetics and mechanism of the Fischer–Hepp rearrangement and denitrosation. Part V. The mechanism of denitrosation." *J. Chem. Soc., Perkin Trans. 2.* 1975; 2141: 107–111.

Dai, N., Shah, A. D., Hu, L., Plewa, M. J., Mckague, B., & Mitch, W. A. "Measurement of Nitrosamine and Nitramine Formation from NOx Reactions with Amines during Amine-Based Carbon Dioxide Capture for Postcombustion Carbon Sequestration." *Environmental Science and Technology.* 2012; 46: 9793–9801.

Ding, Y., Lee, M., & Eatough, D. "The determination of total nitrite and N-nitroso compounds in atmospheric samples." *International journal of Environmental Analytical Chemistry.* 1998; 69(3): 243–255.

Downes, M. J., Elsey, T. S., & Walters, C. L. "Determination of a Non-volatile Nitrosamine by Using Denitrosation and a Chemiluminescence Analyser." *Analyst.* 1976; 101: 742–748.

Drescher, G. S., & Frank, C. W. "Estimation of Extractable N-Nitroso Compounds at the Parts-per- Billion Level." *Analytical Chemistry.* 1978; 50(14): 2118–2121.

Frischmann, M. "Plausibility of Total and Individual Nitrosamine Measurements and Improvements" *IEAGHG Seminar,* 2011

Kulshrestha, P., McKinstry, K. C., Fernandez, B. O., Feelisch, M., & Mitch, W. "Application of an optimized total N-nitrosamine (TONO) assay to pools: placing N-nitrosodimethylamine (NDMA) determinations into perspective." *Environmental Science & Technology.* 2010; 44(9): 3369–3375.

Pignatelli, B., Richard, I., Bourgade, M. C., & Bartsch, H. "Improved group determination of total N-nitroso compounds in human gastric juice by chemical denitrosation and thermal energy analysis." *The Analyst.* 1987; 112(7): 945–949.

Appendix A. Representative peaks of NO elution

Diluted in ethyl acetate, acetic anhydride used to scavenge water
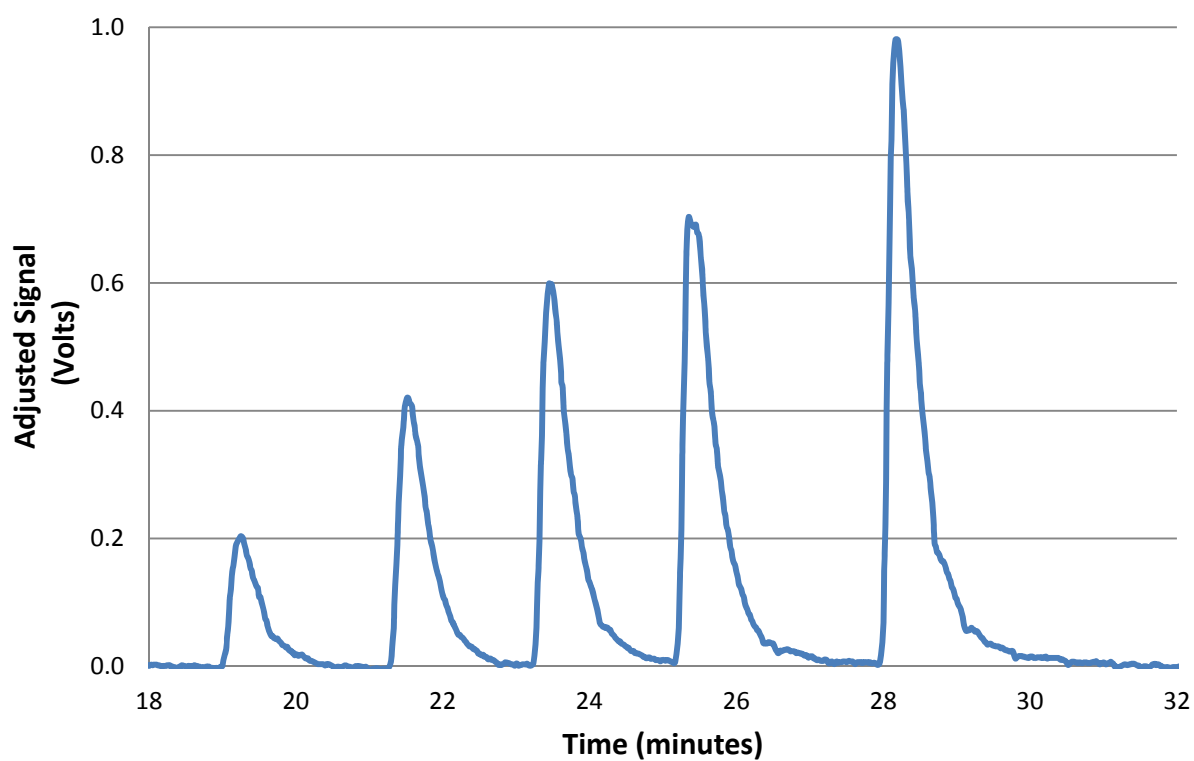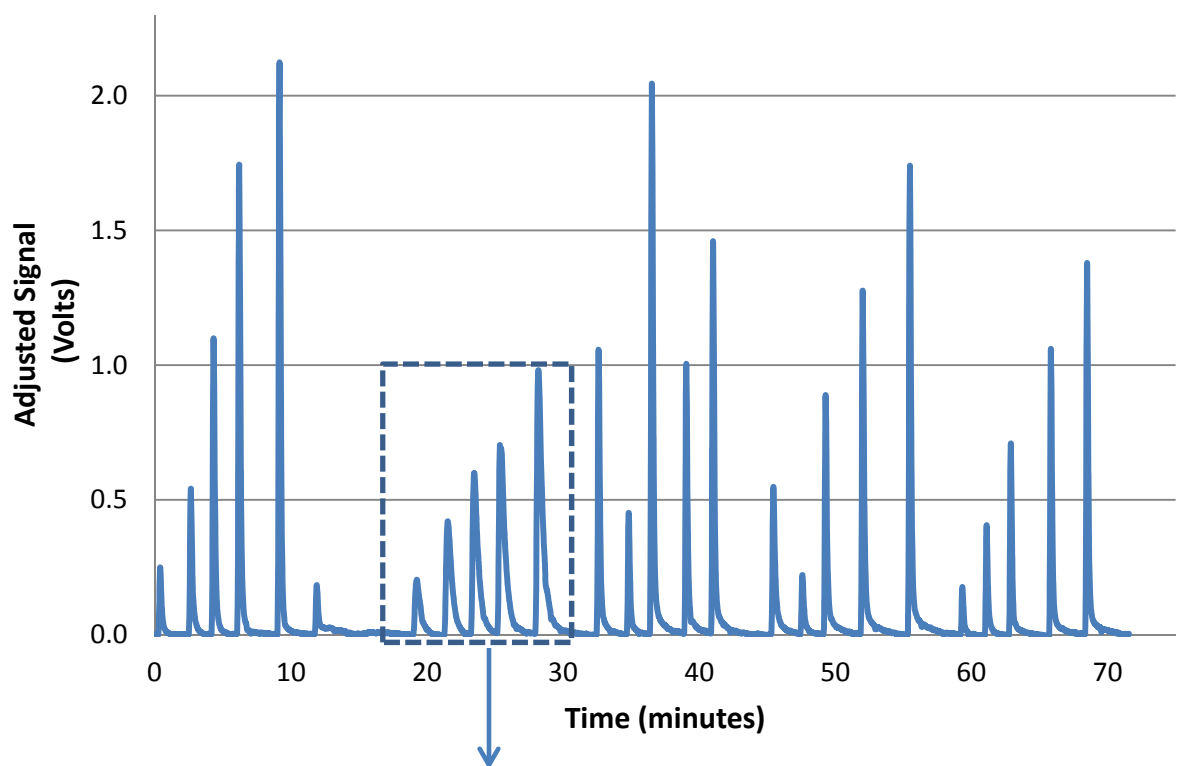
Appendix B: Calibration Curves for Nitrosamines

Diluted in ethyl acetate, acetic anhydride used to scavenge water

MNPZ: $y = 1.92500x$, $R^2 = 0.99476$

NDELA: $y = 1.70022x$, $R^2 = 0.99755$

DNPZ: $y = 1.02435x$, $R^2 = 0.98777$

N-AEP*: $y = 1.94879x$, $R^2 = 0.99649$
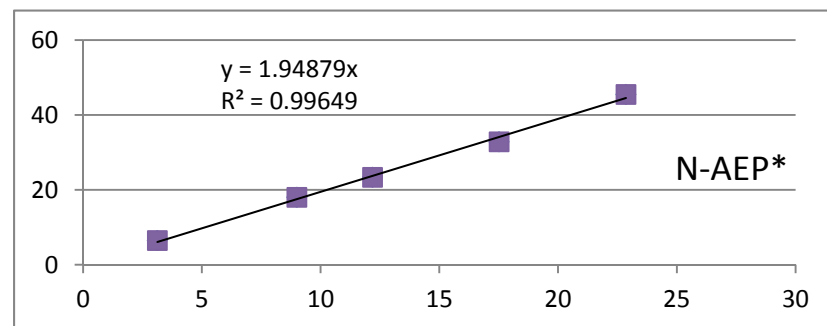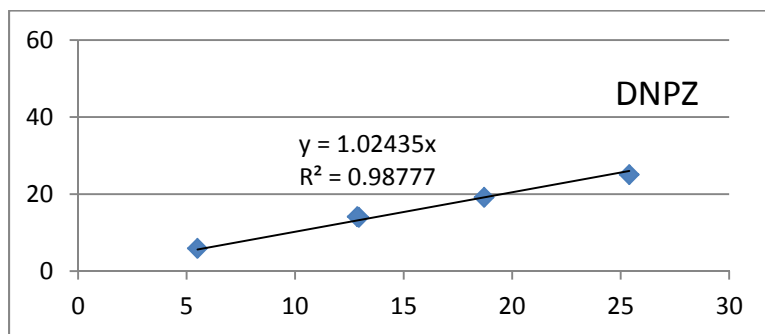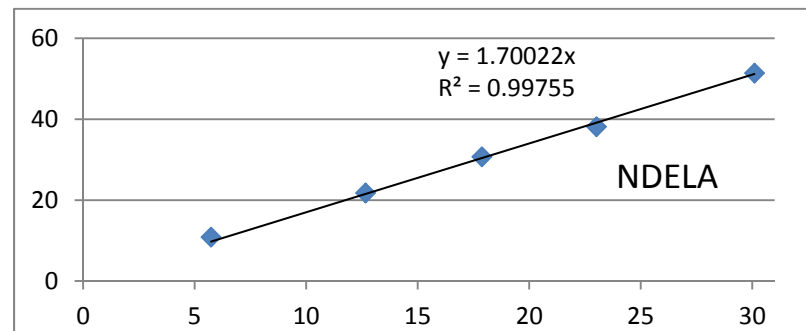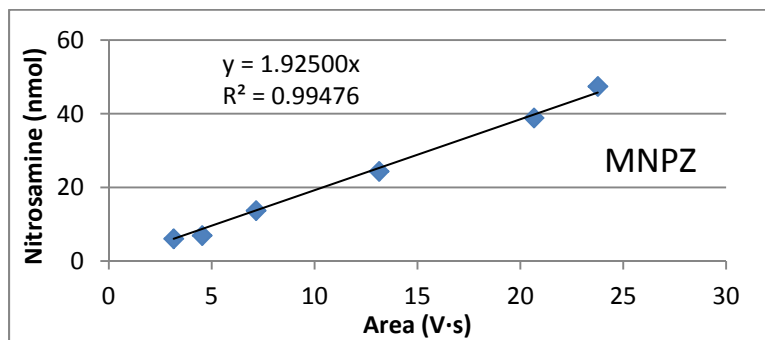
*AEP concentration set so slope matches MNPZ slope

NO_2^-: $y = 2.75117x$, $R^2 = 0.99729$

Y-axis: Nitrosamine (nmol); X-axis: Area (V·s)
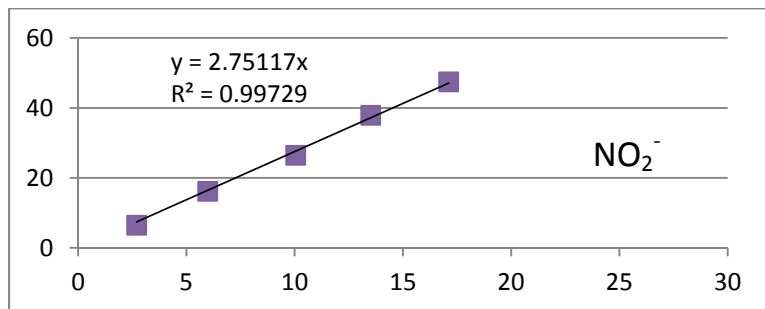
Appendix C: Limit of Quantification

Diluted in acetone, acetic anhydride used to scavenge water
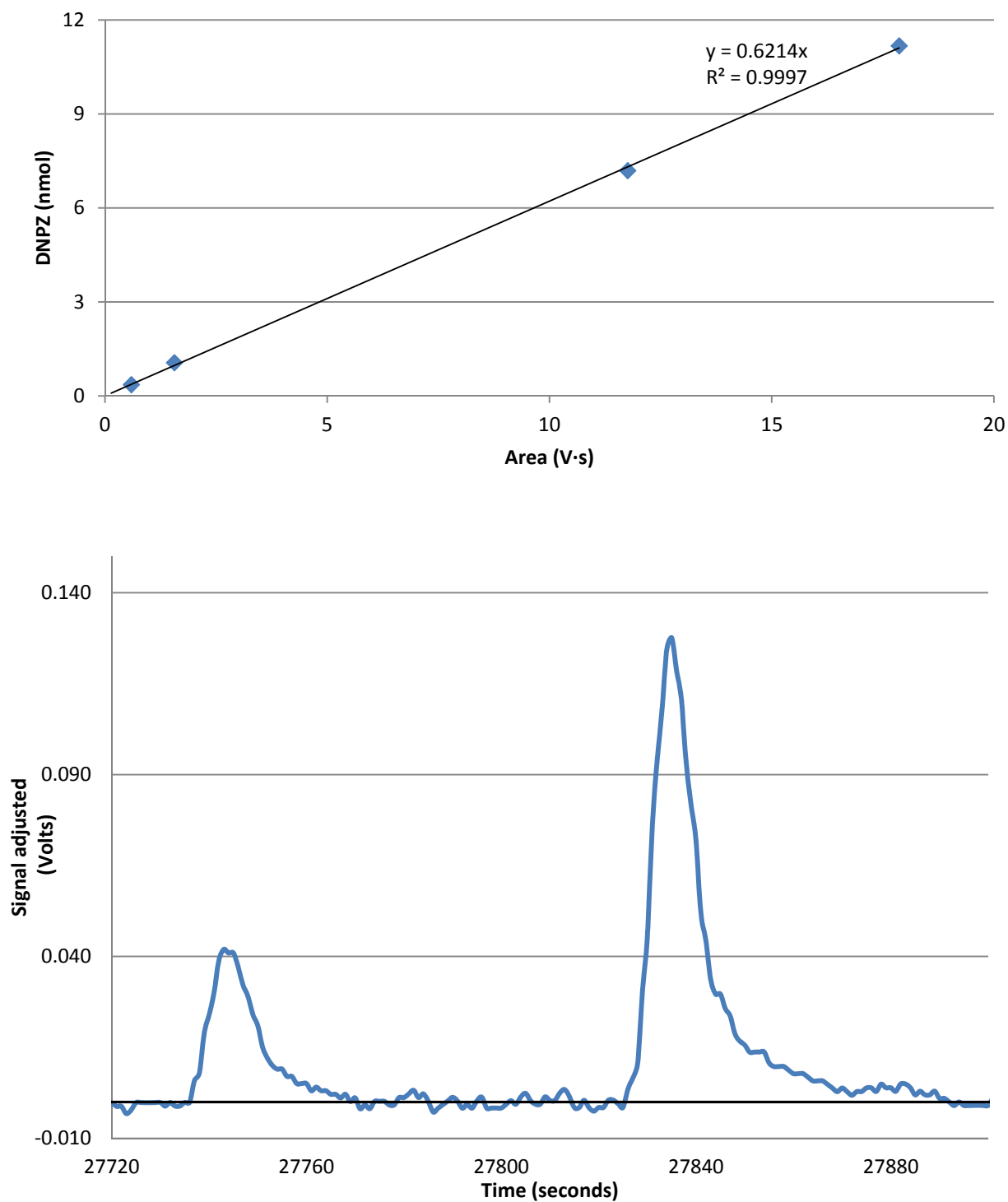
Kinetics of N-nitrosopiperazine formation from nitrite and piperazine in CO2 capture

Journal:	*Environmental Science & Technology*
Manuscript ID:	es-2012-04640f.R1
Manuscript Type:	Article
Date Submitted by the Author:	n/a
Complete List of Authors:	Goldman, Mark; University of Texas at Austin, Department of Chemical Engineering, C0400 Fine, Nathan; University of Texas at Austin, Department of Chemical Engineering, C0400 Rochelle, Gary; University of Texas, Chemical Engineering

SCHOLARONE™
Manuscripts

1
2
3
4
5
6
7
8
9
10
11
12
13
14
15
16
17
18
19
20
21
22
23
24
25
26
27
28
29
30
31
32
33
34
35
36
37
38
39
40
41
42
43
44
45
46
47
48
49
50
51
52
53
54
55
56
57
58
59
60
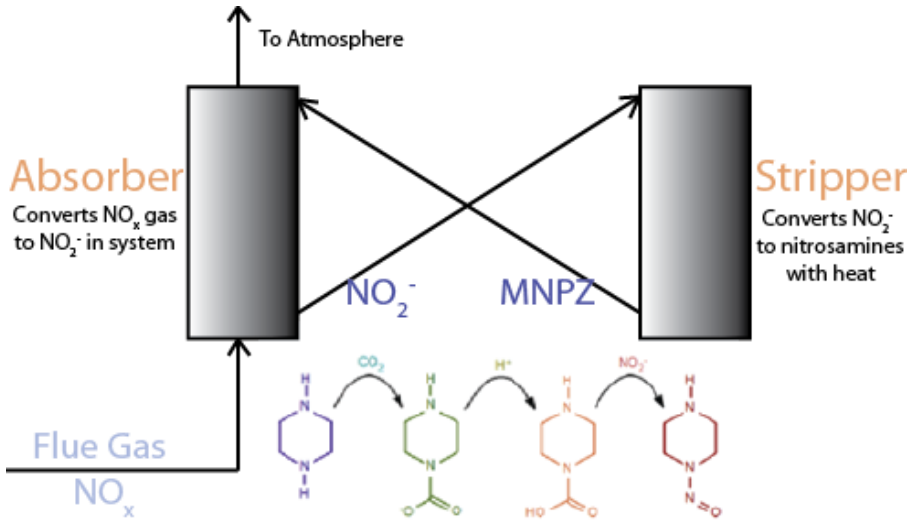
Kinetics of N-nitrosopiperazine formation from nitrite and piperazine in CO_2 capture

Mark J. Goldman, Nathan A. Fine, and Gary T. Rochelle*

The University of Texas at Austin, Department of Chemical Engineering, Luminant Carbon Management Program, 200 E Dean Keeton St. Stop C0400, Austin, TX 78712-1589

Abstract

Piperazine (PZ) is an efficient amine for carbon capture systems, but it can form N-nitrosopiperazine (MNPZ), a carcinogen, from nitrogen oxides (NO_x) in flue gas from coal or natural gas combustion. The reaction of nitrite with PZ was studied in 0.1 to 5 mol/dm^3 PZ with 0.001 to 0.8 mol CO_2/mol PZ at 50 to 135 °C. The reaction forming MNPZ is first order in nitrite, piperazine carbamate species, and hydronium ion. The activation energy is 84±2 kJ/mole with a rate constant of $8.5×10^3±1.4×10^3$ $dm^6mol^{-2}s^{-1}$ at 100 °C. The proposed mechanism involves protonation of the carbamate species, nucleophilic attack of the carbamic acid, and formation of bicarbonate and MNPZ. These kinetics and mechanism will be useful in identifying inhibitors and other strategies to reduce nitrosamine accumulation in CO_2 capture by scrubbing with PZ or other amines.

Keywords

Nitrosamine, amine scrubbing, piperazine, kinetics

Introduction

CO_2 capture by amine scrubbing will be an important technology to mitigate CO_2 emissions from coal- and gas-fired power plants. The process involves scrubbing flue gas with aqueous amine. The amine reacts with CO_2 to form a carbamate. In a stripping column, the carbamate is heated to release CO_2 and regenerate the aqueous amine.[1,2] The CO_2 can then be sequestered underground or used for enhanced oil recovery.[3] Traditional CO_2 removal processes for natural gas treating have used aqueous monoethanolamine (MEA). Concentrated aqueous piperazine (5 mol/dm^3 PZ) is being developed as an alternative solvent. Piperazine (PZ), a cyclic secondary diamine, absorbs CO_2 twice as fast as MEA, has almost twice the capacity of 7 molal MEA, and resists thermal and oxidative degradation better than MEA.[4]

Unfortunately, PZ forms nitrosamines, a class of carcinogenic compounds, at faster rates than MEA under carbon capture conditions. In pilot plant testing of 5 mol/dm^3 PZ on coal-fired flue gas, N-nitrosopiperazine (MNPZ) was found in the solvent at 1 to 3 mmol/kg.[5] MNPZ is a carcinogen with a TD50 of 8.78 mg/kg/day,[6] so the negative environmental implications could hinder application of PZ in carbon capture.

Nitrosamines in CO_2 capture can affect the environment by being directly released from the absorber column through aerosol formation, which are able to pass through mechanisms that trap volatile amines

and nitrosamines.[7,8] Nitrosamines can also be released from accidental spills. After leaving the system, nitrosamines can then disperse into the environment and affect human health. An understanding of MNPZ formation is needed to minimize MNPZ accumulation in the solvent so less MNPZ is released into the environment.

Different nitrogen-containing species can cause nitrosation. NO and NO_2, which are present in flue gas, can form nitrosamines with secondary amines through radical reactions.[9,10] Another path for nitrosation is absorption of NO_2 into the solution as nitrite. A previous study suggests that absorption as nitrite occurs at about the same rate as the direct nitrosation of PZ by bubbling 25 ppm of NO_2 and NO through 2.5 mol/dm^3 PZ at 44 °C.[2] Although that experiment did not include CO_2, the results indicate that nitrosation could occur by direct reaction with NO_x and by reaction with nitrite. This work focuses on the formation of nitrosamines from aqueous nitrite. The stoichiometry of the reaction to form nitrosamines from nitrite is shown in Equation 1.

$$R_2NH + NO_2^- \xrightarrow{catalyst} R_2NNO + OH^- \tag{1}$$
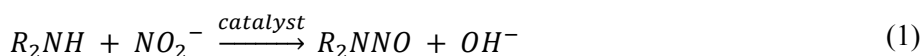
Most of the early literature suggested that nitrosation by aqueous nitrite in basic solutions did not occur,[11] but in 2002, Choi performed an experiment that indicated that carbon dioxide possibly accelerates the formation of nitrosamines from nitrite in basic conditions.[12] Lv et al. proposed that carbon dioxide catalyzes N-nitrosodimethylamine formation by forming a carbamate ion and determined that a concerted mechanism, shown in Figure 1, was favored over a stepwise mechanism.[13] Sun et al. modeled reaction energies of this mechanism and others. They determined the mechanism shown in Figure 1, which required a solvated activation energy of 45 kcal/mol.[14]
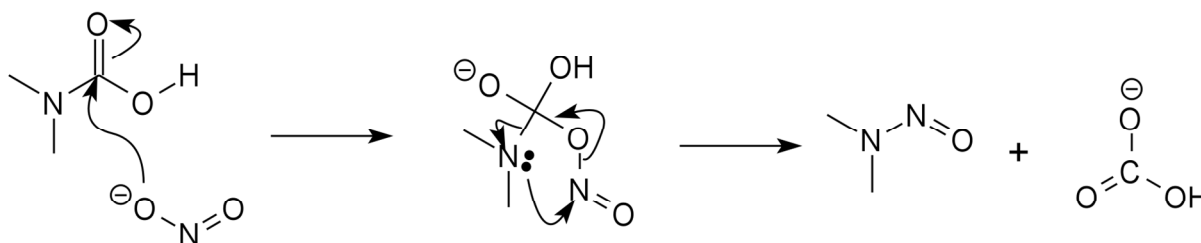
Figure 1. A mechanism for the CO_2-catalyzed nitrosation of dimethylamine modeled by Lv and Sun.[14,15]

Although these theoretical studies have been done, there have been no experimental studies of nitrosation by nitrite at high pH in the presence of CO_2. This work explores the kinetics of MNPZ formation from nitrite at conditions of the stripper in amine scrubbing for CO_2 capture.

Methods.

Solution Preparation and Heating

A list of chemicals and purities is included in the supplemental information. Aqueous solutions were made containing 0.1–5 mol/dm^3 PZ. The solution chemically and physically absorbed carbon dioxide gas

at atmospheric pressure. These solutions were stored in sealed bottles at room temperature. Before being heated, sodium nitrite was added to the solutions at 6 to 10 mmol $NaNO_2$ per mol PZ. In one set of experiments, a phosphate buffer was used to vary pH at low PZ concentrations. These experiments used a solution of 0.1 mol/dm^3 PZ with 0.01 mol/dm^3 $KHCO_3$, which forms carbamate in large yields, and 0.5 mol/dm^3 K_2HPO_4.[9] The pH of the solutions was measured at room temperature and adjusted to the desired value using KOH.

The solutions for each experiment were placed in five to seven 3/8-inch cylindrical steel tubes with Swagelok caps. The tubes were placed in convection ovens at 100–135 °C or in water baths at 50–80 °C. The cylinders were removed at a selected reaction time span and placed in room temperature water to cool rapidly. Within 48 hours of the cylinders being removed, the samples were transferred to amber vials and gravimetrically diluted 20x to 50x for analysis.

Analysis Methods

MNPZ and nitrite in the liquid samples were quantified by HPLC with a Polar Advantage 2 column (Dionex) and UV detection at 240 nm. The HPLC was calibrated with purchased sodium nitrite and MNPZ. Detailed analytical methods can be found in the supplemental information.

CO_2 in the initial solution was determined gravimetrically and confirmed using a total inorganic carbon method.[16] PZ in the sample was prepared gravimetrically and confirmed using an automatic titrator.[16]

The formation of MNPZ followed a first order dependence on nitrite, so a linear regression was performed on the nitrite at various times in the oven or water bath. The regression used Equation 2 which assumes the reaction was first order in nitrite and that all the nitrite formed MNPZ, creating a conservative measurement of MNPZ.

$$\frac{dMNPZ}{dt} = \frac{-d[NO_2^-]}{dt} = k_{obs}[NO_2^-] \tag{2}$$

Equation 3 displays the linearized form of the equation used in analysis.

$$\ln([NO_2^-]) = \ln([NO_2^-]_{initial}) - k_{obs}t \tag{3}$$

The regression solved for the observed first order rate constant, k_{obs}. The k_{obs} values obtained under different conditions can then be compared to determine reaction dependence with other species.

Concentrations of PZ species and pH in solutions containing PZ and CO_2 were estimated by the Independence thermodynamic model developed by Frailie in Aspen Plus®. Detailed descriptions of an adequate previous model with plots of pH and speciation can be found in the literature.[17,18]

Results & Discussion

Table 1 summarizes the loss of nitrite from 50–135 $^{\circ}$C. The rate is reported as k_{obs} estimated from the data from each experiment by Equation 3. This value is compared to the k_{obs} estimated by a global correlation using Equation 7. A significant rate of nitrite disappearance was observed in 0.5–5 mol/dm^3 PZ at 50–100 $^{\circ}$C. The rate was also measured in phosphate buffered solution at 135 $^{\circ}$C at 0.1 mol/dm^3 PZ.

Table 1. Summary of nitrosation experiments. Between 6 and 10 mmol NaNO$_2$ per mol PZ was added to each sample. Total CO$_2$ represents both physically and chemically absorbed CO$_2$. k_{obs} is the observed first order rate constant for nitrite disappearance from each experiment. Yield describes how much nitrite formed MNPZ.

T (°C)	PZ (mol/dm^3)	Total CO$_2$ (mol/dm^3)	pH** (at T)	k_{obs} (s^{-1} 10^6)		Yield (%)
				Exp.	Model (Eq. 7)	
135	0.099 ± 0.004	0.040 ± 0.003	7.37 ± 0.01*	120 ± 10	148 ± 47	114
135	0.099 ± 0.004	0.040 ± 0.003	7.58 ± 0.01*	72 ± 4	90 ± 29	106
135	0.099 ± 0.004	0.040 ± 0.003	7.85 ± 0.01*	52 ± 6	49 ± 16	82
135	0.099 ± 0.004	0.040 ± 0.003	8.04 ± 0.01*	30 ± 2	31 ± 10	112
100	5.0 ± 0.2	1.00 ± 0.08	9.09 ± 0.05**	6.3 ± 0.2	6.9 ± 2.4	94
100	5.0 ± 0.2	2.13 ± 0.17	8.72 ± 0.05**	32 ± 1	35 ± 12	80
100	5.0 ± 0.2	2.94 ± 0.24	8.36 ± 0.05**	112 ± 4	110 ± 38	90
100	5.0 ± 0.2	4.14 ± 0.33	7.69 ± 0.05**	675 ± 26	726 ± 252	94
100	4.9 ± 0.2	3.05 ± 0.24	8.30 ± 0.05**	149 ± 3	131 ± 45	101
100	1.7 ± 0.1	1.07 ± 0.09	8.22 ± 0.05**	70 ± 3	55 ± 19	97
100	0.48 ± 0.02	0.30 ± 0.02	8.18 ± 0.05**	13.7 ± 0.2	17 ± 6	93
100	4.29 ± 0.04	0.011 ± 0.001	8.24 ± 0.01$^+$	3.1 ± 0.1	0.5 ± 0.1	82
80	5.0 ± 0.2	2.96 ± 0.24	8.61 ± 0.05**	13.3 ± 0.3	13 ± 5	79
50	5.0 ± 0.2	2.96 ± 0.24	9.08 ± 0.05**	0.43 ± 0.01	0.3 ± 0.1	99

*Buffered by 0.5 mol/dm^3 phosphate adjusted by KOH. pH measured at room T and corrected to T.
**pH at T estimated by "Independence" in Aspen Plus$^{®}$
+Included 2.5 mol/dm^3 H$_2$SO$_4$, pH measured at room T and adjusted to T, not regressed in the model

The yield of MNPZ is defined as the final MNPZ over the difference in the final and initial nitrite. An average yield of 95±11% was obtained for the 14 experiments discussed here. The high yield indicates no major competing reactions consuming nitrite occur in the PZ solvent. This value is slightly below unity because MNPZ decomposes at these reaction conditions.[19]

Small, but quantifiable, amounts of N, N'-nitrosopiperazine (DNPZ) were found in various samples. However, the nitrite yield to DNPZ was less than 1% under these conditions, so it is not a major product.[19]

Dependence on Nitrite

MNPZ formation is first order in nitrite. Using a linear regression derived from Equation 2, the average coefficient of determination for all experiments is 0.991. Figure 2 shows this first order dependence by the apparent linear decrease of nitrite on a log scale.
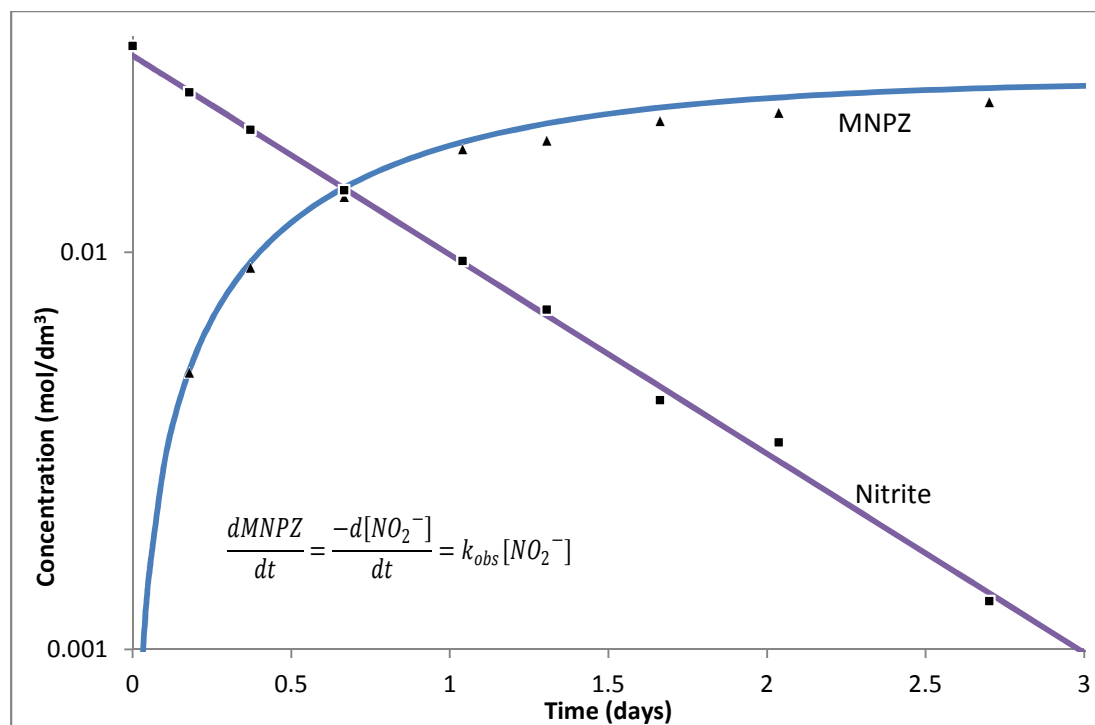
Figure 2. MNPZ formation in 5 mol/dm^3 PZ loaded to 0.60 mol CO_2/mol PZ at 80 °C. Curves calculated with k_{obs} = 13·10^6 s^{-1}

The decrease in nitrite is associated with a stoichiometric increase in MNPZ. The curves were calculated from the equation in the figure using a rate constant, k_{obs} of 13×10^6 s^{-1}. The slightly lower calculated MNPZ may result from MNPZ degradation, bias in the calibration curves, or a yield less than one.

Using data similar to Figure 2, an observed first order rate constant, k_{obs}, was determined from the nitrite for 4 sets of reaction conditions. Experiments were conducted with 5 mol/dm^3 PZ with between 0.2-0.8 mol CO_2/mol PZ, with between 0.5-5 mol/dm^3 Pz and 0.6 mol CO_2/mol PZ, with 5 mol/dm^3 PZ at lower temperature, and with 0.1 mol/dm^3 PZ in a phosphate buffer.

Dependence on pH

Four experiments with equal bicarbonate and PZ and with different proportions of monobasic and dibasic phosphate had a pH at room temperature between 7.1 and 7.8. The van't Hoff equation and thermodynamic data were used to estimate the pH at reaction conditions.[20,21] The pK$_a$ difference of a monobasic phosphate buffer between the oven conditions (135 °C) and room temperature is 0.17. This difference would correspond to a similar change in pH for the four solutions because the solutions are in the range of the phosphate buffer.

The pH measurements at room temperature were adjusted to account for the increase in K$_a$ of the buffer at 135 °C. Figure 3 demonstrates a first order dependence of k_{obs} on H$^+$ concentration determined from the pH with a coefficient of determination of 0.96.
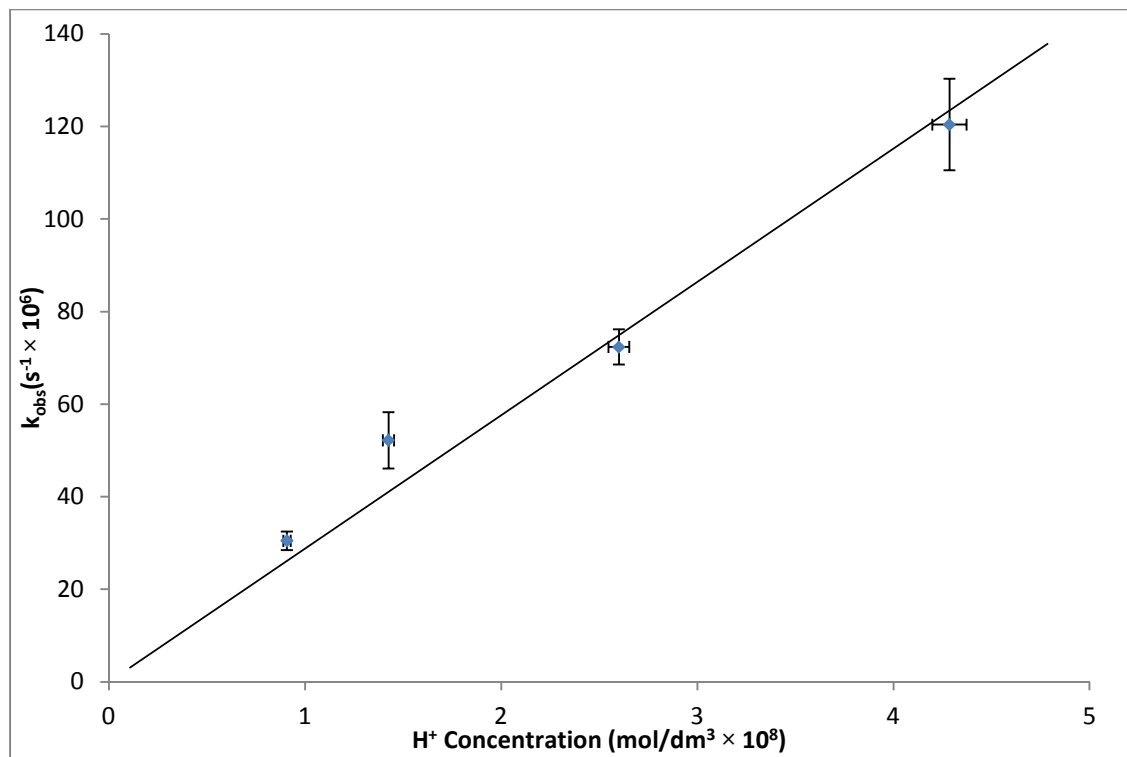
Figure 3. Varying pH in 0.5 mol/dm^3 phosphate with 0.1 mol/dm^3 PZ and a loading of 0.4 mol CO$_2$/mol PZ. The H$^+$ concentration is given by the negative log of the pH.

From this analysis, the observed rate constants were normalized for pH at the reaction conditions by defining k$_2$ using the following equation:

$$\frac{dMNPZ}{dt} = k_2[NO_2{}^-][H^+] \tag{4}$$

The formation of MNPZ, shown by Equation 1, indicates the production of a basic product. Solutions without a phosphate buffer would still have a relatively stable pH because they contain two buffers: protonated PZ/PZ and protonated PZ carbamate/PZ carbamate. This natural buffering effect, along with the minimal concentration of nitrite added, significantly reduces the potential change in pH during nitrosation of the more concentrated PZ solutions.

<u>Dependence on carbamate</u>

Previous work has suggested that CO$_2$ plays a role in nitrosation of CO$_2$ capture solvents. To test the effect of CO$_2$, the authors added strong acid to match the pH of solutions with and without significant quantities of CO$_2$. A 4.3 mol/dm^3 PZ solution with 0.25 mol H$_2$SO$_4$/ mol PZ was heated to 100 °C to determine how nitrosation occurs with low total CO$_2$. The solution absorbed atmospheric CO$_2$ to a low loading of 0.002 mol CO$_2$/mol PZ during solution preparation. The k$_{obs}$ for this condition was 3.1×10^6 s^{-1}. This rate is significantly slower than 112×10^6 s^{-1}, the rate in 5 mol/dm^3 PZ with a loading of 0.6 mol CO$_2$/mol PZ heated to 100 °C. Despite the large rate difference, the pH difference between the two

experiments was only 0.12±0.06. Since the two solutions with different amounts of carbamate resulted in large reaction rate differences, total dissolved CO_2 significantly catalyzes nitrosation.

To understand how absorbed CO_2 affects nitrosation, the speciation of CO_2 inside piperazine solution must be understood. All of the CO_2 added to the system can exist as physically absorbed CO_2, bicarbonate, or as a carbamate with PZ. In our experiments, the majority of CO_2 exists as a carbamate. Since PZ contains two secondary amines, a PZ carbamate molecule can either contain an unprotonated amine, a protonated amine, or a carbamate group on the other amine group. These species are called PZ carbamate, protonated PZ carbamate, and PZ dicarbamate, respectively. At high pH and low total dissolved CO_2, PZ carbamate dominates. As more CO_2 is added, the PZ carbamate concentration starts to decrease and protonated PZ carbamate and PZ dicarbamate concentrations increase. When the total dissolved CO_2 approaches the amount of PZ, significant bicarbonate concentrations arise, but this condition is not often seen in carbon capture systems with PZ. More information about speciation can be found in previous literature.[4,18]

To discover which species containing CO_2 are reactive, the authors used the Independence thermodynamic model in Aspen Plus$^®$ to calculate the pH and speciation of 7 solutions heated to 100 °C.[17] From this, the k_2 for each set of solutions was determined from Equation 4.   A rate constant, k_t, was defined to determine the species that catalyze nitrosation along with the order of concentration dependence.

$$k_t = \frac{k_2}{[C_{species}]^\alpha}$$
(5)

Each species listed in Table 2 was analyzed in the 7 experiments at 100 °C. For each species in Table 2, an order of reaction was found that resulted in the smallest relative standard deviation between the 7 experiments, representing the best correlation between reaction rate and the species concentration.

Table 2. Reaction dependence on different carbamate species. Total dissolved CO_2 represents all CO_2 added to the system. Relative standard deviation of k_t for 7 experiments found using Equation 5.

Species	Optimized α	Relative Standard Deviation of k_t with optimized α	Relative Standard Deviation of k_t with α = 1
Physically Dissolved CO_2	0.30	0.50	1.46
Bicarbonate	0.50	0.51	0.94
PZ carbamate	0.00	0.74	0.91
Protonated PZ carbamate	0.77	0.19	0.30
PZ dicarbamate	0.39	0.37	1.32
Total CO_2 as carbamate	0.87	0.22	0.28
Total Dissolved CO_2	1.09	0.17	0.18

The high errors associated with the individual carbamate species is likely due to multiple carbamate species participating in nitrosation. Multiple PZ carbamate species can catalyze nitrosation as long as the two amine groups on PZ function semi-independently. Previous research indicates that protonation of the

1
2
3
4
5
6
7
8
9
10
11
12
13
14
15
16
17
18
19
20
21
22
23
24
25
26
27
28
29
30
31
32
33
34
35
36
37
38
39
40
41
42
43
44
45
46
47
48
49
50
51
52
53
54
55
56
57
58
59
60

inactive nitrogen on PZ does not make the other nitrogen-containing group unreactive.[22] The ability for multiple carbamate groups to participate in reaction would explain why none of the individual carbamate species had both an order of reaction similar to stoichiometric orders of reaction (0.5, 1, 2) and a low relative error. The total carbamate species correlated better than any particular carbamate species because of this additive affect. Since the different carbamate species are likely to have slightly different rate constants, there is some error associated with using the sum of all carbamate species. However, uncertainties in the speciation model prohibit any meaningful analysis on the individual carbamate rate constants.

The total dissolved CO_2 is a practical way to determine total carbamate concentration in most solutions since physically dissolved CO_2 and bicarbonate are only present at low concentrations. Figure 4 demonstrates this practical correlation in experiments with 0.5 to 5 mol/dm³ PZ over a range of loadings.
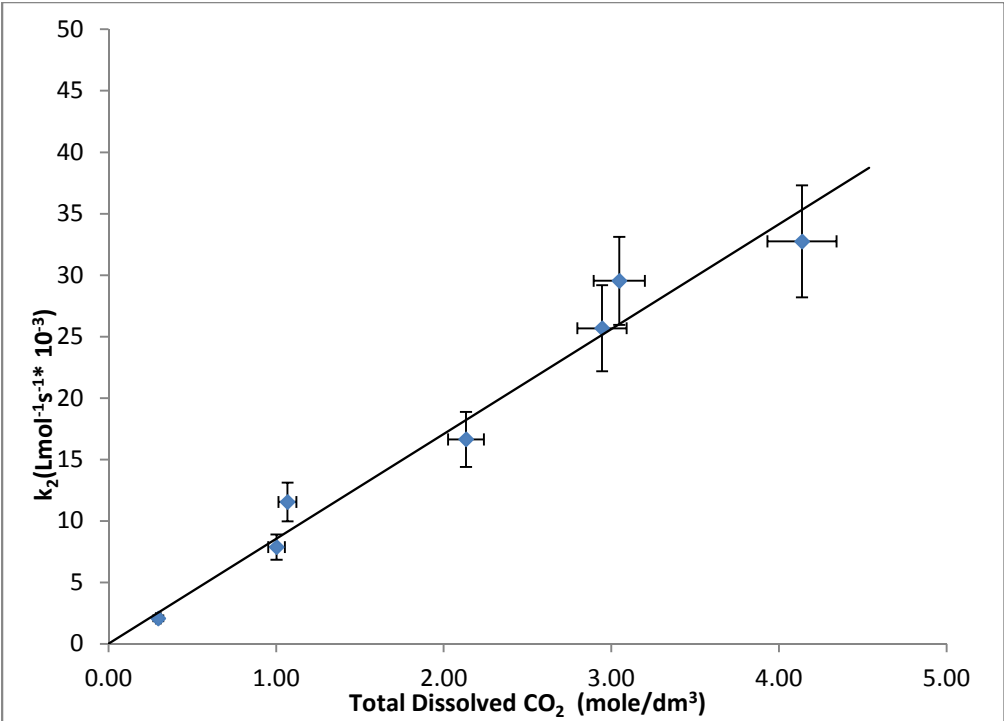
Figure 4. Reaction rate dependence on total dissolved CO_2 in 0.5, 1.7, and 5 mol/dm³ PZ with 0.6 mol CO_2/mol PZ and 5 mol/dm³ PZ with 0.1, 0.2, 0.3, 0.8 mol CO_2/mol PZ.

Using the effect of carbamate, Equation 6 represents a simplified rate equation which agrees with the experimental data.

$$\frac{dMNPZ}{dt} = k_3[NO_2^-][H^+][R_2NCOO^-] \tag{6}$$

R_2NCOO^- corresponds to the carbamate species in the solution, but it is calculated using the total amount of CO_2 added per volume solution. As long as the moles of CO_2 are fewer than the moles of PZ, this approximation will hold. With more CO_2 than PZ, significant levels of bicarbonate form.

Dependence on temperature

Nitrosation is faster at higher temperature. Two effects cause this change: there is more thermal energy to overcome the activation energy, and the pH decreases with temperature due to the temperature dependence of the pK_a of PZ. After normalizing the rate constant for the pH and total CO_2, the activation energy was determined to be 84±2 kJ/mol (Figure 5).
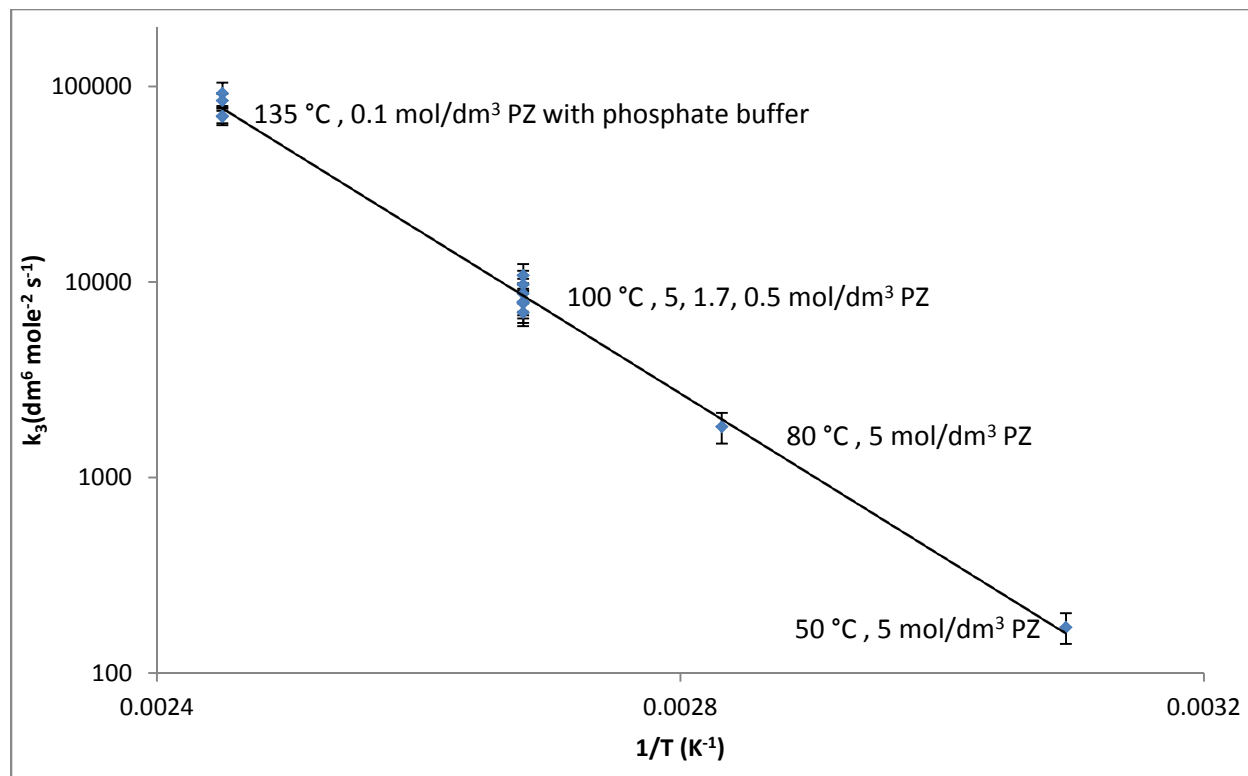
Figure 5. Reaction rate dependence on temperature, activation energy = 84±2 kJ/mol.

Rate Equation and Model

Using the temperature dependence and Equation 6, a model for MNPZ formation can predict nitrosation of PZ by aqueous nitrite in the presence of CO_2. All of the k_3 values, except the experiment with added sulfuric acid, were normalized to 100 °C and averaged to obtain $k_{3,avg} \approx 8.5 \times 10^3 \pm 1.4 \times 10^3$ $L^2 mol^{-2} s^{-1}$.

$$\frac{dMNPZ}{dt} = k_{3,avg} e^{\frac{E_a}{R}\left(\frac{1}{373.15K} - \frac{1}{T_{exp}}\right)} [NO_2{}^-][H^+][CO_2\ added] \tag{7}$$

The CO_2 loading should be less than 1.0 mol/mol PZ for this model to accurately predict kinetics. This model might not be applicable in the presence of significant amounts of formaldehyde which can also catalyze nitrosation at similar conditions as CO_2.[23] Previously published data on pH of PZ can be used to determine the hydrogen ion concentration.[18] Figure 6 shows how the observed first order rate constants, k_{obs}, compare to values predicted from Equation 7.
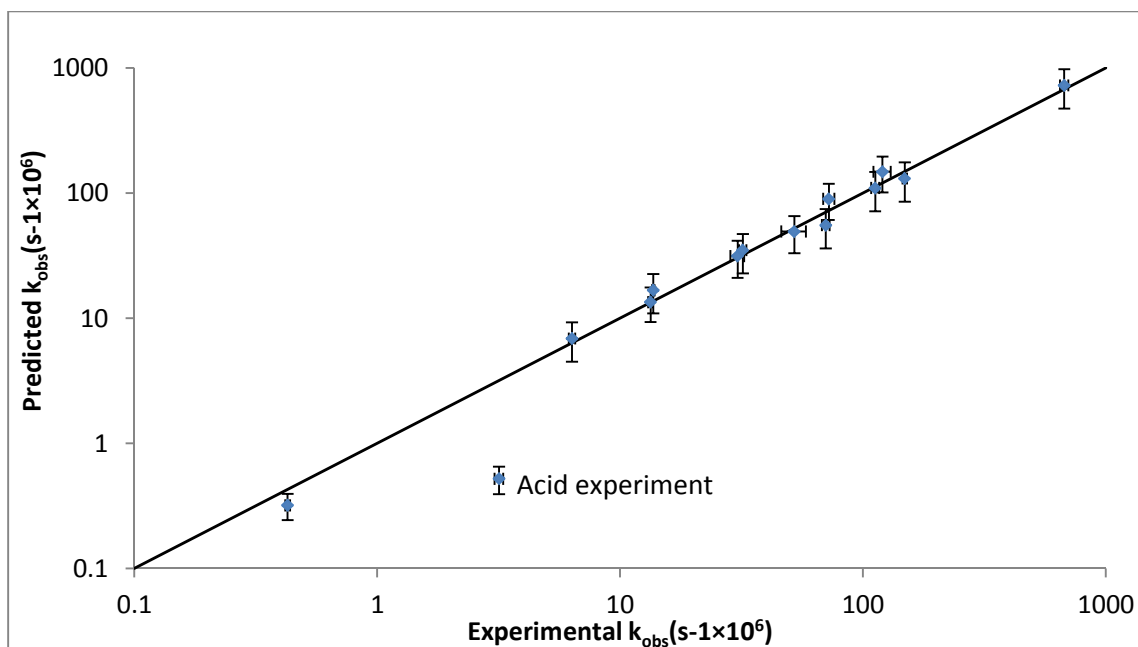
Figure 6. Application of kinetic model to experimental data. The predicted k_{obs} for each experiment was obtained from the kinetic model (Equation 7). The line indicates perfect agreement between experimental and predicted data. The acid experiment was not regressed

In Figure 6, the acid experiment with minimal CO_2 shows significantly higher rate than the model predicts. This indicates that at low carbamate concentrations, a different nitrosation reaction may dominate.

Mechanism

Figure 7 shows a mechanism that would follow the kinetics in Equation 6. This mechanism is similar to that proposed by Lv and Sun.[14,15] Step 1 is an equilibrium acid-base reaction. Since the pKa of the carbamate functional group on PZ is around 6.7±0.2 while the pKa of typical PZ solvent is between 7.7 and 9.1, the equilibrium would lie toward the unprotonated carbamate.[17,24] Step 2 indicates a nucleophilic attack on the carbonyl group by the nitrite ion. Step 3 includes the reformation of the carbonyl group accompanied by the formation of the N-nitrosamine bond in one concerted step. A concerted mechanism for this step was shown to be energetically favored over a stepwise mechanism.[13]
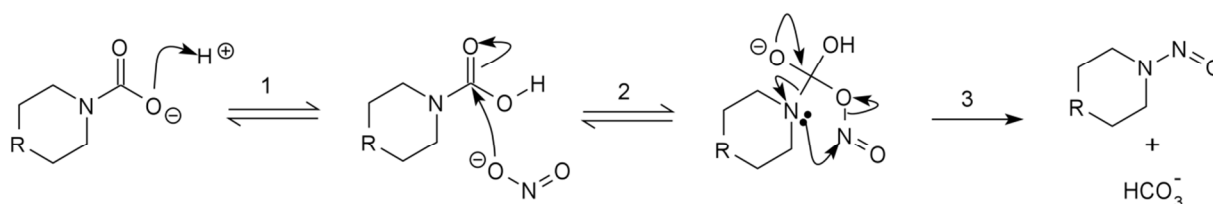
Figure 7. The proposed mechanism for nitrosation of PZ in aqueous carbon capture. The R group can represent NH, $NCOO^-$, or NH_2^+.

1
2
3
4
5
6
7
8
9
10
11
12
13
14
15
16
17
18
19
20
21
22
23
24
25
26
27
28
29
30
31
32
33
34
35
36
37
38
39
40
41
42
43
44
45
46
47
48
49
50
51
52
53
54
55
56
57
58
59
60

Environmental Significance

The formation of nitrosamines can be reduced through the use of nitrite scavengers or amine blends. Nitrite scavengers could prevent nitrosation, but most act through irreversible reactions. The scavenger products would accumulate in the solvent and lower the absorption performance. Using PZ blended with a primary or tertiary amine is another possibility to prevent nitrosamine formation because the primary amines do not form stable nitrosamines and tertiary amines resist nitrosation since an iminium ion is necessary.[11,25] Significant work has already been conducted to study the performance of amine blends, but little research exists on the formation of nitrosamines in these blends. Though initial studies indicate that primary and tertiary species form nitrosamines more slowly in alkaline conditions than secondary amines, formal kinetic studies have not been performed.[2] By determining reaction kinetics of other amines, a blend that reduces stable nitrosamine formation could be utilized.

Another possible way to mitigate nitrosamine concentration is to cause denitrosation of MNPZ. Previous experiments indicate that MNPZ thermally degrades at stripper temperature in carbon capture processes with no increase in equipment costs.[19] Another possibility for denitrosation includes UV degradation,[26] though the opaque nature of degraded PZ solvents would lower the efficiency of this method.

In summary, nitrosation of PZ is a critical problem since it may hinder the use of PZ in carbon capture. Nitrite that forms from the oxidation of NO_2 will react with PZ, especially at stripper conditions, to form MNPZ. The kinetics for nitrosation of PZ in carbon capture conditions will be helpful when designing a system to minimize nitrosamine formation from nitrite. The mechanism provided gives greater understanding of the chemistry behind nitrosation in amine scrubbing.

Author Information

Dr. Gary T Rochelle; Phone: (512) 471-7230; Fax: (512) 475-7824; email: gtr@che.utexas.edu

Acknowledgements

Supporting Information Available

Detailed descriptions of the chemicals used and of the analysis methods appear in supporting information. This information is available free of charge via the Internet at http://pubs.acs.org/.

References

(1)   Rochelle, G. T. Amine scrubbing for CO_2 capture. *Science* **2009**, *325*, 1652–4.

(2)   Dai, N.; Shah, A. D.; Hu, L.; Plewa, M. J.; Mckague, B.; Mitch, W. A. Measurement of Nitrosamine and Nitramine Formation from NO. *Environ. Sci. Technol.* **2012**, *46*, 9793–9801.

(3)   Jessen, K.; Kovscek, A. R.; Orr, F. M. Increasing CO_2 storage in oil recovery. *Energ. Converse. Manage.* **2005**, *46*, 293–311.

(4)   Rochelle, G.; Chen, E.; Freeman, S.; Van Wagener, D.; Xu, Q.; Voice, A. Aqueous piperazine as the new standard for CO_2 capture technology. *Chem. Eng. J.* **2011**, *171*, 725–733.

(5)   Nielsen, P. T.; Li, L.; Rochelle, G. T. Piperazine degradation in pilot plants. Presented at GHGT-11, Kyoto, Japan, November 20, 2012, to be published in *Energy Procedia* **2013**.

(6)   Garcia, H.; Keefer, L.; Lijinsky, W.; Wenyon, C. Carcinogenicity of nitrosothiomorpholine and 1-nitrosopiperazine in rats. *J. Cancer. Res. Clin. Oncol.* **1970**, *74*, 179–184.

(7)   Fulk, S. M.; Rochelle, G. T. Modeling aerosols in amine-based CO_2 capture. Presented at GHGT-11, Kyoto, Japan, November 20, 2012, to be published in *Energy Procedia* **2013**.

(8)   Kolderup, H.; Hjarbo, K. W.; Mejdell, T.; Huizinga, A.; Tuinman, I.; Zahlsen, K.; Vernstad, K.; Hyldbakk, A.; Holten, T.; Kvamsdal, H. M.; van Os, P.; da Silva, E. F.; Goetheer, E.; Khakharia, P. Emission studies at the Maasvlakte CO_2 capture pilot plant. Presented at The University of Texas Conference on CCS, Austin, TX, January 25, 2012.

(9)   Kirsch, M.; Korth, H. G.; Sustmann, R.; de Groot, H. Carbon dioxide but not bicarbonate inhibits N-nitrosation of secondary amines. Evidence for amine carbamates as protecting entities. *Chem. Res. Toxicol.* **2000**, *13*, 451–61.

(10)   Challis, B. C.; Kyrtopoulos, S. A. Rapid formation of carcinogenic N-nitrosamines in aqueous alkaline solutions. *Br. J. Cancer.* **1977**, *35*, 693–696.

(11)   Douglass, M.; Kabacoff, B. The chemistry of nitrosamine formation, inhibition and destruction. *J. Soc. Cosmet. Chem.* **1978**, *29*, 581–606.

(12)   Choi, J.; Valentine, R. L. Formation of N-nitrosodimethylamine (NDMA) from reaction of monochloramine: a new disinfection by-product. *Water Res.* **2002**, *36*, 817–24.

(13)   Lv, C. L.; Liu, Y. D.; Zhong, R.; Wang, Y. Theoretical studies on the formation of N-nitrosodimethylamine. *J. Mol. Struc.-Theochem* **2007**, *802*, 1–6.

(14)   Sun, Z.; Liu, Y. D.; Zhong, R. G. Carbon dioxide in the nitrosation of amine: catalyst or inhibitor? *J. Phys. Chem. A* **2011**, *115*, 7753–64.

(15)   Lv, C.-L.; Liu, Y. D.; Zhong, R.-G. Theoretical investigation of N-nitrosodimethylamine formation from dimethylamine nitrosation catalyzed by carbonyl compounds. *J. Phys. Chem. A* **2009**, *113*, 713–8.

(16)   Freeman, S. A. Thermal Degradation and Oxidation of Aqueous Piperazine for Carbon Dioxide Capture, The University of Texas at Austin, Austin, TX, 2011.

1
2
3
4
5
6
7
8
9
10
11
12
13
14
15
16
17
18
19
20
21
22
23
24
25
26
27
28
29
30
31
32
33
34
35
36
37
38
39
40
41
42
43
44
45
46
47
48
49
50
51
52
53
54
55
56
57
58
59
60

(17)   Frailie, P.; Rochelle, G. T. *Aspen Plus Independence Model*, version 2012; The University of Texas at Austin: Austin, TX, 2012.

(18)   Frailie, P. T.; Plaza, J. M.; Van Wagener, D.H.; Rochelle, G. T. Modeling piperazine thermodynamics. *Energy Procedia* **2011**, *4*, 35–42.

(19)   Fine, N. A.; Goldman, M. J.; Nielsen, P. T.; Rochelle, G. T. Managing n-nitrosopiperazine and dinitrosopiperazine. Presented at GHGT-11, Kyoto, Japan, November 20, 2012, to be published in *Energy Procedia* **2013**.

(20)   Goldberg, R. N.; Kishore, N.; Lennen, R. M. Thermodynamic Quantities for the Ionization Reactions of Buffers. *J. Phys. Chem. Ref. Data.* **2002**, *31*, 231–370.

(21)   Atkins, P. W.; de Paula, J. The response of equilibria to temperature. In *Physical Chemistry*; Oxford University Press: New York, 2006.

(22)   Castro, E. A.; Hormazabal, A.; Santos, J. G. Concerted Mechanism of 4-Cyanobenzoate with Secondary Alicyclic Amines in Aqueous Ethanol. *Int. J. Chem. Kinet.* **1997**, *30*, 267–272.

(23)   Casado, J.; Mosquera, M.; Paz, C.; Rodriguez-Prieto, F.; Vázquez-Tat, J. Nitrite Ion as a Nitrosating Reagent. Nitrosation of Morpholine and Diethylamine in the Presence of Formaldehyde. *J. Chem. Soc. Perkin. 2* **1984**, 1963–1966.

(24)   Scifinder Scholar, online version; Chemical Abstracts Service: Columbus, OH, 2012; RN: 10430-90-7 (accessed Sept 29, 2012); calculated using ACD/Labs software, version 11.02; ACD/Labs 1994-2012.

(25)   Sun, Z.; Liu, Y. D.; Zhong, R. G. Theoretical investigation of N-nitrosodimethylamine formation from nitrosation of trimethylamine. *J. Phys. Chem. A* **2010**, *114*, 455–65.

(26)   Stefan, M. I.; Bolton, J. R. UV direct photolysis of N-nitrosodimethylamine (NDMA): kinetic and product study. *Helv. Chim. Acta.* **2002**, *85*, 1416.

An effective multi-loop control system with storage tanks to improve control performance of CO2 capture

Journal:	*AIChE Journal*
Manuscript ID:	Draft
Wiley - Manuscript type:	Research Article
Date Submitted by the Author:	n/a
Complete List of Authors:	Ziaii, Sepideh; University of Texas at Austin, Department of Chemical Engineering, C0400 Rochelle, Gary; The University of Texas at Austin, Chemical Engineering Edgar, Thomas; University of Texas at Austin, Department of Chemical Engineering, C0400
Keywords:	Process control, Absorption, Aqueous solutions, Coal, Energy

SCHOLARONE™
Manuscripts

An effective multi-loop control system with storage tanks to improve control performance of CO$_2$ capture

Sepideh Ziaii, Gary T. Rochelle, Thomas F. Edgar

McKetta Department of Chemical Engineering, University of Texas at Austin,

Austin, TX 78712-1589

ABSTRACT

A multi-loop feedback control system is proposed to operate CO$_2$ capture with amine solvent efficiently over wide ranges of power plant operation. This work examines potential plantwide control structures in operating CO$_2$ capture in a process flow sheet of a fully integrated dynamic model created in Aspen Custom Modeler$^®$. This study illustrated that controlling the reboiler temperature and solvent circulation rate is an effective strategy in set point tracking and disturbance rejection in response to possible dynamic scenarios. Power plant load reduction, reboiler steam load reduction and foaming in the columns are the scenarios simulated for control configuration validation. This study also presents the effects of liquid residence time in the lean solution tank and rich solution tank on the dynamic performance of CO$_2$ capture in response to possible disturbances. Frequency response analysis is employed to illustrate how changing the holdup time influences the quality of dynamic characteristics such as response time and dampening oscillations.

KEYWORDS

Monoethanolamine; dynamic modeling; process control; CO$_2$ capture; amine scrubbing.

INTRODUCTION

Absorption/stripping using aqueous amine is a mature technology commonly used for removing CO$_2$ from natural gas, hydrogen, and other refinery gases, which makes it

1

applicable to removing CO_2 from flue gas in coal-fired power plants. However, the amine process is energy-intensive and requires economic consideration in both design and operation. For a coal-fired power plant using post-combustion amine absorption/stripping for CO_2 removal, full-load CO_2 capture could reduce net energy output by 11–40% from that of an equivalent plant without CO_2 capture.[1]

Figure 1 illustrates a standard scheme of an absorption/stripping process including the control valves. In the absorber, which is operated at atmospheric pressure and 40–60 °C, the flue gas from a coal-fired plant containing 10–12% CO_2 contacts an amine solution, and CO_2 is absorbed into the solution by physical and chemical mechanisms. The rich solution coming out of the absorber, which typically has a loading of 0.2–0.5 mol CO_2/mol amine, is directed to the stripper, operating at 1.5–2 atm and 100–120 °C. Water vapor accompanying CO_2 from the top of the stripper is condensed and returned to the cycle. The hot lean solution exiting the stripper is cooled by the cold rich solution in a cross heat exchanger (5–10 °C temperature approach) and is furthered cooled to 40 °C before entering the absorber.

The bulk of the energy requirement is due to the heat used for solvent regeneration and the work required to compress CO_2 to pipeline pressure for transport to a storage site. In a typical design, about 50% of the steam is extracted between the intermediate and low-pressure power plant turbines, expanded in a let-down turbine or valve, and then sent to the stripper column for solvent regeneration.

Previous work has enhanced the steady state absorption and energy performance in the conceptual design phase.[2-5] In addition to optimizing the process configuration and solvent selection for the base load, energy use can also be reduced by understanding the dynamics and exploring effective control configurations for transitional conditions. Although dynamics and control are very important with respect to operations, there are very few dynamic models presented for solvent-based absorption/desorption processes. For example, Kvamsdal et al.[6] presented a dynamic model for the absorber and studied

2

the transitional behavior of startup and power plant load variation. Lawal et al.[7] combined the dynamic model of absorber and stripper and simulated operation of the plant in response to the disturbances imposed by the upstream power plant. Prior studies[6-8] have examined the capture behavior isolated from the power plant and CO_2 compression system.

The first part of this paper presents the design of a control system for a capture plant using MEA by implementing a dynamic model of integrated absorption/stripping in Aspen Custom Modeler (ACM®). The dynamic models of the columns are developed with a non-equilibrium (rate-based) model. The rate-based approach has been defined and implemented in several studies on dynamic modeling of reactive distillation columns.[9,10] In addition, by incorporating practical performance models for pumps and the variable speed CO_2 compressor, the model accounts for the operational boundaries created by compressor and pump limitations. This work is unique since it uses a fully integrated model to simulate unsteady-state operations and examines the dynamic performance of a variety of control structures by dynamic simulation.

Developing an effective control system requires implementation of a systematic and coherent strategy regardless of the fact that it may not provide the complete and unique solution. The plantwide control procedure recommended by Seborg et al.[11] is a general strategy that can assist the control system designer to determine how to match controlled and manipulated variables, when to use an advanced control technique, and how to select an appropriate decoupled multi-loop control system. In contrast to previous work[7-9] that did not follow a systematic strategy, this study follows the steps of this plantwide control procedure to develop a multi-loop control system that can effectively handle load variations and disturbances. Partial load operations and foaming in the columns are two dynamic scenarios simulated in this study to validate suggested control structures.

3

Steam load reduction in CO_2 capture has been identified as an important operational scenario, but has not been studied with respect to dynamics and strategies of operation. Coal-fired power plants generate electricity at the base load and might be expected to run CO_2 capture at its full capacity continuously. Operating CO_2 capture flexibly, i.e., implementing an on/off operation, would be economical based on electricity and CO_2 market conditions.[12] In this operation all or part of the steam being used for solvent regeneration or for driving CO_2 compression can be used for power generation with daily peak power demand or high electricity prices.[13]

Load variation in the upstream power plant is another dynamic operation that influences capture performance. Understanding the effects and exploring energy efficient control strategies in response to power plant load variation is an important issue to investigate for developing an adequate control system. Prior work[6,7,14] that simulated the power plant load variation considered only the changes in flue gas inlet condition. They neglected the variation of total steam rate in the power cycle because of load variation. This is an important effect because it affects the operation of stripping and compression when reboiler steam is extracted from the power turbines. This work combines the model of the capture plant with a simple steady state model of steam turbines to take into account steam extraction.

Storage tanks are typically designed for smoothing responses and rejecting disturbances where the established control structure cannot bring further improvement.[15]

According to Luyben[16], considering control performance when the tanks and reactors are designed is very important especially for recycle systems due to the trade-off existing between design and control. However, tank sizing is typically done by rule of thumb rather than by evaluating dynamics and control targets. The second part of this paper examines the role of lean and rich storage tanks in the improvement of capture dynamic performances.

4

SYSTEM MODELING

The dynamic models developed for the absorber and the stripper are rate-based using film theory for liquid and vapor phases. They take into account the impact of equilibrium reactions (for the stripper) and kinetic reactions (for the absorber) on the mass transfer, thermodynamic non-idealities, and hydraulics of the structured packing. Models for the reboiler, absorber sump, and storage tanks are equilibrium stages that solve time variant energy and mass balances. Because the dynamics of heat exchangers, pumps, CO_2 compressor, control valves, and steam turbines are relatively fast, their dynamic effects are ignored by using steady state equations. The details of the thermodynamic model and physical properties are presented in a previous paper. [8]

This section provides the details of the modeling of the absorber column. The formulation of the stripper was presented in detail in Ziaii et al.[8] Similar to the stripper, the absorber column is divided into a number of segments, and time varying energy and mass balances are solved at each time step for both phases for each segment. The following assumptions are made:

1. The variation of the conditions in the radial direction is negligible in both liquid phase and gas phase.

2. Mixed-flow model is applied to determine the bulk properties, meaning that the outlet conditions are equal to the bulk conditions for each phase at each segment.

3. The heat transfer coefficient of the liquid phase is much bigger than that of the vapor phase due to very high thermal conductivity of aqueous solution; therefore, the dominant heat transfer resistance is assumed to be in the vapor phase.

The following equations are mass and energy balances for liquid and gas phases for components i=CO_2, H_2O, N_2, O_2 in the jth segment of the absorber column:

5

$$\frac{dM_{i,j}^{L}}{dt} = L_{j-1}x_{i,j-1} - L_{j}x_{i,j} - \frac{\pi}{4}D_c^2 l_j a_j N_{i,j} \tag{1}$$

$$\frac{dM_{i,j}^{V}}{dt} = V_{j+1}y_{i,j-1} - V_{j}y_{i,j} + \frac{\pi}{4}D_c^2 l_j a_j N_{i,j} \tag{2}$$

$$\frac{dE_{j}^{L}}{dt} = L_{j-1}H_{j-1}^{L} - L_{j}H_{j}^{L} - \frac{\pi}{4}D_c^2 l_j a_j \left(\begin{array}{l} h_j^L(T_j^L - T_j^I) + N_{CO_2,j}\bar{H}_{CO_2,j}^L \\ + N_{H_2O,j}\bar{H}_{H_2O,j}^L \end{array} \right)$$

$$\tag{3}$$

$$\frac{dE_{j}^{V}}{dt} = V_{j+1}H_{j+1}^{V} - V_{j}H_{j}^{V} + \frac{\pi}{4}D_c^2 l_j a_j \left(h_j^V(T_j^V - T_j^I) + N_{CO_2,j}\bar{H}_{CO_2,j}^V + N_{H_2O,j}\bar{H}_{H_2O,j}^V \right)$$

$$\tag{4}$$

It is assumed that heat transfer coefficient is so high that $T_j^L - T_j^I = 0$

$$\frac{dE_{j}^{total}}{dt} = L_{j-1}H_{j-1}^{L} - L_{j}H_{j}^{L} + V_{j+1}H_{j+1}^{V} - V_{j}H_{j}^{V} \tag{5}$$

$$M_{i,j}^{L} = \frac{\pi}{4}D_c^2 l_j h_{tj}^L C_j^L x_{i,j} \tag{6}$$

$$M_{i,j}^{V} = \frac{\pi}{4}D_c^2 l_j(\varepsilon - h_{tj}^L)C_j^V y_{i,j} \tag{7}$$

$$E_{j}^{L} = \frac{\pi}{4}D_c^2 l_j h_{tj}^L C_j^L H_j^L \tag{8}$$

$$E_{j}^{V} = \frac{\pi}{4}D_c^2 l_j(\varepsilon - h_{tj}^L)C_j^V H_j^V \tag{9}$$

$$E_{j}^{total} = E_j^V + E_j^L \tag{10}$$

$$\bar{H}_{i,j}^{L} = \frac{\partial}{\partial x_i}H_j^L \tag{11}$$

$$\bar{H}_{i,j}^{V} = \frac{\partial}{\partial y_i}H_j^V \tag{12}$$

$$H_j^L = x_{CO_2}H_{CO_2}^{ref,V} - x_{CO_2}\Delta H_{CO_2}^{des}(ldg_j, T_{ref}) + x_{H_2O}H_{H_2O}^{ref,V}$$

$$- x_{H_2O}\Delta H_{H_2O}^{vap}(T_{ref}) + \int_{Tref}^{T^L}Cp^L(ldg_j, T)dT \tag{13}$$

$$H_j^V = \sum_i y_{i,j}H_{i,j}^{ref,V} + \int_{Tref}^{T^V}\sum_i y_{i,j}CP_i^{V,ideal}dT \tag{14}$$

It is assumed that MEA is a non-volatile solvent and O_2 and N_2 are not solved in the solution. The mass flux of CO_2 and H_2O is calculated from the following equation:

6

$$N_{CO_2} = KG_{CO_2}(P^*_{CO_2} - Py_{CO_2})$$ (15)

Where KG_{CO_2} is a total mass transfer coefficient that involves the combination of the resistance to mass transfer in both liquid phase (kg'_{CO_2}) and gas phase (kg_{CO_2}).

$$\frac{1}{KG_{CO_2}} = \frac{1}{kg'_{CO_2}} + \frac{1}{kg_{CO_2}}$$ (16)

Liquid side mass transfer coefficient, kg'_{CO_2}, is calculated from a correlation as a function of partial pressure of CO_2 based on data provided by Aboudhier et al.[17]

$$log\, kg'_{CO_2} = -0.42\, log\, P^*_{CO_2}(Pa) - 4.98$$ (17)

The mass transfer resistance for H_2O in the liquid phase is negligible and H_2O mass flux is calculated from the following equation:

$$N_{H_2O} = Kg_{H_2O}(P^*_{H_2O} - Py_{H_2O})$$ (18)

DESIGN BASIS

This study simulates the dynamic operational scenarios in a capture plant initially designed based on the following inlet conditions and design specifications:

- Gas rate and composition: 5.48 kmol/s, 13% CO_2

- Electric rate: 100 MW

- Absorber packing height: 15 m

- Stripper packing height: 10 m

- CO_2 removal with 30 wt % MEA: 90%

- Lean loading: 0.233 mole CO_2/mole MEA

- Reboiler temperature: 120 °C

- CO_2 discharge pressure compressor: 150 bar

- Extracted reboiler steam = 30% total power cycle steam rate

- Steam turbine initial design condition[18]:

  P_{HP}^{in}= 290 bar, P_{IP}^{in}= 60 bar, P_{LP}^{in}= 2.65 bar, P_{LP}^{out}= 0.04 bar

7

Figure 1:

DESIGN OF CONTROL SYSTEM

Amine absorption/stripping is a complex process with respect to control due to the liquid recycle and heat integration between the absorber and the regenerator. A systematic strategy is required to develop a viable control structure working satisfactorily over a range of operating conditions. This work assumes that a multi-loop control approach is sufficient for our control objectives and a multi-variable control system is not necessary. We employ the plantwide hierarchical design procedure[11] to develop control structure alternatives and evaluate their performance in response to identified disturbances.

For operation of CO_2 capture in power plants, it is not required to satisfy any strict production rate or quality specifications. The most important objective in this energy intensive plant is to minimize energy consumption when the plant is operated at various operating loads. Therefore, a real-time optimization should be performed based on current markets to optimize operating conditions. The responsibility of the control system is to bring the plant to the optimal condition smoothly and quickly when a disturbance occurs. Safe operation of equipment such as the pumps and the CO_2 compressor should be addressed in control system design. To operate pumps safely the upstream level must be controlled to prevent cavitation and running dry. Compressor surge is also an unwanted condition that should be avoided by implementing a proper control strategy such as anti-surge control. The stripper pressure should be controlled with minimum oscillation to protect the overhead CO_2 compressor. To minimize thermal degradation of the solvent the reboiler temperature must be kept below the allowable value, 120 °C, for MEA. In summary, the following objectives are considered to evaluate control configurations.

> 1. Control the plant at optimum set points with a smooth and fast response during abnormal conditions.

8

2. Minimize oscillation in the inlet condition of the CO_2 compressor.

3. Control level on inventories

4. Keep $T_{Reboiler} \leq 120$ °C as much as possible during transition time

Identification of potential controlled and manipulated variables and proposing applicable control structures is the next step in the control system design procedure. Liquid levels in the inventories, absorber and stripper sumps, and lean and rich storage tanks are process variables that should be controlled within a practical range. Other than liquid levels, the task of this work is to identify the potential controlled variables among measurable process variables. Table 1 lists the available manipulated variables and potential controlled variables with the location of the measurement and/or the source of an inferential measurement.

Table 1: Potential manipulated and controlled variables for CO_2 capture plant

Process variables	Location/symbol
Liquid level, CV	Absorber sump, H_A
Liquid level, CV	Stripper sump, H_S
Liquid level, CV	Lean tank, H_L
Liquid level, CV	Rich tank, H_R
Flow rate, CV	Reboiler extracted steam , F_s
Flow rate, CV	Absorber sump effluent liquid, F_1
Flow rate, CV	Rich tank effluent liquid, F_2
Flow rate, CV	Stripper sump effluent liquid, F_3
Flow rate, CV	Lean tank effluent liquid, F_4
Lean loading(x_{CO2}/x_{MEA}), CV	Stripper sump effluent, Lldg (Inferred by density or temperature)
Rich loading(x_{CO2}/x_{MEA}), CV	Absorber sump effluent, Rldg (Inferred by density or temperature)
Pressure, CV	Top of the stripper, P_{top}
Temperature, CV	Reboiler, T_{Reb}
CO_2 removal, CV	CO_2 composition and gas rate are measured at absorber inlet and outlet gas streams, Rem
Compressor speed, MV	CO_2 compressor, speed

9

Control valve position, MV	Extracted steam valve, V_s
Control valve position, MV	Absorber sump downstream valve, V_1
Control valve position, MV	Rich tank downstream valve, V_2
Control valve position, MV	Stripper sump downstream valve, V_3
Control valve position, MV	Lean tank downstream valve, V_4

In order to minimize oxidative degradation in the absorber sump, prevent thermal degradation in the stripper sump, and meet hydraulic requirements in the reboiler, the sumps are fitted with level controls manipulating downstream valves (V_1 and V_3), which have the most direct influence on the controlled variables. Based on simulation, adjustment of solvent circulation rate is a strategy driving the plant to the optimum condition during a transitional operation. Therefore, one of the liquid valves (V_2 and V_4) is used for this purpose and the other is employed to control tank levels. The following are two alternatives for controlling tank level by one valve:

1. Control the level of one tank by its downstream valve and let the level in the other tank vary freely.

2. Control the ratio of the level of tanks by one of the downstream liquid valves.

By accommodating the inventories with level controls, three manipulated variables remain to control the plant at the desired operating condition: compressor speed, steam valve (V_s), and liquid valve (V_2 or V_4). To set up a multi-loop single input-single output (SISO) control system, three controlled variables should be selected among the ones listed in Table 1. A preliminary steady state relative gain array analysis (RGA) is performed on different sets of CVs by perturbing the MVs. As a result, five control configurations are found effective; however, some of them show a higher degree of loop interaction. Table 2 summarizes the different structures of major control loops (excluding liquid level control loops) along with their computed relative gain array and preferred MV-CV pairing. The configurations are different in terms of controlled variables and pairing. Based on this analysis, F_L-Lldg-P and F_L-T-P configurations appear to be the least and most interactive systems, respectively.

10

Table 2: Control system structures for MEA plant

Configuration name		RGA (MV-CV pairing)		

F_L-F_S-P

$$\begin{array}{c} & V_2 & V_s & speed \\ F_1 \\ F_s \\ P_{strip} \end{array} \begin{bmatrix} \underline{1.0846} & -0.0001 & -0.0845 \\ -0.0094 & \underline{0.6732} & 0.3362 \\ -0.0752 & 0.3270 & \underline{0.7483} \end{bmatrix}$$

F_L-T-P

$$\begin{array}{c} & V_2 & V_s & speed \\ F_1 \\ T_{reb} \\ P_{strip} \end{array} \begin{bmatrix} \underline{1.0031} & -0.1451 & 0.1420 \\ -0.0101 & \underline{2.5789} & -1.5687 \\ -0.0070 & -1.4337 & \underline{2.4267} \end{bmatrix}$$

F_L-Lldg-P

$$\begin{array}{c} & V_2 & V_s & speed \\ F_1 \\ Lldg \\ P_{strip} \end{array} \begin{bmatrix} \underline{1.0073} & -0.2004 & 0.1930 \\ -0.0155 & \underline{1.0512} & 0.0002 \\ 0.0081 & 0.1852 & \underline{0.8067} \end{bmatrix}$$

Rldg-Lldg-P

$$\begin{array}{c} & V_4 & V_s & speed \\ Rldg \\ Lldg \\ P_{strip} \end{array} \begin{bmatrix} \underline{0.6361} & 0.1695 & 0.1944 \\ 0.3557 & \underline{0.6441} & 0.0002 \\ 0.0082 & 0.1864 & \underline{0.8055} \end{bmatrix}$$

T-Rem-P

$$\begin{array}{c} & V_4 & V_s & speed \\ T_{reb} \\ Rem \\ P_{strip} \end{array} \begin{bmatrix} \underline{0.8972} & 0.0259 & 0.0769 \\ -0.0010 & \underline{0.8057} & 0.1952 \\ 0.1037 & 0.1684 & \underline{0.7279} \end{bmatrix}$$

This study incorporates the following transitional scenarios as the major disturbances influencing the operation of the capture:

1. Reboiler partial load operation: this operation is simulated by reducing the steam flow rate with the extracted steam valve.

11

2. Power plant load reduction: this scenario is simulated by making proportional step changes in both flue gas rate and power cycle total steam rate. According to previous studies[6,7] any change in inlet gas composition is neglected.

3. Foaming in the columns: Foaming in amine solution plants is one of the leading causes of plant upsets. The expansion of liquid due to passage of vapor results in liquid buildup on the packing in the bed. Accumulating liquid in one of the columns leads to reduced liquid holdup in other inventories and endangers the operation of downstream pumps. Due to sudden change in holdup the performance of absorption and/or stripping might be also affected. This work simulates this condition by including a factor in the hydraulic model of the absorber.

Level ratio control (LRC) on storage tanks is an alternative that replaces a conventional one-tank level control to balance the liquid holdup between the lean and rich tanks. Cascade control can provide improved performance over single loop control, especially control loops that manipulate the variable being exposed to upstream disturbances. This case study manipulated steam rate and solvent circulation rate, which are likely to vary because of possible disturbances and fitted the potential control loops with cascade control. Table 3 provides the list of control configurations with modifications (LRC and cascade control) applied for the basic version of each structure.

Table 3: Evaluated basic control configurations with modifications

Configuration	Alternatives
F_L-F_S-P	Basic, Basic+LRC
F_L-T-P	Basic, Basic+LRC, Basic+LRC+T cascaded
F_L-Lldg-P	Basic, Basic+LRC, Basic+LRC+Lldg cascaded
Rldg-Lldg-P	Basic, Basic+LRC, Basic+LRC+Lldg cascaded, Basic+LRC+Rldg cascaded,

12

Basic+LRC+Rldg cascaded+ Lldg cascaded

T-Rem-P　　　Basic, Basic+LRC, Basic+LRC+T cascaded, Basic+LRC+Rem cascaded,

Basic+LRC+T cascaded+ Rem cascaded

The dynamic performance of the proposed control structures is evaluated in response to previously defined disturbances and abnormal conditions. For absorber and stripper foaming the dynamic results are generated for a 10% step change in the packing bed liquid holdup while maintaining control of the loops at their initial set points via PI controllers. For partial load operation, besides looking at small changes in inputs we also consider a wide range of conditions; that is, 80% and 60% reduction in reboiler and power plant load respectively. In all cases of partial load operation, the liquid levels are tightly controlled at their initial set points with PI controllers while the other controlled variables utilize PI controllers at the optimum set points where the lost work is minimized. For power plant load reduction it is also assumed that the control objective is to maintain the removal at its initial design value (90%) as the power plant load varies along with minimizing lost work at the new state. The tuning parameters of PI controllers are calculated by using ITAE correlations to maximize the performance of each loop while other closed control loops are in service.

The simulations of dynamic scenarios with small changes in the magnitude of inputs have shown that all configurations are able to control the liquid levels in acceptable ranges without any problem associated with pump operation. For operation over the narrow range of conditions selected, figures show stripper response because this variable can represent the overall performance of the plant such as response time and smoothness of dynamics and determine if the compressor is operating safely during dynamic scenarios. The following sections present a discussion of dynamic behavior of the control structure in response to the introduced disturbances.

13

Simulation Results

This section presents a discussion of dynamic performance of the control structures in response to the introduced disturbances.

Reboiler steam rate reduction

The simulation outputs have shown that replacing level control on one of the tanks by level ratio control for both tanks did not bring an improvement for all structures excluding T-Rem-P in which LRC improves the pressure response by eliminating undesirable oscillations (Figure 2). Based on the results, loading control, either directly or indirectly performed in structures called F_L-Lldg-P, Rldg-Lldg-P and T-Rem-P, introduces some oscillations in the responses (Figures 2 and 3). Cascade control improves the dynamics in the cases having oscillatory responses, such as F_L-Lldg-P and Rldg-Lldg-P. F_L-T-P does not show oscillatory behavior and so fitting the TC loop with cascade control does not change the response. Figure 4 compares the pressure response for all the control structures subject to steam rate reduction. Although F_L-Lldg-P and Rldg-Lldg-P configurations were fitted by cascade control, their responses are not as smooth and fast as the response of F_L-F_s-P and F_L-T-P.

Figure 2:

Figure 3:

Figure 4: Power plant load reduction

The effects of power plant load reduction on the capture operation is simulated with various control structures by considering the dynamic performance with -10% step changes in both flue gas rate and power cycle steam rate. This study shows that replacing level control by level ratio control has no significant positive or negative effects on dynamic responses in all the configurations. Controlling the rich and lean loading by

14

liquid valve position and steam valve position leads to sustained oscillations that make the plant unstable. Cascading rich loading control loop with a flow controller on the liquid valve could substantially damp the oscillation and stabilize the system. Cascade control on the lean loading has no effect on the response (Figure 5).

The basic version of T-Rem-P structure with or without level ratio control exhibits a dampened response. Cascading either a temperature or a removal control loop with a flow controller makes the response worse and when both loops are cascaded with flow controllers, the system becomes unstable with sustained oscillation (Figure 6). This case is an example of a system in which cascade control has adverse effects on dynamic performance.

Figure 5:

Figure 6:

Figure 7:

According to Figure 7, by comparing the pressure responses provided by the most effective version of control configurations to the partial load operation of power plant, F_L-T(cascade)-P and F_L-F_s-P have the highest rank in terms of smoothness and minimum settling time.

RGA is a well known method to pair the manipulated and controlled variables. However, steady-state analysis shows this method is not always reliable to compare structure with respect to the dynamic behavior during the transition time. Dynamic simulation shows that F_L-Lldg-P is more interactive than F_L-T-P while RGA predicts that F_L-Lldg-P is a less interactive system than F_L-T-P since the diagonal elements are much closer to unity (Table 2).

15

Absorber and stripper foaming scenarios

According to the outputs of simulating absorber and stripper foaming, level ratio control provides a noticeable improvement on dynamics especially for Rldg-Lldg-P in which the response is very oscillatory and for T-Rem-P where unstable sustained oscillation is observed. Applying LRC results in stabilizing and damping the oscillations (Figures 8 and 9).

Figure 8:

Figure 9:

Figure 10:

Cascade control is not an effective strategy for those control structures to reject the foaming disturbance. Furthermore it makes the responses worse by introducing damped or sustained oscillations. The comparison of the control structures (Figure 10) again shows that F_L-T(cascade)-P and F_L-F_s-P have the highest rank in terms of smoothness and minimum settling time.

Partial load operations over a wide range of operating conditions

This part of the study is focused on dynamic performance evaluation over a wide range of operating conditions when the capture plant is run in one of the two partial load operations. Two control configurations are selected among those discussed previously for comparison:

1. F_L-T (cascade)-P: because of its best dynamic performance among all the structures for rejecting disturbances and bringing the plant to the targeted set points for all scenarios.

2. Rldg(cascade)-Lldg(cascade)-P: because it is a highly interactive system that produces oscillatory responses; however, it was successful in set point tracking and disturbance rejection.

16

It should be noted that the storage tanks are fitted with the level ratio control loop. The objective is to examine those configurations in terms of the ability of controlling the capture at new operating conditions and running the pumps and compressor safely in response to the following cases:

      1. Partial load operation of reboiler simulated in two phases:

      Phase 1: Ramping steam rate from 100% to 20% load in 30 min at time = 0

      Phase 2: Ramping steam rate from 20% to 100% load in 30 min at time = 60 min

      2. Partial load operation of power plant; simulated in two phases:

      Phase 1: Ramping flue gas rate and power cycle steam rate simultaneously from 100% to 40% load in 10 min at time = 0

      Phase 2: Ramping flue gas rate and power cycle steam rate simultaneously from 40% to 100% load in 10 min at time = 60 min

Similar to the previous simulations of operation over a narrow range, this work selected the set points of level control loops at the initial design values while the other control loop set points are set at optimal values that have already been obtained by an off-line steady state optimization. Therefore, in current simulations the set points vary with time as the load changes.

According to the simulation outputs, both configurations have the ability to deal with 80% load change in the reboiler steam and maintain the stability of the capture plant. The controlled variables (solvent rate, stripper pressure, lean and rich loading) show fast and smooth set point tracking during forward and reverse phases of this operation.

A few controlled variables are not being controlled effectively. Reboiler temperature is one of the variables that show non-smooth dynamic behavior with relatively large transitional deviations from the set point. This situation is more noticeable for

17

Rldg(cascaded)-Lldg(cascaded)-P where this variable is not controlled directly (Figure 11).

Liquid levels in the tanks are also not controlled well. As shown in Figure 12, the ratio of levels shows a large drop after 0.5 hour which can result in operational problems such as cavitation and the lean tank downstream pump running dry.

Figure 11:

Figure 12:

Simulation of the large change in power plant load (60%) shows that FL-T(cascade)-P perfectly controls the capture at the desired set points with smooth and fast responses for both forward and reverse operations. Rldg(cascaded)-Lldg(cascaded)-P is not a successful structure for control nor does it stabilize the plant condition.

As shown in Figure 13, this configuration forces the stripper pressure to follow the set point initially but just after finishing the input ramp, unstable oscillations are appearing in the whole system, which results in some operational problems such as saturation of liquid valves and eventually failure of the simulation. That is why Figure 13 does not show the complete response of stripper pressure for this configuration.

Figure 13:

FL-T (cascade)-P shows good performance in controlling capture for large changes in operating conditions. It is able to bring the plant to the new operating condition in less than five min, which is relatively short for such a system in which the total liquid residence time is about 11 min.

INFLUENCE OF STORAGE TANKS HOLD UP TIME ON DYNAMICS

The objective of this work is to provide a systematic approach to investigate the influence of the residence time in the lean and rich tank on the quality of dynamics in response to a few types of disturbances. In frequency response analysis, which is used to analyze this

18

dynamic system, we apply a sinusoidal input and sketch a graph showing the output response characteristics versus frequency of the input signal.

Stripper top pressure is selected as the output because it represents the compressor operation and reflects the whole system dynamic behavior. The variation of flue gas rate, total steam rate in power cycle, and absorber and stripper bed liquid holdups are considered as disturbances for this analysis. The plant is fully controlled by the FL-T(cascade)-P configuration (shown in Figure 14), proved to be the most effective control structure among the evaluated ones, at initial set points for all control loops. The simulation is run for each disturbance at a specific input frequency and then the magnitude of the pressure oscillation is calculated relative to the design value in percent.

Figure 14:

The liquid residence time in absorber sump, stripper sump, absorber bed, and stripper bed are initialized at 2, 2, 2, and 1 min, respectively, and they do not change significantly as disturbances are applied. The liquid residence time in the storage tanks is varied to see the effects on the magnitude of the oscillations.

Figure 15 represents the frequency response to the flue gas rate sinusoidal change. As seen for all cases of holdup time in the tanks, there is a critical frequency (ω_c) where the maximum magnitude is located. Based on the simulations it is found that the critical frequency corresponds to the response time of the system to the related input. Since the frequency is the inverse of time, a higher critical frequency is equivalent to a faster response of the system. Therefore this graph can elucidate two important dynamic characteristics: the response time and the magnitude of output change.

Figure 15:

As seen in Figure 15, increasing the τ of the lean tank reduces the response time while at the same time it increases the magnitude of the oscillation, an undesired effect. Increasing

19

the τ of the rich tank produces a more sluggish response, however, there is an optimum

rich tank holdup between 2 and 10 min that minimizes the magnitude. Figure 16, showing

the dynamic response of the pressure to -10% step change in the flue gas rate, is

consistent with the above discussed results. As observed, a 5-min holdup in the rich tank

shows the minimum magnitude for the inverse response and 10-min holdup in the lean

tank provides the fastest response.

Figure 16:

Figure 17:

The change in the absorber bed liquid holdup (foaming) is the other disturbance in which

the associated frequency response is calculated and shown in Figure 17. Similar to the

flue gas rate change, changing the residence time of the tanks influences the dynamics

both in magnitude and response time. In contrast to the flue gas rate, increasing τ of the

lean tank increases the response time while increasing τ of the rich tank makes the

response faster. As observed in this figure, increasing the residence time in both tanks

reduces the magnitude; however, for the rich tank increasing the time from 5 to 10 min

does not have any benefit but adds an additional amine inventory cost. The step response

shown in Figure 18 confirms the interpretations of frequency response.

Frequency response analysis has shown that holdup time in storage tanks does not have a

significant impact on dynamics when the plant is subjected to the power cycle steam rate

change or stripper foaming.

Figure 18:

4.1 CONCLUSIONS

This paper has developed an effective multi-loop feedback control structure for a

CO_2 capture system. Load variation and foaming in columns make this control problem

challenging since they involve a combination of disturbance rejection and set point tracking at the same time.

Frequency response analysis investigated the effects of holdup in storage tanks on dynamic performance. The frequency plots provide important dynamic performance information related to the response time and the magnitude of deviation from the target.

1. The most effective multi-loop control structure is to control the solvent rate by the liquid valve, the reboiler temperature by the steam valve and the stripper pressure by the compressor speed. Replacing the conventional level control on one of the lean or rich tanks by a level ratio control not only keeps the liquid holdup in balance in the tanks but also plays an important role in dampening oscillations for the column foaming scenarios.

2. Controlling rich or lean loading or any combination such as CO_2 removal is not a proper strategy specifically when the plant has to be operated within wide ranges of operation.

3. Cascading CO_2 loading control loops with the flow controller dampens the oscillations in response to the load changes, but performs poorly when foaming occurs in one of the columns.

4. A multi-loop control system with F_L-T (cascade)-P configuration with level ratio control on the storage tanks shows a degree of satisfactory performance, robustness and safe operation that would avoid the costs of developing an advanced multivariable system.

5. Increasing the holdup times in lean and rich tanks is not always helpful to damp the oscillations and reject the disturbances. It may increase either the magnitude of overshoot and inverse responses or the response time of the plant.

21

NOTATION

a	Effective specific area of the packing, m^{-1}
C	Molar density, mol/m^3
D_c	Column diameter, m
E	Energy hold-up, KJ
h	Heat transfer coefficient, KW/m$^2\,K$
h_t	Total liquid holdup, m
H	Enthalpy, KJ/mol
$\overline{H}$	Partial Enthalpy, KJ/mol
k	Mass transfer coefficient, m/s
l	Height of segment, m
L	Liquid flow rate, mol/s
ldg	Loading (moles of CO_2/mole MEA)
M	Molar holdup, moles
MV	Manipulated variable
N	Molar flux, mol/m^{2}s
$P^*_{CO_2}, P^*_{H_2O}$	Equilibrium partial pressure, KPa
P_{CO_2}, P_{H_2O}	Partial pressure, KPa
T	Temperature, K
V	Vapor flow rate, mol/s
x	Liquid mol fraction
y	Vapor mol fraction

Greek Letter

ε	Void fraction of the packing
$\Delta H^{des}_{CO_2}$	Heat of adsorption of CO_2, KJ/mol
$\Delta H^{vap}_{H_2O}$	Heat of vaporization of H_2O, KJ/mol
τ	Response time, sec

Subscripts

j	Segment index

Superscripts

B	Bulk
I	Interface
L	Liquid phase
V	Vapor phase

22

REFERENCES

1. Bergerson JA, Lave LB. Baseload coal investment decisions under uncertain carbon legislation. *Environ. Sci. Technol*. 2007;41:3431–3436.

2. Freguia S, Rochelle GT. Modeling of CO_2 capture by aqueous MEA. *AIChE J.,* 2003;49:1676–1686.

3. Oyenekan BA, Rochelle GT. Alternative stripper configuration for CO_2 capture by aqueous amines, *AIChE J.,* 2007;53:3144–3154.

4. Plaza JM, Chen E, Rochelle GT. Absorber intercooling in CO_2 absorption by Piperazine promoted Potassium Carbonate. *AIChE J.* 2010:56: 905–914.

5. Van Wagener DH, Rochelle GT. Stripper configurations for CO_2 capture by aqueous MEA and PZ. *Energy Proc.* 3011;4: 1323–1330.

6. Kvamsdal HM, Jakobsen JP, Hoff KA. Dynamic modeling and simulation of a CO_2 absorber column for post-combustion CO_2 capture. *Chem. Eng. & Proc.* 2009;48:135–144.

7. Lawal A, Wang M, Stephenson P, Koumpouras G, Yeung H. Dynamic modeling and analysis of post-combustion CO_2 chemical absorption process for coal-fired power plants. *Fuel*. 2010; 89:2791–2801.

8. Ziaii S, Rochelle GT, Edgar TF. Dynamic modeling to minimize energy use for CO_2 capture in power plants by aqueous Monoethanolamine. *Ind. Eng. Chem. Res.* 2009;48: 6105–6111.

9. Gunaseelan P, Wankat PC. Transient pressure and flow predictions for concentrated packed absorbers using a dynamic nonequilibrium model. *Ind. Eng. Chem. Res.* 2002;41:5775–5788.

10. Peng J, Edgar TF, Eldridge RB. Dynamic rate-based and equilibrium models for a packed reactive distillation column. *Chem. Eng. Sci.* 2003;58: 2671–2680.

11. Seborg DE, Edgar TF, Mellichamp DA. *Process Dynamics and Control* (2nd edition). New York:Wiley, 2004.

12. Chalmers H, Gibbins J, Leach M. Initial assessment of flexibility of pulverized coal-fired power plants with CO_2 capture. 3rd International Conference on Clean Coal Technologies for our Future, 2007; Sardinia, Italy.

13. Ziaii S, Cohen SM, Rochelle GT, Edgar TF, Webber ME. Dynamic operation of amine scrubbing in response to electricity demand and pricing. *Energy Proc.* 2009;1: 4047–4053.

14. Schach MO, Schneider R, Schramm H, Repke JU. Control structure design for CO_2 absorption processes for large operating ranges. *PCCC1*, 2011: Abu Dhabi.

15. Faanes A, Skogestad S, A systematic approach to the design of buffer tanks. *Comp. & Chem. Eng.* 2000;24:1395–1401.

16. Luyben WL. Dynamics and control of recycle systems. 1. simple open-loop and closed-loop systems. *Ind. Eng. Chem. Res.* 1993;32: 466–475.

23

17. Aboudheir A, Tontiwachwuthikul P, Idem R. Rigorous model for predicting the behavior of CO_2 absorption into AMP in packed-bed absorption columns. *Ind. Eng. Chem. Res.*. 2006;45:2553–2557.

18. Lucquiaud M. Steam cycle options for capture-ready power plants, retrofits and flexible operation with post combustion CO_2 capture. *Ph.D. Dissertation*, Imperial College, London, England. 2010.
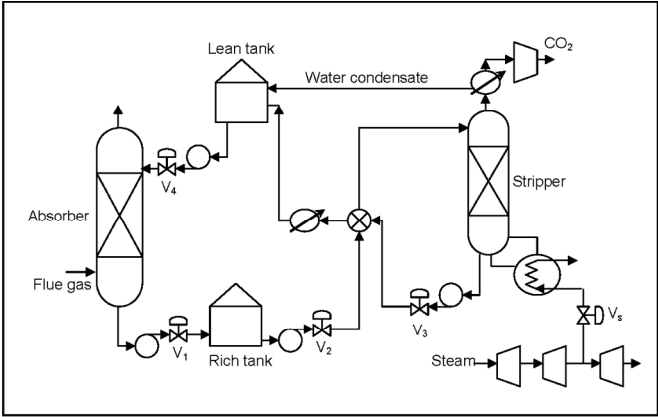
24

1
2
3
4
5
6
7
8
9
10
11
12
13
14
15
16
17
18
19
20
21
22
23
24
25
26
27
28
29
30
31
32
33
34
35
36
37
38
39
40
41
42
43
44
45
46
47
48
49
50
51
52
53
54
55
56
57
58
59
60

Figure 1: Process flow diagram of absorption/stripping process combined with storage tanks and power cycle steam turbines
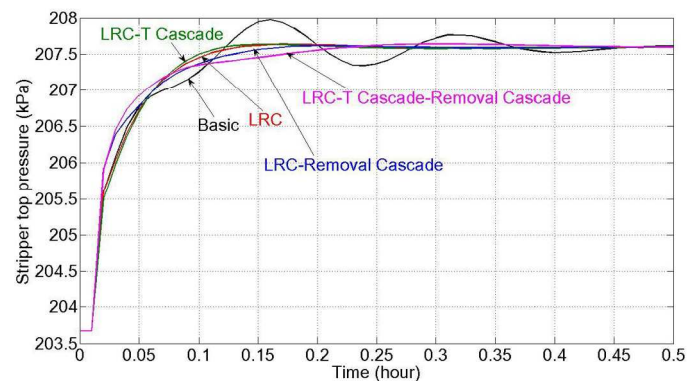
215x279mm (200 x 200 DPI)

Figure 2: Stripper top pressure response in reboiler load reduction (-5% step change), in the presence of T-Rem-P control structure with modifications listed in Table 3. Set points of level control (LC) loops are set at initial values and set points of TC, RemC and PC loops are set at new optimum values.

215x279mm (222 x 189 DPI)

1
2
3
4
5
6
7
8
9
10
11
12
13
14
15
16
17
18
19
20
21
22
23
24
25
26
27
28
29
30
31
32
33
34
35
36
37
38
39
40
41
42
43
44
45
46
47
48
49
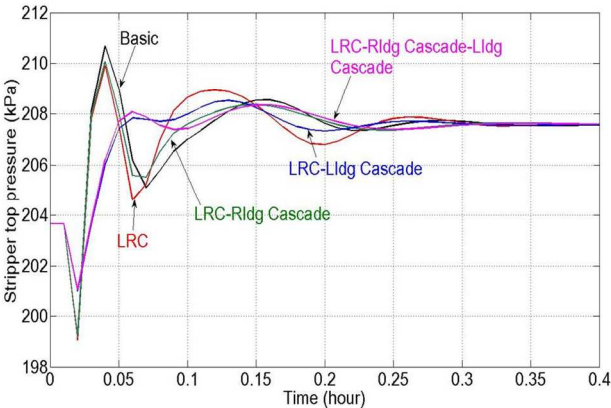50
51
52
53
54
55
56
57
58
59
60

Figure 3: Stripper top pressure response in reboiler load reduction (-5% step change), in the presence of Rldg-Lldg-P control structure with modifications listed in Table 3. Set points of level control (LC) loops are set at initial values and set points of RldgC, LldgC and PC loops are set at new optimum values.
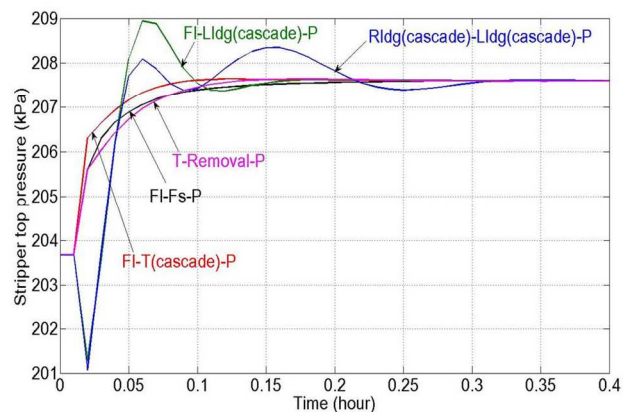
215x279mm (180 x 180 DPI)

Figure 4: Comparison of control structures in terms of stripper top pressure response in reboiler load reduction (-5% step change). Level ratio control (LRC) is considered for lean and rich tanks. Set points of LC and LRC loops are set at initial values and set points of other control loops are set at new optimum values.

215x279mm (180 x 180 DPI)

1
2
3
4
5
6
7
8
9
10
11
12
13
14
15
16
17
18
19
20
21
22
23
24
25
26
27
28
29
30
31
32
33
34
35
36
37
38
39
40
41
42
43
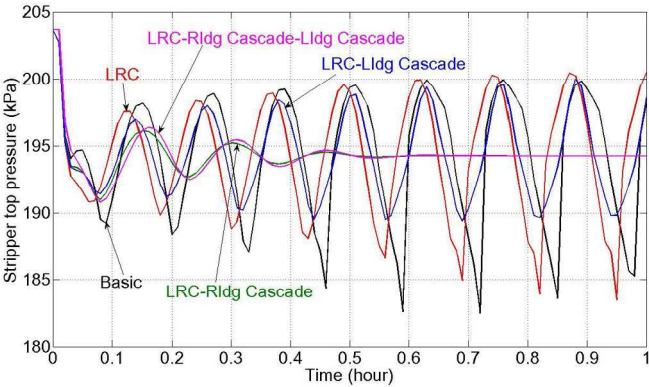44
45
46
47
48
49
50
51
52
53
54
55
56
57
58
59
60

Figure 5: Stripper top pressure response in power plant load reduction (-10% step change), in the presence of Rldg-Lldg-P control structure with modifications listed in Table 3. Set points of level control (LC) loops are set at initial values and set points of RldgC, LldgC and PC loops are set at new optimum values that keep the CO_2 removal at 90% removal.

215x279mm (222 x 194 DPI)

1
2
3
4
5
6
7
8
9
10
11
12
13
14
15
16
17
18
19
20
21
22
23
24
25
26
27
28
29
30
31
32
33
34
35
36
37
38
39
40
41
42
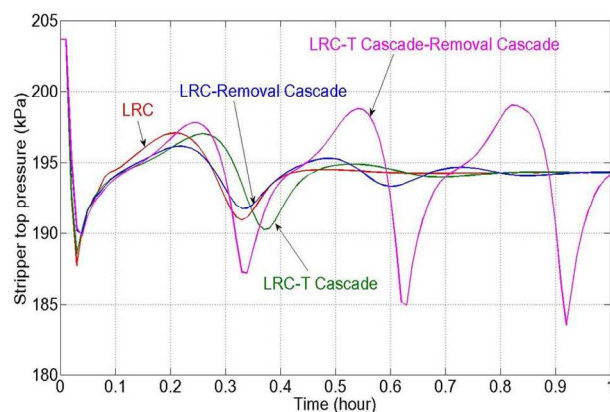43
44
45
46
47
48
49
50
51
52
53
54
55
56
57
58
59
60

Figure 6: Stripper top pressure response in power plant load reduction (-10% step change), in the presence of T-Rem-P control structure with modifications listed in Table 3. Set points of LC loops are set at initial values and set points of RldgC, LldgC and PC loops are set at new optimum values that keep the CO_2 removal at 90% removal.

215x279mm (180 x 180 DPI)

1
2
3
4
5
6
7
8
9
10
11
12
13
14
15
16
17
18
19
20
21
22
23
24
25
26
27
28
29
30
31
32
33
34
35
36
37
38
39
40
41
42
43
44
45
46
47
48
49
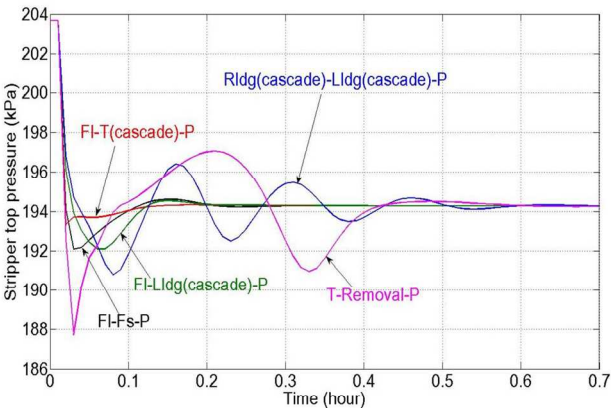50
51
52
53
54
55
56
57
58
59
60

Figure 7: Comparison of control structures in terms of stripper top pressure response in power plant load reduction (-10% step change). Set points of LC loops are set at initial values and set points of other control loops are set at new optimum values that keep the CO_2 removal at 90% removal.
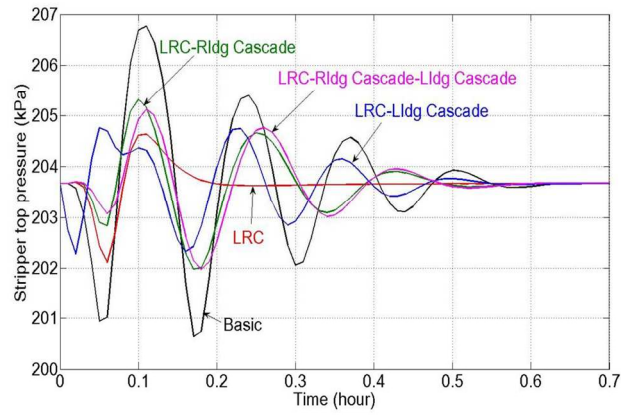
215x279mm (180 x 180 DPI)

Figure 8: Stripper top pressure response to absorber foaming (10% step change), in the presence of Rldg-Lldg-P with modifications listed in Table 3. Set points of all control loops are set at initial values.

215x279mm (180 x 180 DPI)

1
2
3
4
5
6
7
8
9
10
11
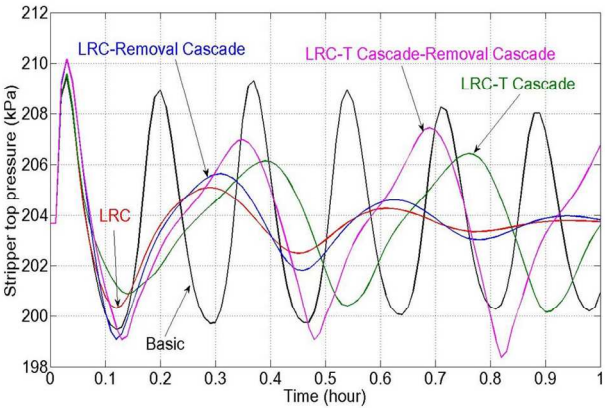12
13
14
15
16
17
18
19
20
21
22
23
24
25
26
27
28
29
30

Figure 9: Stripper top pressure response in absorber foaming (10% step change), in the presence of T-Rem-P control structure with modifications listed in Table 3. Set points of all control loops are set at initial values.

31
32
33
34
35
36
37
38
39
40
41
42
43
44
45
46
47
48

215x279mm (180 x 180 DPI)

49
50
51
52
53
54
55
56
57
58
59
60

1
2
3
4
5
6
7
8
9
10
11
12
13
14
15
16
17
18
19
20
21
22
23
24
25
26
27
28
29
30
31
32
33
34
35
36
37
38
39
40
41
42
43
44
45
46
47
48
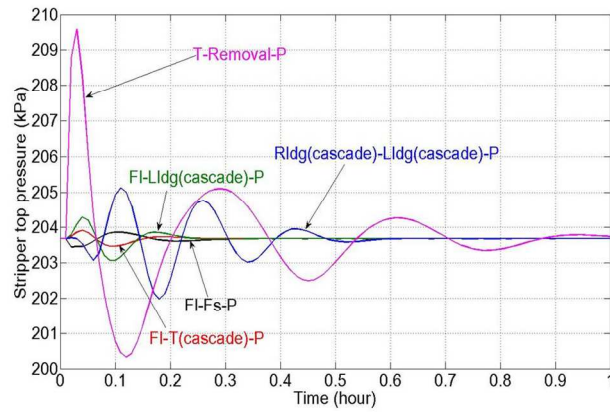49
50
51
52
53
54
55
56
57
58
59
60

Figure 10: Response of control structures as stripper top pressure response to absorber foaming (10% step change). Set points of all control loops are set at initial values.

215x279mm (180 x 180 DPI)

1
2
3
4
5
6
7
8
9
10
11
12
13
14
15
16
17
18
19
20
21
22
23
24
25
26
27
28
29
30
31
32
33
34
35
36
37
38
39
40
41
42
43
44
45
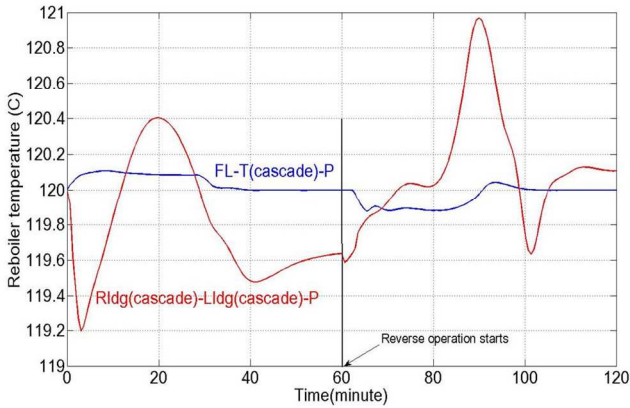46
47
48
49
50
51
52
53
54
55
56
57
58
59
60

Figure 11: Reboiler temperature responses to the ramp change of reboiler steam load from 100% to 20% applied at time = 0 and reverse change applied at time = 60 min. The responses are given for F_L-T (cascade)-P and Rldg(cascade)- Lldg (cascade)-P control configurations.

215x279mm (180 x 180 DPI)

1
2
3
4
5
6
7
8
9
10
11
12
13
14
15
16
17
18
19
20
21
22
23
24
25
26
27
28
29
30
31
32
33
34
35
36
37
38
39
40
41
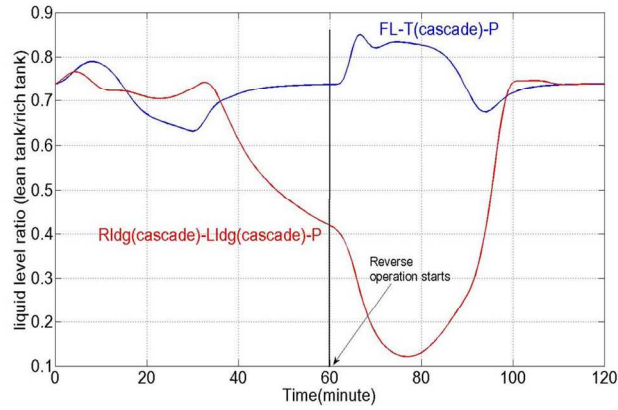42
43
44
45
46
47
48
49
50
51
52
53
54
55
56
57
58
59
60

Figure 12: The responses of liquid level ratio of storage tanks to the ramp change of reboiler steam load from 100% to 20% applied at time = 0 and reverse change applied at time = 60 min. The responses are given for F_L-T (cascade)-P and Rldg(cascade)- Lldg (cascade)-P control configurations.

215x279mm (180 x 180 DPI)

1
2
3
4
5
6
7
8
9
10
11
12
13
14
15
16
17
18
19
20
21
22
23
24
25
26
27
28
29
30
31
32
33
34
35
36
37
38
39
40
41
42
43
44
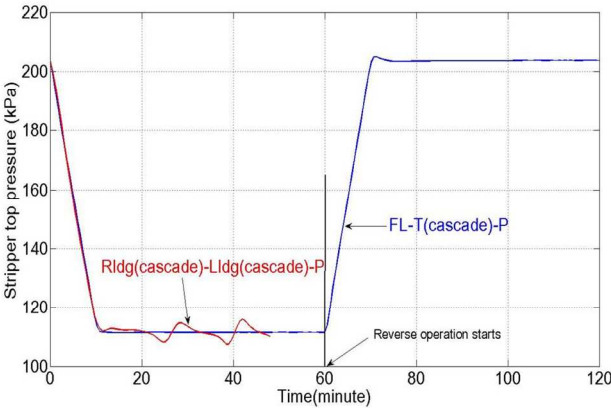45
46
47
48
49
50
51
52
53
54
55
56
57
58
59
60

Figure 13: The response of stripper top pressure to the ramp change of power plant load from 100% to 40% applied at time = 0 and reverse change applied at time = 60 min. The responses are given for F_L-T (cascade)-P and Rldg(cascade)- Lldg (cascade)-P control configurations.
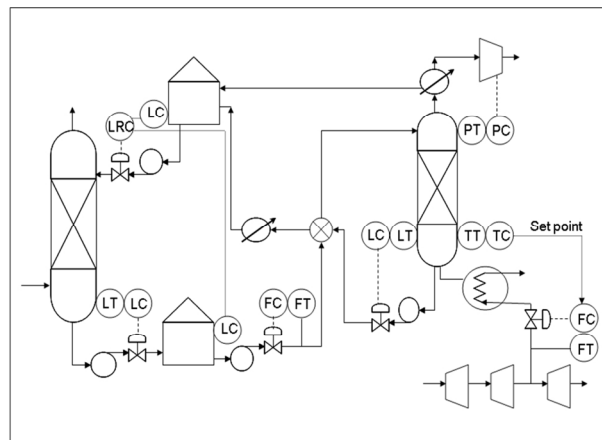
215x279mm (180 x 180 DPI)

Figure 14: Process flow diagram with F_L-T (cascade)-P control configuration
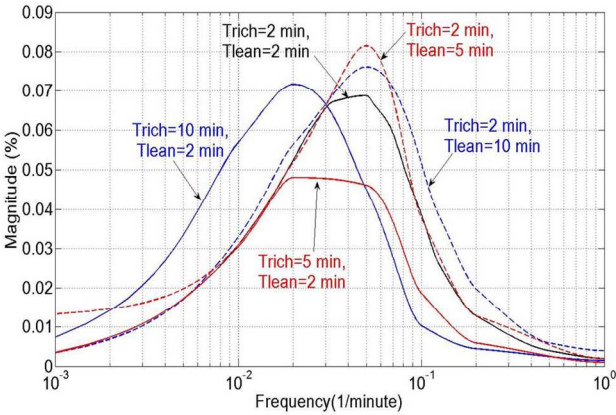
215x279mm (180 x 180 DPI)

1
2
3
4
5
6
7
8
9
10
11
12
13
14
15
16
17
18
19
20
21
22
23
24
25
26
27
28
29
30
31
32
33
34
35
36
37
38
39
40
41
42
43
44
45
46
47
48
49
50
51
52
53
54
55
56
57
58
59
60

Figure 15: Frequency response of the stripper top pressure to ±10% sinusoidal signal in the flue gas rate for different sets of lean and rich tank hold up times. The initial liquid holdup times in other inventories are as follows: $\tau_{absorber}$= 2 min, $\tau_{stripper}$= 1 min, $\tau_{absorber-sump}$= 2 min, $\tau_{stripper-sump}$= 2 min.

215x279mm (180 x 180 DPI)

1
2
3
4
5
6
7
8
9
10
11
12
13
14
15
16
17
18
19
20
21
22
23
24
25
26
27
28
29
30
31
32
33
34
35
36
37
38
39
40
41
42
43
44
45
46
47
48
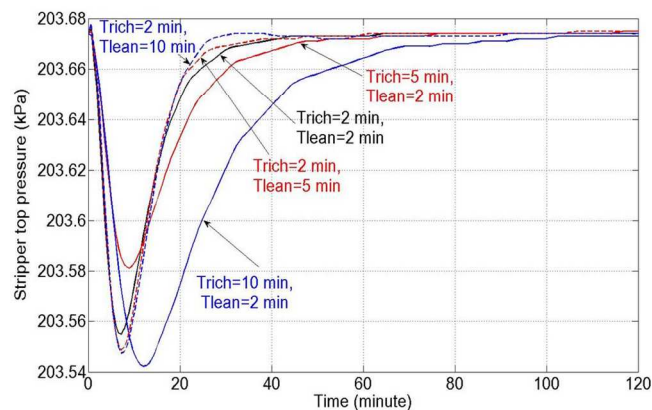49
50
51
52
53
54
55
56
57
58
59
60

Figure 16: The comparison of the effects of initial liquid hold up time in the lean and rich tanks on the stripper top pressure in response to -10% step change in the flue gas rate. The responses are given for F_L-T (cascade)-P. The initial liquid hold up time in other inventories is: $\tau_{absorber}=$ 2min, $\tau_{stripper}=$ 1min, $\tau_{absorber\text{-}sump}=$ 2min, $\tau_{stripper\text{-}sump}=$ 2min.

215x279mm (180 x 180 DPI)

1
2
3
4
5
6
7
8
9
10
11
12
13
14
15
16
17
18
19
20
21
22
23
24
25
26
27
28
29
30
31
32
33
34
35
36
37
38
39
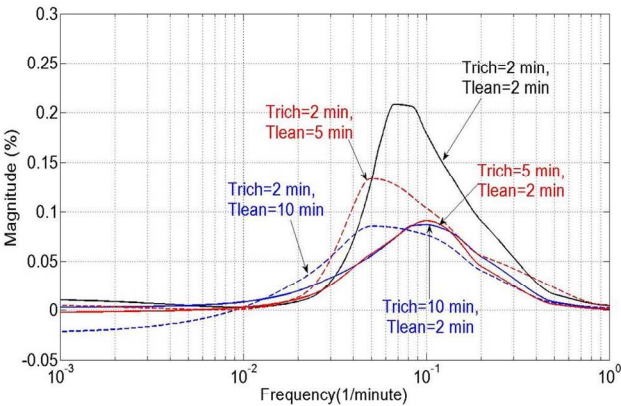40
41
42
43
44
45
46
47
48
49
50
51
52
53
54
55
56
57
58
59
60

Figure 17: Frequency response of the stripper top pressure to ±10% sinusoidal signal of the liquid hold up on the absorber packing bed for different sets of lean and rich tank holdup times. The initial liquid holdup times in other inventories are as follows: $\tau_{absorber}$= 2min, $\tau_{stripper}$= 1min, $\tau_{absorber-sump}$= 2min, $\tau_{tripper-sump}$= 2min.

215x279mm (180 x 180 DPI)

1
2
3
4
5
6
7
8
9
10
11
12
13
14
15
16
17
18
19
20
21
22
23
24
25
26
27
28
29
30
31
32
33
34
35
36
37
38
39
40
41
42
43
44
45
46
47
48
49
50
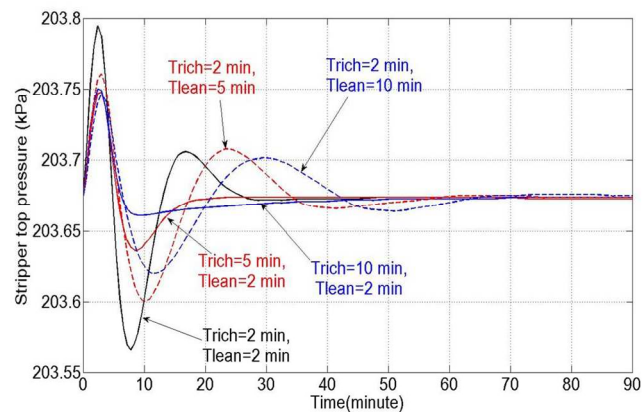51
52
53
54
55
56
57
58
59
60

Figure 18: The comparison of the effects of initial liquid hold up time in the lean and rich tanks on the stripper top pressure in response to -10% step change in the absorber bed hold up. The responses are given for F_L-T (cascade)-P control configuration. The initial liquid holdup times in other inventories are as follows: $\tau_{absorber}$= 2min, $\tau_{stripper}$= 1min, $\tau_{absorber-sump}$= 2min, $\tau_{stripper-sump}$= 2min.

215x279mm (180 x 180 DPI)